

A.D. 1308
unipg
UNIVERSITÀ DEGLI STUDI
DI PERUGIA

Università degli Studi di Perugia

Dipartimento di Fisica e Geologia

Dottorato di Ricerca in Fisica, XXXVII Ciclo

Study of short term variations in the cosmic proton fluxes with the AMS-02 experiment

Supervisors

Nicola Tomassetti
Valerio Vagelli

Candidate

Francesco Faldi

Anno Accademico 2024/2025

Contents

1 Cosmic Rays **8**
- 1.1 Definition and Description . . . 8
- 1.2 Discovery and First Observations . . . 9
- 1.3 Energy Spectrum . . . 11
- 1.4 Origin and Composition . . . 13
  - 1.4.1 Galactic Cosmic Rays . . . 14
  - 1.4.2 Solar Energetic Particles . . . 16
  - 1.4.3 Trapped Particles . . . 17
- 1.5 SEP Acceleration Mechanisms . . . 18
  - 1.5.1 Diffusive Shock Acceleration . . . 18
  - 1.5.2 Magnetic Reconnection . . . 20
- 1.6 Antimatter in Cosmic Rays . . . 22

2 The Solar System **24**
- 2.1 The Sun . . . 24
  - 2.1.1 Solar Activity Cycle . . . 27
  - 2.1.2 Transient Events . . . 29
  - 2.1.3 Heliosphere . . . 32
- 2.2 The Earth . . . 34
  - 2.2.1 Geomagnetic Field . . . 34
  - 2.2.2 Magnetosphere . . . 34
  - 2.2.3 Ionosphere . . . 37
  - 2.2.4 Geomagnetic Rigidity Cutoff . . . 38
- 2.3 Space Weather . . . 40
  - 2.3.1 Radiation Damage to Electronics . . . 40
  - 2.3.2 Radiation Hazards for Biological Organisms . . . 41

3 The AMS-02 Detector **44**
- 3.1 Permanent Magnet . . . 45
- 3.2 Transition Radiation Detector . . . 46
- 3.3 Time Of Flight Detector . . . 49

3.4 Silicon Tracker . . . 50
3.5 Anti Coincidence Counter . . . 53
3.6 Ring Imaging Cherenkov Detector . . . 54
3.7 Electromagnetic Calorimeter . . . 55
3.8 Data Acquisition and Trigger . . . 57
3.8.1 Trigger Signal . . . 59
3.9 AMS Livetime . . . 60
3.10 Installation and Operations . . . 61
3.11 Scientific Results . . . 63
3.12 On-flight and Monte Carlo Dataset . . . 65
3.12.1 On-flight Data . . . 65
3.12.2 Monte Carlo Simulation . . . 66
3.12.3 RTI Dataset . . . 67

4 Proton Flux Measurement 68
4.1 Cosmic Rays Flux Definition . . . 69
4.2 Proton Selection . . . 72
4.3 Exposure Time . . . 75
4.4 Selection Efficiencies . . . 79
4.4.1 Layer 1 Efficiency . . . 79
4.4.2 ToF Efficiency . . . 81
4.4.3 Trigger Efficiency . . . 82
4.4.4 Inner Tracker Efficiency . . . 83
4.5 Acceptance . . . 85
4.5.1 Geometrical Acceptance . . . 86
4.5.2 Data-MC Corrections and Corrected Acceptance . . . 86
4.6 Correction for Energy Loss and Unfolding . . . 88
4.6.1 Energy Loss Estimation . . . 89
4.6.2 Unfolding Procedure: Folded Acceptance . . . 92
4.7 Average Proton Flux . . . 96
4.7.1 Statistical Uncertainty . . . 96
4.7.2 Acceptance and ISS/MC Corrections Systematic Uncertainties 97
4.7.3 Unfolding Systematic Uncertainty . . . 98
4.7.4 Absolute Rigidity Scale Systematic Uncertainty . . . 98
4.7.5 Final Average Flux . . . 99
4.8 Daily Proton Flux . . . 101
4.8.1 Daily Efficiencies, Corrections and Uncertainties . . . 102
4.8.2 Final Daily Flux . . . 104
4.8.3 Daily Flux Interpretation . . . 108

5 Solar Energetic Particle Flux 112
5.1 SEP Finding Algorithm . . . 113

5.2 Polar-pass Event Selection . . . 115
5.2.1 Rigidity Cutoff Alternative . . . 116
5.2.2 Polar-Pass Region Definition . . . 119
5.3 CR Background Subtraction . . . 121
5.3.1 Rigidity to Energy Conversion . . . 121
5.3.2 Proton Flux as Time Series . . . 122
5.3.3 Background Normalization . . . 125
5.3.4 GCR Subtraction Systematic Uncertainties . . . 129
5.4 Polar-Pass SEP Fluxes and Spectra . . . 132

6 SEP Fluxes Interpretation 136
6.1 SEP Spectra at Peak Intensity . . . 136
6.1.1 Features in the SEP Spectra . . . 137
6.1.2 Spectral Fits with PAMELA . . . 139
6.1.3 Spectral Fits with AMS . . . 140
6.2 Temporal Evolution of SEP Events . . . 144
6.2.1 Evolution of the Spectral Index . . . 144
6.2.2 Comparison with GOES Fluxes . . . 147

7 Conclusions 152

A Analysis Binning 157

B Additional SEP Spectral Fits 159

Introduction

The Sun is the primary source of energy in the solar system, behaving also as an efficient particle accelerator. Galactic Cosmic Rays (GCRs) travel inside the Solar System and face the outward flux of solar particles, called solar wind. The latter, being an *ideal plasma*, carries the solar magnetic field along with itself, disturbing the incoming GCR flux. The GCR flux magnitude is in anti-correlation with the intensity of the long term variations of the solar activity cycle, an effect known as *solar modulation of cosmic rays*. In the meantime, the GCR flux is also subjected to short term temporal variations. Approaching solar maximum, in fact, magnetic field lines get twisted and deviate from a dipolar configuration, which sometimes causes them to break (magnetic reconnection). In these events, solar flares and/or Coronal Mass Ejections (CMEs) can be produced. Particles may be accelerated to much higher energies than the typical solar wind and ejected from the Sun, forming the so called Solar Energetic Particles (SEP) flux. As CMEs and SEPs propagate outward through the heliosphere, they carry along a number of interesting properties. CMEs can have significant effects on the Earth's magnetic field, called geomagnetic storms, and both CMEs and SEPs cause significant changes in the radiation environment. The radiation environment in space is normally dominated by GCRs, but a SEP event can suddenly cause a very large increase in the flux of ionizing particles. This radiation poses as serious risk to human activity and electronics in space, which makes it an important subject of study, as humanity is constantly increasing its presence in space. As it propagates through the heliosphere, the shock wave produced by a CME accelerates particles, while also reducing the local flux of GCRs. The latter is an effect called Forbush Decrease (FD) and is caused by the magnetic shielding provided by the plasma inside the CME. The Alpha Magnetic Spectrometer (AMS) is a precision particle detector on the International Space Station (ISS). The detector measures the cosmic rays (CR) fluxes in the rigidity range from 1 GV up to 1 TV (from 400 MeV up to the TeV range for protons). The upper rigidity range of the SEP spectrum can be measured by the lowest rigidity range of AMS.

The development of this project is divided in three phases. During the first phase, we will produce the SEP (proton) energy spectra for all the solar events found by AMS, presenting one of the most precise measurements of SEP fluxes that have

been made in this rigidity range. We will describe the details of our cosmic proton selection on the observables measured by AMS, specifically tailored for low energy measurements. The final result of this phase will be the daily proton flux extended in time up to October 2023, with respect to previous works presented by the AMS collaboration. In the second phase we will adjust the daily proton selection to maximize the statistics at low rigidity, in order to obtain a measurement of the SEP spectra with cosmic protons. We will introduce the concept of *polar-pass* selection, which enables the extension of our measurements also in energy. This process will be fundamental to obtain an informative energy spectrum. The SEP spectra will be obtained via a dedicated background subtraction procedure, eliminating the galactic contribution from the total measured flux. In the third phase, SEP fluxes and spectra will be then evaluated and analyzed, in order to to understand their properties. We will study in detail their characteristics and features in the energy space, together with their temporal evolution. A spectral fit will be performed for a subset of the most intense solar events found with AMS, using empirical models which have been proposed in the past to describe the nature of the acceleration mechanisms and propagation effects. The energy range measured by AMS is of particular interest, since it connects the low energy measurements of spacecrafts devoted to solar physics (KeV-MeV range) to the highest energy measurements of neutron monitors on Earth (above the GeV). This specific energy interval, which has been previously explored only by the PAMELA experiment with comparable precision, could reveal important insights over the possible candidates thought to explain particle acceleration and subsequent transport during SEP events.

The present work is developed in collaboration with researchers of the AMS group of the University of Perugia and INFN, along with the network of institutions of the international AMS collaboration. The work is conducted in the framework of the joint research program between the University of Perugia and the Italian Space Agency, agreement ASI-UniPG 2019-2-HH.0.

Chapter 1

Cosmic Rays

Cosmic Rays (CRs) are a high value source of information for space physics. They represent an alternative and complementary way of studying celestial objects and their environment, in addition to electromagnetic radiation, gravitational waves and neutrino observations. CRs offer a way to probe the relative cosmic abundances of all the species in the periodic table, which are of great interest to understand the composition and the production mechanisms of stars, as well as the composition of the interstellar medium and the galactic magnetic fields. There are countless interesting aspects that can only be studied via CRs. Being CRs mostly charged particles, many techniques used in particle detectors on Earth may be applied to measure, with great precision, their physical properties, such as charge, mass, energy, velocity, direction and provide particle identification.

1.1 Definition and Description

Cosmic rays (CRs) are high-energy particles originating from a range of astrophysical sources, including our Sun, supernovae, and gamma-ray bursts [1]. These particles, which spend a large amount of time traveling inside our galaxy or even between galaxies, serve as valuable tools for studying particle acceleration and propagation mechanisms. These particles are referred to as *primary* cosmic rays until they interact with Earth's atmosphere, giving rise to cascades of secondary particles. Primary cosmic rays consist predominantly of protons (approximately 85%) and alpha particles (about 14%), with trace contributions from heavier nuclei, including elements as massive as uranium. This elemental composition reflects the processes of stellar nucleosynthesis and provides insight into the conditions inside supernova remnants and other astrophysical sources, responsible for acceleration. Overall the detected particles consist of 98% baryons and 2% leptons. In addition to their matter components, primary cosmic rays contain antimatter particles, such as positrons and

antiprotons, though these are present in low abundances. Notably, no conclusive evidence of heavier anti-nuclei has been observed to date. The presence of antimatter in cosmic rays is particularly interesting due to the potential discovery of primordial antimatter and dark matter decay channels. Upon entering Earth's atmosphere, primary cosmic rays interact with atmospheric nuclei, triggering a cascade of particle collisions known as *extensive air showers*. These interactions produce a variety of secondary particles, primarily pions and kaons, which subsequently decay into muons. Muons, due to their longer lifetimes, dominate the flux of secondary cosmic rays reaching Earth's surface, offering an accessible window for ground-based studies of high-energy cosmic phenomena. Muons constitute the majority of what is referred to as *secondary* cosmic rays when they reach Earth's surface. The remaining cosmic rays that survive this process of decay and arrive at the Earth's surface encompass electrons, positrons, and photons, the latter also being products of decay. At sea level, the flux of cosmic ray muons peaks at an energy of approximately 1 GeV, with an average flux of about one particle per second per square centimeter. However, it's important to note that this flux is not isotropic on the Earth's surface due to localized effects, such as solar activity or the Earth's magnetic field. The precise measurement of primary cosmic rays in space, before they interact with Earth's atmosphere, relies on sophisticated particle detection techniques. Many of these methods, such as calorimetry and Cherenkov detection, are adapted from those used in ground-based colliders, enabling detailed studies of particle charge, energy, and mass in cosmic rays. Understanding the composition and interaction of cosmic rays lays the foundation for studying solar energetic particles (SEPs), a subset of cosmic rays originating from solar events. The unique characteristics of SEPs, including their variability and potential for reaching extreme intensities, are the focus of this thesis.

1.2 Discovery and First Observations

Natural radioactivity was already known in the late XIX century, thanks to the discovery of radiation emitted by phosphorescent bodies by Henri Bequerel [2], but the majority of radiation phenomena was thought to be originated from rocks and soil. A few years later, Peter and Marie Curie observed that an electroscope (Fig. 1.1, left) in the presence of radioactive materials had different rates of discharge, depending on radiation intensity of the source, proving that the instrument could be used to probe this invisible radiation.

Using a lighter and transportable version of the electroscopes of his time (Fig. 1.1, right), Theodore Wulf measured the intensity of radiation at the bottom and at the top of the Eiffel Tower, expecting a decrease of intensity with height in the case of sole ground-base origin of this radiation. Wulf observed only a slight decrease in his measurements, weakening the previous hypothesis, but still concluded that the

origin was from ground materials.

Another important contribution came from Domenico Pacini, who questioned the standing hypothesis by measuring the discharge rate of his electroscope on the surface and below the Tyrrhenian see, ruling out the contribution of ground radiation, thanks to the absorption of water.

The final step in the comprehension of this problem came from the use of a simple but effective instrument, which is still used today: the air balloon. After a few inconclusive attempts in measuring air ionization with a balloon up to 1500 m, Victor Franz Hess conducted similar experiments reaching an altitude of 5200 m, showing that ionization reached a minimum at about 1000 m, but increased rapidly after [3]. The reason for the observed minimum was first hypothesized by Erwin Schrödinger, who predicted in his thesis that the soil radioactivity decrease could be compensated by an extraterrestrial component up to 3000 m. In any case, Hess' experiments not only confirmed that most of the radiation in the atmosphere was originated from outside Earth, but, by performing the same investigation at night, he showed that the results were consistent with daylight experiments, ruling out any major contribution from the Sun. The particles that could reach Earth's atmosphere, as we know today, were indeed the most energetic ones of galactic origin (as shown in section 2.2.4).

At the time, the source of this atmospheric ionization was still thought to be mostly neutral, as the only type of radiation that was observed to be penetrating matter was gamma emission. A crucial experiment to determine if cosmic rays, as the name started now to be used, were indeed neutral or charged particles was conducted by Jacob Clay, who measured ionization at different latitudes thanks to several ship voyages around the globe. He concluded that ionization increased with increasing latitude, giving more credit to the hypothesis of charged radiation.

In the same years, a different experiment, utilizing a new instrument and a new technique, arrived at the same conclusion. In 1927 the Geiger-Müller counter [4] was invented and allowed to specifically measure the intensity charged particle radiation produced in alpha and beta decay. Thanks to this new type of instrumentation and the coincidence technique [5], Bothe and Kohlhörster were able to measure the incidental direction of these particle, confirming the corpuscolar and charged nature of the atmospheric radiation. To end the debate on charged cosmic rays, Arthur H. Compton conceived an experiment on a global scale to measure ionization at different latitudes, finalizing what previously found by Bothe and Kohlhörster.

In the 1930s, Bruno Rossi was investigating the charge sign of cosmic rays, exploiting the geomagnetic field to see if charged radiation had a preferential direction. If the radiation was predominantly positive, in fact, he would have observed preferentially a westward incoming direction, eastward otherwise. The latter was precisely what

was observed, and this east-west effect was independently observed by Alvarez and Compton in the same years. Incidentally, Rossi observed that multiple Geiger counters in his measurement apparatus simultaneously discharged in several occasions: this lead to the hypothesis, later studied in depth by Pierre Auger, that cosmic rays interacted with particles in the air, producing a cascade of secondary particles, called *extensive showers*.

To this date, high altitude balloon experiments and extensive ground experiments, inspired by the early 90s experimental discoveries, are widely used to investigate the nature of cosmic rays, together with the more recent approach of space-borne detectors which brought into space spectrometric techniques directly investigating the primary charged particles.

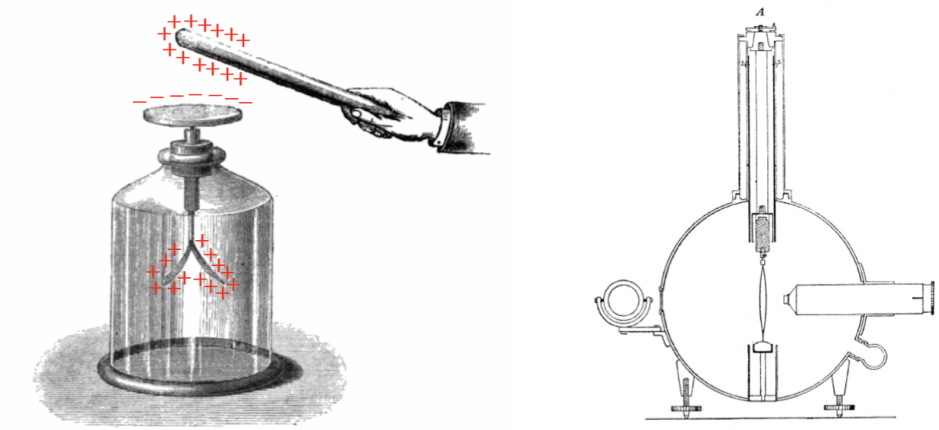

Figure 1.1: **Left:** Drawing of a gold-leaf electroscope, typical of the late XIX century, used for charge measurements (Sylvanus P. Thompson (1881)). **Right:** Original drawing from Theodore Wulf of his version of the electroscope, based on wires of metallized glass instead of gold leaves, used to measure natural radiation inside the atmosphere.

1.3 Energy Spectrum

The cosmic ray spectrum describes the distribution of particle flux as a function of energy, typically expressed in units of $p/(m^2\, sr\, s\, GeV)$. This spectrum encompasses a vast range, from low-energy particles influenced by the Sun to ultra-high-energy cosmic rays of extragalactic origin. The cosmic ray energy spectrum is characterized by an approximate power-law behavior, $\Phi(E) \propto E^{-\gamma}$, where $\Phi(E)$ represents the

flux of particles at energy E, and γ is the spectral index. This power-law distribution spans over 12 orders of magnitude in energy, highlighting the diverse origins and acceleration processes of cosmic rays. Deviations from the pure power law point to changes in the dominant sources or mechanisms of cosmic ray acceleration. Fig. 1.2 shows the combined measurements of multiple experiments, starting from one hundred KeV up to one ZeV (or one trillion KeV). We can observe at least three distinct regions, in which the spectral index of the power law is different [6].

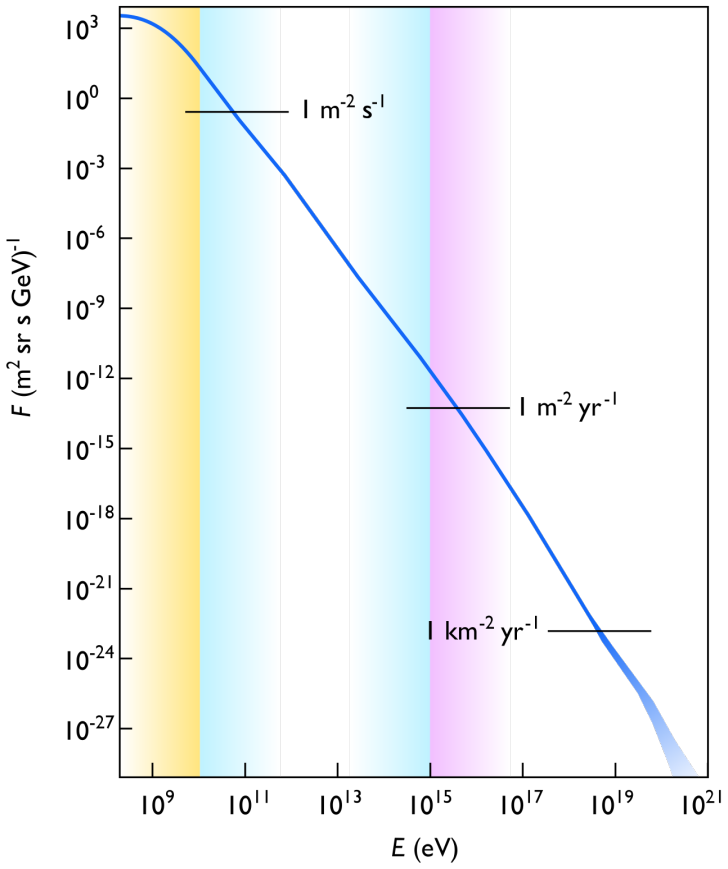

Figure 1.2: Combined measurements of the cosmic ray energy spectrum, highlighting key regions dominated by solar, galactic, and extragalactic influences. The spectral features (knee and ankle) indicate transitions in cosmic ray origin and acceleration mechanisms (Sven Lafebre - own work, after Swordy [7] and De Angelis [8]).

The low-energy region of the spectrum, ranging from approximately 0.1 GeV to 10 GeV, is dominated by solar modulation [9], where the Sun's magnetic field and

solar wind significantly influence the flux of galactic cosmic rays. This region also includes transient events such as solar energetic particles (SEPs) and Forbush decreases, which introduce short term variability. The flux peaks around 1 GeV due to the interplay of low-energy galactic cosmic rays and the intense solar wind particle population. Understanding this region is critical for space weather studies and for distinguishing between galactic and solar contributions to the spectrum. The middle-energy region, spanning from 10 GeV to 1 PeV, is primarily attributed to galactic cosmic rays (GCRs) accelerated in supernova remnants (SNRs). In this range, the spectrum follows a power-law index of $\gamma \simeq 2.7$, suggesting efficient particle acceleration via shock mechanisms (e.g. Fermi acceleration) in astrophysical environments. The transition at the *knee* (1 PeV) marks a softening of the spectrum ($\gamma \simeq 3$), which may indicate a maximum energy limit for particles accelerated by SNRs or a change in propagation effects in the galaxy. The flux above 1 EeV (the *ankle*) steepens again, suggesting a transition from galactic to extragalactic cosmic ray sources. Ultra-high-energy cosmic rays (UHECRs) in this range are likely accelerated by active galactic nuclei (AGN) or gamma-ray bursts, though their precise origin remains a topic of active research [10]. Measurements in this region are challenging due to low fluxes and the need for extensive ground-based arrays or high-altitude balloon experiments. The highest energy region can be observed in detail in Fig. 1.3, where the flux is multiplied by an x power of 2.6.

SEPs predominantly populate the low-energy region of the cosmic ray spectrum. Their variability, driven by solar activity, introduces significant deviations from the power-law behavior observed in galactic cosmic rays. Understanding the energy distribution of SEPs is critical for characterizing their acceleration mechanisms, such as diffusive shock acceleration in coronal mass ejections, and for predicting their impact on space weather and Earth's magnetosphere.

1.4 Origin and Composition

The radiation environment in the Solar System comprises a diverse mix of high-energy particles from galactic, solar, and terrestrial origins, spanning a wide energy spectrum. These populations include galactic cosmic rays (GCRs), which dominate the high-energy flux, solar energetic particles (SEPs), which are transient and variable, and trapped particles, which are confined within Earth's magnetosphere. This section focuses on the composition and origin of these particles, with particular emphasis on SEPs, their unique characteristics, and their implications for particle acceleration processes.

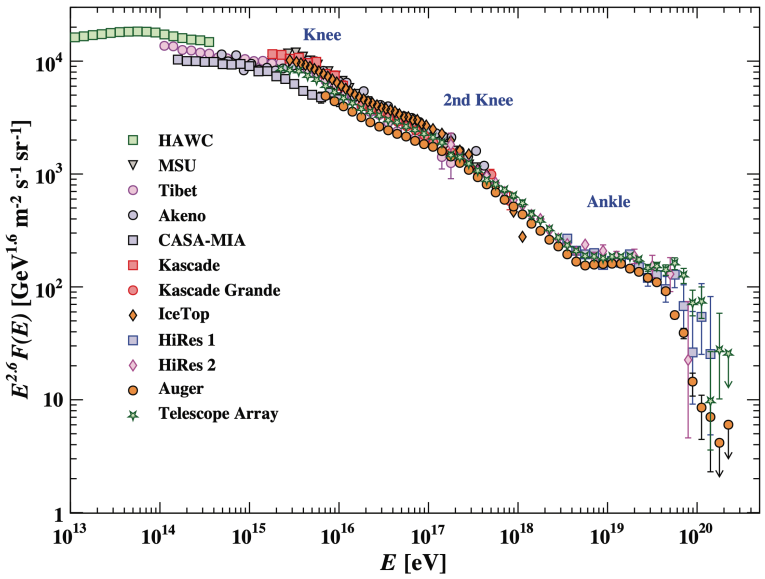

Figure 1.3: The high energy spectrum (multiplied by an x power of 2.6) in detail with the contribution of multiple experiments [11]: here the *knee* and *ankle* regions are particularly visible, underlying different populations of cosmic rays. An additional feature, called second *knee*, is also highlighted at around 230 PeV, corresponding to a softening of the spectrum [12].

1.4.1 Galactic Cosmic Rays

While thermal acceleration processes, like the black body radiation from a star, can explain the very low energy particle flux in CRs, these are not suitable to describe the power law spectrum up to the knee and beyond. Another factor that indicates the non-solar origin of this portion of spectrum is a change in composition, shifting towards heavier elements the higher the energy: elements that are usually produced in extreme events such as supernovae (SN). The current interpretation for the broken power law that CRs exhibit above the solar modulation region is that the acceleration mechanism is rigidity dependent and the maximum energy reached by a proton is 1 PeV [13]. In this scenario, heavier nuclei could reach energies Z times higher than protons, where Z is their charge. The best candidate source providing an explanation for this behavior are Type II supernovae, where shock waves can accelerate nuclei up to the knee energies, thanks to the Fermi type-I process (see section 1.5). This theory is supported by many observations, like gamma ray observations of supernova remnants (SNR) [14] [15] [16], X-ray observations [17] [18] and by the broadening of spectral lines in optical observations [19]. Gamma rays can give hints on the acceleration of ions, since they are generated as a result of inelastic collisions between high energy nuclei and interstellar gas, after the secondary Π_0 decay in two photons. Another clue supporting the theory of

SNRs as main CR accelerators is the measured abundances of elements in CR nuclei, compared to the abundances inside the solar system, shown in Fig. 1.4. During the Type II supernovae final phases, elements heavier than iron are produced and they have been found in cosmic ray composition. Furthermore, elements such as Lithium, Beryllium and Boron are not produced by stellar nucleosynthesis during the star main sequence phase: the higher abundance in galactic cosmic rays is an indicator that CRs interact with protons of the interstellar medium (ISM), producing lighter elements via spallation processes [20].

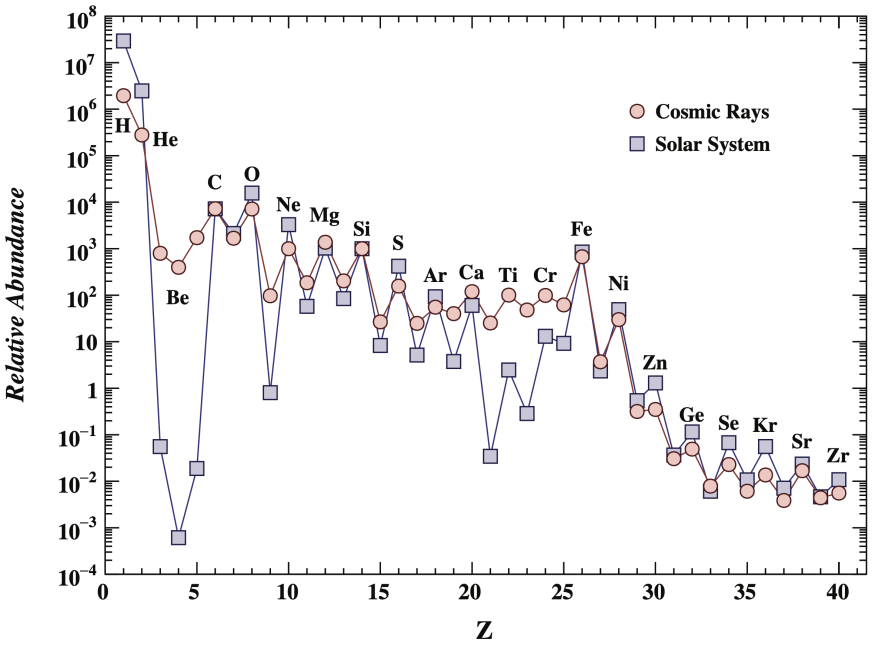

Figure 1.4: Nuclear abundances of Galactic Cosmic Rays (pink dots) compared to abundances in the Solar System (blue squares) [11]. The higher traces of Li, Be, B and metallic elements favors the hypothesis of SNRs as primary source of GCRs. These light nuclei are not produced by stellar nucleosynthesis, but they are likely originated as secondary products via spallation with the interstellar medium.

The amount of particles that can be injected into the acceleration process and the maximum energy that can be reached with shock acceleration in SNRs is still unclear, although it is believed that they could be responsible for the spectra up to the *knee* region and possibly beyond.

Although it is still mostly unknown, the current explanation for the existence and observed spectrum of the so called *Ultra High Energy Cosmic Rays* (UHECR), particles with energy above the *ankle*, is that they are originated from powerful sources outside the Milky Way. The most accredited sources are Active Galactic Nuclei (AGN) and/or Starburst Galaxies (SBG) [21].

1.4.2 Solar Energetic Particles

Solar energetic particles (SEPs) are transient bursts of high-energy particles accelerated during extreme solar events, such as coronal mass ejections (CMEs) and solar flares (see section 2.1.2). Unlike the solar wind, which typically consists of low-energy particles (up to 4 keV), SEPs can reach energies of several GeV, enabling them to penetrate Earth's magnetosphere. In addition to their higher energy, SEP intensity can increase more than four orders of magnitude that of the baseline CR flux, therefore constituting a significant threat to spacecraft, astronauts, and ground-based systems. The composition of SEPs, primarily protons, helium nuclei, and trace heavier elements, reflects the solar plasma and provides insights into the acceleration and transport processes occurring in solar eruptions. Isotopes are also extremely interesting, as the relative abundance to the main stable isotope was observed to vary greatly during different SEP events [22].

SEPs exhibit significant temporal variability, with event durations ranging from a few hours to several days, depending on their source and acceleration mechanisms. In fact, after a long debate on their origin and acceleration mechanisms, multiple observations seem to agree in dividing SEP events in two categories: *impulsive* and *gradual*. Impulsive SEPs, associated with magnetic reconnection in solar flares, are short-lived and enriched in helium-3 and heavy ions. Gradual SEPs, driven by shock acceleration in CMEs, are longer-lasting and characterized by a broader energy spectrum. Real case scenarios are expected to involve a combination of the two mechanisms, depending on the magnetic connection that drives charged particles along the Sun's magnetic field, between the source and Earth. More details on the sources of acceleration and transport effects between the Sun and Earth will be given in the section 1.5. The following paragraphs will describe the main properties of the two types of SEP populations, as presented in [23].

Impulsive SEP Impulsive SEPs were originally discriminated by the huge increase in $^3He/^4He$ ratio and later also associated to A/Z enrichment in isotopic composition. These properties are compatible with a two-fold acceleration mechanism, driven by solar jets (see section 2.1.2), involving magnetic reconnection and wave-particle resonant absorption. Magnetic reconnection occurs in solar jets and samples ions inside active regions, causing enhancements in A/Z abundances by factors of ~ 1000 from He to Pb. $^3He/^4He$ ratio can be enhanced by even a factor of ~ 10000 by wave-particle resonance. The latter can be caused by a large amount of streaming electrons, which also produce type III radio bursts. The impulsive nature of these events is originated by the optimal connection between the source and the observes, since particles are injected directly into open field lines that are created on the magnetic reconnection site. These charged particles then travel along the field lines undisturbed and with little diffusion, leading to a tight temporal profile

for the observer.

Gradual SEP Gradual SEPs identify the largest events that have ever occurred and are called *gradual* because of their slow decay rate. These events are connected to the emission of a fast and wide CME (see section 2.1.2). In the case of CME-driven shock wave acceleration, the transport becomes fundamental to understand changes in the initial population. The initial population can indeed be composed by a mixture of ambient plasma and residual super-thermal ions from multiple impulsive SEP events. Another interesting aspect of gradual SEPs is the bulk of trapped plasma inside the magnetic field of the CME, which acts as a *reservoir*, gradually injecting particles into the shock front over time. In gradual SEP events, the shock waves can also reaccelerate seed particles from previous impulsive events. These seed particles often carry distinct compositional signatures, such as enhanced heavy-ion abundances, which can influence the overall particle population observed. Intensity and energy are spatially uniform but they decrease with time as the CME volume expands. These particles could be responsible for the long duration fluxes observed at low energies in cosmic rays on Earth (see chapter 6 for a detailed analysis).

Understanding the temporal and compositional variability of SEPs is crucial for improving space weather forecasting and mitigating their impact on our everyday life. Both the temporal and rigidity dependence of SEPs will be investigated in this thesis, focusing on the highest rigidities reached by these events which are measured by the AMS experiment.

One of the primary challenges in SEP studies is distinguishing solar contributions from background galactic cosmic rays, particularly during periods of low SEP flux. Additionally, particle transport models must account for complex magnetic field structures and scattering processes that modify the observed energy spectra and composition.

1.4.3 Trapped Particles

Trapped particles, consisting primarily of electrons and ions, are trapped in a complex motion inside Earth's inner magnetosphere [24], within the Van Allen radiation belts (see section 2.2.2). These particles originate from two main processes: the influx of solar plasma during geomagnetic storms and secondary production from interactions of cosmic rays with atmospheric nuclei. While the outer belt is dynamic and influenced by solar activity, the inner belt is more stable, with particle lifetimes extending over years. Particles with the right energy to be stored inside the inner belt are usually deflected by the magnetic field before reaching that region, so the most likely origin of those trapped electrons and protons is by decay of neutrons produced in collisions between cosmic rays and atmospheric atoms. The main constituents of this population are electrons and protons, with the former reaching

energies up to 7 MeV and the latter up to 600 MeV; there is also a small population of heavier nuclei, which can reach up to 50 MeV/Z.

The trajectory of trapped particles is the composition of three motions [25]: a spiral motion along field lines, a drift motion due to gradients in the field and a bouncing motion where field lines converge (at the poles). Once a particle is trapped inside these regions, especially inside the inner Van Allen belt, it can stay trapped for a long time, as the trajectory is very stable.

The trapped particle density is time dependent due to different effects. The intensity of solar activity is directly correlated to the density of electrons and anti-correlated to the density of protons inside the outer belt. The normal day-night cycle also influences the outer belt for about one order of magnitude in density, while solar storms can vary it up to three orders of magnitude.

The study of trapped particles is interesting not only to protect astronauts and instrumentation in space from high doses of radiation, but also a potential background to SEP studies, such as for experiments on low Earth orbits (LEO) (as is the case for AMS on the ISS). The LEO orbits are, in fact, tend to cross the inner Van Allen belt over a specific region called *South Atlantic Anomaly* (SAA, see section 2.2.2), which must be taken into account when studying CR fluxes, especially protons.

1.5 SEP Acceleration Mechanisms

The acceleration of solar energetic particles (SEPs) is governed by two primary processes: diffusive shock acceleration (DSA), associated with coronal mass ejections (CMEs), and magnetic reconnection, typically observed in solar flares. These mechanisms define the characteristics of gradual and impulsive SEP events, respectively, and are central to understanding the variability and energy distribution of SEPs. These two mechanisms are common among a variety of other astrophysical objects, but they will be presented here with the specific interest for SEP origin.

1.5.1 Diffusive Shock Acceleration

DSA, also known as first-order Fermi acceleration, is a small scale version of the process that occurs in supernova remnants for acceleration of GCRs. In the solar system environment, it occurs at shock fronts formed when CMEs propagate through the solar corona and heliosphere. This process relies on the interaction between charged particles and turbulent magnetic fields upstream and downstream of the shock front. The mechanism is extensively presented in [26], but the basic concepts are the following. The main ingredient is a shock front, which is a transition layer between two different media, propagating through a plasma and changing its state. The fundamental differences with a shock front of an expanding gas due to an explosion,

for example, is the low density and magnetic properties of the plasma, which change the nature of the kinetic energy transfer from collisional to electromagnetic. Plasma density is, in fact, much greater in the downstream medium (inside the shock) and so is the magnetic field. When charged particles of the upstream medium cross the shock front, they encounter a turbulent magnetic field that accelerates them back towards the direction of motion of the shock. As the shock progresses, it sweeps more and more plasma from the external environment, which generates an increasingly stronger magnetic field on the upstream. The particle that was reflected from the downstream magnetic field now encounters the newly formed field on the upstream, which then reflects it back towards the shock. During each crossing, particles gain energy due to the relative motion of the scattering centers and the shock front. This energy gain is proportional to the shock velocity, making the process first-order in nature. A sketch of the process is presented in Fig. 1.5. The energy gain per cycle is approximately:

$$\Delta E \sim \frac{v_{shock}}{c} E \tag{1.1}$$

The probability of escaping the region after n cycles is $P_{escape} \sim 1/n$, which leads to an energy spectrum of:

$$f(E) \propto E^{-\gamma} \tag{1.2}$$

The spectral index γ is related to the compression ratio r of the shock:

$$\gamma = \frac{r+2}{r-1} \tag{1.3}$$

which for highly compressed shocks ($r = 4$) leads to a $\gamma \simeq 2$, compatible with observed SEP spectra. This process is repeated for many cycles until the energy of the particle is sufficiently high to overcome the opposing magnetic field, freeing the particle into the ISM.

Gradual SEP events are characterized by broad energy spectra, often extending to GeV energies, and a composition reflective of the solar corona. The spatial extent of the CME shock enables the acceleration of a large population of particles, resulting in widespread SEP events observed across the heliosphere. These large events typically exhibit smooth temporal profiles and are dominated by protons, with small contributions from alpha particles and heavier ions. The acceleration efficiency depends on the shock speed, with faster and wider CMEs producing higher-energy particles.

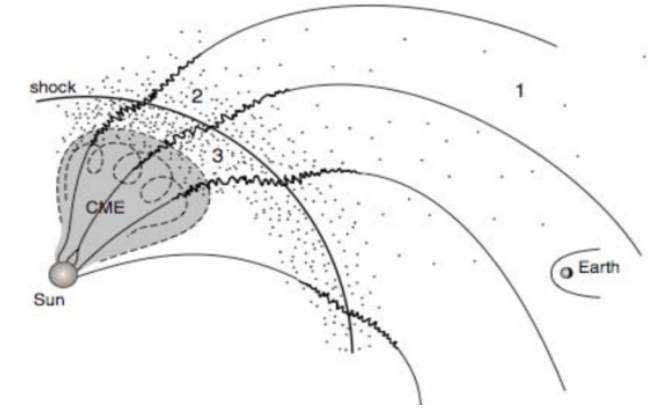

Figure 1.5: Illustration of a CME, creating a discontinuous turbulent magnetic field near its shock front, which is responsible for scattering and acceleration of charged particles [27].

1.5.2 Magnetic Reconnection

The second mechanism is responsible for many different kinds of phenomena: from the northern lights inside Earth's magnetosphere to electron/positron pair production on pulsars [28]. In the case of SEPs, magnetic reconnection plays a role in accelerating the trapped plasma inside the flux tubes, in which the magnetic field of the Sun is frozen, whenever they come in contact and suddenly break in a small reconnection site (often named *x-point*). The x-point is a localized region of intense electric fields, where charged particles are accelerated along open field lines. This process is often accompanied by the formation of solar jets and the ejection of magnetically confined plasma. The reconnection rate, determined by the plasma inflow velocity and magnetic field strength, influences the energy gained by particles. The electric field is generated by moving charges inside the strong magnetic field of the Sun, which is concentrated near the x-point, hence during reconnection it is approximately given by:

$$E \simeq -\frac{v \times B}{c} \tag{1.4}$$

where v is the plasma velocity and B is the magnetic field. Therefore we can estimate the energy gain of a particle with charge q, traveling for a path dl inside the reconnection site, as:

$$\Delta E = q \int E \cdot dl \tag{1.5}$$

This process is illustrated in Fig. 1.6: when two magnetic field lines of opposite sign

come in contact, e.g. in plasma loops that occur on the Sun's surface, particles are accelerated above and below the x-point. A population of charged particles is accelerated towards the surface of the sun, while a second one is free to escape following the newly created field line from the reconnection. Most of the magnetic energy released by the magnetic field into kinetic energy of the particles is then dissipated through thermal radiation of soft X-rays (up to sub-millimeter), though some of the particles that formed the old population inside the flux tube are now free to escape, becoming SEPs. Acceleration by magnetic connection is a non-thermal process, associated with the observation of a power law spectrum, which is in agreement with all the SEP spectra observed by multiple experiments.

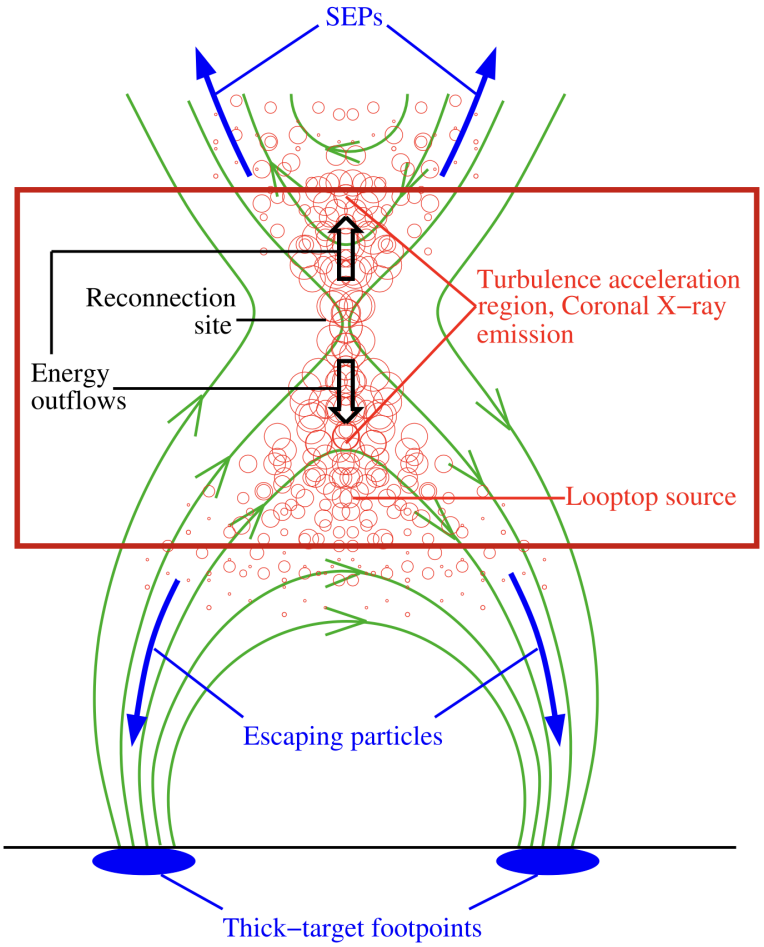

Figure 1.6: Schematic view of the Sun's magnetic field at a reconnection site (x-point). The energy released by the magnetic field is transferred to charged particles, which in turn re-emit it as X-rays or simply escape following the open lines as SEPs [29].

The two mechanisms of SEP acceleration highlight the complex interplay of plasma and magnetic fields in the solar system. While DSA explains the widespread, high-energy nature of gradual SEPs, magnetic reconnection accounts for the localized, compositionally unique characteristics of impulsive events. It is likely that both play a role in major solar activity events, where the possibility of hybrid events is not excluded. The hybrid nature of this problem complicates enormously the effort for classification of SEP events, especially considering that their understanding also requires accounting for transport processes, such as diffusion, adiabatic cooling, and energy-dependent propagation. These effects can in fact modify the observed spectra and obscure the signatures of the underlying acceleration mechanisms. Quantitative models and observational constraints continue to refine our understanding of these mechanisms and constitute a wide discipline, especially regarding magnetohydrodynamic simulations of CME origin and propagation [30].

1.6 Antimatter in Cosmic Rays

Cosmic antimatter is one of the most interesting frontiers in physics that is yet to be fully explored, leading to potentially ground-braking discoveries on the origin of the universe, with primordial antimatter, as well as Dark Matter, with its possible decay in matter-antimatter pairs. We continuously observe antimatter in cosmic rays, but most of the contribution, especially for elementary particles, comes from interaction and decay of primary CRs in the atmosphere and on the *interstellar medium* (ISM). Positrons can be produced in the decay of charged pions, which are generated in proton-proton or proton-ion collision with ISM or the atmosphere and antiprotons can be produced directly in collisions with the ISM. There could be a secondary production of anti-nuclei via spallation, such as anti-deuteron [31] and anti-helium, but currently only e^+ and $\bar{p}$ have been directly observed in CRs [32]. Due to the extremely low cross section of such secondary production, a direct measurement of anti-nuclei by current experiments would be interpreted as *primordial antimatter*.

Primordial Antimatter Objects in our local universe appear to be made exclusively of ordinary matter, an observation that is consistent with the composition of cosmic rays. The current Big Bang theory requires an initial symmetrical distribution of matter and antimatter and it's still unclear what mechanism led to the disparity that we observe today. In the early Universe, pair production and annihilation were in thermal equilibrium, which led to the production of equal amount of matter and antimatter. One of the mechanisms that could have actively produced the asymmetry we observe today is *baryogenesis* [33]. The interest over this topic began to rise when the violation CP invariance was first observed in 1964 [34], being one of the requirements (Sakharov conditions [35]) for this process to take place. Another condition is the violation of the baryon number, which is not predicted by

the current Standard Model of particles. On the other hand, antimatter could be present in the Universe still on this date, but in separate separate domains, such as entire stars and galaxies made by anti-nuclei. The isolation of matter and antimatter could then be caused by the accelerated expansion of the Universe. The observation of anti-nuclei heavier than hydrogen ($A \geq 4$) would be a strong indication of such hypothesis, given that the sensitivity of current experiment to secondary produced anti-nuclei is too small.

Antimatter From Dark Matter Decay The positron and antiproton fluxes could also be interesting as possible decay channels of dark matter particles, such as WIMPS. Anomalies in the high end of the cosmic positron spectrum, for example, could be interpreted as possible candidates of heavy dark matter (> 30 GV) decay products from the galactic halo [36]. The majority of single-charged antimatter in cosmic rays is produced as secondary product of interactions between primary cosmic rays and the interstellar medium (ISM). When high-energy protons or nuclei collide with neutral atoms, secondary particles such as pions can be created. Subsequently charged pions decay into muon or antimuon and their respective neutrino, which in turn decay into electrons and positrons. Antiprotons, on the other hand, can be produced as products of inelastic proton-proton collisions [37]. Recent measurements of the positron flux with AMS [38] and PAMELA indicate that an additional source term is needed to explain the observations, although there could be other conventional sources that have yet not been explored, such as acceleration in astrophysical objects [39]. However production by interactions with the ISM may need to be further investigated [40].

Chapter 2

The Solar System

The Sun is part of a group that constitutes about 7.6% of all the stars in the Milky Way [41], the G-type stars of the main sequence. It serves as the central source of energy and charged particles in the heliosphere, shaping the space weather environment of the Solar System. Its radiative output spans the electromagnetic spectrum, from infrared to X-rays, occasionally emitting gamma-rays, while its continuous ejection of plasma, known as the *solar wind*, carries the solar magnetic field into interplanetary space. The solar wind, under quiet solar activity, usually reaches energies up to 4 MeV.

Occasionally the Sun accelerates high energy particles, the SEPs, that can reach much higher energies (> 1 GeV) and are usually accompanied by the aforementioned hard X-ray and gamma emissions. In addition to the radiation, during these short-lived events of a few days, an entire portion of the magnetic field of the Sun can be separated, forming a closed loop and carrying outward momentum and all the ionized plasma trapped inside.

These phenomena have profound effects on the heliosphere and the near-Earth environment, influencing the propagation of cosmic rays and the dynamics of Earth's magnetosphere. This chapter provides an overview of the Sun's structure, solar activity, and its interaction with the heliosphere, culminating in a discussion of the impact of GCRs and SEPs on human activity in space.

2.1 The Sun

G-type stars, like the Sun, spend about 10 billion years in the main sequence. Their effective temperature is around 5800 K, placing the peak of their black body spectrum within the optical green-yellow frequency band [42]. The Sun will fuse hydrogen into helium for most of its life, via the *proton-proton chain* process. Once the

hydrogen runs out, the star will start fusing the produced helium, not before leaving the main sequence and becoming a red giant [43]. The faith of these type of stars is to expand into a planetary nebula, leaving the nucleus as remnant which becomes a *white dwarf*.

The structure of a typical G-type star is pictured in Fig. 2.1. The core is the region where the nuclear fusion takes place, with temperatures reaching over 15 million Kelvin. In contrast to the other types of stars, the core is surrounded by a *radiative* zone, where fusion stops occurring, but the temperature is so high that the only possible mean of energy transport is through radiation. After this portion, which extends up to 70% of the solar radius, there is a *convection* zone, where temperatures are finally low enough to sustain convective loops from the radiative zone to the surface.

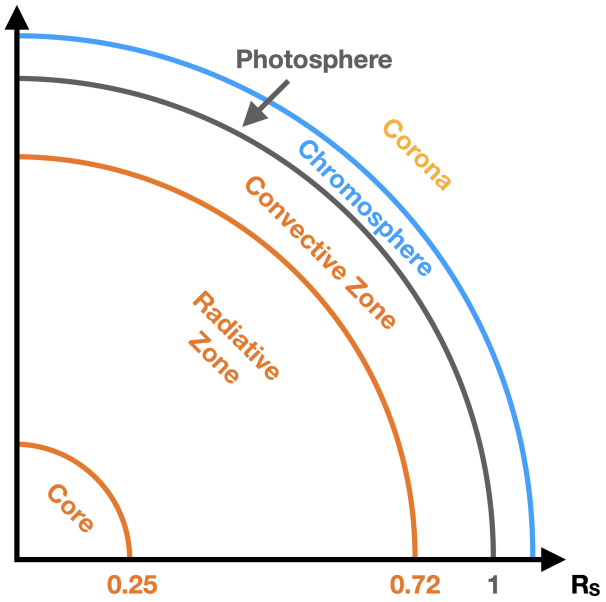

Figure 2.1: Schematic view of the internal structure of the Sun.

The surface itself is called *photosphere*, as this is the first region from the core that can be directly observed with light, since the internal regions are opaque to photons. On the photosphere we observe the typical granularity that signifies the presence of convection, as shown in Fig. 2.2. The photosphere is also the region where sunspots appear: these spots are darker and cooler than the surrounding area, since they are markers of a highly concentrated magnetic field, which prevents convection from occurring, letting the surface cool down. The sunspots have been observed to be large as much as three times the radius of Earth and their temperature is usually around 4500 K, while usually the surface is 5800 K.

The Sun is also equipped with a large atmosphere with many layers. Just above the

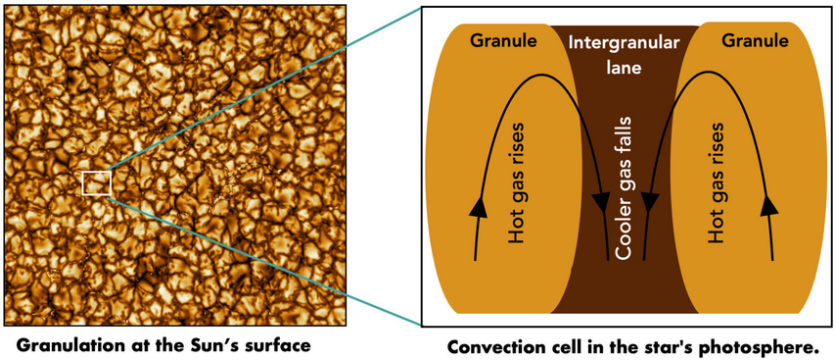

Figure 2.2: Surface granularity on the Sun's photosphere, typical of the motion due to convection (credit: Daniel K. Inouye Solar Telescope and [44]).

photosphere we find the *chromosphere*, which extends up to 2000 km from the surface of the Sun. Over the first 500 km, the temperature actually decreases allowing for molecular gasses to exist, but then it rapidly increases up to 20000 K. This increase ionizes the hydrogen, producing the typical Hα emission line, which gives the name *chromosphere* to the region (from the Greek word for color, *chroma*). After a thin transition region, kinetic temperature of plasma increases even further inside the *corona*, reaching up to 2 million Kelvin. This incredibly high temperature was first deduced from the observation of a few emission lines on the Sun's spectrum during an eclipse, particularly those of iron and calcium, with a high degree of ionization [45]. However the corona consists of a very rarefied plasma, with a density of 4×10^8 atoms per cubic centimeter, 13 orders of magnitude lower than the Earth's atmosphere. The low density, which outclasses any type of vacuum that has ever been reached on Earth, is the reason why such high temperatures are maintained without any significant heat loss. The corona is visible from Earth during total solar eclipses (see Fig. 2.4).

The current composition of the Sun, as observed on the photosphere, consists of 74.9% hydrogen, 23.8% helium and about 1.3% heavier nuclei, between oxygen, carbon, neon, iron and others [46]. Being the core surrounded by a radiative zone, all the products of nuclear fusion are trapped inside it, hence the Sun accumulates helium inside the core until fusion is not possible anymore. Being helium heavier than hydrogen, in fact, it precipitates inside the core, leaving the actively fusing hydrogen shell progressively thinner. This process causes the star to grow in size and become a red giant, while the core becomes more dense with helium. The core gravitational contraction during the hydrogen shell phase is still not sufficient to ignite helium fusion and the core starts to collapse into degenerate matter, only supported by the degeneracy pressure of Pauli's exclusion principle. Therefore, while pressure remains constant in degenerate matter, temperature increases as the hydrogen shell depletes, fusing the remaining hydrogen into helium. For stars like the

Sun, between 0.5 and 2.2 solar masses, the critical temperature for helium ignition is reached and a new fusion process starts: the triple alpha process [47]. However, the core pressure still remains constant due to degeneracy, until the radiation pressure is enough to sustain a further expansion, which would cool and regulate the core temperature. Therefore pressure and volume remain constant while temperature increases dramatically in a runaway fusion event called *helium flash* [48]. The helium flash is extremely short-lived, lasting a few seconds, but rapidly emits energy at a rate 10^{11} times higher than the corresponding main sequence star. Almost all the energy produced in this way is converted into thermal expansion of the outer layers, which eventually will form a planetary nebula and leave a dense degenerate core made of carbon and oxygen.

2.1.1 Solar Activity Cycle

Solar activity is the collection of all phenomena that describe the non-linearity of the Sun over time and energy. These include solar flares, CMEs, sunspots, variations of solar wind velocity, magnetic field and adjacent parameters. All of these phenomena tend to occur with a frequency that varies over a 11-year cycle, due to the changing magnetic field of the Sun. The first observation that solar activity might have been varying with time came from the observation of the number of sunspots on the surface of the Sun. The first one to systematically observe sunspots and their behavior was Galileo Galilei in 1610, although there are recordings of Chinese astronomers who first noticed the presence of darker regions on the Sun. The sunspot number as solar activity parameter, though, was created by Rudolf Wolf in 1848 [49], who defined it as follows:

$$R = k\,(10\,g\,+\,s) \tag{2.1}$$

where R is Wolf's sunspot number, g is the number of sunspot groups, s is the total number of individual sunspots and k is a correction factor that varies with the observer and the quality of the observation.

This definition is still used today as *International Sunspot Number* (ISN), although with some adjustments to improve accuracy and consistency, in order to maintain compatibility with older observations. Modern techniques, like by analyzing radioisotopes in tree rings [50] and ice cores, allow also to extrapolate this number backwards in time for several millennia.

Sunspots appear usually in pairs on the two different hemispheres of the Sun. This is because they signify the presence of the entry and exit points of strong magnetic tubes (concentrated field lines), with opposite polarity at the surface [51]. Their structure is characterized by a dark central part, where the magnetic field is the

strongest, surrounded by a lighter area that appears filamentary, with a less intense magnetic field. Sunspots typically last from a few days to several weeks. They can form, grow, shrink, and eventually dissipate as the magnetic field weakens.

The sunspot number is directly correlated to the Sun's magnetic activity, as in its magnetic field starts with a dipolar configuration, slowly progressing towards a chaotic toroidal field in an 11-year period. This periodicity is referred to as *solar cycle* and spans between solar *minimum* and solar *maximum*. After each solar maximum the magnetic field reverses polarity, effectively creating a 22-year cycle. As the name suggests, during solar maximum we usually observe the most sunspots (Fig. 2.3), but also an increased frequency in transient energetic events (see section 2.1.2).

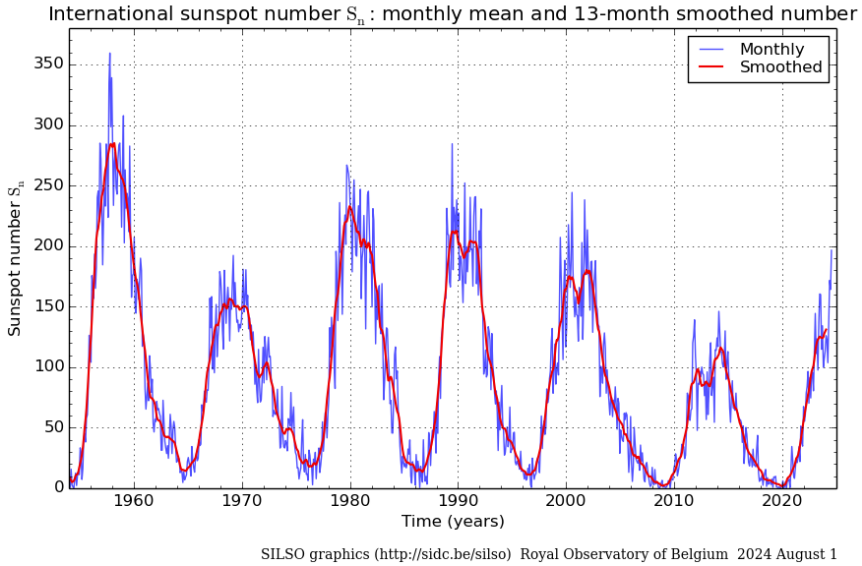

Figure 2.3: The monthly sunspot number and the 13-month smoothed curve. We are currently traversing the solar maximum of solar cycle 25, since the start of sunspots systematic recording. (Credit: Royal Observatory of Belgium).

At the beginning of a solar cycle, sunspots tend to appear at higher latitudes, around 30° to 35° north and south of the solar equator. As the cycle progresses, new sunspots form progressively closer to the equator. By the end of the cycle, most sunspots are observed within about 5° to 10° of the equator, reflecting the chaotic configuration of the magnetic field.

Another direct measurement of solar activity is the *solar flux index* (SFI), which probes the radio emission from the sun at the specific wavelength of 10.7 cm. Solar flux provides an estimate of the total radiated energy and it is specifically useful for radio communication on Earth, as higher flux values correspond to a higher degree

of ionization of the outer Earth atmosphere (high frequency radio communications are enhanced by high ionization).

There are many other indices connected to solar activity, although most of them describe it indirectly by measuring geomagnetic quantities. Among these we recall the *K-index*, which quantifies disturbances in Earth's horizontal magnetic field by comparing geomagnetic fluctuations to a quiet day. The K-index is measured with the magnetometer of a single geomagnetic station on Earth, while the *Kp-index* is a global average of 13 observatories between 44 degrees and 60 degrees northern or southern geomagnetic latitude. The *K-index* has many other derivations which also describe geomagnetic disturbances during solar storms [52]. All of the geomagnetic indices quantify the effects of solar storms on Earth, but they are still important for cosmic ray analyses that rely on instruments inside the geomagnetic field, such as AMS. For the purpose of this thesis, geomagnetic disturbances are a second order effect that changes the value of the geomagnetic cutoff (see section 2.2.4).

The chaotic and twisted configuration of the Sun's magnetic field at the end of a cycle is empirically explained by its differential rotation with latitude and the fact it can be treated as an ideal plasma. In this approximation, in fact, the Alfvén's theorem states that magnetic field lines are frozen-in the plasma [53], therefore they get twisted as the plasma moves faster at the equator than near poles. In some cases, the flux tubes formed by the twisted magnetic field can be forced above the surface, generating the spectacular plasma loops called *solar prominences* (see section 2.1.2). A solar prominence is the basic structure from which most of the other transient phenomena can occur, such as CMEs and solar flares.

2.1.2 Transient Events

Although it constantly emits a stream of low energy charged particles from its surface, the Sun is capable of accelerating particles at much higher energies, in a similar way supernova remnants accelerate GCRs, only on a smaller scale. CMEs are by far the most prominent features of solar activity, but the Sun also produces other transient phenomena, sometimes connected with the emission of a CME.

Coronal Mass Ejection: Coronal mass ejections (CMEs) are large-scale ejections of plasma and magnetic field structures from the Sun's corona into the heliosphere. When solar maximum approaches, the twisted magnetic field can snap and create a separate domain of plasma confined in a closed loop of magnetic field, called *Coronal Mass Ejection* (CME). The phenomenon that causes the release of energy and creates a separate magnetic domain is called *magnetic reconnection* (see section 2.2.2). This is a process in which oppositely directed magnetic field lines break and reconnect, releasing stored magnetic energy. This reconnection occurs in regions of complex magnetic field topology, such as active regions near sunspots. The release

of magnetic energy propels a large volume of plasma outward, forming a magnetic flux rope that expands as it moves away from the Sun.

CMEs are observed in white-light coronagraph images as expanding plasma loops. Spacecraft like SOHO and STEREO provide critical data on CME structure, speed, and direction. An example of CME is shown in Fig. 2.4. The plasma, which is emitted radially from the source, then travels with supersonic speed with respect to the interplanetary medium and solar wind (1000 km/s compared to a background of 400 km/s), creating a shockwave. The plasma carried by CMEs can reach up to 10^{12} - 10^{13} Kg and kinetic energies of 10^{25} J [54]. In this scenario, shock-front driven acceleration is thought to be the main acceleration process in gradual SEPs [23], very similarly to the DSA process that drives the acceleration of GCRs in supernova remnants. Gradual SEP events associated with CMEs last from hours to days, with particle fluxes distributed widely across the heliosphere. This broad spatial distribution results from the large extent of CME-driven shocks, which can span tens of solar radii.

Solar Flares: Solar flares are localized, short-duration explosions in the Sun's atmosphere caused by the sudden release of magnetic energy stored in the Sun's magnetic field. They are closely associated with impulsive SEP events. They can be observed around active regions near sunspots and can last up to several hours. Solar flares are primarily visible in the UV and X-ray spectrum and can coincide with the starting phase of a CME, when magnetic reconnection takes place.

Flares occur when magnetic reconnection in the corona releases energy stored in twisted magnetic field lines. The released energy heats the local plasma, drives particle acceleration, and produces intense electromagnetic radiation across a broad spectrum (radio, UV, X-rays, gamma rays). Their energy release can be equal to 10^{22} - 10^{25} [54] over timescales ranging from minutes to hours. The energy released powers particle acceleration, plasma heating, and radiation production. Flares are also often associated with Type III radio bursts, indicative of electron acceleration. The impulsive nature of these events favors acceleration of heavier ions, with respect to gradual events. In [23] it is shown that there are significant enhancements in the abundances of heavy elements. These enhancements are observed to follow a power-law dependence on A/Z, which means that elements with higher A/Z ratios, typically heavier nuclei, are more efficiently accelerated during these events.

The most common categorization of solar flares is presented in [55], where flares are assigned a category based on their peak intensity. The scale is logarithmic, where the three letters C, M and X represent, respectively, a tenfold increase in peak intensity staring from the first class, named B. Each class is assigned also a number from one to nine (often with decimal precision), which represents the finer sub-class. An exception is the X class which can be associated with any number, as

was the case for the most powerful solar storm recorded with modern instruments in 2003, estimated (due to instrument saturation) to be about X45.

Solar Jets: Solar jets are narrow, collimated streams of plasma ejected from the Sun's surface, often in association with active regions and small-scale reconnection events. These phenomena are triggered by magnetic reconnection occurring in open magnetic field configurations. Reconnection allows plasma to escape along open field lines, forming narrow outflows with speeds up to 500 km/s [56]. Although less significant than flares and CMEs, jets can accelerate ions through wave-particle interactions and magnetic turbulence. They are particularly effective at accelerating electrons, producing Type III radio bursts. Jets appear as bright, narrow features in extreme ultraviolet (EUV) and X-ray images. High-resolution observations from the Solar Dynamics Observatory (SDO) have revealed their fine structure and dynamics. A recent study [57] suggests that solar jets might be a different aspect of the same acceleration mechanism that drives all the energetic phenomena on the Sun's surface.

Solar Prominences: *Prominences* are large filaments that extend outwards from the photosphere and usually complete a closed loop. They phenomenologically represent *flux tubes*, a mathematical description in MHD of plasma frozen inside the magnetic field lines. These may result in the production of a CME in case of magnetic reconnection. These large, loop-like structures of dense plasma suspended above the photosphere by magnetic field lines often serve as precursors to CMEs [58]. Instabilities, such as the kink instability, can cause prominences to erupt, triggering CMEs. Prominences are observed in $H\alpha$ emission, appearing as bright loops on the limb of the Sun or dark filaments against the disk.

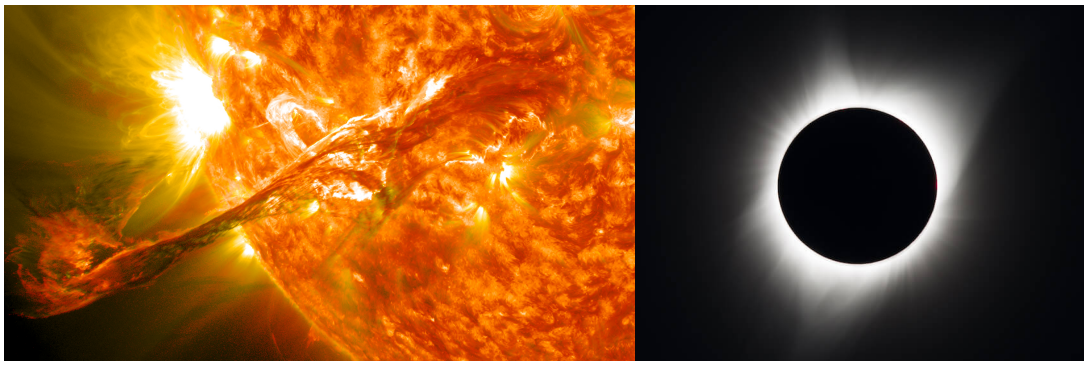

Figure 2.4: **Left:** An image of a Coronal Mass Ejection captured on August 31th 2012; the event was not directed towards Earth, but the CME connected magnetically with the magnetosphere, causing visible auroras. (Credit: NASA). **Right:** Image of the solar corona taken during a total eclipse on August 21 2017 in Madras, Oregon (credit: NASA/Aubrey Gemignani).

2.1.3 Heliosphere

As introduced previously, the plasma ejected from the sun as solar wind can be treated as an ideal plasma [53], described by Alfvén's theorem. For this reason, solar wind carries along the Sun's magnetic field and stretches it into the *Interplanetary Magnetic Field* (IMF). The volume influenced by the IMF is called *Heliosphere*. The IMF, structured into an Archimedean spiral by the Sun's rotation (see Fig. 2.5), dictates SEP propagation through pitch-angle scattering and magnetic mirroring. Particles encounter increased scattering during solar maximum, altering their reach to 1 AU. in addition to that, the Sun has a tilted magnetic axis with respect to the ecliptic plane (defined by its rotation axis), which means that the spiral actually is not planar, but it follows a wave motion over the ecliptic plane.

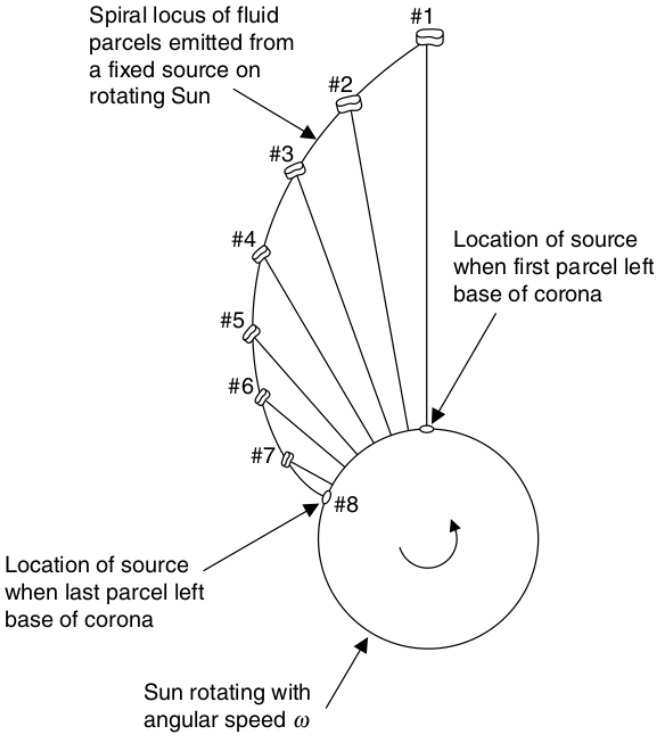

Figure 2.5: Formation of a spiral arm of the IMF. Plasma is emitted radially from the Sun's surface and at a regular rate, causing the field line, carried by the plasma, to describe an Archimedean spiral. Image taken from [59]

.

Being the Sun's magnetic field dipolar in first approximation, the IMF in the northern hemisphere of the heliosphere retains one distinct polarity, the opposite in the southern; this configuration creates the so called *Heliospheric Current Sheet* (HCS), a layer of separation between the two polarities [60]. Solar wind parameters including speed, temperature, density, and composition vary with distance from the HCS,

while the drift motion of CRs is heavily influenced by the polarity of the IMF. Since the dragged IMF does not evolve as a planar spiral, it means that the HCS is also wavy in nature, as can be seen in Fig. 2.6. Being Earth on the ecliptic plane, it is alternatively influenced by differently oriented magnetic fields, depending on the position with respect to the HCS. For this reason, the observed CR fluxes at Earth are also modulated by the HCS. The width of the HCS is approximately 10000 km at 1 AU and the field polarization is gradually rotating while crossing it, instead of simply flipping. The tilt angle between magnetic and rotation axes of the Sun is variable over time, being $\alpha \lesssim 10^\circ$ during solar minimum and $\alpha \gtrsim 70^\circ$ during solar maximum (wavy current sheet). The heliosphere is surrounded by the *termination shock* at 85 AU, where solar wind slows down from supersonic speed and proceeds to slow even further until the boundary of the solar system, the *heliopause*, at about 120 AU. The heliopause represents the surface where solar wind pressure is balanced with the flux of ISM particles, respect to which the Sun is in relative motion. In some models there is also a bow shock in the relative direction of motion between the heliosphere and the ISM, but recent measurements seem to agree on the velocity of the solar wind being subsonic, without evidence for the existence of a bow shock [61].

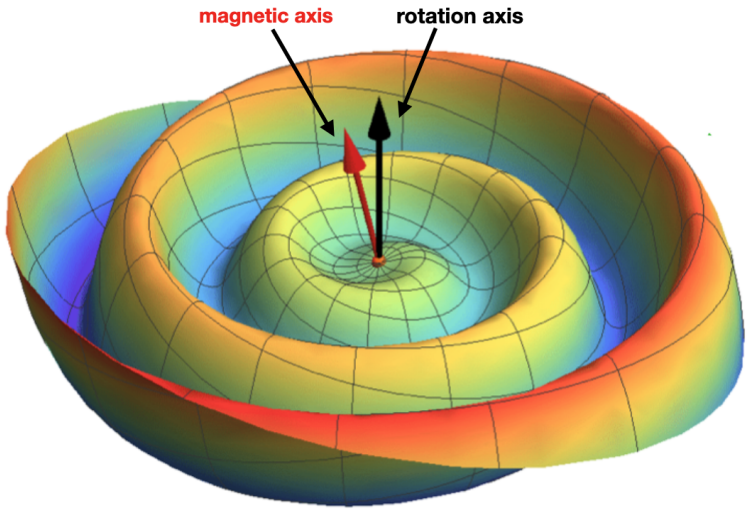

Figure 2.6: A three-dimensional view of the Heliospheric Current Sheet, the physical boundary between the northern and southern heliosphere, with different magnetic polarities. The spiral structure is caused by the radial emission of plasma combined with the Sun's rotation, while the waveform behavior in the vertical axis is caused by the relative angle between magnetic and rotaion axis of the Sun (credits: Miguel Reis Orcinha).

2.2 The Earth

In this section we will focus on the key aspects of the complex system of Earth's magnetosphere, which is influenced by solar storms, but can also influence the measurement of charged particle fluxes, as in the case of the AMS experiment. The geomagnetic field is, in fact, the main shield from the dangerous radiation that constantly reaches Earth from space, although while doing so, it limits our capability of studying the constituent of that radiation. Most of the details will be given about the so called *geomagnetic rigidity cutoff*, or simply *cutoff* in the following chapters, which determines the lower limit in energy for charged particles that can reach Earth.

2.2.1 Geomagnetic Field

Earth's magnetic field is generated by the molten core of the planet, which acts as a dynamo. Origin and composition of the inner core are still mostly unknown, but by analyzing seismic wave velocities it seems to be composed by an inner solid or slightly molten crystalline nucleus (1220 km in radius), surrounded by a liquid iron shell (3485 km in radius). This configuration can explain the dynamo effect, which is further supported by the presence of liquid iron, being highly conductive. The main component of the geomagnetic field, dipolar in nature, arises from the currents that flow inside the molten iron shell, with the dipole axis tilted by about 11° from the Earth's axis of rotation. The north pole, where field lines are directed outwards, coincides with the south geographic pole, although for convention it is defined as geomagnetic south pole so that they match. The dipolar structure of the geomagnetic field is shown in Fig. 2.7. Secondary contributions to the total geomagnetic field come from the ionization of the upper magnetosphere (see section 2.2.2), which influences and is influenced by the inner component, and also from external sources, like the IMF. All these sources are variable in time, both on long term (for the inner magnetic field) and on the short term (as the solar storms that change the external field), hence we need a complex model to fully describe it. One of the most known and used models is the IGRF model [62], which takes into account long term variations to the inner field. For studies concerning cosmic rays, the IGRF model is often complemented by the Tsyganenko model [63], which models the external field, including during solar storms.

2.2.2 Magnetosphere

The *magnetosphere* is the region of influence of the geomagnetic field. There is a clear separation layer between the geomagnetic field and the external interplanetary magnetic field (IMF), called magnetopause. Sharp gradients of magnetic field intensity and plasma density define this boundary on the day side of the magnetosphere,

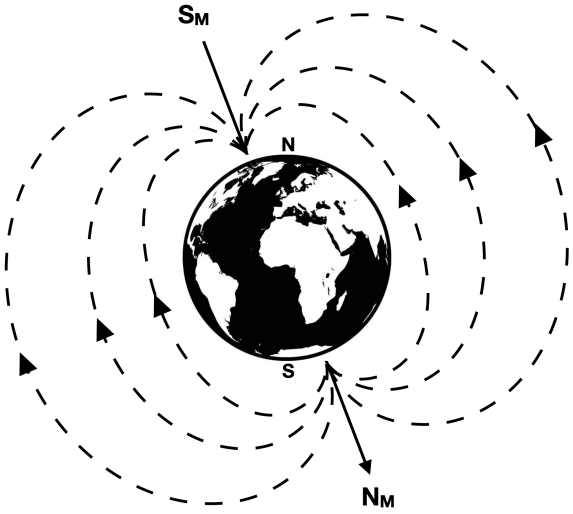

Figure 2.7: Sketch of the dipolar structure of the geomagnetic field. The magnetic axis is tilted by about 11° (slowly changing over time) and its north pole is located in proximity of the geographical south pole.

while on the lateral and night side it can still be defined by MHD simulations [64].

The magnetosphere is divided in an *inner* portion, where the field is still considered to be dipolar, and an *outer* one, where it starts to be influenced in shape by the IMF. The outer magnetosphere is compressed towards Earth by the solar wind on the day side, while on the night side it stretches in a long tail away from Earth. This image is pictured in Fig. 2.8.

The solar wind is supersonic relative to the interplanetary medium, hence it creates a bow shock on the day side of the magnetopause, where particles are drastically decelerated and forced to change direction. When the interference caused by the IMF or, in the case of a solar storm, by the approaching CME is strong enough, *magnetic reconnection* can occur [65]. The latter is a phenomenon in which anti-parallel field lines of the CME and the geomagnetic field can fuse, changing their topology. Magnetic reconnection can occur on the day side, merging the two fields and creating pockets of plasma between them, and on the night side, where the stretched lines snap, forcing the plasma in the pockets towards the inner magnetosphere. These phenomena are pictured in Fig. 2.10. Part of the magnetic energy is converted into kinetic energy of charged particles, accelerating them either inside the magnetosphere or away from it. These particles can then be trapped inside the *plasmasphere*, i.e. the inner magnetosphere with closed magnetic field, where they drift along the field lines. When the charged particles accelerated by magnetic reconnection reach the ionosphere, usually near the poles, they give birth to northern lights by ionizing atoms in the atmosphere.

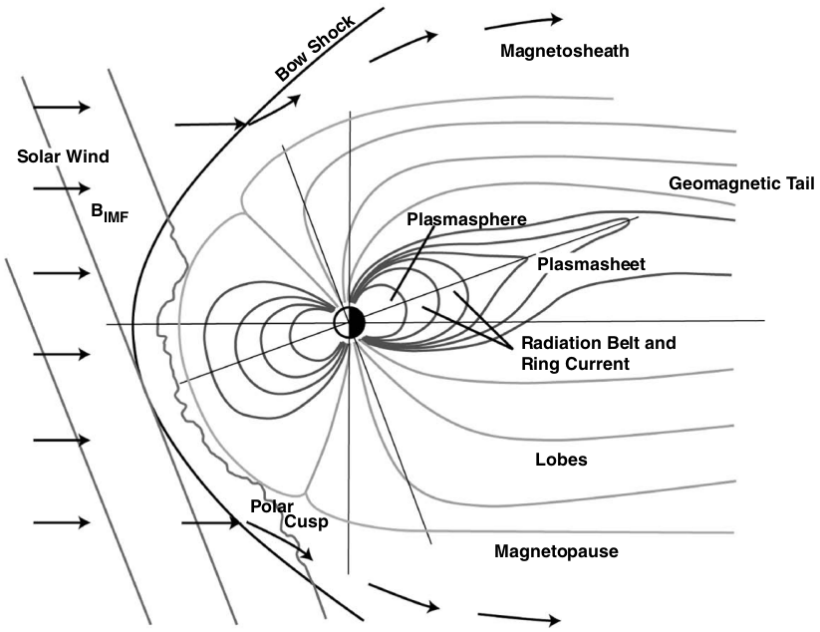

Figure 2.8: A schematic of the magnetosphere showing the field lines arrangement and the various elements that characterize the geomagnetic field. The interaction with the IMF, carried by the solar wind, deforms the geomagnetic field into its typical lobe and tail structures. Image taken from [59]

.

Charged particles of different charge, trapped inside the geomagnetic field, give rise to a complex system of currents around Earth. The flow of charged particles perpendicular to the field lines are called *ring currents*. These currents generate a secondary magnetic field, which opposes to the main geomagnetic field, weakening it. The bigger the influx of particles from a solar storm, the stronger the ring currents, enforcing a greater weakening effect of the geomagnetic field. Another set of currents is called *field aligned currents*, which transport charged particles inside the magnetosphere along the magnetic field lines. The topology of these currents is shown in Fig. 2.9.

There are notably two main regions inside the inner magnetosphere, called *Van Allen belts*, in which particles are trapped during solar storms by the *magnetic reflection* effect [66]. Here particles are forced into a spiraling motion around the closed field lines and a drift motion that follows Earth's rotation, which shape the Van Allen belts into a toroidal volume. The inner belt is very close to Earth, reaching about 200 km in altitude on the lowest point, and is composed by electrons and positive ions, while the outer belt consists only of electrons. The inner belt is responsible for the *South Atlantic Anomaly* (SAA), a region where the Low Earth Orbits (LEO) of satellites on Earth intercept the Van Allen belt, saturating the instrumentation of

detectors that measure charged particles [67].

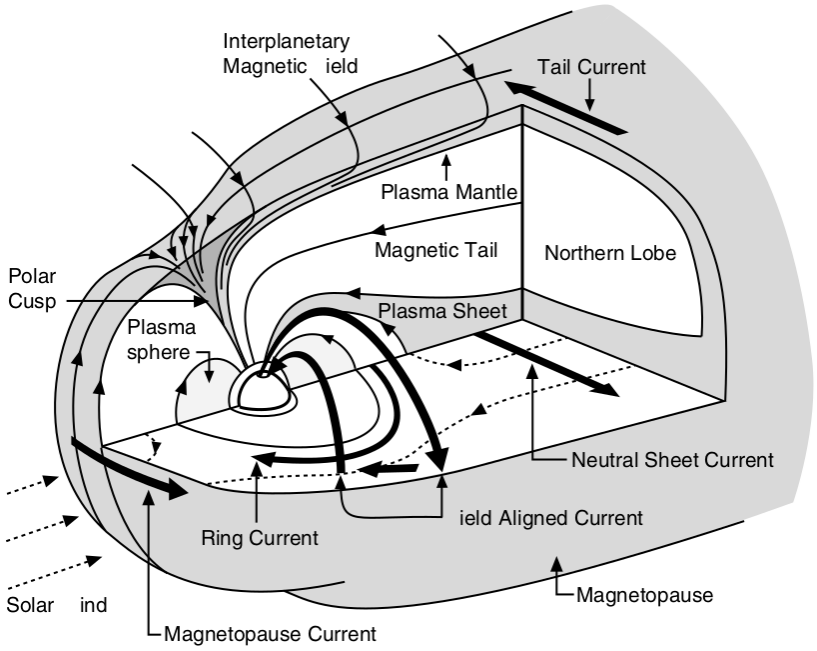

Figure 2.9: A three-dimensional view of the magnetosphere, where *ring* currents and *field aligned* currents are visible. Image taken from [59]

.

2.2.3 Ionosphere

The ionosphere identifies a collection of layers, inside the Earth's atmosphere, in which particles are continuously ionized and free electron can coexist with neutral particles for a long time, before recombining with ionized nuclei. This is possible given the low density of the atmosphere at high altitudes. Most of the ionosphere is, in fact, located above 80 km from ground, with the outermost layer located beyond 280 km from the surface. The stratification of the ionosphere can be observed in Fig. 2.11. The conditions of the latter, specifically its density and ionization, influence the operation of satellites in LEO orbits, as the ISS. Most of the free ions and electrons are located in the outer ionosphere, given the low density of gases, and are primarily produced by the photoelectric effect from the Sun's radiation; this also means that ionization is not evenly distributed around the globe, but mostly concentrated on Earth's day-side. There is, however, still appreciable level of ionization also on the night-side, especially at the highest altitudes, as recombination of free electrons takes a time proportional to atmospheric pressure [68].

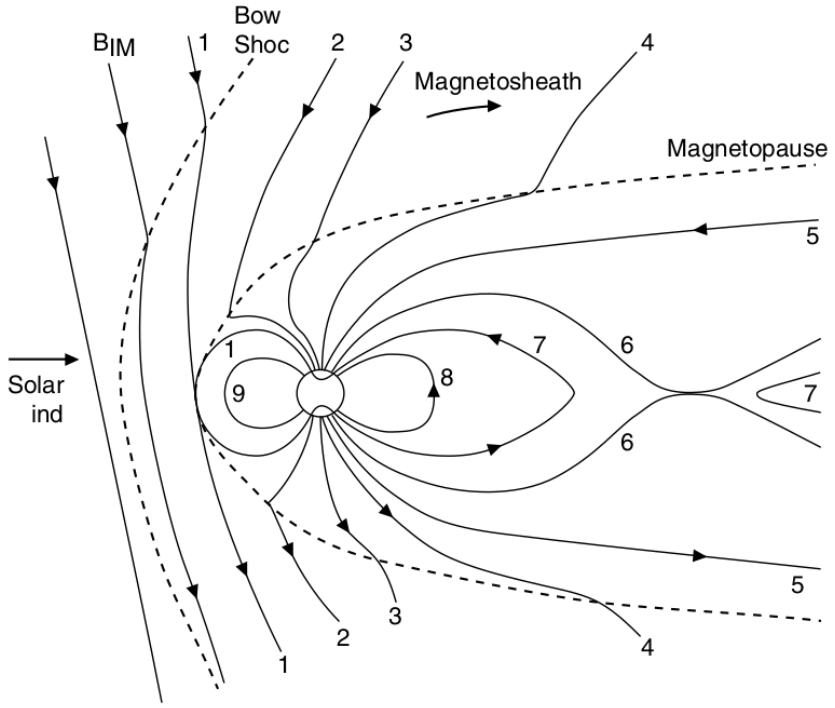

Figure 2.10: In this schematic, magnetic field lines (1) from a CME are coupled to the geomagnetic lines on the day side (2 and 3) via magnetic reconnection. This phenomenon causes the plasma contained in the CME to populate the magnetosphere, stretching its tail to the point where a second magnetic reconnection occurs (6 and 7 lines form an inner and outer loop), accelerating the plasma towards Earth. Image taken from [59]

.

2.2.4 Geomagnetic Rigidity Cutoff

Depending on their pitch angle and azimuthal angle with respect to Earth's axis, incoming charged particles inside the magnetosphere might encounter a stronger or weaker magnetic field. The field is stronger over the equator, where field lines are perpendicular to the average direction of motion, and weaker at the poles, where lines are almost parallel to it. The *Magnetic Rigidity Cutoff* is a function of altitude, azimuthal and polar angles, which defines a minimum rigidity for charged particles to reach a certain depth inside the magnetosphere. It describes the lower boundary below which particles are just deviated by the Lorentz force exerted by the geomagnetic field and cannot be observed at a specific point in space. One of the most known implementations of this function is the Störmer rigidity cutoff

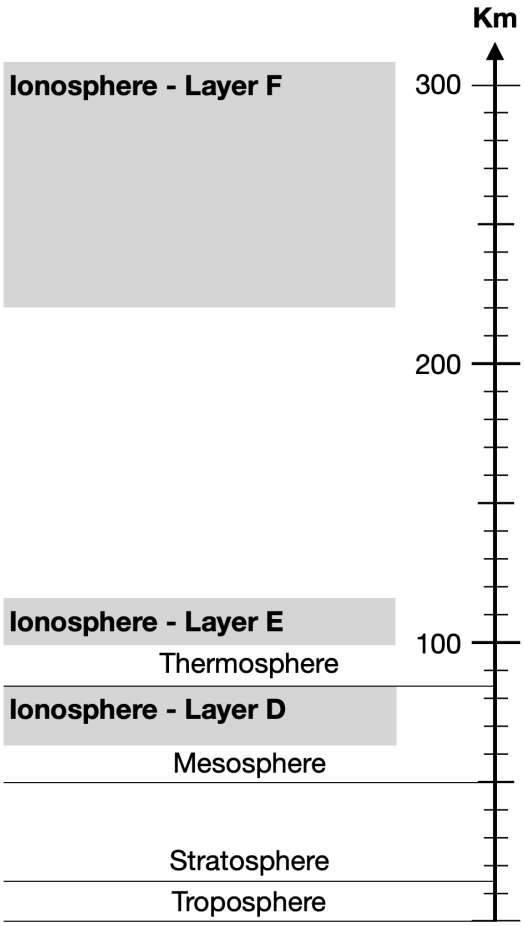

Figure 2.11: The three layers of the Ionosphere. The Layer F is the largest and can affect the measurements of charged cosmic rays for experiments in the Low Earth Orbits.

($R \leq R_c$), given by:

$$R_c = \frac{M_E}{r^2} \frac{cos^4\Theta_{mag}}{[1 + \sqrt{1 - Q \cdot sin\theta \cdot sin\phi \cdot cos^3\Theta_{mag}}]^2} \tag{2.2}$$

where Q is the particle charge, θ and ϕ are the polar and azimuthal angles with respect to the local zenith, Θ_{mag} is the geomagnetic latitude and M_E is the Earth's magnetic moment. The rigidity cutoff function is essential, in the context of cosmic rays studies within the Earth's magnetosphere, in order to separate the primary cosmic rays of galactic and solar origin and secondary or trapped particles that may be produced inside the magnetosphere.

Geomagnetic Cutoff in AMS The ISS, where the AMS experiment is positioned (see chapter 3), follows a LEO orbit with an average altitude of about 400 km. Given

the specific orbit of the ISS, the AMS capacity of detecting primary cosmic rays is heavily influenced by the geomagnetic field. While using a parametrization of the rigidity cutoff, like the Störmer cutoff, would be perfectly viable, a more accurate approach in case of AMS is generating a map of the cutoff by *backtracing* particles inside a model of the geomagnetic field. This is of curse only possible thanks to the accurate measurement of the pitch angle and energy of incoming particle with AMS. Backtracing, in fact, consists in solving the equation of motion of a given particle inside a model of the geomagnetic field, with pitch angle and energy at the detector as initial conditions, tracing back the origin of that particle [69]. In the case of AMS, the model of choice for the geomagnetic field is the IGRF model.

2.3 Space Weather

Space Weather is the study of the effects of solar activity on Earth, in its proximity and on other celestial objects inside the Solar System. The extension of human activity in space is becoming increasingly important, therefore we have to carefully consider the impact that all kinds of dangerous sources inside the heliosphere may threaten. This includes the effects of solar activity in terms of doses of radiation absorbed by astronaut in space, especially during extravehicular missions, but also in terms of damage caused to satellites and electronics in general. Space dosimetry is an ever-growing field of nuclear astrophysics, as the interest for long duration missions with human crew has increased over the last decade, for example in prospect for human missions on Mars. As for electronics in space, these studies are of fundamental importance for those systems that have become vital for a modern life on Earth, like telecommunications, GPS satellites and also power grids in case of extremely violent solar storms.

2.3.1 Radiation Damage to Electronics

Satellites are vital components of modern life, supporting communication, data transmission, weather forecasting, and scientific research. Depending on their mission, satellites typically operate within one of four primary orbital categories: *Low Earth Orbit* (LEO), *Medium Earth Orbit* (MEO), *High Earth Orbit* (HEO), or *Geostationary Orbit* (GEO).

LEO satellites orbit at altitudes ranging from a few hundred to a few thousand kilometers. They are often used for applications requiring low latency communication, direct Earth observation, or rapid data exchange between space and the planet's surface. For example, the International Space Station (ISS) follows a quasi-circular LEO orbit at altitudes between 330 km and 410 km.

Deploying satellites in LEO is more cost-effective compared to higher orbits, but

it comes with challenges. Despite the thin atmosphere at these altitudes, atmospheric drag remains a factor, causing gradual orbital decay. While the ISS uses onboard propulsion to maintain its trajectory, most LEO satellites lack such systems. In some cases, external interventions, such as the Space Shuttle's adjustments to the Hubble Space Telescope, are required to correct their orbits. Otherwise, their operational lifespan is largely determined by their initial altitude. As a satellite descends below 200 km, the atmospheric drag intensifies rapidly, leading to re-entry and disintegration within hours.

Severe space weather events can further reduce the lifespan of LEO satellites by increasing atmospheric density and ionization, which exacerbate drag effects.

Satellites in higher orbits are free from atmospheric drag but face other significant threats due to space weather phenomena [51]:

- **Surface Charging:** Satellites encounter both positive and negative charges in space, but the electron-rich environment of the magnetosphere can cause differential charging on their surfaces. This can lead to sudden discharges between materials, posing a serious threat to sensitive electronic components or optical detectors.
- **Deep Dielectric Charging:** Satellites traversing the Van Allen radiation belts are exposed to high-energy electrons capable of penetrating the spacecraft's hull. These electrons can charge the dielectric materials within circuit boards, potentially causing breakdowns, short circuits, and system failures over time.
- **Single Event Upsets:** Ionizing particles, such as cosmic rays or energetic solar ions, can alter the state of memory bits in digital electronics, leading to unintended signals or malfunctions. These disturbances can trigger severe system errors if not properly mitigated. A common practice in qualification for space electronics, in order to exclude spurious false signals or malfunctions, is to include multiple redundant systems.
- **Solar UV Material Degradation:** Without the protective shielding of Earth's atmosphere, satellites are directly exposed to intense solar ultraviolet (UV) radiation. This exposure can degrade materials like polymers, altering their chemical properties and reducing their functionality. Solar panels, in particular, suffer efficiency losses over time due to prolonged UV exposure.

2.3.2 Radiation Hazards for Biological Organisms

Ionizing radiation poses a significant threat to biological organisms by damaging cells at the molecular level. Particles with sufficient energy to remove electrons from atoms can alter their chemical properties, impairing essential biological functions.

Different types of ionizing radiation affect organisms in distinct ways. A key distinction is between electromagnetic radiation (such as photons and electrons) and nuclear radiation. Energetic photons and electrons, upon interaction, typically initiate electromagnetic showers, losing their energy quickly. In contrast, ions gradually lose energy through multiple collisions in a process known as multiple scattering. Charged particles primarily lose energy through inelastic collisions with target atomic electrons, a process described by the Bethe-Bloch formula for stopping power:

$$-\frac{dE}{dx} = 4\,\pi\,N_a\,r_e^2\,m_e\,c^2\,\rho\,\frac{Z}{A}\,\frac{z^2}{\beta^2}\left[\frac{1}{2}\,ln\left(\frac{2\,m_e\,c^2\,\gamma^2\,\beta^2\,T_{max}}{I^2}\right) - \beta^2 - \frac{\delta}{2} - \frac{C}{Z}\right] \tag{2.3}$$

where:

- $N_a \equiv$ Avogadro's number, $6.022 \cdot 10^{23}$.
- $r_e \equiv$ classical electron radius, $2.817 \cdot 10^{-15}$ m.
- $\rho \equiv$ density of the material.
- $Z \equiv$ atomic number of the absorbing material.
- $A \equiv$ mass number of the absorbing material.
- $z \equiv$ incident particle charge in units of e.
- $I \equiv$ mean excitation potential.
- $T_{max} \equiv$ maximum kinetic energy which can be imparted to a free electron in a single collision.
- $\beta = v/c$ of the particle.
- **Density effect, -$\frac{\delta}{2}$:** the charged particle polarizes the absorber material, hence the farther atoms are subjected to a shielded electric field and the particle loses less energy. This effect intensity increases with the incident energy.
- **Shell correction, -$\frac{C}{Z}$:** This term is introduced to cancel out the divergence of the base term for $\beta \to 0$.

Exposure to ultraviolet (UV) radiation is widely known to damage skin, with prolonged exposure increasing the risk of skin cancer (melanoma). Higher-energy photons, such as X-rays and γ-rays, can penetrate soft tissues, potentially damaging internal organs and DNA.

One common consequence of radiation exposure is the formation of free radicals—highly reactive molecules like hydroxyl radicals (OH*). These radicals readily disrupt cell

membranes, causing cell rupture and destruction. White blood cells and hematopoietic stem cells, which produce both white and red blood cells, are particularly sensitive to radiation. Their destruction compromises the immune system, increasing vulnerability to infections and other diseases.

Damage becomes critical when radiation affects nucleic acids (DNA) or proteins. Alterations to these complex molecules can impair cellular functions and potentially trigger cancer. While DNA has some capacity for self-repair, excessive radiation exposure can cause irreparable damage.

The impact of radiation on the human body is quantified using the *equivalent dose*, measured in sieverts (Sv, defined as J/kg) or rems (radiation equivalents in man), where 1 Sv equals 100 rem. This measure accounts for variations in radiation types, deposited energy, and their biological effects.

The average annual equivalent dose for a U.S. citizen is approximately 6.2 millisieverts (mSv) or 620 millirem (mrem), with the majority originating from naturally radioactive isotopes in the Earth's crust [70]. Medical sources contribute about half of the total dose, while space radiation accounts for only 0.33 mSv (5%).

Astronauts, however, face significantly higher radiation exposure. In LEO, astronauts typically receive about 0.1 rem per day—nearly one-sixth of an average U.S. citizen's annual dose. During a solar storm, exposure can rise to 10 to 1000 times the usual levels, potentially reaching lethal doses if protective shielding is unavailable [51]. Accurate predictions of solar activity are therefore essential for safeguarding human space missions.

The lethal dose for most humans is approximately 600 rem, although severe health complications can arise well before reaching this threshold.

Chapter 3

The AMS-02 Detector

The Alpha Magnetic Spectrometer (AMS-02, hereby referred to as AMS, [71]) is the most complex particle detector in space, installed on the ISS external hull of the ISS and in operation since May 2011. It will be active for the entire duration of the ISS mission, currently planned to end on 2030. AMS takes advantage of all the knowledge from particle detectors on Earth, using sophisticated instruments like silicon tracking systems, while also satisfying the strict quality standards of space missions, with multiple redundancy over all of its sub-detectors and electronics. The peculiarity of AMS as a space experiment, currently only shared with the PAMELA experiment ([72]), is the presence of a large magnet with a uniform magnetic field in a specific direction, inside which the tracking system is positioned. This configuration provides unique matter-antimatter separation capabilities, allowing for the measurement of the charge sign of crossing particles, depending on the direction of its curvature inside the magnetic field.

Another advantage of AMS is the Low-Earth Orbit (LEO) in which it is positioned. In fact the geomagnetic field on this type of orbit is still sufficiently intense to allow for a rigidity cutoff to exist (see section 2.2.4). The presence of the cutoff is necessary to separate the primary component of cosmic rays from the secondary and trapped component, the latter being deviated by the magnetic field before reaching the detector.

The study of primary cosmic rays is, in fact, one of the main objective of AMS, in order to comprehend the origin and composition of all the species in the periodic table that can be measured with this design. Among the main objectives we include the search for primordial antimatter [73], the indirect detection of dark matter particles [74] and new kinds of matter [75] and finally the study of temporal evolution of cosmic rays over multiple solar cycles. The detection of antimatter nuclei heavier than hydrogen would be a clear indication of the existence of primordial antimatter,

before the event that led to the inequality between matter and antimatter we observe today. These nuclei would likely be originated from isolated dominions of antimatter that are currently existing, rather than be produced in collision and nucleosynthesis from ordinary matter, as the cross section for this occurrence is extremely small. As for dark matter, many candidates are thought to be neutral particles that could decay in matter and antimatter pairs, which would be observable as excesses in the spectra. Antiprotons and positron are the perfect species to look for these kind of excesses, as the background processes that produce them are low and can more easily be accounted for. Another indicator of the presence of dark matter decay could be offered by the observation of anisotropy in the fluxes, as many forms of dark matter are thought to be independent from the galactic rotation. Finally exotic matter could be observed in the form of *strangelets*, ordinary matter that is made by strange quarks, as it's thought to be produced in extreme events in the universe and remain stable while traveling inside the galaxy.

AMS is provided with five sub-detectors, arranged in series along one of the orthogonal axis to the magnetic field direction. The order of AMS instrumentation is determined by the destructiveness of each measuring technique, with the most destructive detectors positioned on the bottom of the experiment with respect to particles incoming direction. The Transition Radiation Detector (TRD) is the first instrument, measuring the transition radiation left by leptons which allows to distinguish positrons from protons and antiprotons from electrons. The two pair of scintillator layers of the Time of Flight (ToF) is positioned one above and one below the magnet, measuring the temporal delay between them and triggering the data acquisition to record physical events. Inside the magnet, the seven layers of the Inner Tracker are located, which precisely track the position of each crossing particle, while the remaining two layers of the Tracker are positioned above the TRD and below RICH, extending the lever arm of the measurement. Below the lower ToF there is the Ring Imaging Cherenkov (RICH) detector, exploiting the Cherenkov effect to precisely measure velocity of relativistic particles. Finally the last element in AMS is the Electromagnetic Calorimeter (ECAL), providing measurement of energy for leptons and lepton/hadron separation. A picture of the instrument is shown in Fig. 3.1, together with a schematic view of its subsystems. In the following sub-sections, a detailed description of the above-mentioned instruments is presented.

3.1 Permanent Magnet

The permanent magnet is a fundamental component for the search of antimatter and dark matter, since it allows AMS to measure the charge sign of particles, in addition to precisely measure their rigidity alongside the tracker. Charged particles moving inside a uniform magnetic field are subjected to the Lorentz force, which bends their trajectory on the orthogonal plane to the magnetic field direction. The

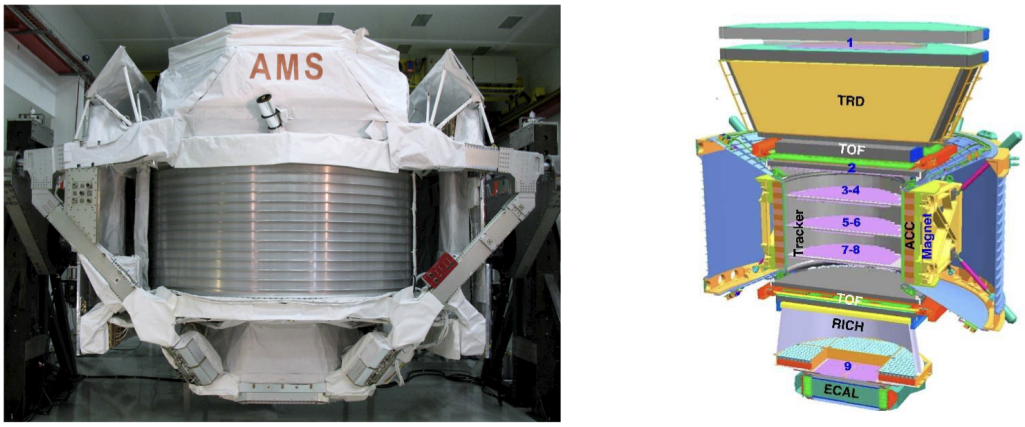

Figure 3.1: **Left:** A picture of the AMS-02 experiment before its launch. **Right:** Schematic view of its five sub-detectors.

curvature and direction of the trajectory depend on energy, absolute charge and charge sign.

The magnet was originally developed and used in AMS-01 [76], but after the abandon of the design of a superconducting magnet, it was also adopted for AMS-02. The configuration of its 6400 Nd-Fe-B magnets, shown in Fig. 3.2, is such that the internal magnetic field is uniform and parallel to the y axis on AMS coordinate system (it's actually the definition of the axis) with an intensity of 0.15 T, while maintaining the external field as low as possible, being the intensity less than 0.02 T. The magnet has a toroidal shape, 1 m in diameter and height. Its magnets have a dimension of $5 \times 5 \times 2.5$ cm^3 and are arranged in 100 rings. The permanent magnet ensured greater stability and duration of the AMS experiment, while the originally intended superconducting magnet needed to be cooled via liquid helium, dramatically decreasing its lifespan.

AMS has its own coordinate system, based upon the direction of the magnetic field generated by the magnet. The coordinate system center coincides with the center of the torus, the x axis is parallel to the uniform magnetic field lines, the z axis corresponds to the torus main axis and the y axis completes the right-handed Cartesian system (also called *bending direction*), as pictures in Fig. 3.2.

3.2 Transition Radiation Detector

The Transition Radiation Detector is the instrument on top of AMS, with the primary purpose to separate leptons from baryons, in particular positrons from protons and antiprotons from electrons [77]. Antimatter is one of the most interesting as-

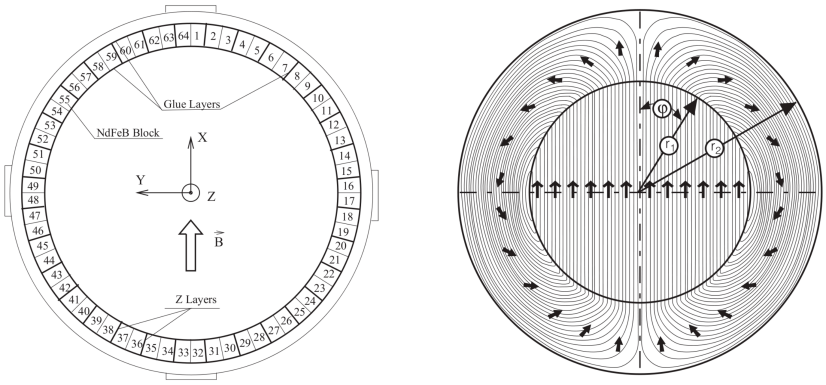

Figure 3.2: **Left:** Configuration of the AMS magnets, with the reference frame based on the orientation of their magnetic field. **Right:** Orientation of the magnetic field.

pects in cosmic rays and the flux of antiparticles is several orders of magnitude lower than that of their ordinary matter counterparts; for this reason, AMS adopted different methods to ensure the highest possible rejection power of the large background constituted by the same-charged particles as the antiparticles in study. The proton rejection power of the TRD is shown in Fig. 3.4.

The detector consists of 328 modules arranged in 20 layers. Each module contains a radiator made by two alternating materials with different refractive indexes. The radiator is on top of 16 straw tubes filled with a $Xe - CO_2$ mixture, where a tension of 1600 V is applied, acting as ionization chambers. The external shell of the tubes is the cathode and a wire, placed along the axis of the tube, is the anode. The support structure of the TRD has a truncated pyramidal shape with an octagonal base, with the larger base on top, following the maximum angle of acceptance with the rest of the sub-detectors.

The operating principle of the TRD is based upon the radiation emitted by a charged particle while crossing materials with two different refractive indexes. A charged cosmic ray that hits the different interfaces inside the radiator, in fact, has a chance of emitting photons in the soft X-rays. The intensity of radiation is proportional to the Lorentz factor $\gamma = \mathrm{E/m}$, hence lighter particles, like electrons and positrons, will produce more photons [78]. These photons will then ionize the neutral Xe gas and produce a current collected at the electrodes inside the tube. The presence of CO_2 in the gas mixture is to ensure that additional photons emitted by the ions produced inside the tube will be absorbed by the gas, acting as quencher for the cascading ions. Xe and CO_2 are in a 80:20 proportion.

The TRD also offers the possibility of measuring particles trajectory and the spatial resolution depends on the orientation of the straw tubes: orthogonally to the tubes, position on each layer is determined by the location of the tube that produced the

current, with an uncertainty that depends on the thickness of each tube, while on the direction parallel to the AMS axis it is given by the height of the layer with respect to the center of the AMS coordinate system. For this reason, 12 out of 20 layers are oriented with straw tubes on the x axis in the AMS coordinate system, perpendicular to the AMS magnetic field direction, allowing for a better spatial resolution on the measurement over the bending direction, while 4 are placed on top and 4 on the bottom of the TRD with tubes parallel to the y axis, allowing for multiple measurements on three coordinates.

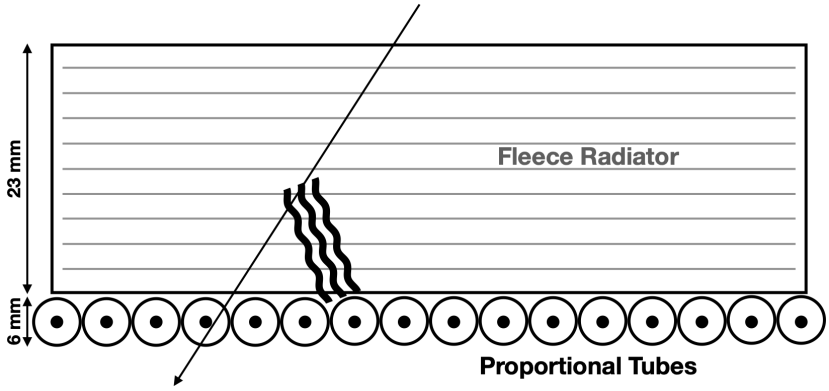

Figure 3.3: Schematic view of one of the 20 TRD modules, composed by a fleece radiator and 16 proportional tubes.

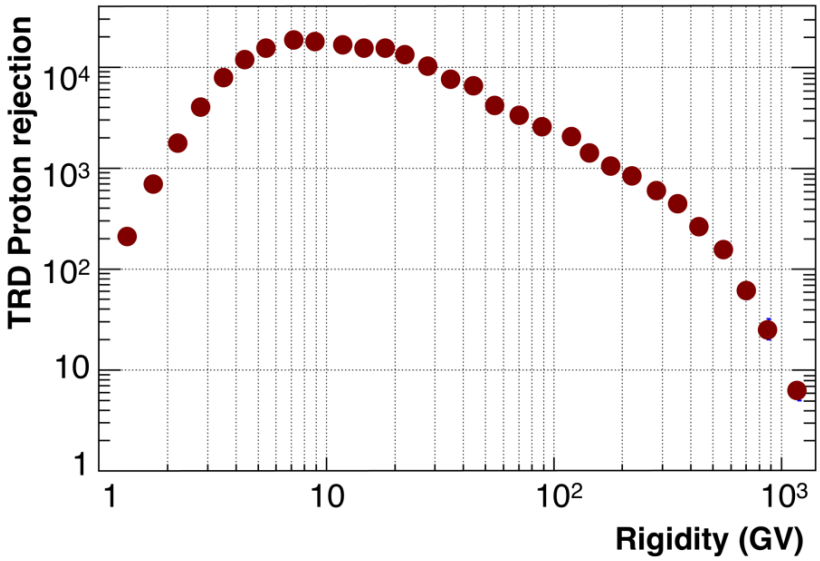

Figure 3.4: The combination of signals of the energy deposit in the 20 layers of the TRD produces the proton rejection factor in figure[79]. Above 400 GV, the rejection factor is decreases, since protons start to produce transition radiation.

3.3 Time Of Flight Detector

The Time of Flight is a fundamental instrument that provides the charged particle trigger signal for the entire experiment, while measuring the traveling time of crossing particles, hence their velocity βc, and charge Z [80].

It consists of 4 layers made by long paddles of plastic scintillators, with two of said layers placed just above the magnet and two below, in an alternating orientation of paddles. Each layer consists of 8 paddles, 10 for the third layer. The ToF paddle placement is shown in Fig. 3.5. A paddle is made by a block of polyvinyltoluene scintillator in a rectangular or trapezoidal cut about 12 cm wide, 110-130 cm long and 1 cm thick, adjacent to each other and overlapping for about 0.5 cm, in order to eliminate any gaps in the central area. Being each pair of layers mutually perpendicular, their configuration allows for a two-dimensional position measurement, with a spatial resolution of 12×12 cm^2.

When a charged particle crosses the scintillator block, it emits light which is then collected on both of the short sides of the block by custom photomultipliers (PMT). The scintillator block and the photomultipliers are connected by light guides, tailored in shape and angle for each paddle, in order to reduce any effect of the external magnetic field of AMS on the PMTs. The PMTs operate at high voltage and are designed with a tight layout of the dynode structure, to improve light collection efficiency in the presence of the magnetic field.

The anode signal produced by PMTs is analyzed and compared with a *low threshold* (LT, $\sim$ 20% proton MIP signal), a *high threshold* (HT, $\sim$ 50% proton MIP signal) and a *super high threshold* (SHT, $\sim$ 400% proton MIP signal). Ht and SHT signals are part of the *Level 1* trigger signal to identify $Z \geq 1$ and $Z > 1$ charged particles respectively. The LT signal is read by the time to digital converter (TDC) system, which starts a chronometer. As soon as the second signal is produced on the lower ToF layers, the chronometer is stopped and the delay information is evaluated.

The time delay measured by the TDC Δt is combined with the path length measured with the Tracker Δs to calculate the velocity in units of c, also known as β: $\beta = \Delta s/c\Delta t$. ToF can measure β in this way for particles that reach at maximum 98% the speed of light, considering that the lower and upper ToF layers are about 1.2 m apart.

The temporal resolution is between 48 and 160 picoseconds, depending on the species of cosmic ray, increasing for higher charges. This translates into a very high velocity (or rather β) resolution, which is about 4% for protons. 2% for He nuclei and 1.2% for C nuclei.

The temporal information is also used to determine whether the particle is downgoing or up-going, which is fundamental to distinguish matter from antimatter, as

a positive up-going particle could be mistakenly reconstructed as negative down-going with same absolute charge. The fraction of up-going particles mistaken for down-going is less than one over 10^9 particles.

Each ToF layer provides also an independent estimation of the absolute charge, inferred from the PMT signal collected at the anode, which is a measure of deposited energy: $\frac{dE}{dx} = \propto Z^2$. The anode signal becomes saturated for ions with charge Z>4, so the dynamic range is increased up to Z=30 by using the PMT dynode signal instead.

The trigger signal, named *fast trigger* (FT) at this stage, is produced when there is an energy deposit in at least 3/4 ToF layers; The details on the different trigger signals are discussed in section 3.8.

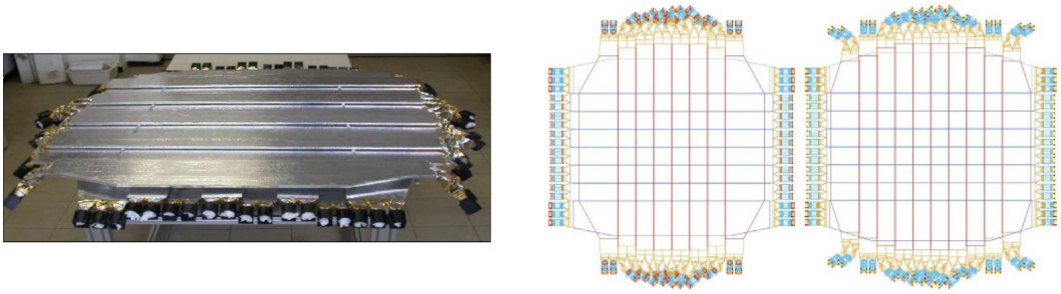

Figure 3.5: **Left:** Picture of the upper ToF scintillation plane. **Right:** Orientation of the ToF paddles on the upper and lower layers, with the disposition of the PMTs on both ends of each paddle.

3.4 Silicon Tracker

The AMS silicon tracking system (TRK) is one of the largest ever built for space measurements, with a total effective sensible area of about 6.2 m^2 [81] [82]. It is composed by nine layers of silicon micro-strip detectors, seven of which are positioned inside a large permanent magnet. Each layer is formed by several *ladders*, a series of silicon sensors bonded tighter in a daisy chain configuration, with the same orientation of the strips. The tracker counts a total of 2264 silicon double-sided micro-strip sensors, positioned on 192 ladders. Layer 1 is located just above the TRD, extending the lever arm of the rigidity measurement to the top of the detector, therefore outside the permanent magnet. Layers 2-8 are inside the magnet and most of them are coupled in pairs with orthogonal direction of ladders (L3-L4, L5-L6 and L7-L8). These Layers follow the circular shape of the interior of the magnet, except on the y coordinate, where part of the circular arc is missing (see

Fig. 4.1). Finally Layer 9, which is smaller and rectangular in shape, is positioned at the bottom of the detector, above the ECAL.

The main purpose of a tracking system inside a magnet is to record the position of crossing particles with high accuracy and precision, providing a measurement of their rigidity R, i.e. the particles momentum p divided by the charge Z, measuring the radius of the bent trajectory due to the Lorentz force.

$$R = \frac{pc}{Ze} \tag{3.1}$$

This measurement can be improved in precision and rigidity range, especially at very high rigidities, by utilizing Layer 1 and Layer 9, which extend the lever arm of the measured trajectory. Layer 1 is also necessary to remove contamination from fragmented nuclei, which can be mistakenly reconstructed as other species, allowing to determine if the particle interacted inside the TRD or in any material between L1 and L2. When using all the 9 layers for the rigidity measurement, we refer to the AMS tracker configuration as *full span*. The Maximum Detectable Rigidity (MDR) with the full span configuration, for which dR/R = 1, is 2 TV for protons and electrons and 3.2 TV for helium nuclei. The rigidity resolution of the tracker is itself dependent on rigidity (see Fig. 3.6): it is mostly constant at low rigidity, where it's dominated by multiple scattering, while it increases linearly at higher rigidities. Higher energy particles are less effected by the magnetic field, so their trace inside the tracker will be almost a straight line.

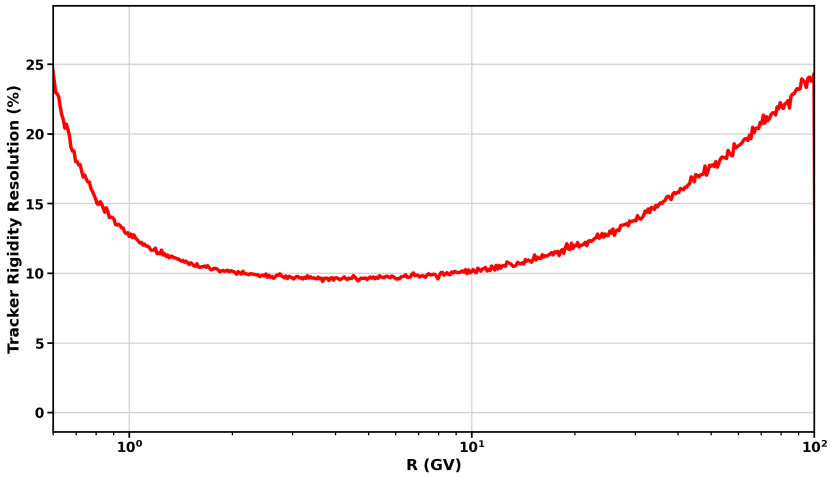

Figure 3.6: Tracker rigidity resolution with the Inner+Layer1 configuration, calculated with the new dataset 3.12.1 during the evolution of this work 4.8. The resolution is worse at the lowest rigidities due to multiple scattering, while at the highest it is worsened by the reduced lever arm of Inner+Layer1 configuration. See section 4.2 for more information on the various tracker configurations.

Each layer of the tracker also provides an independent measurement of the absolute charge Z, which is proportional to the energy deposited inside each sensor. The charge resolution using all the inner tracker layers is $\Delta z = 0.05$ for particles with Z=1. On top of the absolute measurement, the tracker is the only sub-detector that can determine the charge sign, according to the bending direction of the particle and the up-going or down-going direction determined by the ToF.

The basic component of the tracker is the silicon sensor, a rectangular silicon plate with planar dimensions dimensions 72×41 mm^3 and a thickness of 300 μm. Each sensor has metallic strips implanted on top and bottom surfaces, orthogonal to each other, for a bi-dimensional measurement of position. The choice of thickness and double-sided strip implants design was made to minimize the amount of material that particles would need to cross, in order to avoid as much as possible energy losses and multiple scattering. The sensor has three main substrates, with a central n doped silicon wafer surrounded by a series of $p+$ doped (with a higher number of implants than p doping) silicon strips on one side and $n+$ strips on the other side; the strips act as charge-collecting electrodes. The implantation pitch is 25.5 μm for the $p+$ side and 104 μm for the $n+$ side. These implants act as a mono-dimensional array of p-n junctions. A charged particle that passes through the sensor, to which is constantly applied a potential difference of ~ 80 V, generates electron-hole pairs that travel to the opposite sign strips. Electrons will flow towards the $p+$ strips, where they are collected and determine the y coordinate (on the bending direction), while holes travel towards the $n+$ strips, determining the x coordinate. Since the readout signal of the strips is analog and the strips are capacitatively coupled, the spatial resolution is higher than the simple distance between the strips, since we are able to measure the center of mass of the collected charge. In fact, on the y axis (bending direction) in the AMS coordinate system the resolution is about 10 μm and 30 μm on the x axis for Z=1 particles.

An important aspect of the tracker is its calibration system. The tracker was first extensively tested on Earth before its lunch at CERN SPS with 180 and 400 GeV/c proton, electron, positron and pion beams, at different energy and positions, in order to determine its rigidity resolution and scale; it was also calibrated measuring cosmic muons fluxes on Earth [83]. Being a space experiment, AMS experiences, throughout each orbit, several extreme temperature changes and conditions that will stress the materials in different ways, misaligning the myriad of sensors. It is imperative to calibrate the position of each sensor, in order to reduce the systematic uncertainty over the measurement. For this reason the tracker is accompanied by a tracker alignment system (TAS) [84], which provides a way to monitor the stability of the tracker modules in space. The TAS is provided with 20 infrared laser beams, which emulate vertical rigid tracks, used to evaluate any possible deviation from a stable geometry of the inner tracker. As for Layer 1 and Layer 9, they are aligned to the inner tracker using cosmic rays in a 2 minute window, with a precision of 5

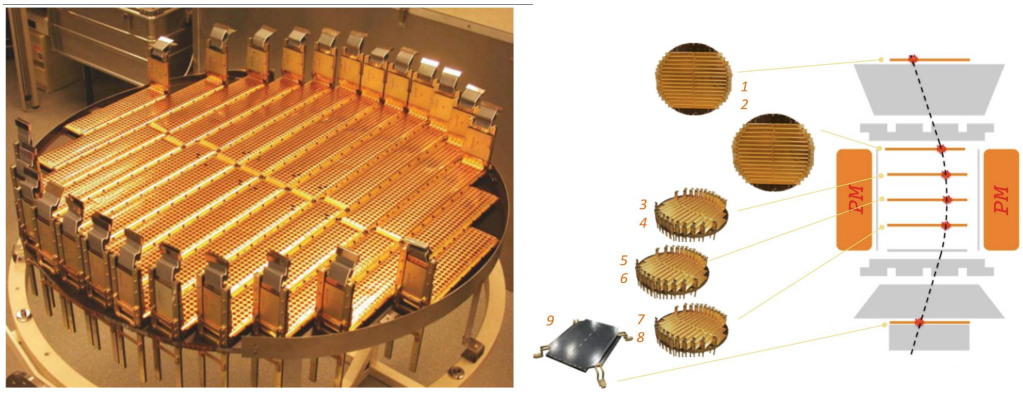

Figure 3.7: **Left:** Inner layer composed by several readout units (ladder): the readout electronics is installed at the end of each ladder. **Right:** Silicon Tracker Layer layout in AMS-02.

μm and 6 μm respectively.

Whenever an event is recorded, due to the large amounts of readout channels (about 200000 channels) in the tracker, only the ones that contain a physical signal are stored. The operation of discarding non-physical channels is handled by dedicated circuits called *tracker data reduction* (TDR).

Although the power consumption of a single channel is small ($\sim$ 0.7 mW), when dealing with the large number of channels in the tracker, heat becomes a concern and must be dissipated. This task is performed by the *upgraded tracker thermal pump system* (UTTPS, [85]), a dual-phase CO_2 cooling pump that operates in a closed loop. The UTTPS replaced the old *tracker thermal control system* (TTCS, [86]) after its degradation in 2019, via a series of 4 extra-vehicular activities by NASA, to extend the lifetime of AMS.

3.5 Anti Coincidence Counter

The anti-coincidence counter (ACC) consists of 16 scintillator paddles, 8 mm thick, inserted vertically inside the magnet and around the inner tracker, providing a veto signal for the experiment [87] [88]. The light is collected by several wavelength-shifter fibres, with a diameter of 1 mm, and transmitted to 16 PMTs at the edge of the magnet. The veto is triggered in case of a particle that:

- crosses the detector from the side, outside the acceptance cone.
- is detected by ToF, producing a trigger, but not the other instruments.
- Heavily interacted inside the tracker, producing many secondary particles.

The above cases lead to events that are either impossible to reconstruct or too complicated to correctly identify and could be mistakenly reconstructed as other species. The ACC signal is part of the complex *Level 1* trigger signal described in 3.8.1.

3.6 Ring Imaging Cherenkov Detector

The *Ring Imaging Cherenkov* (RICH) is a detector that takes advantage of the Cherenkov light emitted by charged particles to measure accurately their velocity [89] [90]. This detector is complementary to the ToF measurements, as ToF can only determine the velocity for low energy particles (up to 5 GV), and performs with grater efficiency for highly relativistic particles. Indeed the Cherenkov effect manifests when a charged particle crosses a medium with a higher velocity than the phase velocity of light in that medium ($\beta_{thr} = 1/\mathrm{n}$, where n is the refractive index of the material); the particle emits a cone of light, whose aperture angle of emission depends on the velocity of the particle.

The RICH has three main components (see Fig. 3.8): a radiator plane, a detection plane and a mirror, with the detection plane presenting a 64×64 cm^2 hole in the middle that matches the shape and size of the calorimeter below (in order to minimize the material above the calorimeter). The radiator plane is populated with two materials that have a different refractive index. The outer region of the radiator plane is installed with silica aerogel tiles with a thickness of 2.5 cm and refractive index $n = 1.05$, while the area above the hole is covered by sodium fluoride (NaF) crystals, which have a higher refractive index equal to $n = 1.334$ and a thickness of 0.5 cm. The choice of NaF crystals in the middle of the plane was made to maximize the collection of light around the hole and to extend the velocity measurement (Fig. 3.9). The aerogel can measure velocities for $\beta_{thr}^{AGL} = 0.95$, while the threshold for NaF is $\beta_{thr}^{NaF} = 0.75$. After the particle emitted a cone of light, the cone expands traveling along the gap between the radiation and detection planes, allowing for its expansion. The light is finally collected on the detection plane, where 680 PMTs are installed. The gap in between the two planes is surrounded by a truncated conical mirror which reflects the light back on the detection plane, to collect as much light as possible (Fig. 3.8). The top plane of the truncated cone shape (the radiation plane) is circular with a radius of 60 cm, while the bottom plane (the detection plane) measures 67 cm. The hight of the gap is 60.5 cm.

The particle velocity (β) is determined by measuring the radius of the circular shape detected by the PMTs, from which the aperture angle (θ_c) of the cone is inferred:

$$\beta = \frac{1}{n \cdot cos\theta_c} \tag{3.2}$$

particles with higher velocities produce wider cones. The RICH is also capable of determining the charge, by measuring the intensity of the emitted light, as it's linearly proportional to the charge.

The RICH velocity measurement is the most accurate at high rigidities, with a resolution of $\frac{\Delta\beta}{\beta} < 1.2 \times 10^{-3}$ for Z<26. The charge measurement resolution is $\Delta Z < 0.5$. The measurement of β with RICH, combined with the Tracker rigidity, allows to estimate the mass of the particle with excellent resolution.

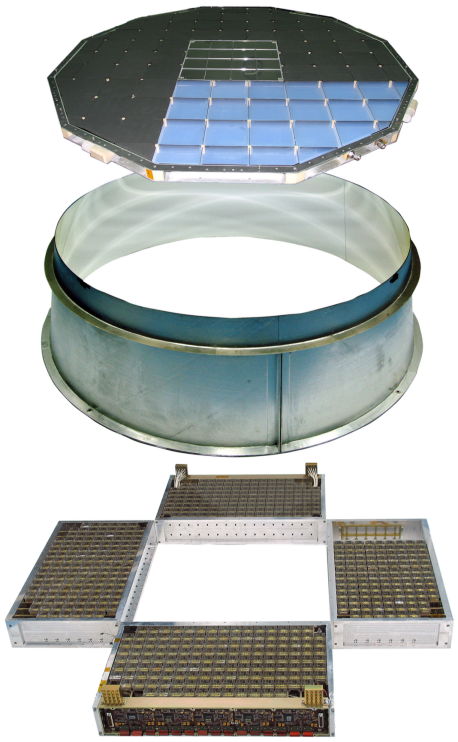

Figure 3.8: The three RICH main components: radiator plane, conical mirror and detection plane.

3.7 Electromagnetic Calorimeter

A calorimeter is a detector that performs a destructive measurement, inferring particles energy by forcing an interaction with a dense material and containing the shower of products inside the sensible area. In the case of the Electromagnetic Calorimeter (ECAL), this task is specifically aimed at containing and measuring the energy of leptons, while hadrons are usually not fully contained or do not interact at all. This choice was made primarily for two reasons: hadronic calorimeters, like the ones used in particle physics on ground accelerators, require overall a large mass to be able

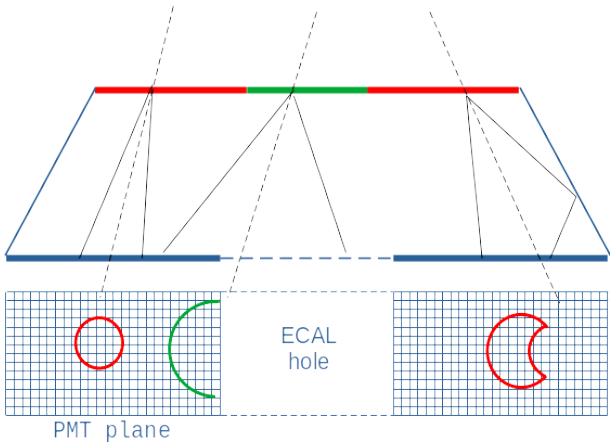

Figure 3.9: This picture shows three possible signals from a particle with the same property: a particle is fully detected after crossing the AGL radiator (left), the NaF radiator (center image, with a wider ring) or part of the light cone is reflected by the mirror for the AGL signal (right).

to fully contain the particles, which is not practical for a space mission; secondly, ECAL allows to discriminate leptons from hadrons solely from the shape of the shower and wether it is fully contained or not [91] [92] [93].

The ECAL is a sampling calorimeter, made by 9 modules called *superlayers* [94]. Each superlayer is 18.5 mm thick and contains 11 layers of scintillator fibers, 1 cm in diameter, housed in between layers of lead foil, 1 cm thick. The fibers are held together with lead foils by epoxy resin. Fibers are read out only on one of the ends by PMTs, which are coupled to multiple neighbouring fibers via light guides in what is called a *cell* (see Fig. 3.10). PMTs are placed in alternating cells on both ends of the fibres, in order to avoid mechanical interference. All the 50000 fibers in ECAL are read out by 324 PMTs, 36 per superlayer, for a total of 1296 photosensor. Each anode is coupled with 35 fibers, in an active area of 9×9 mm^2. Each superlayer contains fibers placed in one direction and the 9 superlayers are stacked in such a way that fibers have an alternating orientation on both the x and y axis in the AMS coordinate system. This structure allows for 3D measurements of the shower development, similarly to the ToF measurements. The lead interleaving is a dense material where the interaction happens: leptons produce photons that are absorbed by the nearest fibers and then collected by the PMTs.

Nuclei can interact with ECAL, with primarily protons that have a 50% chance of interaction, but the stopping power of ECAL is not sufficient to contain the shower and only the initial interactions are captured. In addition to this distinction, hadronic showers are also different in shape than those produced by electromagnetic interaction, as they contain all the products resulting from strong interactions.

The energy resolution has been measured during beam tests on Earth and is given by:

$$\frac{\sigma(E)}{E} = \frac{10.4 \pm 0.2}{\sqrt{E(GeV)}}\% \oplus (1.4 \pm 0.1)\% \tag{3.3}$$

as function of energy E [95]. The linearity of the response of ECAL energy measurement is within 1% in the range [6, 250] GeV. The results of measurements at beam tests are shown in Fig. 3.11. In the case of electrons and positrons, thanks to the 3D profile of leptonic shower, the energy measurement resolution is 2% for electrons at 100 GeV and the angular resolution on the determination of incident angle is better than 1° for energies higher than 100 GeV [96].

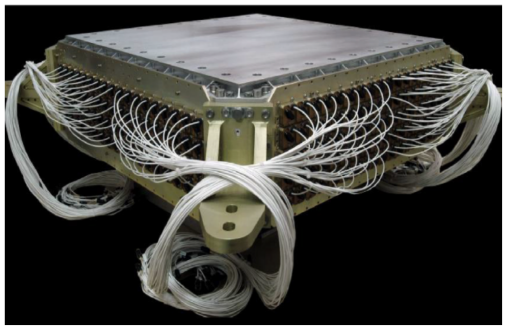

(a) ECAL Structure

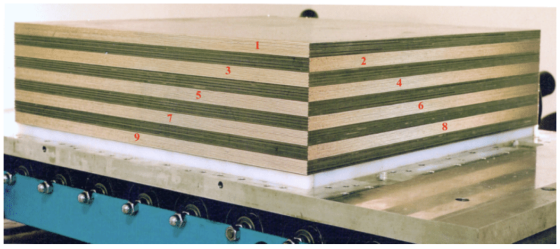

(b) ECAL Distribution of Superlayers

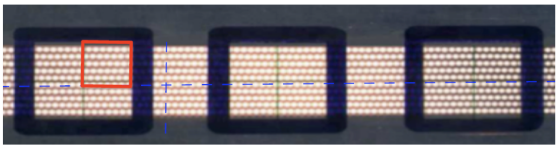

(c) Superlayers Structure

Figure 3.10: **a:** Picture of the complete ECAL structure, with all the PMT channel readouts cables visible. **b:** Picture of the ECAL pancake and the distribution of the superlayers **c:** Detailed view of a superlayer, with the single cell of optic fibers identified by the red square.

The 3D imaging capabilities of ECAL are used in conjunction with multivariate analysis techniques, in order to separate the dominant proton background from the single charged leptonic species, namely electron and positron [93]. The proton rejection power of ECAL is shown in Fig. 3.12.

3.8 Data Acquisition and Trigger

The *Data Acquistion* (DAQ) system is the collection of 300000 *Front-End* (FE) electronics channels, attached to each AMS sub-detector, and about 300 computational

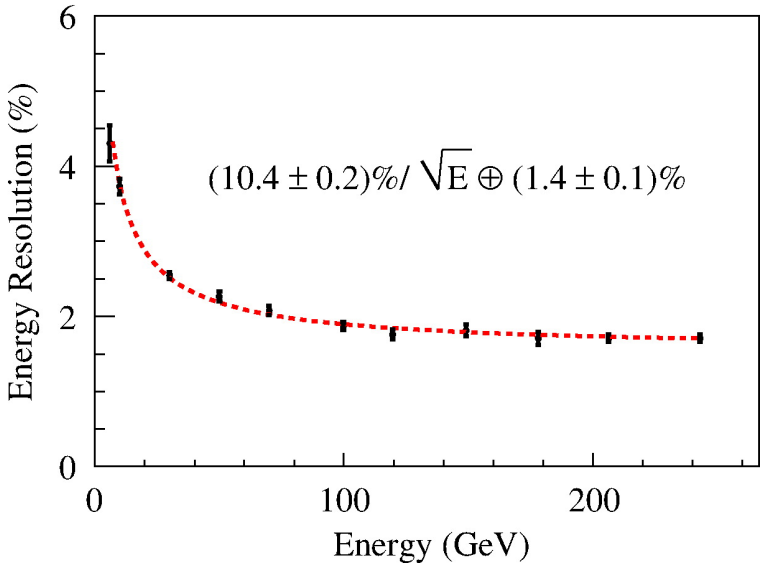

Figure 3.11: Energy resolution of the ECAL as measured with electron and positron test beams.

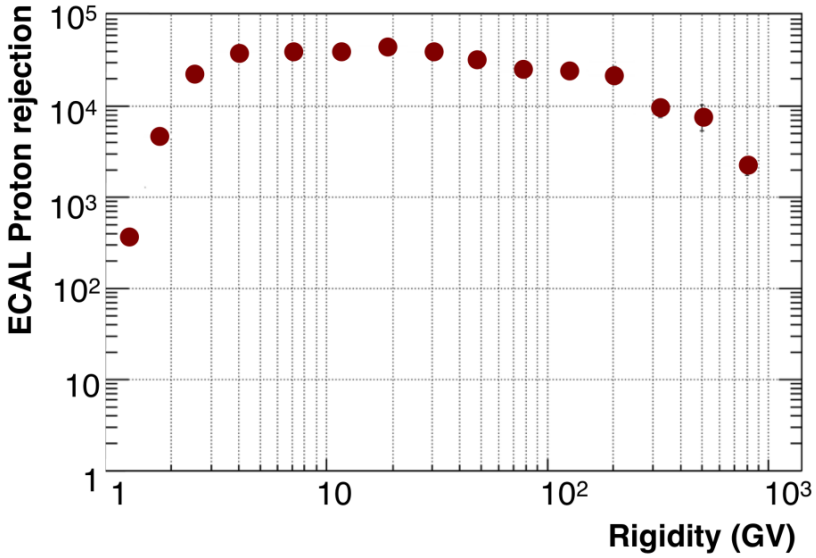

Figure 3.12: The shower topology inside the ECAL, along with the rigidity measurement, is used to achieve proton rejection for charge 1 particles.

nodes. Most of said nodes (264) are dedicated to collect raw signals from the FE boards and perform a first data reduction. Their designation is *xDR*, where *x* stands for the specific sub-detector (U = TRD, S = ToF and ACC, T = Tracker, R = RICH and E = ECAL) and *DR* for *Data Reduction*. The signal from the *xDR* is then collected by 14 double-redundant low-level DAQ computers (JINF). In the meantime,

8 nodes called SDR process the raw signals from ToF and ACC to produce the fast trigger and communicate with 2 JLV1 boards to produce the Level 1 trigger. All the signals from JINF, SDR and JLV1 boards is collected by the four redundant high-level DAQ computers (JINJ) and sent to the main computer JMDC, also four times redundant, for recording. The schematic of the Data Acquisition process is shown in Fig. 3.13. To minimize the amount of dead time introduced by the processing, data is buffered at each step go the DAQ chain. The AMS DAQ system operates at a maximum trigger rate of 2 kHz and and average event size of 2 kB. Data is collected in $\sim$ 23 min batches called *run*. A full ISS orbit contains exactly 4 runs, each starting at the maximum (or minimum) polar latitudes and at the crossing of the equator. During the crossing of the equator a calibration of the sub-detectors is performed. The equator is the region in which the rigidity cutoff is higher, hence the trigger rate is lower, which is the best condition for calibration purposes. Pedestal and noise values are measured for each channel, which will the be used by xDRs during the event data reduction procedure.

Finally the complete files containing the DAQ runs are transmitted to NASA's White Sands Test Facility on Earth, via satellite communication. From there, data is sent to the Payload Operations Integration Center (POIC) in MSFC and copied to the Payload Operation Control Center (POCC) of CERN and Taiwan. The two control centers are dedicated to non-stop monitoring of AMS and its data acquisition, during 8-hours shifts equally distributed among the collaboration members.

3.8.1 Trigger Signal

The AMS trigger signal is a combination of the electronic signals from ToF, ACC and ECAL. These inputs are handled by a dedicated board called JLVL1, which adjusts the time delay between them, performs the pre-processing and finally combines them following the Level 1 logic shown in 3.8.1. Since the production of the Level 1 trigger introduces some dead time inside the detector, a simpler trigger signal, called *fast trigger*, is produced using the signal from ToF and ECAL, enabling the subsequent production of the Level 1 trigger. There are two kinds of fast trigger: one for charged particles, generated by ToF on the particle crossing its scintillators, and one for photons, generated by ECAL upon detection of an electromagnetic shower. The different fast trigger signals are:

- **FTC:** signal coincidence in 3/4 layers of ToF, within a 240 ns gate, with a pulse height greater than 0.5 times the one generated by a MIP proton (*High Threshold*, HT). This is a generic trigger for charged particles.
- **FTZ:** signal coincidence in 4/4 layers of ToF, within a 640 ns gate, with a pulse height greater than 3.5 times the one generated by a MIP proton (*Super High Threshold*, SHT). This trigger is specific to slow ions.

- **FTE:** energy deposition in ECAL indicating a particle with energy greater than 1 GeV. This trigger is specific to leptons (electron and positron) and photons.

The logical *or* of the fast triggers is evaluated and combined by passive electronics to generate one or more among seven complex Level 1 trigger signals to start the DAQ chain ([97]):

- **Unbiased Charged:** HT signal is produced in 3/4 TOF planes. A pre-scale factor of 100 is applied to reduce the trigger rate.
- **Single Charge:** HT signal in 4/4 TOF planes, no ACC fired.
- **Normal Ion:** SHT signal in 4/4 TOF planes.
- **Slow Ion:** SHT signal in 4/4 TOF planes, delayed gate width (640 ns).
- **Electron:** HT signal in 4/4 TOF planes, ECAL energy deposit above threshold in both projections.
- **Photons:** ECAL energy deposit above threshold in both projections, ECAL axis inside AMS field of view.
- **Unbiased EM:** ECAL energy deposit above threshold in both projections. A pre-scale factor of 100 is applied to reduce the trigger rate.

Once any combination of the above signals is produced, the system is set in a *busy* state for 220 μs and the data acquisition takes place.

3.9 AMS Livetime

The estimation of the amount of time in which AMS is not in a busy state, called *livetime*, is essential to properly evaluate the rate of particles, as it will be described in detail in section 4.3. Livetime is calculated by evaluating the ratio between the events that were recorded and the total number of events, every second. It is highly dependent on the particle trigger rate, in particular where the rigidity cutoff is low and many low energy particles reach the detector. The rate increases in polar regions and inside the SAA. The latter (see section 2.2.2) is a problematic region for AMS, as the rate of trapped particles is so high that it saturate the DAQ, nullifying livetime.

The ISS orbits around the Earth at an altitude between 330 km and 410 km completing 15.7 orbits per day. The orbit plane is inclined by 51.6° with respect to the Earth equator. Maps of geodetic coverage of ISS are shown in Fig. 3.14 and 3.15 .

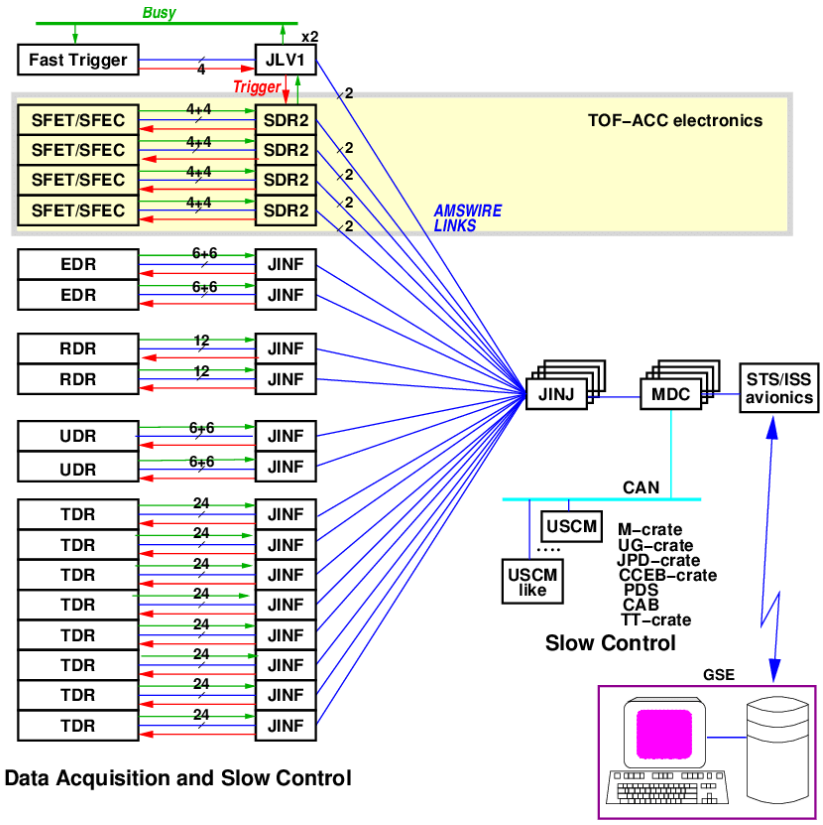

Figure 3.13: Diagram of the DAQ process.

3.10 Installation and Operations

AMS was assembled in July 2010 in a dedicated clean room at CERN. It was later subjected to a series of beam tests to check the alignment of each sub-component and to asses the detector performance. In particular, since the available beams at CERN SPS were both leptonic and hardonic, the rejection power between the two categories was studied in depth for TRD and ECAL.

The whole detector was shipped to NASA's Kennedy Space Center in Florida on August, where it spent about six months to be integrated as payload on the Endeavour Shuttle. The launch of Endeavour happened on May 16th 2011 on mission STS-134 and upon arrival (approximately 2.5 hours later) AMS electronics were powered on to be tested. AMS was finally installed and became operational on May 19th, where it will be located until the end of ISS mission. AMS DAQ has been continuously running since its installation, with a few exceptions related mostly to planned servicing. The major period of shutdown began on November 15th, 2019 when the extravehicular operations of astronauts led to the replacement of the TTCS, after a series of failures in the redundant cooling system. AMS resumed nominal data

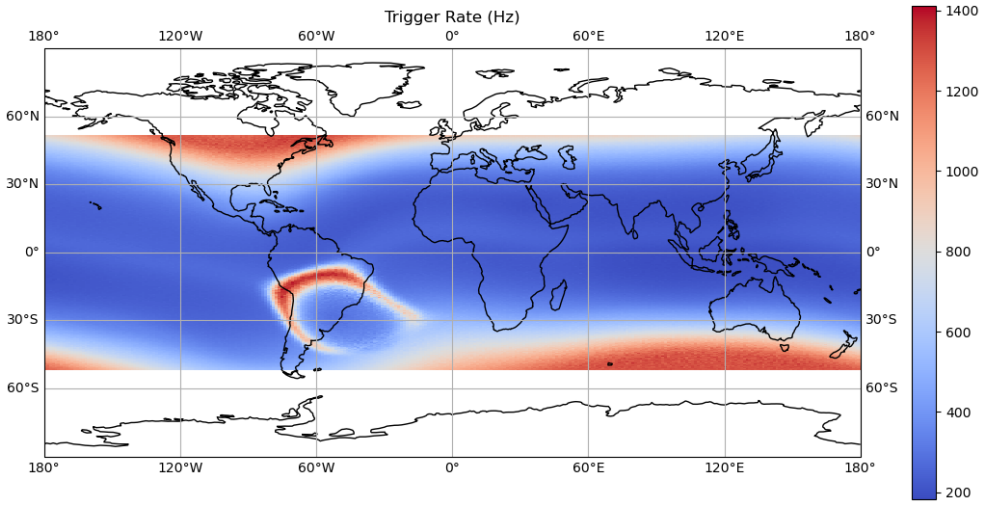

Figure 3.14: Map of the *trigger rate* measured by AMS during quiet periods. The map also illustrates the geographical region covered by the ISS (-51.2° to 51.2° in latitude). In absence of SEP events, the trigger rate spans from 200 Hz at the equator to 1500 Hz near polar regions. The boundaries of the SAA region are also visible, while inside the SAA the livetime, hence the rate, is effectively null (see also Fig. 3.15).

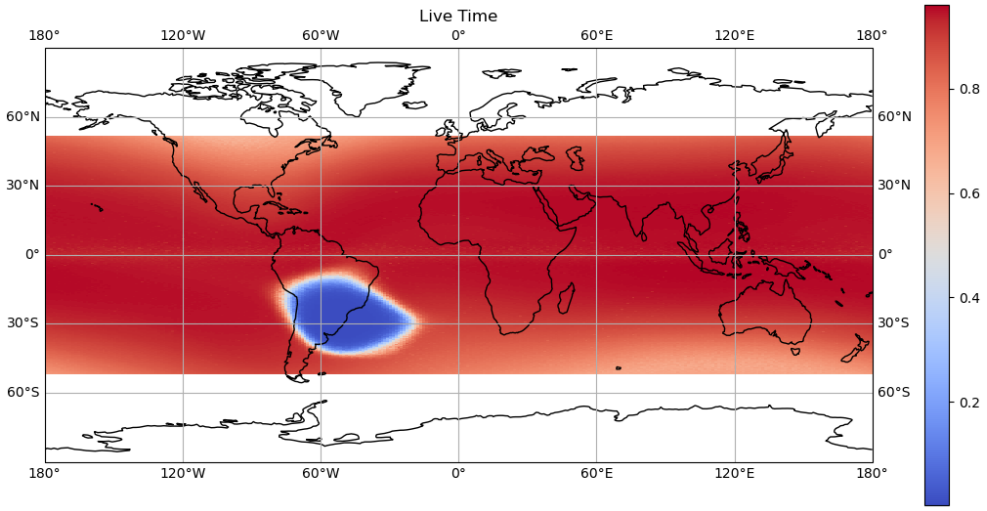

Figure 3.15: Map of the AMS livetime fraction during quiet periods. The average value is 0.9, while on polar regions and especially inside the SAA, it drops due to the high rate of incoming particles.

taking on January 27th 2020.

Another series of extra-vehicular activities concerning AMS is planed for 2026, this

time for the installation of an upgrade to the Tracker. After more than 12 year of scientific progress using AMS results, the need for an increased acceptance became clear, which finally led to the decision of installing an additional layer to the silicon tracker. It will be positioned above layer 1, covering all the field of view of TRD (about 4 m in diameter), hence the name *Layer 0*. The Layer 0 plane is currently being built, as its components have already undergone multiple tests separately.

The main purpose for an AMS upgrade is to study, with grater precision and at higher rigidity, the excess flux observed in the positron flux (see section 3.11), especially considering that some models predict the presence of a cutoff at rigidities compatibles with those that can be reached with the upgrade. In any case, the upgrade will be useful in many other fields, such as extending the flux estimation for heavy nuclei for which we currently lack statistics.

3.11 Scientific Results

The AMS collaboration scientific activity is constantly ongoing, with 27 papers already published and several currently in development. Many of the AMS publications were well received by the scientific community and led to hundreds of related publications on the various topics. In this section, the most relevant achievements, reported in [32] for a detailed dissertation, will be summarized.

primary electron and positron fluxes Leptons in cosmic rays are one of the most invaluable sources of information between all the charged particles, yet they are rare and require a strong rejection power from the overwhelming proton background (with the same absolute charge). Cosmic electrons and positrons have already been used in the past to search for new physics, such as Dark Matter decay and the presence of interesting astronomical objects, such as pulsars and supernova remnants [98]. Leptons are in fact primary cosmic rays, they arrive to AMS directly from the source, as they are not produced by interaction of other species. They also must be originated in the local region surrounding the solar system, as they tend to loose energy very quickly by interacting with galactic magnetic fields, due to their low mass. For this reason, anisotropy studies over electron and positron fluxes might hint at the presence of neighbouring sources or interesting new effects in the local space environment.

The most interesting result in this topic came from the positron spectrum estimation [99]. The positron flux is well described by the sum of a term associated with the positrons production by collision in Cosmic Rays, which dominates at low energies, and a new source term of positrons (see Fig. 3.16). The $e^{\pm}$ abundance at higher energies could be originated from dark matter annihilation or from other astrophysical sources like pulsars.

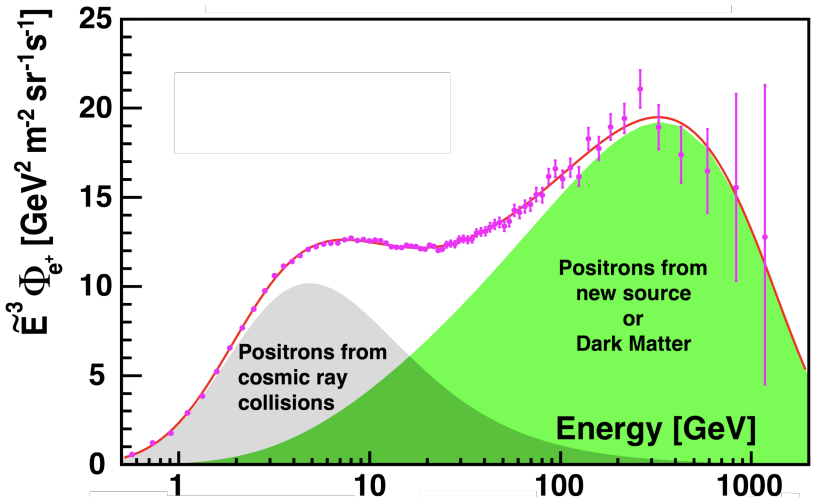

Figure 3.16: Latest measurement of the positron flux with the AMS detector. The spectrum in rigidity presents a second source of positrons which is not compatible with secondary production. The most probable explanations involve astrophysical sources, such as pulsars, or dark matter decay.

Other candidates as decay products of Dark Matter include proton and antiproton pairs. The small signal of this decay channel would be impossible to distinguish over the large background of protons; on the other hand, antiprotons have very few sources of background, dominated primarily by production via interactions of other CR nuclei. As discussed before, the presence of the magnet allows AMS to separate different sign charged particles with the same absolute charge, which is essential if we want to measure the antiproton spectrum. The $\bar{p}$ measurement from AMS has set high expectations for interesting results and the first AMS publication [100] showed a different behavior in the ratio between the antiproton and the proton fluxes below 60 GV. These differences may indicate additional sources for antiproton over the dominating secondary population.

Dark Matter is also searched in other possible decay channels, such as anti-deuterium ($\bar{D}$) at low rigidities and photons in the γ frequencies.

When talking about anti-matter, another interesting aspect is the search for heavy anti-nuclei, starting from anti-helium. These species have never been observed before and are yet to be observed by AMS too. Their detection would be a strong evidence of the existence of clusters of isolated antimatter, possibly even entire galaxies, which could explain the primordial unbalance between ordinary matter and antimatter. The only other possible source of anti-nuclei, in fact, would be the production by nucleosynthesis from already existing anti-protons; a rare process that would represent a low background for any possible dark matter signal.

Aside from the study of anti-matter, the main AMS objective is to precisely measure the rigidity spectra of all the possible CR species in the periodic table. Starting from the most abundant, the proton and helium spectra have been measured up to 1.8 TV and 3 TV respectively [101] [102], as well as their time dependence in [103] and [104]. These studies provide valuable insight on CR genesis and propagation, such as the boron/carbon abundance ratio, which gives an estimation of the residence time of CRs inside the Milky Way [105].

AMS is also actively searching for strangelets, hypothetical heavy baryons containing the strange quark, which are thought to form stable matter inside neutron stars [106].

Finally among the secondary, yet very important objectives, AMS is constantly updating the temporal series of CR fluxes, in order to understand the propagation of cosmic rays inside the solar system and produce models that could be used to predict the fluxes inside the interstellar medium.

3.12 On-flight and Monte Carlo Dataset

The data streamed from AMS to the various data centers on Earth, like POCC at CERN, is always accompanied by one or more Monte Carlo production that mimics the behavior of cosmic rays with the detector. The simulations are used to asses the detector performances in the case of a clean sample, estimate the detector acceptance and they can also be mixed together to evaluate the contamination of a determined species due to fragmentation from heavier nuclei. The Monte Carlo simulation is essential to produce accurate fluxes and understand the detector.

3.12.1 On-flight Data

With *on-flight* data we refer to the actual dataset collected by AMS during its operational time. Raw AMS data is collected and stored every quarter of ISS orbit in root files called *runs*. Each run consists of about 22 minutes of data taking and 7 $\times$ 10^5 events on average. These files contain the digital readouts of the electronics and must be processed to be translated in a physically meaningful, event-based format for the analysis. The data processing is done in two steps. The first step of the reconstruction is performed on the flight as raw data is downloaded from the ISS. This is done to validate the acquisition, monitor the AMS instrumentation inside the POCC and calculate the calibration of each sub-detector, required for the production of the second step of the reconstruction. The latter is performed offline, usually every 6 months, and contains every useful information for the physical analysis, including some useful data from the ISS called *Run and Time Information database* (RTI) (see section 3.12.3). Every iteration of the physical dataset (second step) is named *pass N*, where *N* identifies the iteration, and extends the previous iteration with

new data and improved reconstruction techniques. The current iteration of the dataset, which is used in this work, is *pass 8*. The current dataset includes all the recorded events from *19-05-2011* to *10-11-2023*. The *pass N* datasets include all the foreseeable corrections related to hardware and conditions of the detector, such as calibrations of the tracker after every half-orbit or corrections to all subsystems affected by thermal expansion over the day-night cycle. The actual dataset we used for our analysis is handled by the italian community through the NAIA production [107].

3.12.2 Monte Carlo Simulation

AMS data analysis is supported by a complete Monte Carlo simulation constructed with the Geant4 simulation toolkit [108]. This simulation is fundamental to calculate the complex acceptance of the detector and to understand all the systematic uncertainties that arise from inefficiencies in sub-detector reconstruction, after we apply a certain selection. The detector geometry is carefully reproduced inside the simulation using pre-flight blueprints and mechanical specifications used in its construction. Geant4 also provides the tools to simulate particle generation and interaction with active (e.g. detector sensors) and passive (e.g. structure and electronics) components of the spectrometer. The simulation provides as output the raw sub-detector recorded signals, the reconstructed parameters of the particle that interacted, as well as the original simulated parameters of that particle. The full generation is usually carried out as an isotropic particle generation, following a power law rigidity dependence, from a 3.9 m cube that encompasses the whole detector. Since AMS acceptance is mono-directional, the generation is usually limited to only the face of the cube on top of the detector, in order to minimize the waste of production time and resources. Both the simulation software and the main Monte Carlo productions for all the CR species are maintained by the AMS collaboration. The Monte Carlo production follows the same revisions that the on-flight data reconstruction undergoes, so each *pass* of the on-flight dataset is accompanied by one or more Monte Carlo production for each species. As for the on-flight dataset, Monte Carlo productions are also translated into common productions for the Italian community under the NAIA project.

In the specific case of protons, two main Monte Carlo dataset are produced. The first is a standard isotropic production from the top plane, following the 1/R distribution in the rigidity range [0.5, 100] GV. The second is in the range [0.5, 4000] GV, but with preferential particle direction towards Layer1; the generation is still isotropic, but if a particle does not cross the Layer1 plane it will not be recorded. The latter is useful for its higher statistic sample, given the lightweight generation, but it cannot be used for the Layer1 efficiency estimation (see section 4.4), since it would provide a biased sample for the calculation. For the purpose of the analysis of this work,

the firs Monte Carlo dataset, non Layer 1 focused, was chosen, as the maximum simulated rigidity of 100 GV is in any case grater than the highest rigidity of interest for SEP studies (about 10 GV).

3.12.3 RTI Dataset

AMS orbits the Earth every $\sim$ 93 min. The event trigger rates varies from 200 Hz near the equator to about 2000 Hz near the Earth's magnetic poles. The average event acquisition rate is about 700 Hz. The events from each quarter of the ISS orbit (from near the pole to the equator or vice versa), about 23 min, are arranged in sequence as one run and recorded into a local file to be transmitted on Earth. The AMS Run and Time Information (RTI) software records detector information for each second, including the detector status, run, collected events, livetime, geomagnetic cutoff (based on the IGRF model and Stoermer model), AMS position, particle reconstruction and so on. This software is designed to monitor general conditions of the detector and manage calculation of exposure time in AMS data analysis. To perform AMS data analysis, it is necessary to select the effective data collection time when the detector was in normal operating conditions. Periods of abnormal detector operation should be excluded from the data analysis. The RTI database provides a quick access to all the aforementioned parameters, being it a standalone object from the actual data ntuples containing all the events. The RTI separate ntuple is usually stored in the same file of a given run at the time of the second data processing (offline).

Chapter 4

Proton Flux Measurement

The proton flux estimation in CRs is fundamental to understand the SEP evolution within Earth's environment, since most of the particles that arrive on Earth from the Sun are the constituents of the star itself, mostly protons and a small helium component.

Starting from AMS-02 raw data, a multi-step analysis strategy was developed from the AMS collaboration, in order to determine the impact of each step in the flux calculation. This strategy is standardized for the heavier nuclei analysis, which focuses more on the high end of the rigidity spectrum, so it was later modified to get the most out of the low rigidity measurements, which are essential for the SEP flux estimation. We will first describe the estimation of the average proton flux, which is the average flux measured in a defined temporal interval, giving all the details concerning the calculation for each step. We chose to build the average flux between the start of data taking of AMS-02 in May 2011 and October 2023, which extends the 12.5-year proton flux published in [109]. This interval was chosen to have a first comparison between our own flux and the already published flux from the collaboration.

The second part of this chapter is dedicated to the time-resolved proton flux, with daily granularity, focusing more on the key differences with the average flux estimation process. The average flux is in any case needed to compute some of the necessary elements in building the time-resolved proton flux (see section 4.8).

Both the average and daily analysis, in the setup described in this chapter, are meant to study the overall properties of the GCR protons, such as their variability in rigidity and in time, but without focusing on the solar component. The purpose of the fluxes presented in this chapter is therefore to show the degree of consistency between our work and the previous attempts made by the AMS collaboration. The daily flux will then serve as cornerstone for the SEP flux estimation in the next

chapter.

4.1 Cosmic Rays Flux Definition

The flux of nuclei of a given species in the periodic table, e.g the proton as nucleus of hydrogen, is defined as the number of counts that our detector has identified as the species of interest (i.e. that passed a selection on the measured variables), inside the effective area of the detector, per unit of time, measured rigidity and solid angle. The general expression of the cosmic-ray flux follows the form:

$$\Phi(t, R) = \frac{dN(t, \bar{R}(R))}{d\bar{R}(R)\ dt\ d\Omega\ dA} \tag{4.1}$$

where Φ is the incoming flux in true rigidity of particles R, N is the number of selected counts, $\bar{R}$ is the rigidity measured by the detector, t is the time of observation, Ω is the solid angle containing every possible CR trajectory inside the detector and A is its effective area, as seen by the incoming particles. This flux is time dependent since we measure it inside the heliosphere, which is a very active region in terms of charged particles due to the Sun's influence, and it is dependent on the true rigidity because of the physical processes that generate these particles at the source. The explicit dependence of measured rigidity on its true value will be henceforth omitted. To get to the final formulation of the flux, as we have calculated it in practice in the analysis, we will make the following considerations and assumptions. We start by asking what would be the rate of particles crossing the detector effective area with true rigidity (Eq. 4.2) and the actual rate of detected particles in measured rigidity (Eq. 4.3), given the true flux $\Phi(t, R)$:

$$\frac{dN(t, R)}{dR\ dt} = \int_A dA \iint_\Omega d\Omega\ \Phi(t, R) \tag{4.2}$$

$$\frac{dN(t, \bar{R})}{d\bar{R}\ dt} = \int_0^\infty dR \int_A dA \iint_\Omega d\Omega\ \Phi(t, R)\, L(t)\, \theta(t, R)\, \epsilon_s(t, R)\, \epsilon_g(R, \Omega, A)\, P(\bar{R}|R) \tag{4.3}$$

The count rate expressed as function of measured rigidity in Eq. 4.3 is basically the true rate in which the flux is multiplied, under the integral, by a kernel function constituted by the following efficiencies and effects of measurement:

- L(t) is the livetime of the detector as described in section 4.3. It is defined as the fraction of a second in which AMS can register new events and is not busy processing the previous events.

- $\theta(t, R)$ is a step function that determines, for every second, if any event in that second was above the rigidity cutoff threshold (section 2.2.4), therefore excluding secondaries.
- $\epsilon_s(t, R)$ is the factorization of all the selection efficiencies that will be described in section 4.4. Each and every cut made in the selection for a particle comes with an efficiency. For example, if we require that the particle passes through a specific layer of the tracker, maybe the particle indeed went through the layer but it didn't deposit energy because it crossed a non sensitive area in between sensors. All the efficiencies are dependent on arrival direction and impact position, however this dependence, albeit being marginal, has been studied by the AMS collaboration and taken into account in the Monte Carlo simulation. The same efficiencies are, in fact, calculated also in the simulation and the ratio between the two is then evaluated. The ratio is used to correct our result for the differences between the on-flight dataset and the simulated one. This procedure will be described in detail in section 4.5.2.
- $\epsilon_g(R, \Omega, A)$ is called the geometrical efficiency. It is a function that describes the geometry of the detector and how particles can be detected as a consequence. In particular, the presence of a magnet makes it rigidity dependent, since less energetic particles with the same mass will be deviated more, causing them eventually to exit the geometrical volume too early and not be detected. This efficiency is constituted by a pure geometric factor, which is described by the layout of the detector sensitive area within the portion of the detector considered for the analysis. Therefore, we do not consider it to be time dependent, as the layout remains calibrated and is unchanged in time. Small detector inefficiencies, such as the loss of sensors in the tracker layers, are taken into account in the $\epsilon_s(t, R)$. Major damage to the sub-detectors or future upgrades (see section 3.10), which cannot be taken into account as inefficiencies, would affect the geometric factor.
- $P(\bar{R}|R)$ is the probability of measuring a different rigidity due to finite resolution of the detector and other effects, such as energy losses in the detector material. When using binned data, as we will do, it becomes the so called *migration matrix*.

The only dependence on solid angle and transverse detector area is in the geometrical efficiency; integrating it on those variables we obtain what we call *geometrical acceptance* (Eq. 4.4).

$$Acc(t, R) = \int_A dA \iint_\Omega d\Omega \; \epsilon_g(R, \Omega, A) \tag{4.4}$$

The best way to obtain a distribution from the measurements of a counting ex-

periment is to bin our data, as we will do now. By integrating the above rates in properly chosen bins of rigidity R_i and time T_i (see section A), we obtain binned counts.

$$\int_{R_i} dR \int_{T_i} dt \frac{dN(t,\bar{R})}{d\bar{R}\ dt} = N(t_i, R_i) \tag{4.5}$$

We will now integrate the left hand side of Eq. 4.3, using the migration matrix to transform R into $\bar{R}$ under the integral. The migration is actually studied separately using an iterative unfolding procedure, described in section 4.6, but for now we will write the result as a simple matrix product.

$$N(t_i, R_i) = \int_{R_i} dR \int_{T_i} dt\ L(t)\ \theta(t,\bar{R})\ \Phi(t,\bar{R})\ Acc(t,\bar{R})\ \epsilon_s(t,\bar{R}) \tag{4.6}$$

Performing the integrals we obtain the binned form of selected proton counts.

$$N(t_i, R_i) = \Delta(t_i,\bar{R_i})\ \Phi(t_i,\bar{R_i})\ Acc(t_i,\bar{R_i})\ \epsilon_s(t_i,\bar{R_i})\ \Delta\bar{R} \tag{4.7}$$

Where $\Delta\bar{R}$ is the measured rigidity bin width and $\Delta T(t_i,\bar{R_i})$ is the *exposure time*, i.e. the fraction of time spent by AMS in a live status above the rigidity cut-off threshold (section 2.2.4). Note that in the following expression we used the approximation of slowly varying functions inside the bin for flux, acceptance and efficiencies, though this is only true if the rigidity bin width is small and the binning is distributed according to a logarithm. This careful consideration is necessary because we know that the CR flux varies, with respect to rigidity, following a steep power law distribution.

The binned form of our flux is now obtained by simply inverting Eq. 4.7.

$$\Phi(t_i,\bar{R_i}) = \frac{N(t_i, R_i)}{\Delta T(t_i,\bar{R_i})\ Acc(t_i,\bar{R_i})\ \epsilon_s(t_i,\bar{R_i})\ \Delta\bar{R}} \tag{4.8}$$

The last step in order to obtain the final formulation of the flux, as it will be used in the practical calculation, is to incorporate the selection efficiencies in the acceptance, in what we call *corrected acceptance*. The detailed description of this step is reported in sections 4.4 and 4.5.2.

$$\Phi(t_i,\bar{R_i}) = \frac{N(t_i, R_i)}{\Delta T(t_i,\bar{R_i})\ Acc_{corr}(t_i,\bar{R_i})\ \Delta\bar{R}} \tag{4.9}$$

4.2 Proton Selection

The event selection is a series of cuts on the observables measured by AMS, with the intent of obtaining the purest sample possible of a given CR species, in this case protons. The final selection varies depending on the configuration of the AMS detector considered in the analysis. The configuration chosen for SEP selection, in which we want to maximize the statistic at low energies, is called Inner+Layer1, as we utilize the inner portion of the AMS tracker and the top external layer (Layer 1) to reconstruct tracks, therefore excluding the bottom layer (Layer 9). This decision limits our maximum detectable rigidity (MDR) at about 100 GV, since the increased lever arm provided by the Layer 9 is necessary to obtain a measurement of the highest rigidity particles, which undergo a lesser deflection by the magnetic field. The increase in statistic given by the Inner+Layer1 configuration is deemed a priority over high rigidity measurements, since 100 GV is in any case above the maximum expected rigidity for any possible SEP event. In principle it is possible to increase the acceptance by utilizing just the inner tracker, but Layer 1 is necessary to exclude protons that underwent interactions with the detector components above the inner tracker and lost energy, or were produced by fragmentation from heavier cosmic nuclei, such as helium.

The same selection is applied to both AMS on-flight data and the Monte Carlo production for protons (section 3.12).

The following selection, divided by categories, is the standard Inner+Layer1 selection used in the collaboration, tuned for protons. The differences between this selection, used for comparison with previous results, and the final SEP selection are presented in section 5.2.

Pre-selection This selection includes all the data quality cuts made upon the RTI tree present in the NAIA ntuples (section 3.12), in order to exclude seconds of bad data acquisition, or seconds in which AMS was not in nominal configuration or inside the SAA. The pre-selection cuts are:

- Live time fraction greater than 0.05.
- AMS zenith angle lower than 25°.
- Difference in PG and MD Layer1 alignment lower than 35 μm.
- Outside SAA region.
- Number of triggers / number of events greater than 0.98.
- Number of errors not negative.
- Number of errors / number of events lower than 0.1

- Discard first second of Run.

The live time cut is made to ensure that the detector was not in a saturated state due to very high rate of incoming particles; unfortunately, during the maximum intensity of the strongest SEP events, it may happen that the live time is null for a few minutes, making impossible to calculate the particle rates. The zenith angle cut ensures that the ISS, hence AMS, was in the optimal attitude for data taking; during ISS docking operations, in fact, the ISS can be tilted, resulting in AMS pointing in a non-zenithal direction. The last four cuts are quality cuts on data acquisition, to ensure that each run of DAQ has a significant number of physical events. Finally the first second of each run is excluded, since it may happen that buffered events at the end of the previous run will be copied to the current one, overestimating the actual count rate for the first second.

Trigger Selection The main purpose of this cut is to select events that triggered with a signal corresponding to physical events (see section 3.8 for details on the trigger logic). Even though there is a specific *single charged* trigger signal, in principle designed for protons, we leave this association to the cuts on physical measurements, therefore accepting any of the following:

- **Single Charged:** High Threshold on 4/4 ToF hits, 0 ACC hits.
- **Normal Ions:** Super High Threshold on 4/4 ToF hits.
- **Slow Ions:** Super High Threshold on 4/4 ToF hits, delayed gate width.
- **Electrons:** 4/4 ToF hits, ECAL energy deposit above threshold in both projections.

The logical or of the above trigger conditions is called *Physical Trigger*.

Inner Tracker Selection The inner tracker is responsible for the main rigidity measurement, so the following cuts make sure that the track is well reconstructed by asking a low χ^2 of its fit, a minimum number of hits well distributed and so on. The *fiducial volume* is essentially a boundary in the x and y coordinates, corresponding to the true tracker layers' active area dimensions, to ensure that the fit of the track is passing within those limits. Notably the shape of the tracker layers, excluding Layer 9, is not rectangular but rather circular with two missing segments on the y coordinate, as pictured in Fig. 4.1. For this reason, this cut is made on the radius R_{fid} and y coordinate Y_{fid} of each plane. This selection, as for the other instruments that can measure charge by energy deposition, includes charge cuts:

- Number of hits in tracker greater than 4 on magnet bending direction (y side).

- Inner tracker hits follows the logic: L2 and (L3 or L4) and (L5 or L6) and (L7 or L8).
- Normalized χ^2 of the inner track lower than 10.
- Charge measurement with inner layers between 0.7 and 1.5.
- Inner charge root mean squared error lower than 0.4.
- Inner Fiducial Volume. For each layer from Layer 2 to Layer 8,
  R_{fid} less than: [62, 46, 46, 46, 46, 46, 46] cm.
  Y_{fid} less than: [40, 44, 44, 36, 36, 44, 44] cm.

ToF Selection This selection includes charge and β quality cuts on ToF measurements:

- β greater than 0.4.
- Charge measurement with energy deposition on ToF layers between 0.5 and 2.5.

Layer 1 Selection This selection includes charge, fiducial volume and boundary on normalized residual of track in Layer 1, to ensure that the particle was a *good* proton at the top of the detector:

- Charge measurement with Layer 1 between 0.6 and 1.9.
- Layer 1 Fiducial Volume. R_{fid} less than 62 cm, Y_{fid} less than 47 cm.
- Normalized residual on Layer 1 lower than 10 cm.
- Normalized χ^2 of the track, including Layer 1, lower than 10.

The normalized residual between Layer 1 hit and Inner tracker fit extrapolation, calculated on the y-coordinate, is defined as following:

$$\frac{(y^{L1} - y^{L1}_{INN\,Fit})^2}{y^{L1}_{INN\,Fit}} = \chi^2_{IL1} \cdot ndf_{IL1} - \chi^2_{INN} \cdot ndf_{INN} \tag{4.10}$$

Geomagnetic Rigidity Cutoff Cut The last cut in the selection checks if the particles we measure have a rigidity above the maximum rigidity cutoff 2.2.4, ensuring that the particle is a primary cosmic ray. Cutoff values are calculated by the AMS collaboration and are stored, for each second of data acquisition, inside the RTI database 3.12.3:

- Inner+L1 rigidity measurement greater than Max. IGRF cutoff.

To test the quality of all the cuts applied in this proton selection, we produced a series of test distributions of the many observables measured by AMS, in order to show the effectiveness of those cuts. The most relevant examples of these distributions can be seen in Fig. 4.2, before applying the selection, and in Fig. 4.3, after the application. The rigidity distribution of selected events, i.e. the *counts*, is shown in Fig. 4.4

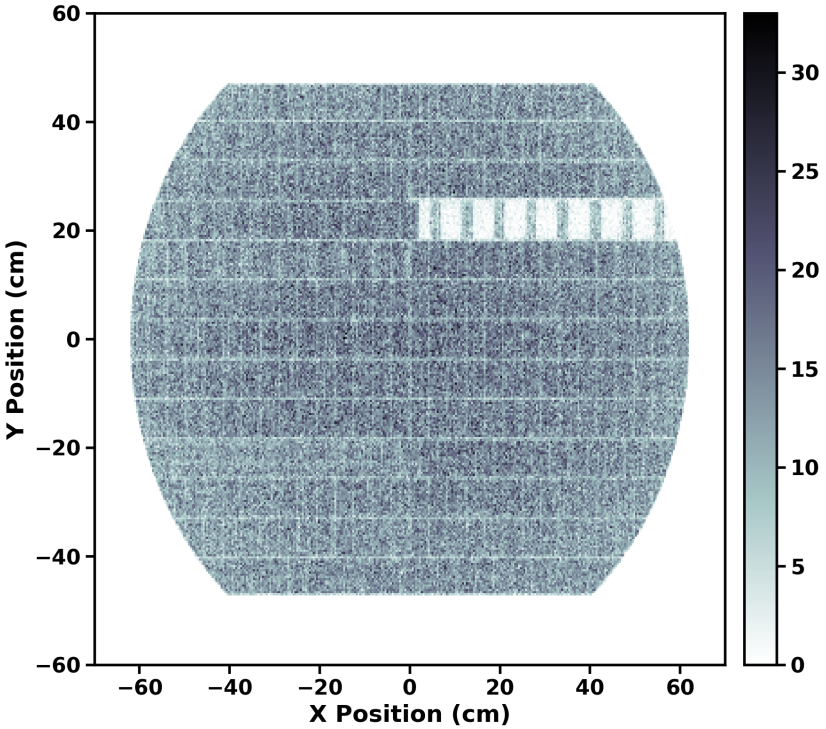

Figure 4.1: Picture of the Layer 1 taken with hit position of detected protons. The peculiar circular shape, with cut arcs on the y coordinate, is visible, along with the details of ladders and sensors. This shape is shared by all the first 8 layers, while Layer 9 is rectangular. Notably, a faulty ladder is visible in the top right corner, due to noisy electronics.

4.3 Exposure Time

An intermediate step, between obtaining the counts distribution and the calculation of the flux, is to compute the proton rate, i.e. the number of selected events per unit of time. The rate is defined as the number of selected counts divided by the rigidity interval (bin width) and by the exposure time. For the latter, we must consider that AMS is not always found in a *ready* state for data acquisition and generally we find that the fraction of each second in which the detector is capable

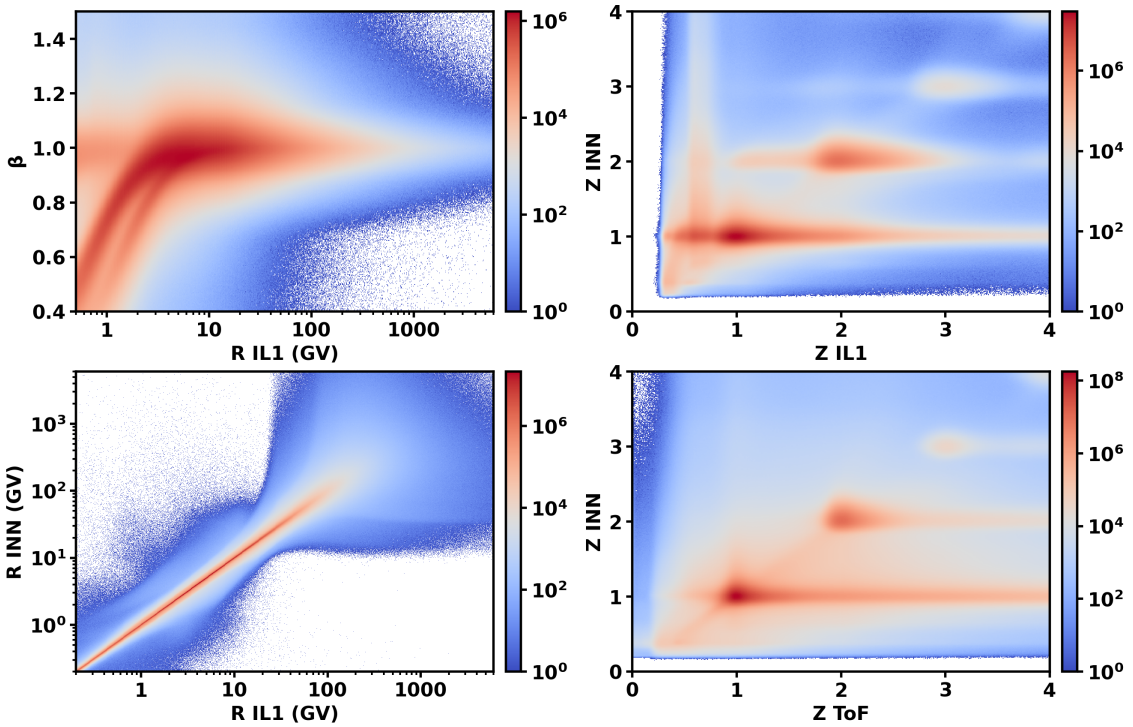

Figure 4.2: The four plots in this picture, built with the on-flight dataset, show examples of some of the most relevant observables measured by AMS in comparison with each other, before the application of any selection. **Top Left:** Beta factor VS Rigidity with Inner+L1 configuration. Most of the particles with R $>$ 5 GV are relativistic ($\beta = 1$), but at lower rigidities we can distinguish multiple populations with different mass. **Top and Bottom Right:** The charge measured with the inner tracker layers VS the charge with Inner+L1 configuration and ToF layers, respectively. With no selection applied, we distinguish the first three charges (H, He and Li). **Bottom Left:** Rigidity reconstructed with inner tracker VS Rigidity with Inner+L1 configuration.

of registering an event, called *live time*, is less than 1. This is especially true if we consider the high incoming particle rates that we expect for SEP events. The *live time* information is contained inside the RTI database, which has one-second granularity, so the exposure time histograms are filled at the start of each second of data acquisition instead of every triggered event.

With this concept in mind, the simplest form of exposure time would be given by the sum of seconds, weighted by the live time, over a given time interval (day). The formal expression is reported in Eq. 4.11.

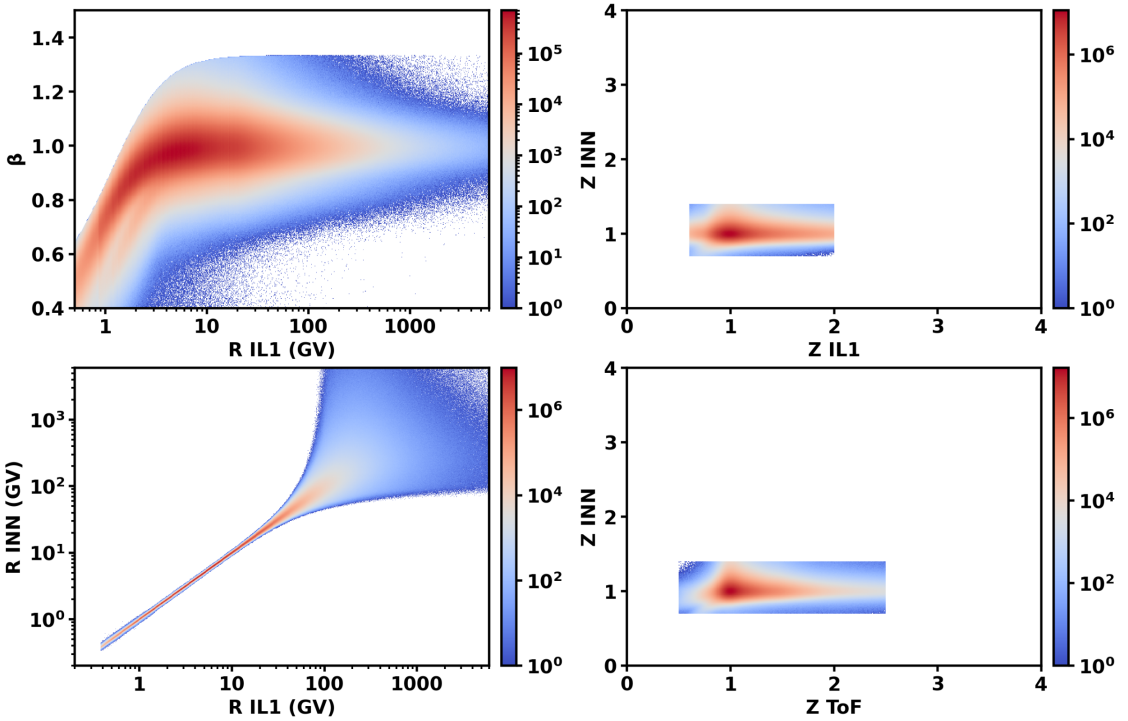

Figure 4.3: The plots shown in this picture are identical to those shown in Fig. 4.2, but we applied the proton selection. We can clearly see the effect of the cuts that affect directly the observables, such as the charge cuts on the Z distributions an the mass cut on the β VS R. The presence of mostly one branch in the β VS R, the good agreement between the two rigidity measurements and the charge selection show that we are indeed selecting a good sample of protons.

$$\Delta T(t_i, \bar{R}_i) = \int_{R_i} dR \int_{T_i} dt \; L(t) \; \theta(t, \bar{R}) \tag{4.11}$$

Since AMS is located inside Earth's magnetosphere, there is an additional factor to consider in the exposure time calculation, which is the geomagnetic rigidity cutoff. The rigidity cutoff is essentially a function, dependent on position, direction and altitude, that gives a lower boundary on rigidity for pure primary detection. We require the rigidity to be above cutoff to ensure that the flux we are measuring is exclusively composed by primary cosmic rays. Hence, in order to properly estimate the exposure time, we must multiply the live time fraction inside the integral in Eq. 4.11 by the cutoff value for the given second. The rigidity cutoff is also studied separately by the AMS collaboration and its values are reported inside the RTI database.

The exposure time and proton rate for the average flux inside the published time

interval are shown in Fig. 4.4 and Fig. 4.5 respectively.

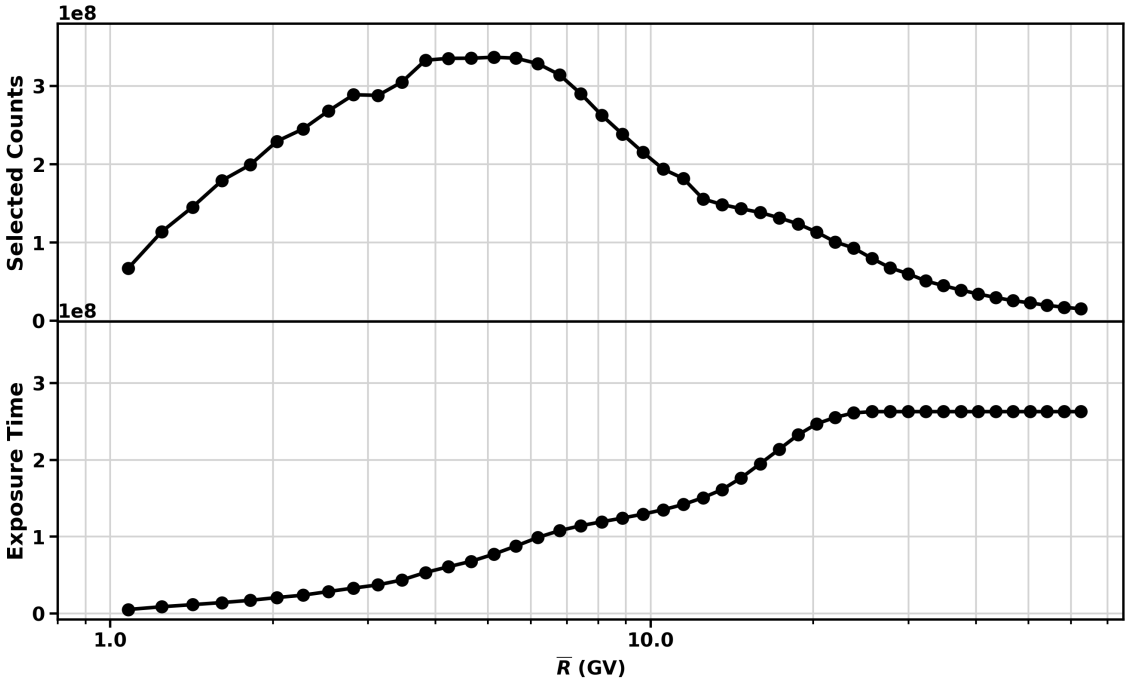

Figure 4.4: **Top**: Rigidity distribution of events that passed the proton selection. **Bottom**: Exposure time of AMS as function of rigidity.

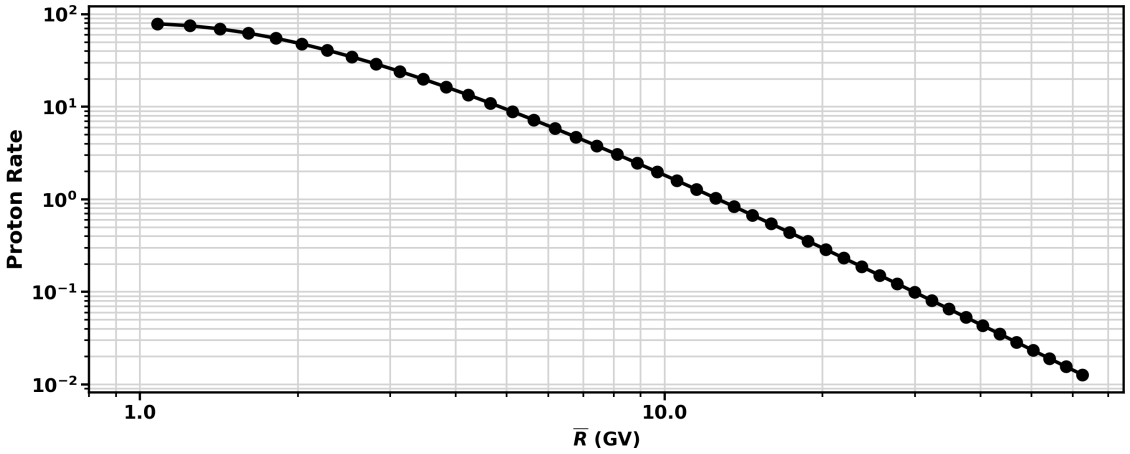

Figure 4.5: Proton count rate, resulting from the division of the selected counts distribution by the exposure time and bin width ΔR.

4.4 Selection Efficiencies

In the ideal case of a detector with perfect resolution and no source of smearing of measurements (see section 4.6 for more details on smearing effects), it is always possible to separate the purest sample of particles with simple cuts. In reality, making a cut always means to lose a fraction of good candidate events and accepting another of bad events. There is always a trade off between purity of the sample and sample size: the more we tighten cuts, the purest the sample will be at the cost of loosing physically meaningful events. We define as selection efficiency the probability of measuring a good particle, given that the particle crossed the detector. This is done separately for each selection category (Layer1, ToF, Trigger, Tracker) described in section 4.2, given that the cuts in each category are correlated, but assuming independence between categories. We want to estimate these efficiencies to calculate how many good particles we are loosing when making those cuts and divide the rate by these efficiencies, as shown in equation Eq. 4.8. In practice, this probability is calculated as the fraction of events that passed an overall tighter selection, plus the given category, over the number of events that passed only the tighter selection. The tighter selection is meant to select the purest sample of events, without the use of the detector component relative to the category cuts for which we want to estimate the efficiency; this can be very similar to the cuts made in the actual selection of events, or we can make new additional cuts, provided that the tighter selection is independent from the category cuts under study. This last problem becomes challenging, for example, in the selection efficiency for the Inner Tracker category, since we can not use the inner tracker measurements at all for the tighter selection and we have to rely only on other instruments, such as ToF, for charge and rigidity measurements. All the selection efficiencies are calculated for both the real on-flight dataset and the Monte Carlo simulation, as both datasets undergo the proton selection. For this reason, in order to take into account the differences between the real dataset and the Monte Carlo, we will calculate the ratio of those quantities, also called *Data/Monte Carlo corrections*, which will be described in section 4.5.2.

4.4.1 Layer 1 Efficiency

The Layer 1 efficiency is the probability of getting a good Layer 1 hit and a charge compatible with a proton, given that we registered a good proton with information from the Inner Tracker and ToF alone. For this efficiency we only use the fit and rigidity from the Inner Tracker, for example to calculate the χ^2 or the Fiducial Volumes. The denominator and numerator of this efficiency are the following:

Denominator

- Has passed the Pre-selection.
- Has Physical Trigger.
- β greater than 0.4.
- Charge measurement with energy deposition on Upper ToF layers between 0.5 and 1.7.
- Charge measurement with energy deposition on Lower ToF layers between 0.5 and 1.7.
- Number of hits in tracker greater than 4 on magnet bending direction (y side).
- Inner tracker hits follows the logic: L2 and (L3 or L4) and (L5 or L6) and (L7 or L8).
- Normalized χ^2 of the inner track lower than 10.
- Charge measurement with inner layers between 0.7 and 1.5.
- Inner charge root mean squared error lower than 0.4.
- Inner Fiducial Volume. As in Inner Tracker Selection.
- Layer 1 Fiducial Volume. As in Layer 1 Selection.
- Inner rigidity measurement greater than Max. IGRF cutoff.
- Number of ToF Clusters is 4 or less
- Number of Tracker tracks is 1
- No ACC fired

Numerator

- Denominator + Layer 1 Selection.

The last three cuts in the denominator of the L1 efficiency were introduced to regularize in time this efficiency. They make sure we only select events with a single track, both in ToF and Tracker, and no secondary production or fragmentation triggered the ACC. This is fundamental for the L1 efficiency in particular, as we do not have the information of the particle being an actual proton before the upper Tof, which therefore might be produced by fragmentation of heavier nuclei on the L1 itself or inside the TRD. We in fact observed a time dependence of this efficiency, worsening when the rate is higher, hinting that there were bad events polluting its sample. This issue was mostly removed by the introduction of these last three cuts.

The Layer 1 efficiency, for both on-flight Data and Monte Carlo, is shown in Fig. 4.6.

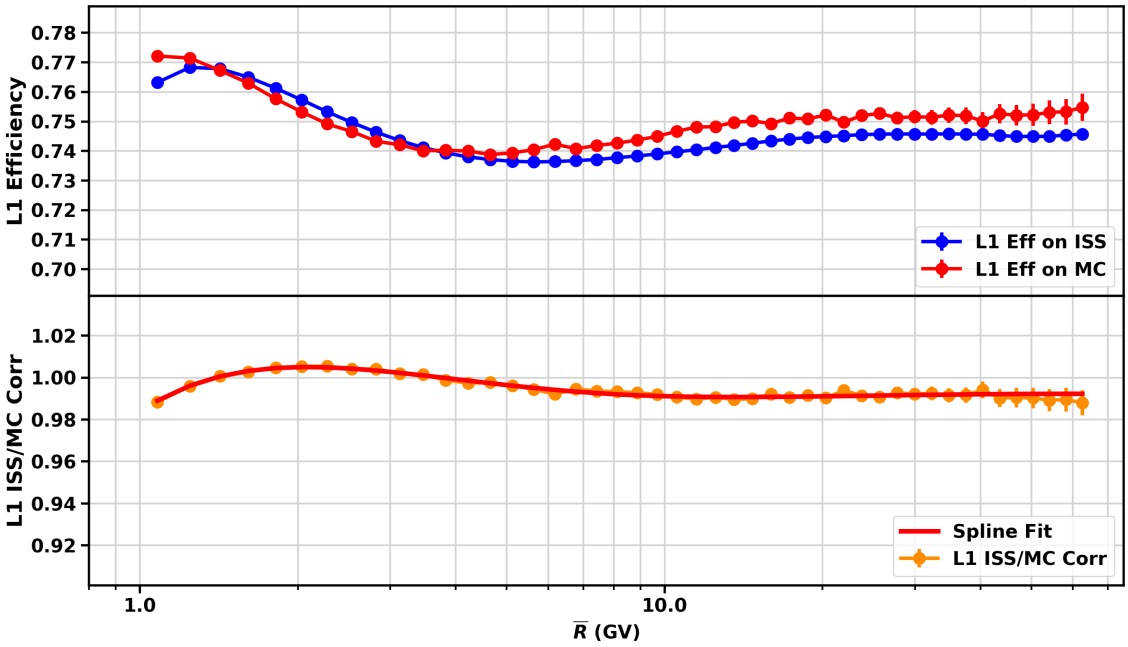

Figure 4.6: **Top**: Layer 1 pickup efficiency on the real dataset (ISS, blue) and on Monte Carlo (MC, red) **Bottom**: Data/Monte Carlo correction for the Layer 1 pickup efficiency, i.e. the ratio between efficiency on Data and efficiency on Monte Carlo.

4.4.2 ToF Efficiency

The ToF efficiency is the probability of getting β and charge compatible with a proton, given that we registered a good proton with information from the Tracker.

Denominator

- Has passed the Pre-selection.
- Has Physical Trigger.
- Number of hits in tracker greater than 4 on magnet bending direction (y side).
- Inner tracker hits follows the logic: L2 and (L3 or L4) and (L5 or L6) and (L7 or L8).
- Normalized χ^2 of the inner track lower than 10.
- Charge measurement with inner layers between 0.7 and 1.5.
- Inner charge root mean squared error lower than 0.4.
- Charge measurement with Layer 1 between 0.6 and 1.9.

- Distance between hit on Layer 1 and inner track fit extrapolation lower than 10 cm.
- Normalized χ^2 of the track, including Layer 1, lower than 10.
- Inner Fiducial Volume. As in Inner Tracker Selection.
- Layer 1 Fiducial Volume. As in Layer 1 Selection.
- Inner+L1 rigidity measurement greater than Max. IGRF cutoff.

Numerator

- Denominator + ToF Selection.

The ToF efficiency, for both on-flight Data and Monte Carlo, is shown in Fig. 4.7.

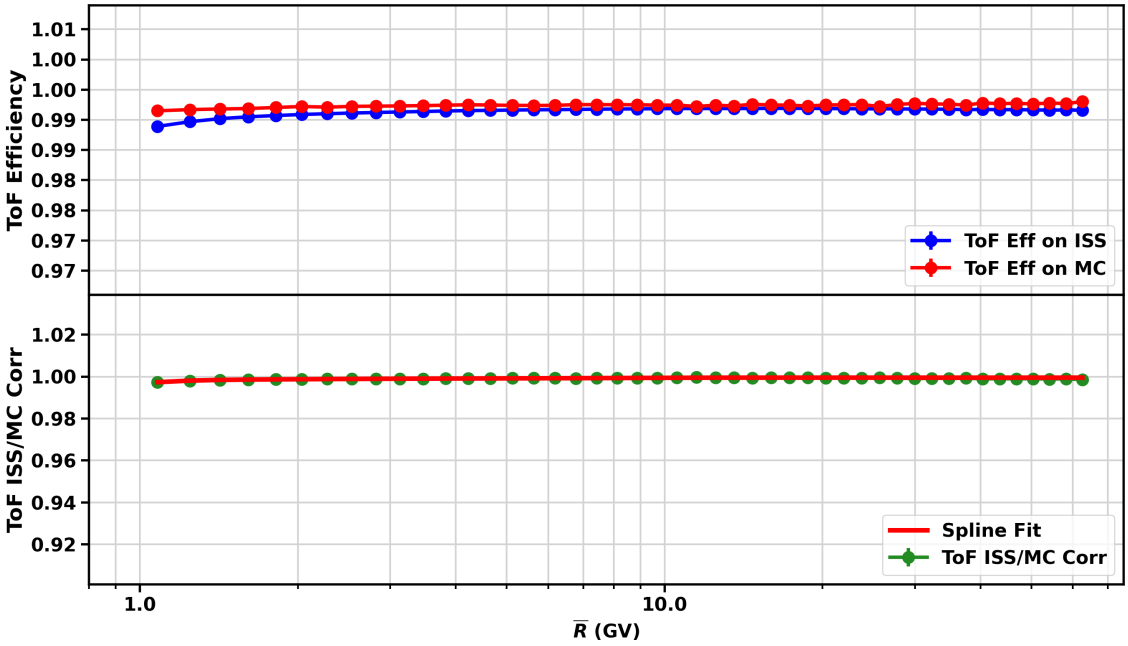

Figure 4.7: **Top**: ToF efficiency on the real dataset (ISS, blue) and on Monte Carlo (MC, red) **Bottom**: Data/Monte Carlo correction for the Tof efficiency, i.e. the ratio between efficiency on Data and efficiency on Monte Carlo.

4.4.3 Trigger Efficiency

The Trigger efficiency is the probability of the detector producing a physical trigger signal, given that a good proton crossed the detector. Of course any event is registered only if the trigger condition is met, so we don't have a direct way of calculating this efficiency, not having access to the events that did not produce

the trigger signal. The trigger efficiency for detectors at accelerators on Earth is calculated by sending a test beam at the detector and counting how many events triggered, but in space this possibility is excluded. This is where the *unbiased trigger* signals (*unbiased charged* and *unbiased EM* in section 3.8.1) become fundamental: these signals identify particles that triggered a "weaker" condition, so they are not considered physical, but constitute a larger sample than the physical ones. One of the downsides of using the unbiased trigger signals is that they are pre-scaled, at hardware level, by a factor of 100 for the unbiased ToF (signal 1) and 1000 for the unbiased ECAL (signal 7). This feature severely limits our statistical sample when calculating the efficiency for daily fluxes.

Denominator

- Same Selection as in 4.2, except for the trigger condition. Here we accept any physical or unbiased trigger, were the unbiased trigger are multiplied by the pre-scaling factor in the on-flight data (see Eq. 4.12).

Numerator

- Denominator + physical trigger requirement.

The Trigger efficiency is defined by the following formula and, for both on-flight Data and Monte Carlo, is shown in Fig. 4.8.

$$\epsilon_{TRIG} = \frac{N_{PHYS}}{N_{PHYS} + 100[0]\, N_{UNB}} \tag{4.12}$$

4.4.4 Inner Tracker Efficiency

The Inner Tracker efficiency is the probability of having good track and charge, given that we registered a good proton with information from the ToF and Layer 1. This is a another challenging efficiency to calculate, since this time we cannot use the inner tracker, which provides the main measurement of rigidity and charge. This is done by heavily relying on the rigidity calculated from β in ToF. The ToF track is also used to calculate the χ^2, both in spatial coordinates and in time, together with the Fiducial Volumes.

Denominator

- Has passed the Pre-selection.
- Has Physical Trigger.
- β greater than 0.4.

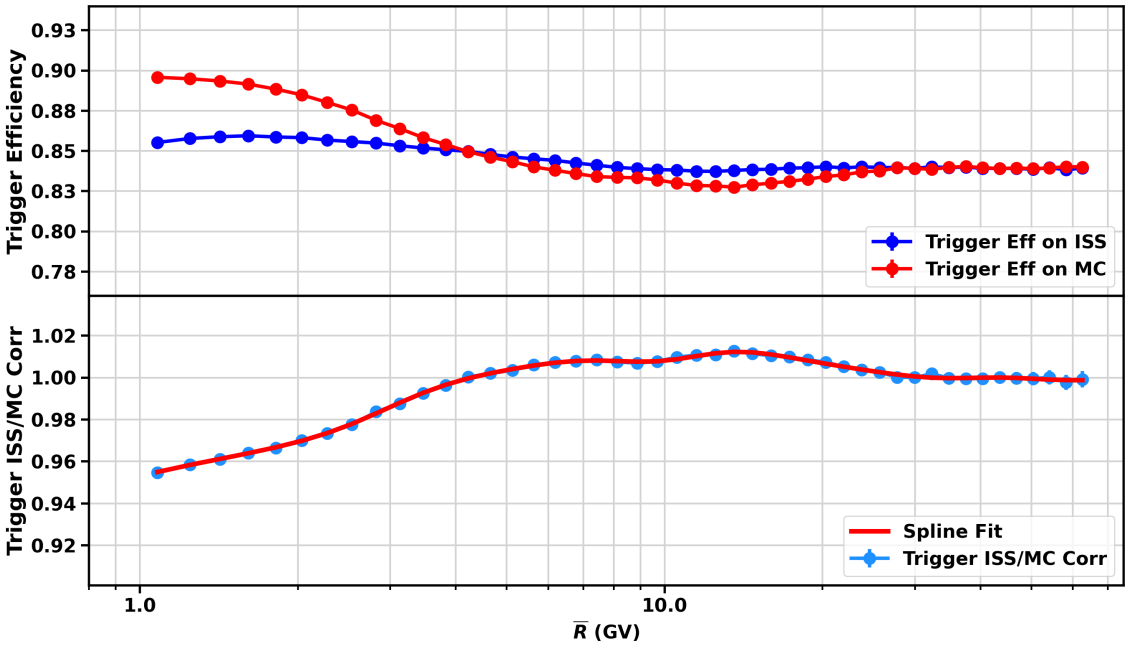

Figure 4.8: **Top**: Trigger efficiency on the real dataset (ISS, blue) and on Monte Carlo (MC, red) **Bottom**: Data/Monte Carlo correction for the Trigger efficiency, i.e. the ratio between efficiency on Data and efficiency on Monte Carlo.

- Normalized χ^2 of the ToF track in coordinates lower than 2.
- Normalized χ^2 of the ToF track in time lower than 2.
- Charge measurement with energy deposition on Upper ToF layers between 0.7 and 1.3.
- Charge measurement with energy deposition on Lower ToF layers greater than 0.7.
- Inner Fiducial Volume. As in Inner Tracker Selection.
- Layer 1 Fiducial Volume. As in Layer 1 Selection.
- Charge measurement with Layer 1 between 0.6 and 1.9.
- Rigidity obtained from β measurement greater than Max. IGRF cutoff.

Numerator

- Denominator + Inner Tracker Selection.

The Inner Tracker efficiency, for both on-flight Data and Monte Carlo, is shown in Fig. 4.9.

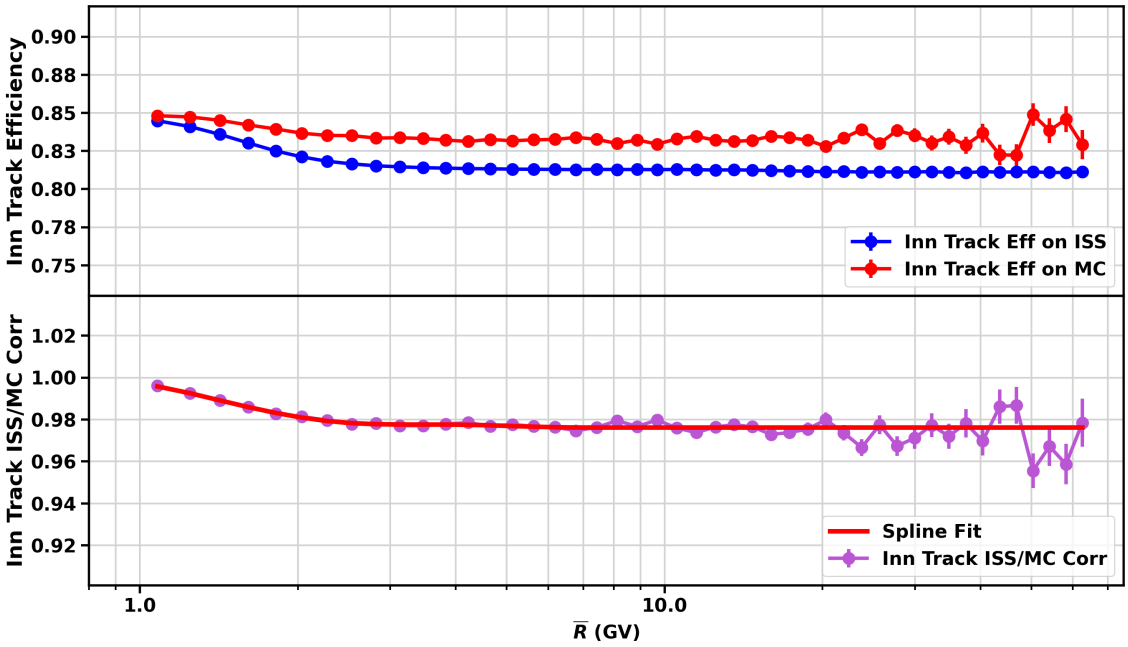

Figure 4.9: **Top**: Inner Tracker efficiency on the real dataset (ISS, blue) and on Monte Carlo (MC, red) **Bottom**: Data/Monte Carlo correction for the Inner Tracker efficiency, i.e. the ratio between efficiency on Data and efficiency on Monte Carlo.

4.5 Acceptance

In particle physics, the *acceptance* is a function that describes the angular and spatial efficiency of particle detection, usually with respect to energy (or rigidity) of incoming particles. For a generic experiment that utilizes a magnet, the acceptance of a detector is dependent not only on rigidity, but also position and direction at the entrance of the magnet, on charge ans so on. In the case of AMS, as we will see, some approximation allow us to dramatically simplify this calculation and arrive to a formulation of acceptance solely differential in rigidity. We will refer to the previous definition as *Geometrical Acceptance*, which we will later define quantitatively.

In general, if we had an ideal instrument in which the response of each sub-detector and the properties of its materials are known, it could be calculated analytically solving Eq. 4.13. In reality though, any detector used in true particle experiments is too complex for a complete analytical description of its components, so we make use of the full Monte Carlo simulation of the instrument (section 3.12).

In any case, the calculation of a differential acceptance in angular direction of incoming particle could prove to be a useful resource for the study of spatial distribution of SEPs, as will be discussed in the conclusions.

4.5.1 Geometrical Acceptance

The geometrical acceptance is defined as the integral, over the transverse area and all the possible CR trajectories in the solid angle aperture of the detector, of the geometrical efficiency $\epsilon_g(R, A, \Omega)$:

$$Acc_{geom}(R) = \int_A \iint_\Omega \epsilon_g(R, A, \Omega)\ dA_\perp\ d\Omega \tag{4.13}$$

The geometrical efficiency can be calculated via the Monte Carlo simulation as the ratio between the simulated events that pass the selection over the total generated events:

$$N_{sel}(R) = N_{gen}(R)\ \epsilon_g(R)\ \Rightarrow\ \epsilon_g(R) = \frac{N_{sel}(R)}{N_{gen}(R)} \tag{4.14}$$

Integrating over the area and angle, considering that CRs in the Monte Carlo are generated isotropically in a 3.9x3.9 m^2 orthogonal square to the AMS z-axis, we get:

$$Acc_{geom}(R) = \frac{N_{sel}(R)}{N_{gen}(R)}\ A_\perp\ \Omega = \frac{N_{sel}(R)}{N_{gen}(R)} \cdot 3.9^2 \cdot \pi \tag{4.15}$$

The geometrical acceptance histogram is then fitted with a spline function using the *Autospline* algorithm, inspired by the LxSmoother algorithm described in [110], in order to smooth the histogram and remove statistical fluctuations. The histogram and its fit are shown in comparison with the corrected acceptance (see next section) in Fig. 4.12.

A schematic of the solid angle described by AMS acceptance is shown in Fig. 4.10.

4.5.2 Data-MC Corrections and Corrected Acceptance

The selection efficiencies described in the previous section will be included in the analysis in the form of *Data/Monte Carlo Corrections*, which we will hence define.

Since the acceptance is calculated using Monte Carlo simulated events, we need to address the differences between the Monte Carlo dataset and the real one. We therefore correct the geometrical acceptance for the ratio between each efficiency calculated on the real dataset and the same efficiency calculated on the Monte Carlo. Each of these corrections is defined as follows:

$$Corr(\bar{R}) = \frac{\epsilon^{Data}(\bar{R})}{\epsilon^{MC}(\bar{R})} \tag{4.16}$$

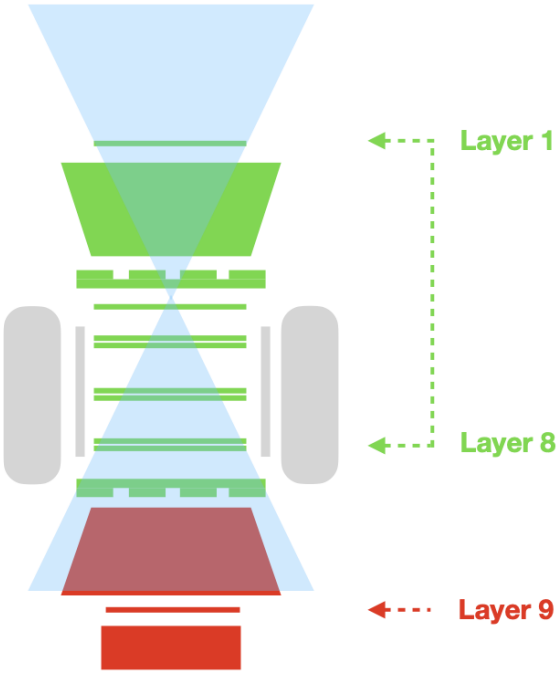

Figure 4.10: Schematic of AMS acceptance with the Inner+L1 configuration. This configuration uses all the sub-detectors from Layer 1 to the lower ToF (pictured in green), excluding RICH, Layer 9 and ECAL (pictured in red), favoring higher statistics over higher MDR.

Each correction is smoothed utilizing the same Autospline algorithm used for the geometrical acceptance. This regularization is necessary, since we are dealing with ratios of efficiency histograms with extremely reduced sample size, due to the tighter cuts included in the denominator. This will become especially relevant when dealing with the daily flux. Fig. 4.11 shows the comparison between all the spline fits of the four corrections, together with the total correction. The four Data/Monte Carlo corrections (Layer 1, ToF, Trigger and Inner Tracker) are then multiplied together to get the *total correction*, which in turn is multiplied to the geometrical acceptance to get the *corrected acceptance*, Acc_{corr}. This formulation corresponds to the acceptance that appears in the flux equation in Eq. 4.9. Fig. 4.11 shows the comparison between the spline fit for all the Data/Monte Carlo corrections, together with the total correction. Fig. 4.12 shows the corrected acceptance in comparison with the geometrical acceptance and its fit. Since the total correction is the factorization of the four Data/Monte Carlo corrections, there might be a risk of overcorrection, connected to the underlying correlation between efficiencies. However the cuts in the main selection (section 4.2) are carefully chosen over independent variables, minimizing cross-correlation between each cut. This translates into minimally cor-

related efficiencies, where the numerator of the four efficiencies is constituted by only selection cuts pertinent to that particular efficiency. For example the probability of detecting a good proton in the layer 1 of the tracker (Layer 1 efficiency) does not include any selection cut over the quantities measured by the ToF, hence its independent from it.

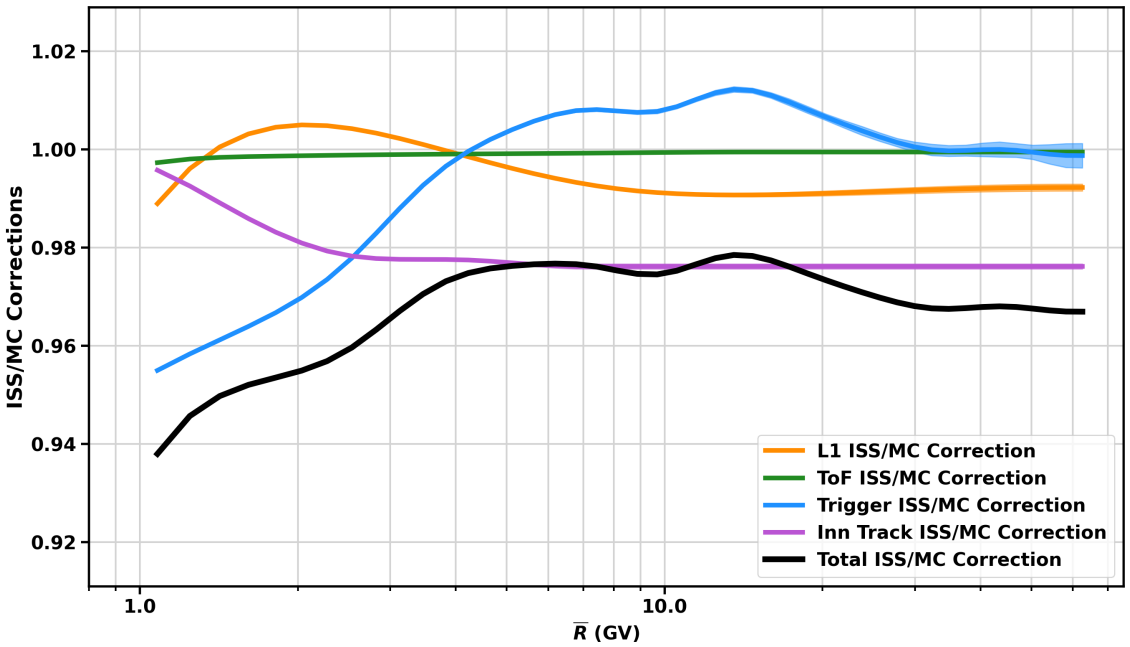

Figure 4.11: Overview of all the Data/Monte Carlo corrections and their product as *total correction* (black).

4.6 Correction for Energy Loss and Unfolding

In this section we will describe the possible sources of bias and smearing of measurements due to physical effects, such as energy loss, and detector effects, such as finite resolution. The most valuable tool in understanding the performance of our detector is the Monte Carlo simulation, which gives as an unbiased look at the true properties of each simulated particle. A common way to visualize the effects of smearing and bias in measurements, especially when dealing with unfolding, is to compute the *migration matrix* (or *smearing matrix*). In our case, since the main observable used in this analysis is the rigidity calculated by measuring the curvature radius of the particle track, the migration matrix is defined as the bi-dimensional distribution of measured rigidity against the generated rigidity of particles. This matrix is pictured in Fig. 4.13, where the binning is constant in logarithm with 1000 bins between the rigidity boundaries of generation in Monte Carlo production; a schematic of its

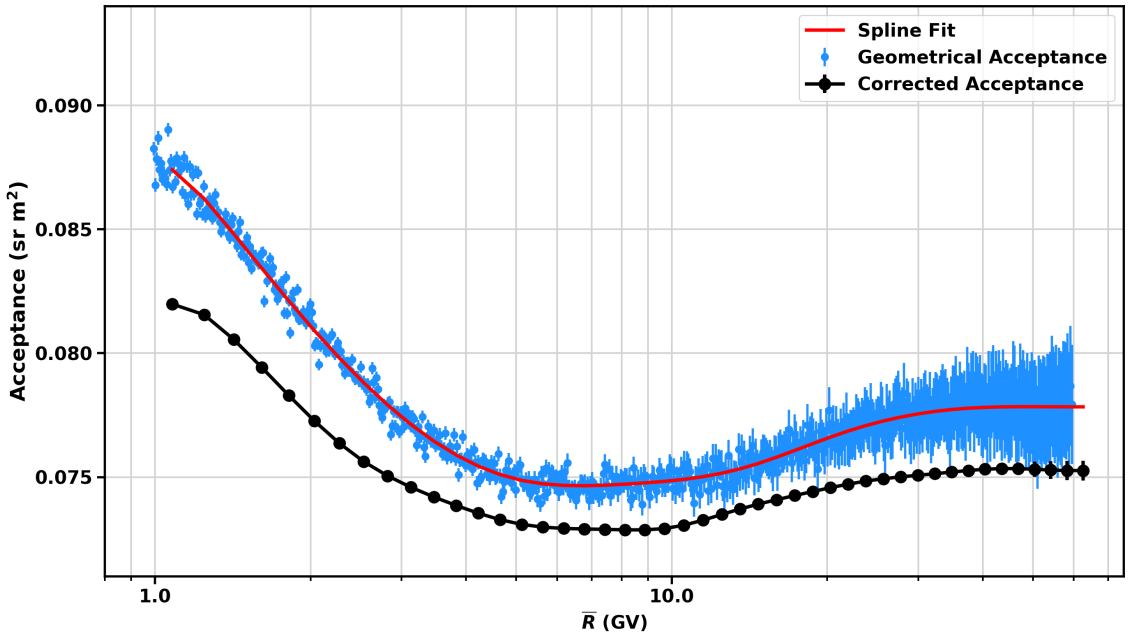

Figure 4.12: The geometrical acceptance (blue) is smoothed using a spline fit (red) and finally corrected by the total correction (green).

properties is drawn alongside the matrix. The migration matrix will be often referenced in the following subsections, in order to calculate the necessary corrections to rigidity and get the true distribution of selected events.

4.6.1 Energy Loss Estimation

Particles at low rigidity measured by AMS are more affected by multiple scattering than at high rigidity. For this reason, when a low rigidity particle crosses the detector, each rigidity measurement will be biased by the amount of energy lost by the particle inside the detector material above the measuring sensor. The effect of energy loss is visible in the migration matrix as a deviation from diagonality (see Fig. 4.13 at the lowest rigidity).

To evaluate the effects of energy losses in the rigidity measurement of each event, an average correction was calculated, according to the method described below. This procedure was conceived to effectively correct the rigidity measurement of each event, predicting that the subsequent *unfolding* algorithm would have suffered from this large deviation from the diagonal in the migration matrix; in hindsight, this was not necessary, but the method is still worth describing and becomes essential in case of alternative methods of unfolding (such as direct invertion of the migration matrix). First we calculated the distribution of the relative difference between $1/\bar{R}$

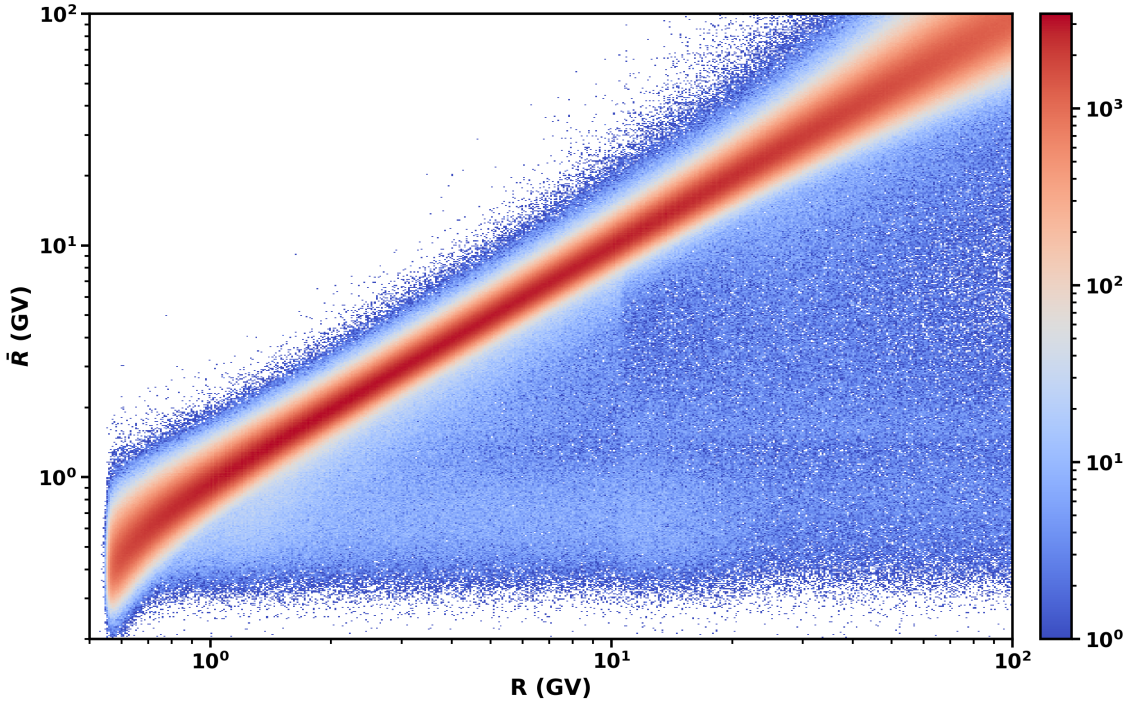

Figure 4.13: The AMS migration matrix, built with the Monte Carlo dataset. Reconstructed rigidity (y-axis) and generated rigidity (x-axis), for each reconstructed event, are plotted in this bi-dimensional histogram. The vertical smearing, with respect to the diagonal, indicates the resolution of the detector at a given rigidity; the horizontal displacement indicates the range of possible generated rigidities that can give us a measurement of the corresponding reconstructed rigidity.

and 1/R, as function of the true rigidity R (see Fig. 4.14). The reason for choosing the distribution of inverse of rigidity, instead of directly rigidity, is that the tracker actually measures a quantity proportional to $1/\bar{R}$; so $1/\bar{R}$ will be distributed according to a normal distribution, which is not guaranteed for the distribution of $\bar{R}$.

The one-dimensional projection, for each bin in true rigidity, along the y axis is the normal distribution of measured rigidity, given the true rigidity value of the bin (see Fig. 4.15). Therefore, the standard deviation of this normal distribution is the rigidity resolution of the detector, for a given true rigidity, while the mean value is the shift due to energy losses. In the case of an ideal detector, with no energy losses, the distribution would be, in fact, centered around zero. We can finally define as *energy loss factor* the series of mean values as function of true rigidity. The series of mean values is then regularized with a polynomial fit (up to the fourth degree) and presented in Fig. 4.15.

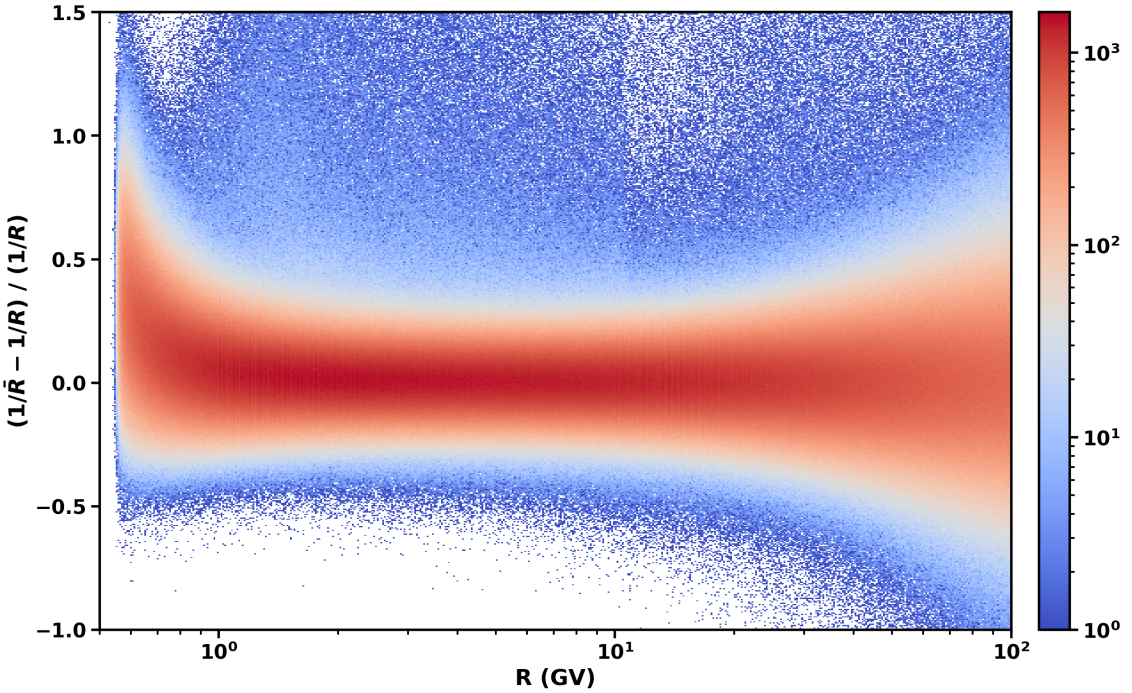

Figure 4.14: Distribution of the relative difference between the inverse of reconstructed rigidity ($1/\bar{R}$) and the inverse of true rigidity (1/R), as function of true rigidity (R). Each slice on the y-axis is the normal distribution of the tracker measurement at a given true rigidity. The standard deviation of this distribution indicates the tracker measurement rigidity resolution, while the mean is the displacement of said measurement from the true value. At the lowest rigidities we can observe a displacement due to energy losses from multiple scattering.

The correction for energy loss is ultimately taken into account by the unfolding procedure, which will be described in the next section, but in order to apply the above function directly to each rigidity measurements, the following algorithm is suggested. Since in the on-flight dataset we don't have access to the true rigidity, it becomes necessary to extract the value of R from the definition of the energy loss function (pictured in Fig. 4.15), henceforth called $\eta(R)$:

$$\eta(R) = \langle \frac{1/\bar{R} - 1/R}{1/R} \rangle \;\Rightarrow\; R = \bar{R}\,(\eta(R) + 1) \tag{4.17}$$

We then use the Newton's root finding algorithm to solve for R, with the measured $\bar{R}$ as fixed point. The Newton's method is an iterative algorithm that requires the first derivative, as follows:

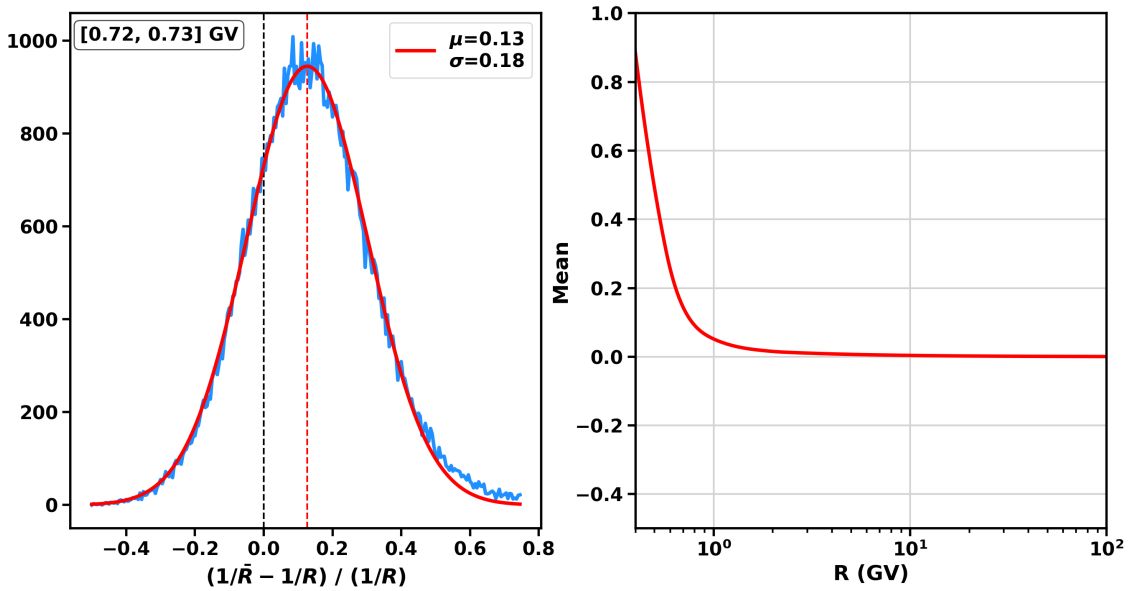

Figure 4.15: **Left**: A slice of the distribution in Fig. 4.14. We obtain a normal distribution per rigidity bin, each one representing the rigidity resolution (σ) and energy loss factor (μ) at a given rigidity. **Right**: The energy loss correction factor as obtained by fitting all the normal distribution in the previous step with a normal distribution. The red line is the fit of all the values with a fourth degree polynomial function.

$$\begin{cases} f(R) = \bar{R}\,(\eta(R) + 1) - R = 0 \\ f'(R) = \bar{R}\,\eta(R) - 1 = 0 \end{cases} \tag{4.18}$$

Which, after n iterations gives:

$$R^n = R^{n-1} - \frac{f(R^{n-1})}{f'(R^{n-1})} \tag{4.19}$$

4.6.2 Unfolding Procedure: Folded Acceptance

Unfolding is a procedure meant to correct for the effects of detector measurements, specifically when dealing with binned data. Both the uncertainty on the measurement and the propagation of these uncertainty over the rigidity calculation make so that the rigidity measurement will have a certain resolution, itself rigidity dependent. This means that when we build the rigidity distribution of the selected events, which is an histogram with a determined binning, certain events will end up in the wrong bin due to the migration effect induced by rigidity resolution (see Fig. 4.16) If

we want to obtain the true rigidity distribution, unaffected by the measurement, we must correct for this effect. While this problem can be approached in many ways, the chosen one for this work and widely used in the AMS collaboration is called *Folded Acceptance*.

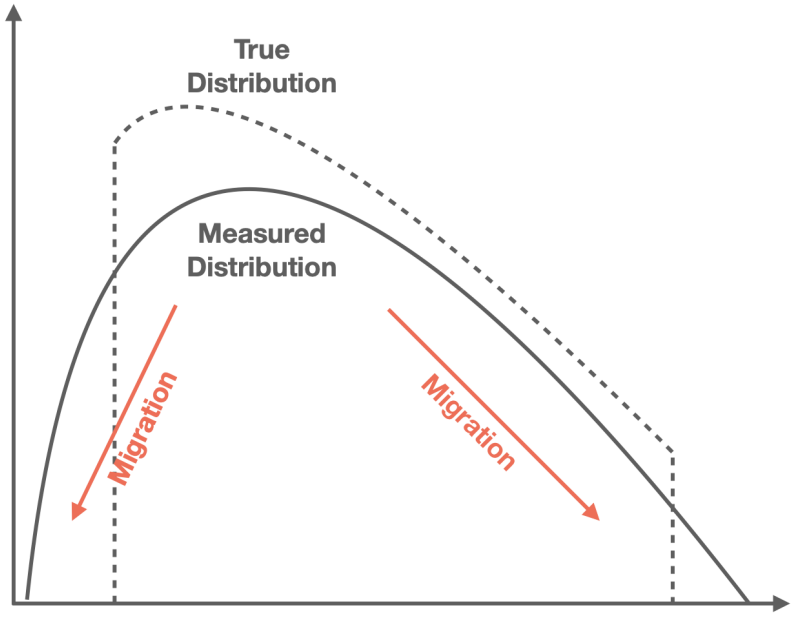

Figure 4.16: Schematic of the true distribution of CR counts, e.g. generated with the Monte Carlo (dashed line), opposed to the measured distribution (full line). The latter includes all the effects of smearing due to finite resolution, which forces the measurement in the wrong bins. The migration is prevalent where the resolution is worse, at the lowest and highest rigidity, see also Fig. 3.6.

The Folded Acceptance method is an iterative process, in which we calculate the folded acceptance of the detector using Monte Carlo events that pass the selection over each iteration, reweighing those events with a certain criterion. This process is described in detail in the following section and depicted in the diagram in Fig. 4.17.

At *iteration 0* we inject an arbitrary external flux into the unfolding algorithm, serving as "prior" for the subsequent calculation. The injected flux is at first regularized by the Autospline algorithm, which results in an analytical model of its rigidity dependence. The spline model of the injected flux is then integrated over each bin of the Monte Carlo selected events (*MC sample*) to build the new *MC sample* histogram and used to reweigh each events that passed the selection according to the following weight:

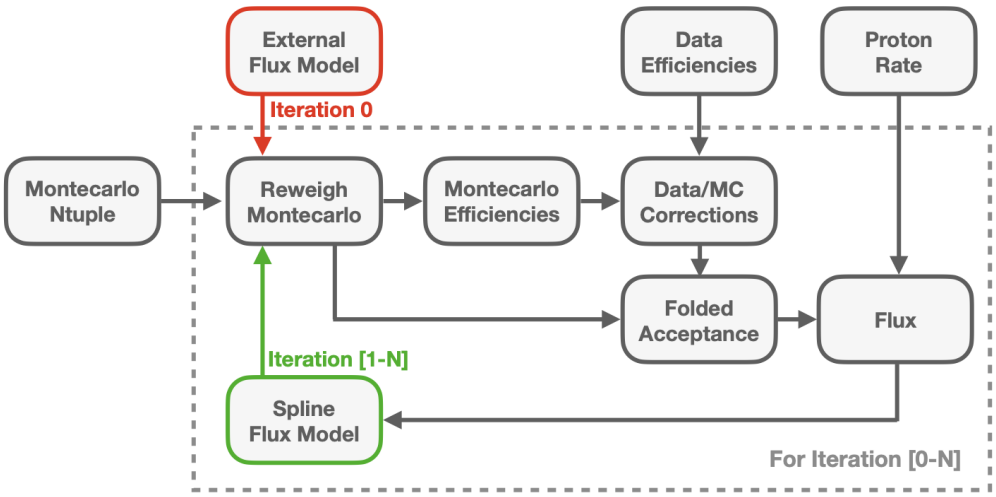

Figure 4.17: Unfolding diagram for the Folded Acceptance method. The Monte Carlo sample, which passed the proton selection, is reweighed according to the CRs power law, such as it follows the measured distribution. With this sample we can calculate efficiencies and the geometrical acceptance. Combining the Monte Carlo efficiencies with those on data, we obtain the corrections to be applied to the geometrical acceptance, resulting in a *folded corrected acceptance*. Using this folded acceptance we calculate the flux as usual, following Eq. 4.9. The flux is finally regularized with a spline fit, which in turn will be used from iteration 1 to N as reweighing function for the Monte Carlo. This procedure is convergent to the true distribution of the flux in rigidity and it is stopped after N iterations according to the criterion described in the text.

$$Weight = f(R) \cdot R \cdot \ln\left(R_{max}/R_{min}\right) \tag{4.20}$$

where R is the generated rigidity for the event, R_{max} and R_{min} are the maximum and minimum boundaries for simulated rigidity in the Monte Carlo. The Monte Carlo ntuple containing all the selected events, which is reweighed event by event at the start of each iteration, is never reweighed before the unfolding procedure. This means that the rigidity distribution is the same distribution determined when the Monte Carlo was generated in the first place. In the case of Monte Carlo productions of the AMS collaboration, events are generated simply following $\frac{1}{R}$ in order to approximate the power law behavior of cosmic rays, and this is the reason why we multiply the flux model in Eq. 4.20 by $R \cdot ln(R_{max}/R_{min})$. The logarithm of this ratio represents the normalization factor of the distribution before reweighing, which corresponds to the integral of $\frac{1}{R}$ in the production range $[R_{max}, R_{min}]$. The

reweighing procedure is further explained in Fig. 4.18:

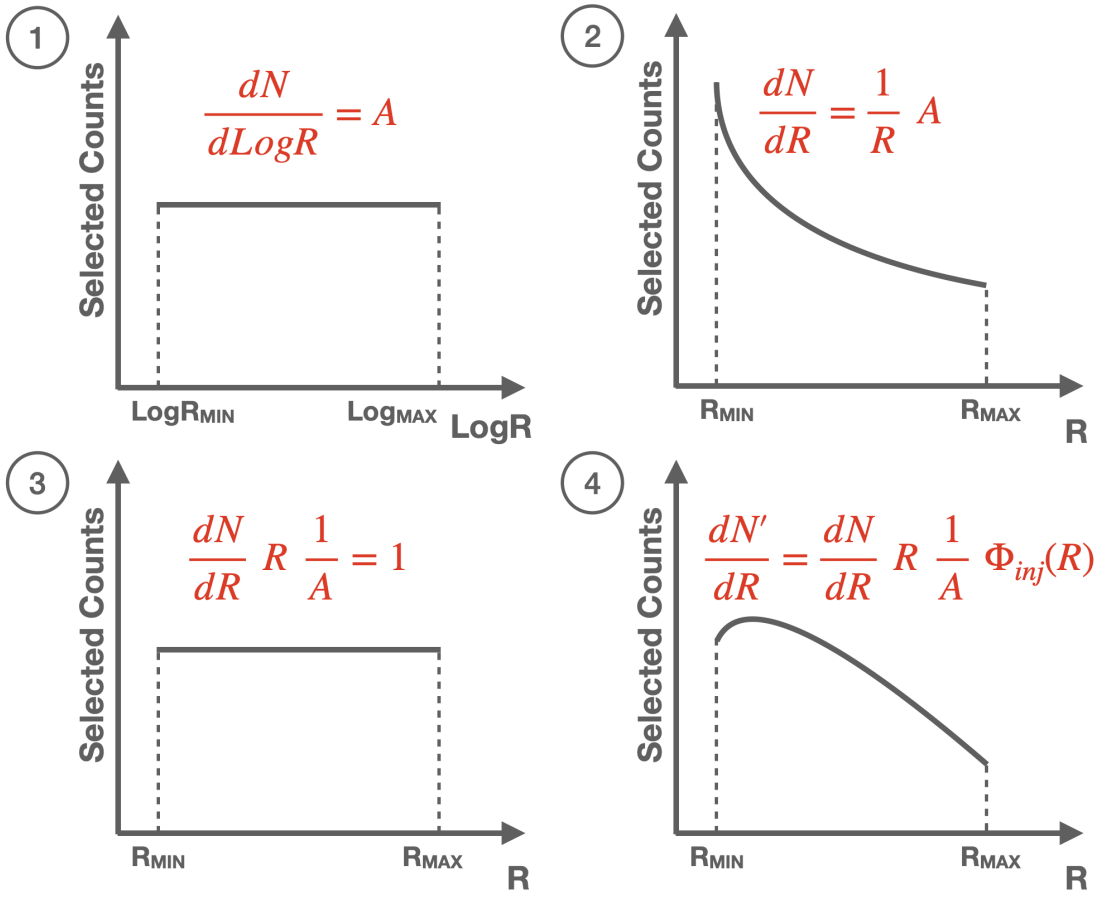

Figure 4.18: Schematic of the reweighing procedure. The Monte Carlo is produced by generating events following a constant distribution in the Log(R) space (1). This means that our sample is distributed, in the R space, according to 1/R with a normalization factor A (2). To reweigh the Monte Carlo according to our distribution of preference, such as the power law of CRs, we first transform it to a constant distribution in linear space (3). Finally we can obtain the desired distribution by simply multiplying (3) by the external proton flux (4).

With the resulting ntuple of selected Monte Carlo, reweighed by the external flux, efficiencies and folded geometrical acceptance are calculated. Efficiencies on data are divided by those on Monte Carlo to obtain corrections, which are then multiplied to the geometrical acceptance to obtain the corrected folded acceptance. Finally the iteration 0 flux is computed by combining the proton rate with the corrected folded acceptance calculated at this stage. The iteration 0 flux is regularized in the same way as the external injected flux, using the *Auto-Spline Algorithm* and used as new flux model for reweighing Monte Carlo during *iteration 1*.

In principle it is possible to use any distribution as external initial flux, though if the injection flux has a similar shape to the expected result (e.g. a power law), the unfolding algorithm converges faster. In any case, the final unfolded flux, after N iterations, will be the same within the systematic errors arising from the unfolding procedure, which will be discussed in section 4.7.3.

This iterative procedure will eventually stop after N iterations, with the criterion for convergence being the maximum relative difference of *iteration N* flux and *iteration N-1* flux, among all bins in rigidity, lower than a certain threshold. In our case, we ask for the difference between the last two iterations, in a given rigidity bin i, to be less than 0.5% (see Eq.4.21).

$$\frac{\Phi_i^N - \Phi_i^{N-1}}{\Phi_i^{N-1}} < 0.005 \tag{4.21}$$

The flux at last iteration is the final unfolded flux that appears if Fig. 4.20, as well as all the efficiencies and acceptance shown before in this chapter.

4.7 Average Proton Flux

In this section we will present the final unfolded average flux as function of rigidity, i.e. the *proton spectrum*, integrated in time between May 2011 and October 2023. The average flux is useful to study long term variations in the flux, such as the 11-year solar cycle, since the effects of short term effects are averaged over time. In our case, as we are mostly interested in the latter, the average flux is still useful both for comparing our selection method with previous results and as a basis for the daily selection procedure. Notably, all the previous publications about the proton flux with AMS involved *pass7* datasets, which greatly differ from the current standard *pass8* (e.g. the track finding algorithm was changed between the two datasets). The chosen interval (2011-2023) is currently the latest updated available dataset and we will compare the flux produced with our selection, over this time interval, to other productions internal to the collaboration (currently unpublished) within the same range. This was done to avoid most of the possible sources of discrepancy and to ensure compatibility with other near-future publications of the AMS proton flux.

4.7.1 Statistical Uncertainty

The complexity of the experiment and the way we manipulate data lead to different kinds of uncertainty. The first source of uncertainty, which is intrinsic to any counting experiment, is the statistical error due to a limited set of data. When we measure the rate of cosmic rays hitting the detector and bin the results with

respect to rigidity, the bin counts represent random and independent occurrences of an event that follows the physical laws describing the processes behind acceleration and propagation of these particles. The distribution of random and independent events follows the Poisson distribution, hence the statistical uncertainty related to each rigidity bin is $\sqrt{N}$, where N is the number of counts in that bin. The rigidity distribution of statistical uncertainties, for the average flux calculation, is pictured in Fig. 4.19. This uncertainty will be calculated separately for each day in the daily proton flux procedure.

In all the other cases, we talk about systematic uncertainties, which are related to the choice of construction for the Monte Carlo simulation, the usage of a specific unfolding method and so on. We will proceed to evaluate these sources following the method as in past proton flux productions [109]. In the remaining of this section we will then discuss each contribution to the systematic uncertainties.

4.7.2 Acceptance and ISS/MC Corrections Systematic Uncertainties

Throughout the flux computation procedure, we extensively made use of our Autospline algorithm, in order to smooth the distributions of Acceptance and data to Monte Carlo corrections. Each correction, as described in section 4.5.2, is the ratio of the efficiencies on data and on Monte Carlo and, in the scenario where each trial is independent and has only two outcomes (success or failure, as in passing the selection), the statistical uncertainty in efficiency can be approximated using the binomial distribution:

$$\Delta\epsilon = \sqrt{\frac{\epsilon(1-\epsilon)}{N_{tot}}} \tag{4.22}$$

where ϵ is the efficiency and N_{tot} the total number of events in the denominator. These uncertainties are then propagated to the correction via standard propagation of errors:

$$\frac{\Delta c}{c} = \sqrt{\left(\frac{\Delta\epsilon_{ISS}}{\epsilon_{ISS}}\right)^2 + \left(\frac{\Delta\epsilon_{MC}}{\epsilon_{MC}}\right)^2} \tag{4.23}$$

where c is the value of the correction, Δc its uncertainty, ϵ_{ISS} is the efficiency on data with its uncertainty $\Delta\epsilon_{ISS}$ and MC stands likewise for Monte Carlo. These statistical uncertainties are then considered when fitting each correction with the spline function.

In general, the model that we use to fit our data can change drastically their interpretation, hence we quantify the effect of choosing a particular model over any other as a systematic uncertainty. In the case of our spline algorithm, we decided to construct a confidence interval based on the fit results, corresponding to a confidence level of 68%. The symmetric confidence interval is shown, for each ISS/MC correction, in Fig. 4.19 as *Correction Systematics*. This procedure was also applied for the calculation of the acceptance systematic, shown in the same figure.

4.7.3 Unfolding Systematic Uncertainty

As already previously discussed, the iterative *Folded Acceptance* method is just one of many options available to approximate the true rigidity distribution of the flux and each method has its own flaws. In the case of the *Folded Acceptance* method, we rely heavily on the accuracy of the description given by our Monte Carlo simulation, meaning that if our Monte Carlo production is biased in any way, it will reflect this bias onto the unfolding correction. This is because the unfolding is actually performed by reweighing each event in the Monte Carlo by a tentative flux, computing a new acceptance function based upon the new weights; if the distribution of events follows the wrong generated cosmic rays distribution, the procedure will always converge to the same result, but not the correct one, even if just slightly off.

To evaluate this systematic, we decided to implement a bootstrapping method as follows. We start by changing the input geometrical acceptance at iteration 0 by randomly varying each bin value within its own variance. This would give us a different geometrical acceptance from the measured one which is still physical. The new acceptance would then be input to the unfolding procedure and we would save the resulting acceptance at iteration 1. After repeating this procedure for 1000 times (an arbitrary large number to fill an histogram), the distribution in each rigidity bin of iteration 1 acceptances has been calculated, giving us a standard deviation for every rigidity. The values of standard deviations as function of rigidity are then considered as *unfolding systematic*. This systematic contribution can be observed in Fig. 4.19.

4.7.4 Absolute Rigidity Scale Systematic Uncertainty

The last contribution to the total systematic uncertainty derives from the binned representation of the corrected acceptance. The acceptance is a function of true rigidity, which in principle can be described analytically. Since we derived it by means of a Monte Carlo simulation, our description is done necessarily via histograms. This means that within a predefined rigidity bin, the acceptance is represented by a single value, corresponding to the average of the acceptance function within the bin width. When using this binned representation, as we must do to

use Eq. 4.9, we neglect the slight variation that the acceptance might present within each bin, as the distribution inside the bin might not be symmetric and taking the value at the center does not correspond to the true value of the function. Therefore we have to take into account this variation as systematic uncertainty.

To quantify this contribution, we calculated the absolute variation of the acceptance function with respect to measured rigidity, considering as probability to be measuring a determined rigidity to be uniform. In other words, the systematic uncertainty due to binned acceptance is given by the product between the module of the derivative of the acceptance function, calculated in $\bar{R}$, and the standard deviation of the uniform distribution in a given bin ($\Delta \mathrm{R}/\sqrt{12}$), as in Eq. 4.24. The absolute rigidity scale systematic is presented in Fig. 4.19.

$$\sigma_{scale} = \left| \frac{dAcc_{corr}}{d\bar{R}}(\bar{R}) \right| \frac{\Delta R}{\sqrt{12}} \tag{4.24}$$

The total uncertainties in the daily proton flux measurement are the result of the summation in quadrature of all the above contributions, as shown in Fig. 4.19.

4.7.5 Final Average Flux

The final average flux is shown in Fig. 4.20 and compared to the independent flux production from AMS collaborators in the rigidity range [1, 60] GV. The flux of this work presents differences of less than 2% across the considered rigidity interval, being in agreement with the previous publication within its total uncertainty. Our flux is systematically underestimated, with respect to the other production, below 1 GV. Our interpretation for the differences relies on the different calculation for the threshold in the geomagnetic rigidity cutoff cut (see section 4.2). A *safety factor* can be multiplied to the maximum value of the IGRF cutoff, in order to ensure that only primary cosmic rays are selected. In absence of this information, we were not able to reproduce the exact safety factor used in the other production. The safety factor was, in any case, devised for the study of the GCR proton flux and will only impact our measurement of the daily proton flux by a few percent with respect to the reference flux from AMS, while our SEP-only flux will be independent from the standard daily procedure. In fact, as we will see in section 5.4, the GCR proton flux - including secondaries and trapped particles - constitutes a background for the SEP-only flux; additionally we will entirely remove the rigidity cutoff cut and replace it with an alternative selection, specifically tailored for SEPs. Therefore the differences between the two daily proton flux productions should not impact our final result. Despite the differences obtained on our proton spectrum, we proved that the selection developed for this work is robust and consistent with other independent productions.

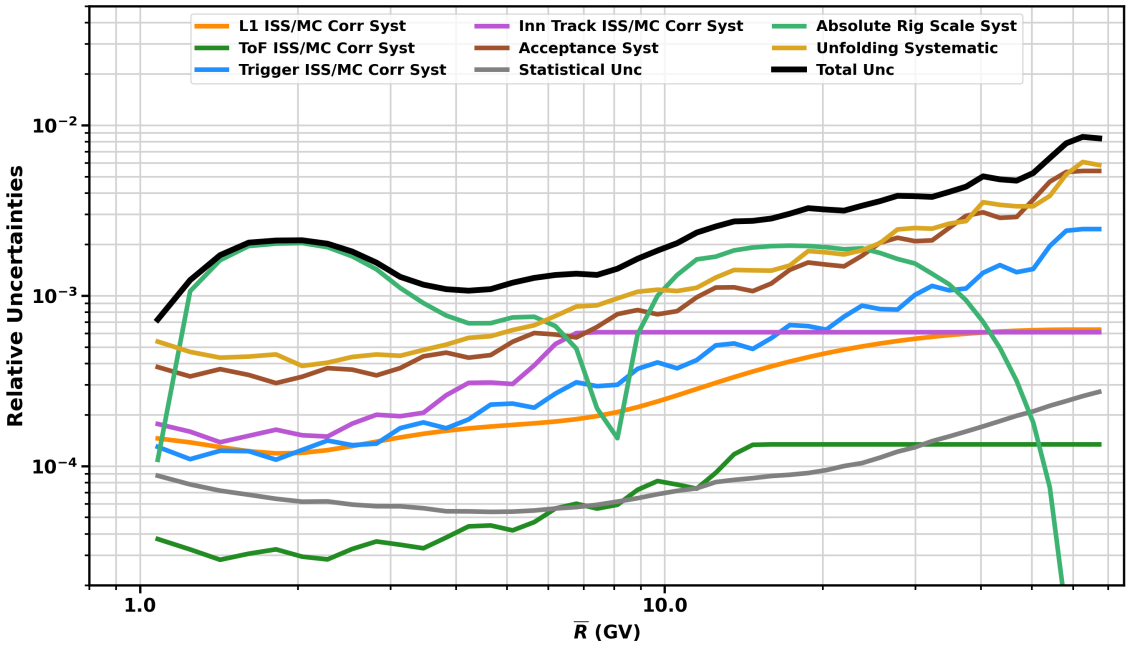

Figure 4.19: An overview of all the systematic contributions in the average flux calculation. These include the confidence intervals from the spline fit of the four ISS/MC corrections and the acceptance, the systematic uncertainty obtained by bootstrapping the unfolding procedure at the first iteration and the rigidity scale systematic. The waviness in some of the histograms relative to spline fits is due to the spline fit being more precise where the knots are positioned. The plot also shows the poissonian statistical uncertainty related to proton counts. The black line is the factorization of all the sources of uncertainty. Note that, in the case of the average flux, the total uncertainty is dominated by systematic uncertainties rather than the statistical one.

The computation of the average and, as we will see in the next section, the daily flux resulted in the production of a robust code for the analysis of AMS raw data. The result presented in this section is comparing the first two production of the proton flux with the pass8 dataset and, as time progresses, many adjustments will surely arise and a better convergence of the independent analyses will be reached, although there is already a good agreement. This process will eventually lead to the publication of the updated proton flux as AMS collaboration and it is important to have at least two independent analyses converging to the same result. Additionally, the current analysis is based on the *Ntuple for AMS-Italy Analysis* software [107], which provides a common powerful framework between the AMS Italian community for all the current studies carried out by the collaboration. The proton analysis is an important tool that can be easily utilized and adjusted even by other members of the collaboration, thanks to the modularity and common language of NAIA.

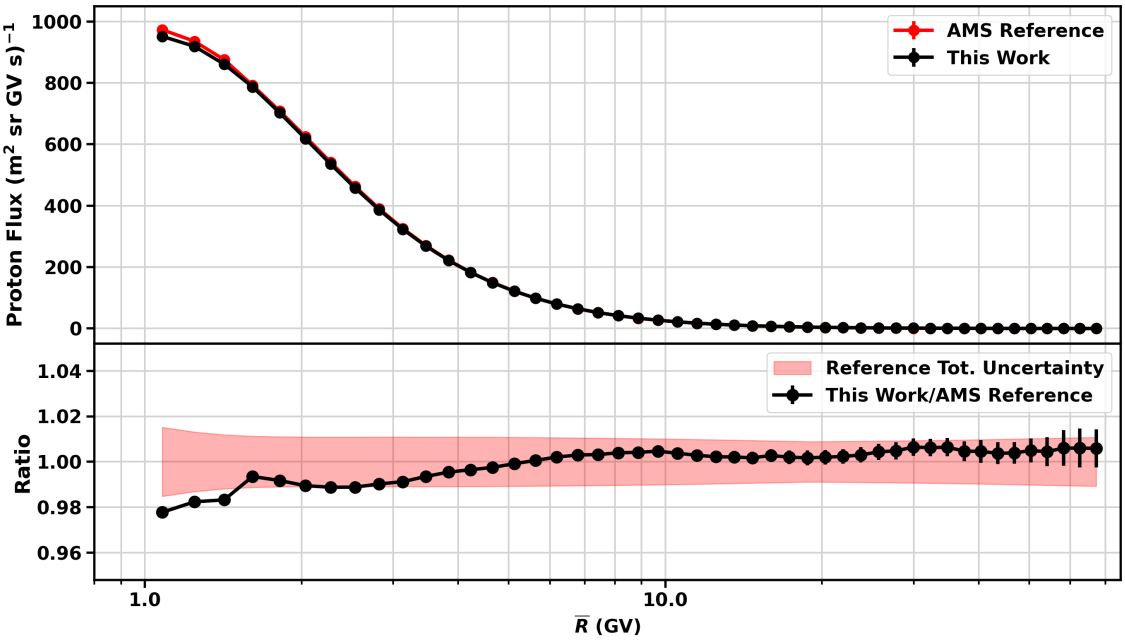

Figure 4.20: **Top**: The average proton rigidity spectrum of this work (black) compared with the internal reference flux from AMS collaborators (red). **Bottom**: Ratio between our spectrum and the reference one, within the interval [1, 60] GV. The error band in red indicates the total uncertainty of the published flux. The 2% level differences are due to a different definition of the geomagnetic rigidity cutoff, therefore selecting a more restrictive sample at low rigidity. These differences are do not affect the SEP-only fluxes shown as our final result, as we will use and independent method for SEP selection.

4.8 Daily Proton Flux

The final step with the proton selection described in this chapter is the compilation of several proton daily fluxes, each given at different rigidity intervals, corresponding to the rigidity binning of the proton spectrum presented in the previous section. In order to facilitate the production of multiple fluxes and spectra, the histogram of each distribution involved in the flux calculation was designed to be two-dimensional, with the rigidity binning on the y-axis and time binning (A) on the x-axis. The average flux shown before is a special case of the general time-resolved production, where we integrated the corresponding histograms over all the time bins, resulting in an average proton rigidity spectrum (section 4.7).

For the average flux, the proton analysis was conducted in two steps. The first step involved selecting protons, while the second encompassed calculating efficiencies, corrections, and acceptance through the unfolding procedure, ultimately resulted in

the spectrum. In contrast, the time-resolved analysis required an additional step. The initial selection phase is shared with the average flux procedure, as we had already prepared histograms of counts and efficiency numerators and denominators with daily granularity. The second step, which involves obtaining the spectrum, follows a process similar to that of the average flux analysis but is performed for each individual day in the dataset, including unfolding. Once the daily spectra are derived, they can be combined to form time series, representing proton fluxes within each rigidity bin.

We will start by introducing the main difference between the average and daily analyses: the treatment of daily efficiencies and corrections. In the subsequent subsection we will present all the sources of uncertainty that we considered in the calculation of the daily and flux in Fig. 4.23, after which there will be a brief discussion on the known and unknown features of the daily proton flux, as well as the unprecedented point of view on SEP events of AMS.

While the average flux was already calculated with the new *pass8*, the daily flux presented in this section represents the first production of the time resolved proton flux with all the currently available dataset, spanning between May 2011 and October 2023.

4.8.1 Daily Efficiencies, Corrections and Uncertainties

The procedure to obtain daily spectra is not generally dissimilar to what has been presented in the previous sections for the average analysis, with the main difference being in the treatment of daily corrections. Instead of producing individual corrections for each day, we decided to re-scale the average functions shown in 4.5.2, in order to maintain the average functional form. The scaling function is given by the spline fit of the ratio between the daily efficiency on data and the average one, as written in Eq. 4.25. The spline fit is performed with four knots in logarithmic scale up to 10 GV, in order to capture the daily variations at low rigidity, while using a constant scaling factor at the highest. The daily variations are caused by short term effects, such as different levels of solar activity and geomagnetic conditions, hence they should not be present at high rigidity. The purpose of the fit is to filter the statistical fluctuations, regularizing the ratio in the rigidity space. An example of the daily/average ratios used to perform the re-scaling is shown in Fig. 4.21, together with the spline fit as rigidity regularization. The confidence interval from the fit is considered as systematic uncertainty for each day and summed to the daily corrections via standard propagation of errors. An exception was made for the daily trigger efficiency, as the sample for the unbiased triggers (see section 4.4) is too small to compute the efficiency in a daily timescale. Hence we integrated the trigger efficiency in a 15-day window centered on the current day, in order to calculate the scaling factor.

$$Corr_{Daily}(t,R) = Corr(R)\ \frac{\epsilon^{Data}_{Daily}(t,R)}{\epsilon^{Data}(R)} \tag{4.25}$$

Note that the systematic uncertainties derived from the fitting procedure will be propagated to the corresponding correction systematic uncertainty via summation in quadrature: the final relative uncertainty shown later in this section will therefore contain both contributions.

The final relative uncertainties are calculated in a similar way as in the average procedure, with the main difference being the much shorter temporal integration time of just one day. For this reason, the dominant contribution comes from the statistical uncertainty. An example of uncertainties for the day 16 May 2012 are shown in Fig. 4.22.

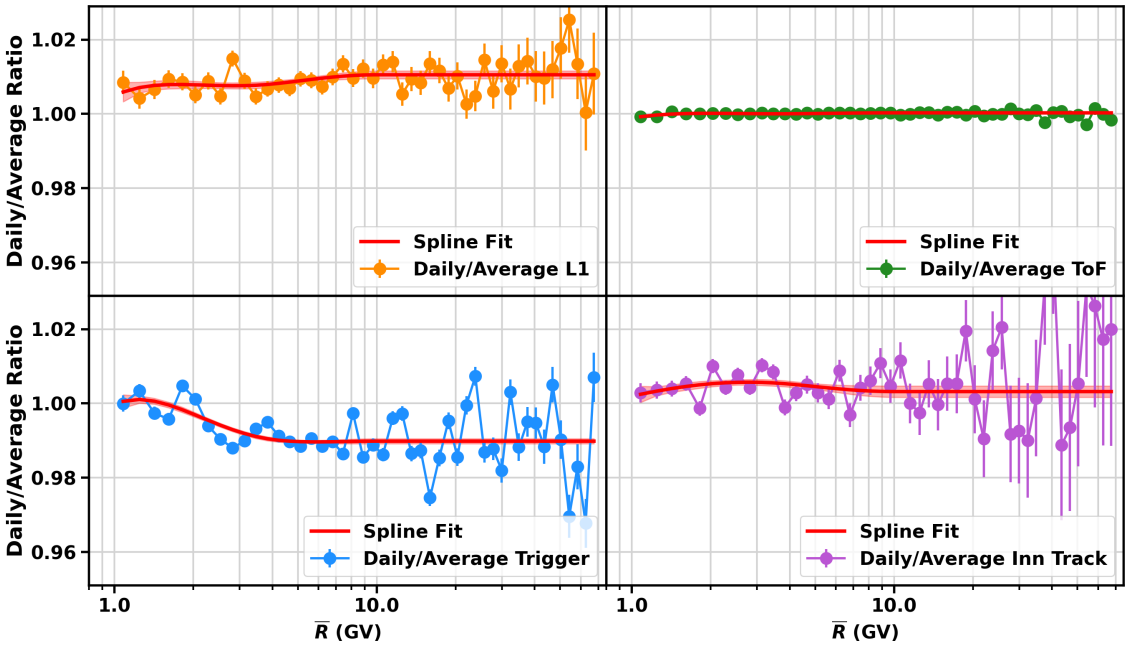

Figure 4.21: Example of daily scaling factors for the four corrections, calculated as the ratio of the daily and average efficiencies, for the day 16 May 2012. These ratios have been regularized in rigidity using a spline function fit with a three knots and a constant above 10 GV. The systematic uncertainty is quoted as 68% confidence interval, obtained from the spline fitting procedure, and propagated to the corrections via summation in quadrature.

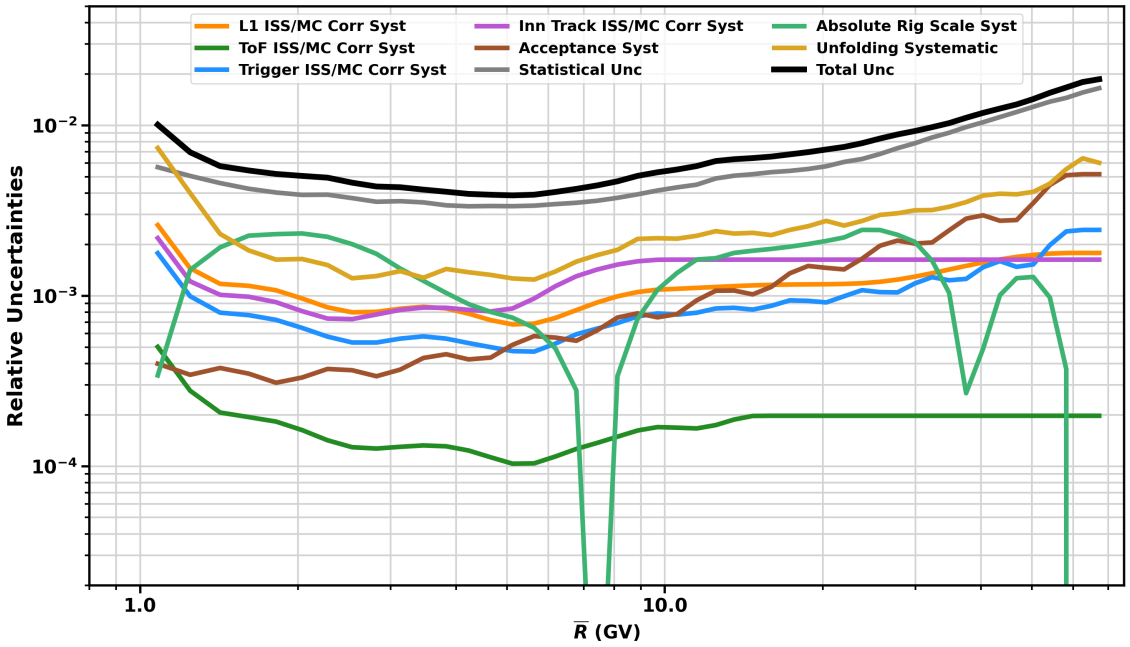

Figure 4.22: An example of all the systematic contributions in the daily flux calculation for the day 16 May 2012. These include the systematic uncertainty obtained by bootstrapping the unfolding procedure at the first iteration, the rigidity scale systematic and the confidence intervals from the spline fit of acceptance and the four ISS/MC corrections. The latter also contain the contribution from the daily/average ratios. The plot also shows the statistical uncertainty related to proton counts, which is dominant in the daily spectrum. The black line is the factorization of all the sources of uncertainty.

4.8.2 Final Daily Flux

Eq. 4.9 is then calculated for each day in our available dataset to obtain the daily-integrated spectra. After this computation, we can finally produce the time-dependent daily proton flux for each rigidity bin. The latter is computed by systematically plotting the content of the ith rigidity bin, out of N rigidity bins, for all the daily spectra; if we repeat this process for all the rigidity bins we will obtain N time-dependent proton fluxes for different rigidity intervals.

An example of the time-dependent daily proton flux, for the lowest rigidity bin [1, 1.16] GV, is shown in Fig. 4.23. In this low rigidity range, the flux exhibits a noticeable variation, spanning a difference of almost 540% between the minimum of February 2014 and the maximum around June 2020. Another interesting feature is the noticeable drop in September 2017, which was also observed at Earth as a ground level enhancement (GLE) [111]. This perturbation is the composite effect of multiple Forbush Decreases caused by an intense activity period on the Sun's

surface, corresponding to two of the most intense solar flares observed for the entire 24th solar cycle. Fig. 4.24 shows the overall temporal behavior of the daily proton flux for the first 26 rigidity bins, i.e. up to 10 GV. In the plotted range we can appreciate the stronger modulation of cosmic rays for the lowest rigidity bins, while the same effect, despite being still present, is much milder for the highest. This variability is also emphasized in Fig. 4.24, where all the spectra, for each daily measurement, are plotted together.

Finally the flux is also shown in comparison with the previously published daily flux [109] in Fig. 4.25, for the first and 17th bins of the publication, which correspond to the rigidity range of interest for our SEP spectral analysis in the next chapter. Our flux was purposefully built as close as possible to the published one, still maintaining an independent analysis, and it results consistent with the previous one. The shaded red band that is shown in Fig. 4.25 represents the published total uncertainty from the previous AMS publication. In the latter, additional time-dependent systematic uncertainties were considered, connected to the four efficiencies (Layer 1, ToF, Trigger and Inner Tracker) time series, which were regularized also in the time domain to reduce fluctuations.

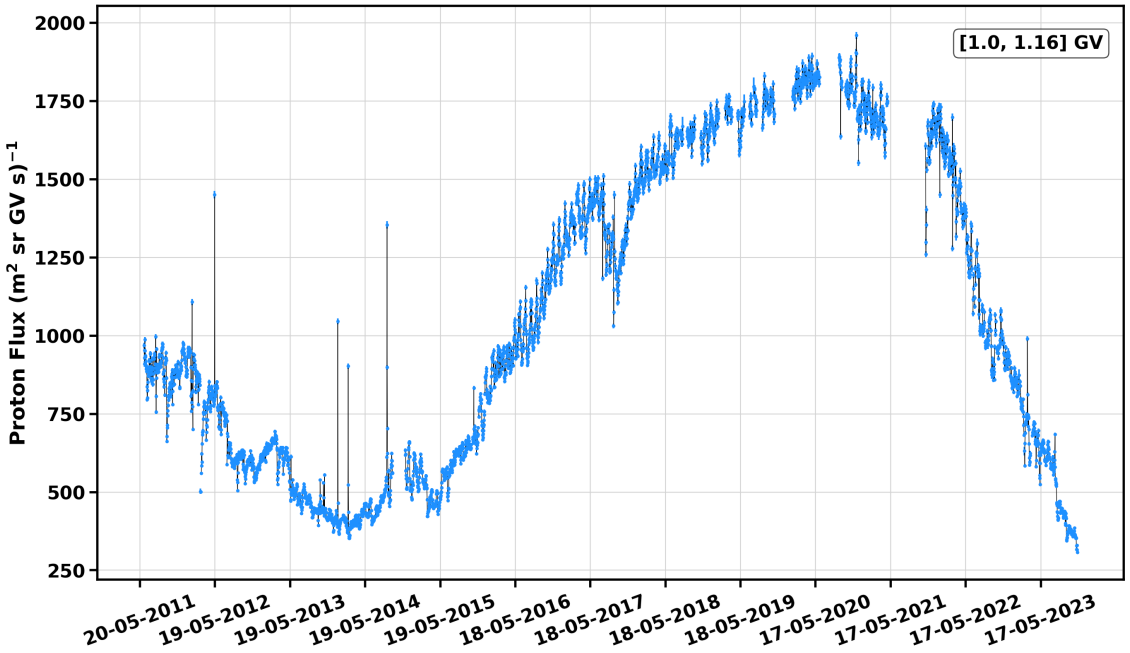

Figure 4.23: Daily proton flux for the rigidity bin [1, 1.16] GV. Some features arise at a first glance, like the presence of sudden increases, related to SEP events, and a general temporal variation. This global variation of about 540% is related to the solar activity cycle. With the latest dataset we now cover a full 11-year cycle. See the content of the next section for more details on the daily flux variability.

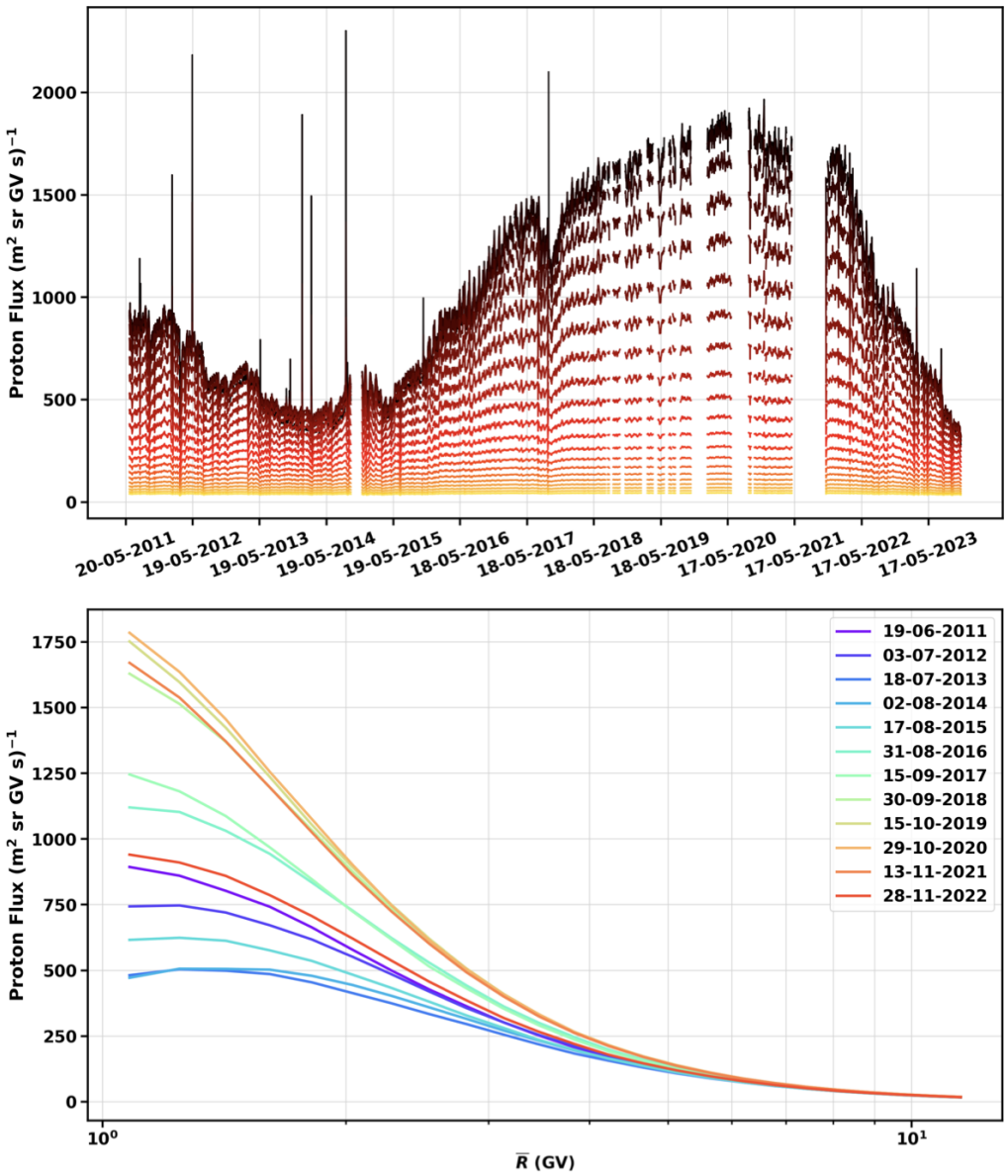

Figure 4.24: **Top:** The daily proton flux in 26 rigidity intervals, from 1 to 10 GV. Higher rigidity tends to the yellow, brighter color. The flux is greatly variable at the lowest rigidity intervals, while at the highest the effect is almost negligible. Lower rigidities appear to be more sensitive to the variation of solar activity, being more suppressed near the solar maximum of 2014, where the flux for the first two rigidity bins is lower than the third bin. The SEP contributions are only visible for the first bins, up to 2 GV. Forbush Decreases, such as in September 2017, are prominent even up to 10 GV. **Bottom:**Daily proton spectra for a subset of twelve days of the analysis dataset (one per year) and in the [1, 10] GV interval. The overall intensity is modulated by solar activity, being reduced near the solar maximum of 2014 and increased near the solar minimum of 2020.

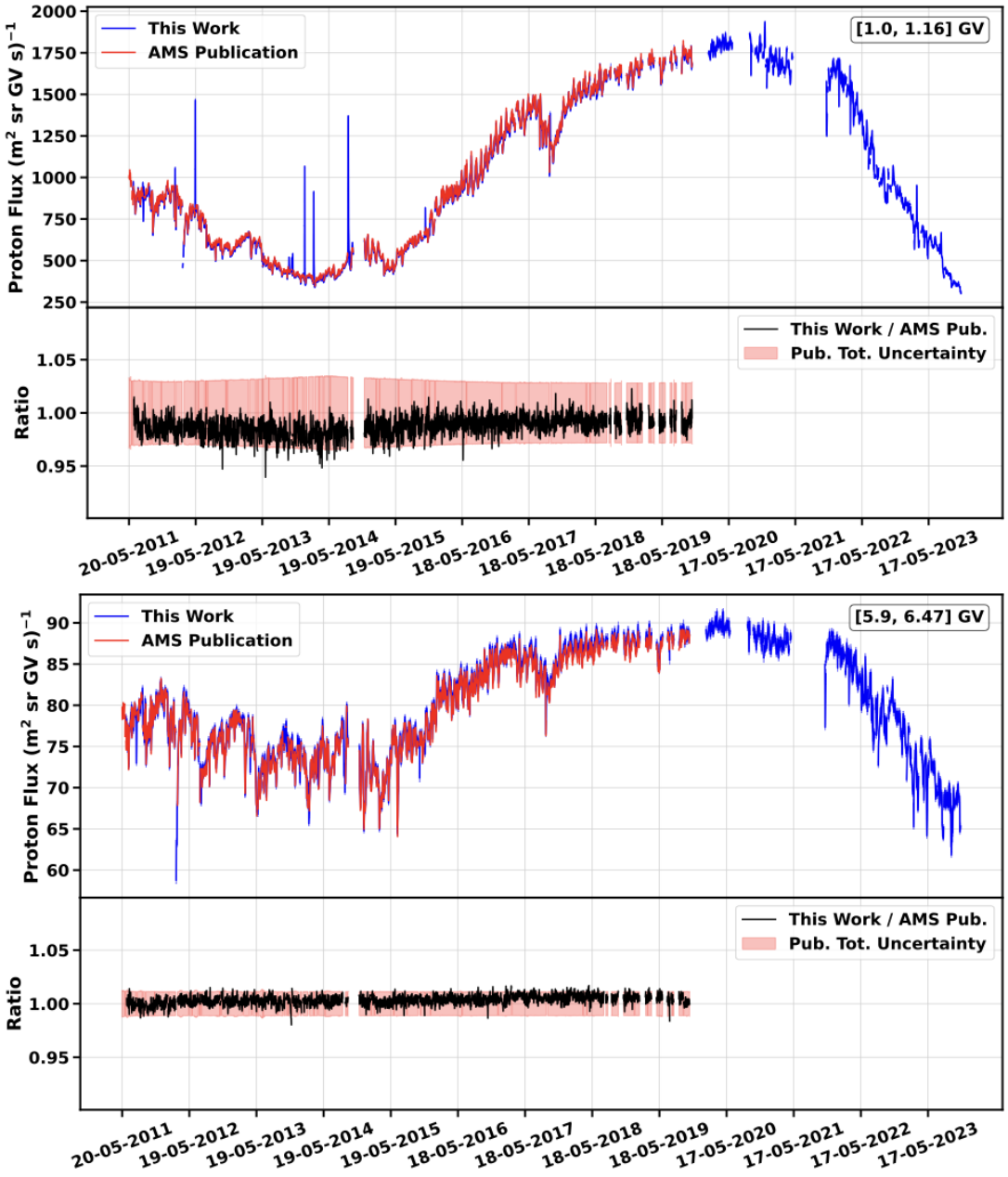

Figure 4.25: Daily proton flux from this work (blue), from May 2011 to October 2023, compared with the previous AMS publication (red) [109]. The three plots show the fluxes, starting from the first bin of the publication [1, 1.16] GV, up to the [5.9, 6.47] GV bin. In the lower part of each plot, the ratio between our flux and the published one is shown within the temporal interval of the published and with its total uncertainty displayed as a shaded band. Some periods were intentionally removed from the published proton dataset, corresponding to the SEP events.

4.8.3 Daily Flux Interpretation

The effects of different changes in the interplanetary environment cause variations in the total CR flux over different timescales. These effects are primarily caused by solar activity and therefore they are especially visible at rigidity lower than 100 GV, as higher rigidity particles of galactic origin can cross unperturbed the solar system. As seen in Fig. 4.23, many interesting features and temporal variability are visible at first glance. The three main variations are:

- long term variation: the flux is mostly anti-correlated with the solar activity cycle of 11 years. This effect is particularly visible in Fig. 4.26, where the flux is superimposed to the monthly sunspot number, the most common solar activity index. Solar activity *modulates* the incoming GCR flux, lowering its intensity when the solar activity is higher.

- Non-recurrent short term variations: we can observe these phenomena as either occasional sudden increases or moderately long decreases in the flux. These phenomena can be identified, respectively, as SEP events and Forbush Decreases. They are related to the interactions of CRs with the transient solar phenomena described in 2.1.2 and can last from a few hours up to several days. The occurrence of these short term variations is higher during solar maxima, following the higher sunspot number, which leads to a higher probability of formation of active regions. An in-depth study of these events will be the main focus of the next chapter, while a detailed view of the non-recurrent events of 2014 is given in Fig. 4.28.

- Recurrent short term variations: the flux presents multiple periodicities (9, 13.5 and 27 days period), connected to the presence of one or more co-rotating active regions, which are originated by *coronal holes* over the Sun's surface [109]. 27 days is in fact the average period of rotation of the Sun (as its rotation is differential in latitude), which is evident as periodicity in the proton flux when there is one major active region on its surface. This periodicity is halved, or even a third, when two or three active regions are present and evenly spaced on the Sun's surface. Coronal holes are cooler regions where the magnetic field lines are mostly open, allowing for the escape of a larger population of charged particles (hence we see an increased flux when they face Earth). This phenomenon, especially for the sub-periodicities of 9 and 13.5, is particularly visible in 2016 (see Fig. 4.27), as compared for example to the 2015 flux. In 2016 have been observed, in fact, multiple coronal holes, symmetrically placed around the entire equatorial region of the Sun. Periodicities are more likely to be observed for active regions near the Sun's equator, as they are better magnetically connected to the ecliptic plane, hence to Earth.

All the effects mentioned above are an evidence of the complex variability by which

CRs are affected inside the heliosphere. The complexity is further emphasized by the presence of different behaviors during two consecutive 11-year solar activity cycles, with opposite polarity of the Sun's magnetic field. The polarity of the magnetic field affects the properties of transport for differently charged particles. During a solar cycle with positive polarity ($A > 0$), where field lines are oriented outwards on the Sun's north magnetic poles, positive particles like protons tend to drift towards the inner heliosphere following the HCS (i.e. along the ecliptic plane), while during negative polarity they are mostly directed over polar trajectories. Since most of the CRs that we observe at Earth are positive, the overall intensity of cosmic rays is higher during positive polarity solar cycles, in the same phase with respect to negative polarity. The *charge-sign* effect in solar modulation was observed in AMS data and discussed in [112].

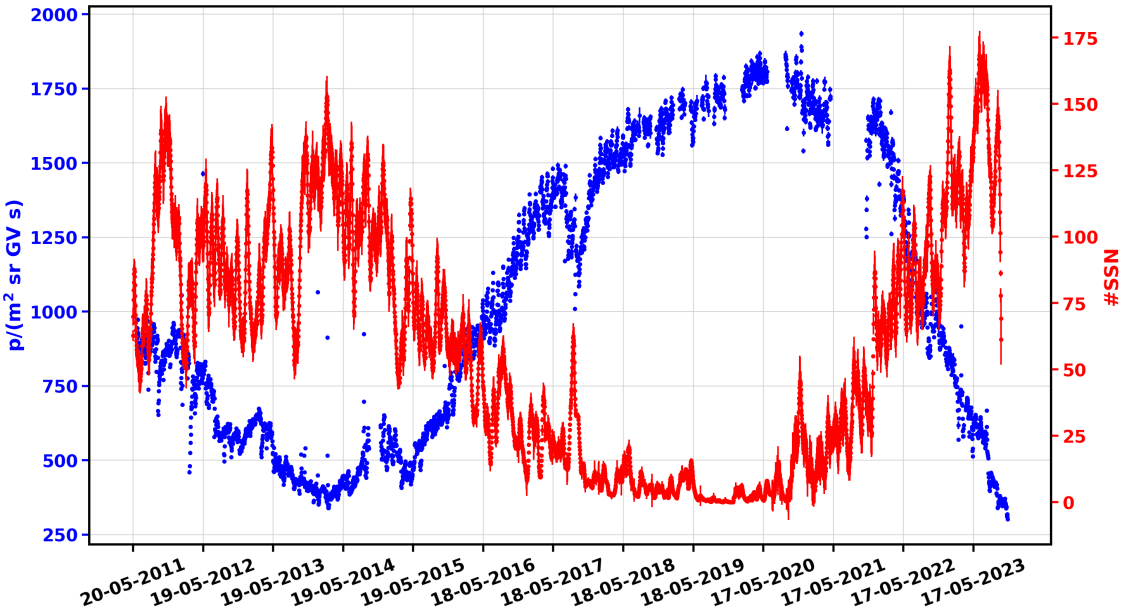

Figure 4.26: Daily proton flux from this work, in the [1, 1.16] GV interval, to which the average Sunspot Number (SSN, [113]) is superimposed. The central moving average is performed over 27 days. This figure shows the anti-correlation between the CR flux and the solar activity, as the charged solar flux is higher during the maxima and suppresses the incoming GCR flux from outside the Heliosphere.

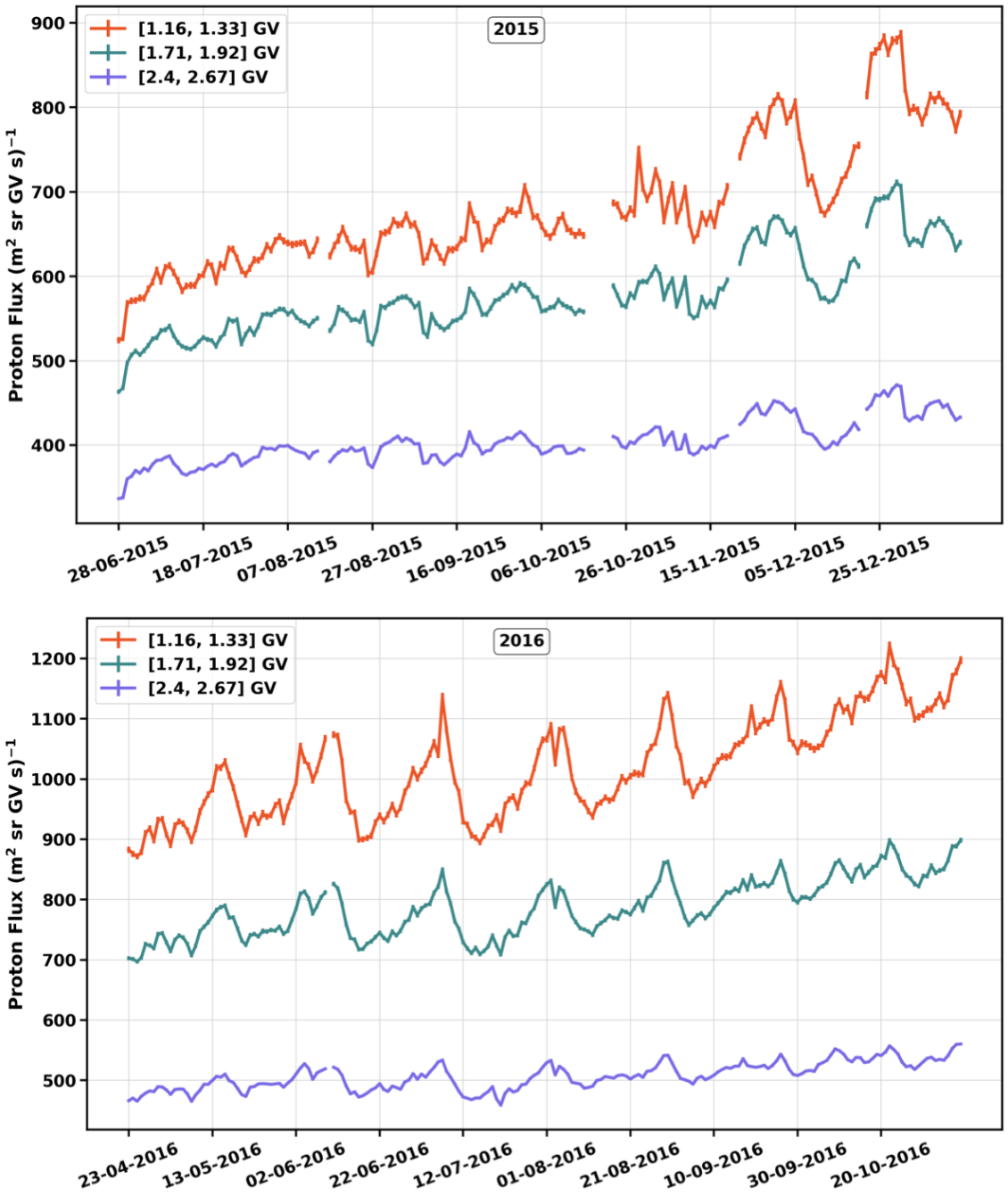

Figure 4.27: This figure shows two details of the daily proton flux, for three different rigidity intervals, in which the recurrent temporal variations are evident in 2016, while the repeating pattern is not visible in 2015. This effect is related to the presence of one or more coronal holes on the surface of the Sun, as explained in detail in [109].

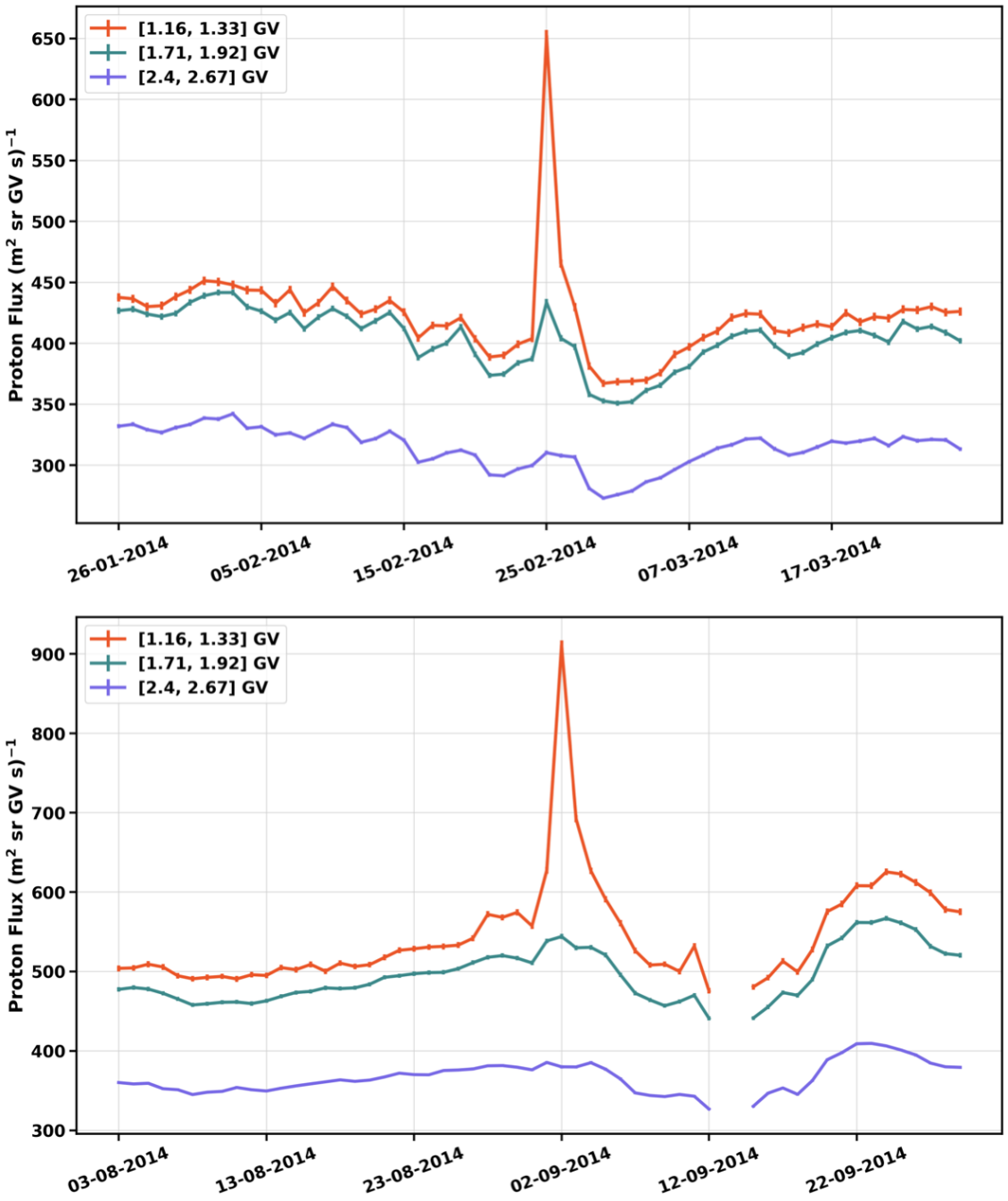

Figure 4.28: This figure shows two non recurrent variations on the daily proton flux in 2014 (25-02-2014 and 02-09-2014), which have been identified as SEP events. An SEP event is often observed as a sudden increase in the flux, with a slower decay in time; SEP events are often followed by Forbush decreases, long interval of several days in which the total flux is suppressed in the presence of a CME in the magnetospheric environment [114].

Chapter 5

Solar Energetic Particle Flux

The SEP fluxes and spectra presented in this work will be based on our daily proton flux shown in the previous chapter, henceforth referred to as *total flux*. The SEP flux is essentially the solar component of the total flux, from which the galactic component has been subtracted. Before performing the GCR subtraction, we will describe the dedicated proton selection, tailored to maximize the detection of SEPs, which we call *polar-pass* proton selection.

In principle, we could obtain a daily SEP flux by performing the subtraction, using methods described in section 5.3, directly from the daily total flux. However, the flux would result from the integration over a full day, with the selection only taking care of identifying good protons. As we know, though, AMS is only sensitive to SEPs when crossing small regions near the geomagnetic poles, where the rigidity cutoff is the lowest. This means that when we integrate over a full day, AMS will be exposed only to galactic protons for the majority of its operational time and we are entrusting the background subtraction procedure to obtain a pure sample of solar protons. In addition to this problematic, if we integrate the flux over the whole orbit, we must use a cutoff function in order to exclude the secondary and trapped population of protons, which is especially prominent near the equator as we will see.

The alternative to this approach is to integrate the flux over the specific window in which AMS is sensitive to SEP events, i.e. the magnetic polar regions. The main issue with this approach is the limited statistics for efficiency calculation, resulting from integrating the flux in such short ranges.

In this chapter we will start by describing the *SEP Finding Algorithm* used to define the candidate intervals, corresponding to high solar activity, in the AMS dataset. The subsequent section will be dedicated to the differences, in the proton selection, between the polar-pass and the standard daily approach. We will then describe our own background subtraction strategy, which will be applied to every SEP candidate.

Finally we will present some examples of background-subtracted SEP spectra in detail.

5.1 SEP Finding Algorithm

The first problem we need to address in the study of SEP fluxes is how to properly define the interval in which we observe an SEP event. At first glance, looking at the raw AMS dataset, the most prominent solar events leave a distinctive and sudden increase in the number of counts, which is clearly visible also in the ancillary measurement defined as *trigger rate*. The latter is simply the number of triggered events per second and is considered a low-latency parameter, since it is essentially based on the number Fast Trigger flags raised (see section 3.8.1). The count of triggered signals is later stored inside the RTI dataset, together with the livetime fraction, from which we can simply calculate the trigger rate as number of fast triggers per second divided by the livetime. The reduced dataset containing the trigger counts and livetime is part of the telemetry data which is constantly streamed to Earth, in order to monitor the correct functioning of each component of the detector.

Being the RTI parameters available almost in real time, the possibility of calculating a rate of triggers every second inspired the development of a *SEP Finding Algorithm*, described in [115], designed to monitor and *now-cast* the presence of SEP event candidates. As the algorithm was already been used for this purpose, we decided to draft the initial list of SEP intervals using the same principle.

We will now summarize the core functioning of the SEP Finding Algorithm. The first ingredient is the definition of a *quiet level* for the trigger rate, which must be done dynamically due to the high short term variability introduced in the rate by solar modulation. The quiet level is essentially determined by calculating a moving average of the rate, starting from five days prior and ending the interval before the considered one (the rate is integrated in one-minute intervals). The values of mean and standard deviation are calculated and stored for different cutoff intervals. At this point we consider the trigger rate measurement for the current one-minute interval, calculating a significance value associated to the distance from the average, as following:

$$S(i) = \frac{r(i,j) - \mu(i,j)}{\sigma(i,j)} \tag{5.1}$$

where i is the temporal index, j is the index of the cutoff interval corresponding to the current measurement, $r(i,j)$ is the trigger rate, $\mu(i,j)$ is the moving average and $sigma(i,j)$ the associated standard deviation. If the significance is greater than

the desired threshold (in [115], $7\,\sigma$ was found as optimal threshold), we identify the interval as *potential* SEP event. The final confirmation is given after observing three or more consecutive intervals above threshold. The list of SEP events found with this method, where we added the potential match with a solar flare and CME, is shown in Tab. 5.1.

#	Start Date	Flare Class	CME Location	CME Time	CME Speed
1	2011 Jun 07	M2.5	S25W52	06:50	1400
2	2011 Aug 04	M9.3	N14W40	04:10	1950
3	2011 Aug 09	X6.9	S12W62	08:30	1175
4	2011 Sep 07	N.A.	N.A.	N.A.	N.A.
5	2011 Sep 23(22)	X1.4	N10E90	11:24	1000
6	2011 Nov 04(03)	X1.9	S07E160	22:39	1100
7	2012 Jan 23	M8.7	N41W26	04:00	2211
8	2012 Jan 28(27)	X1.8	N40W75	16:39	2200
9	2012 Mar 07	X5.4	N30E60	00:36	2200
10	2012 Mar 13	M7.9	N25W43	17:52	2250
11	2012 May 17	M5.1	S10W75	01:48	1500
12	2012 Jul 07(06)	X1.1	S35W65	23:12	1200
13	2012 Jul 12	X1.4	S17E06	16:54	1400
14	2012 Jul 17	M1.8	S30W54	14:24	1100
15	2012 Jul 23	Backside	S15W144	02:36	3435
16	2012 Sep 28	N.A.	N05W30	02:25	1160
17	2012 Nov 08	Backside	S17W176	11:09	1285
18	2013 Mar 05	N.A.	N10E35	04:24	1900
19	2013 Apr 11	M6.5	S07E25	07:36	675
20	2013 Apr 24(23)	N.A.	S08W80	20:54	400
21	2013 May 23	M5.0	N10W80	13:24	1200

Table 5.1: List of all the SEP events found with the help of the SEP Finding Algorithm on the AMS dataset, from May 2011 to October 2023. The date refers to the first day in which AMS detected a sudden increase in the measured flux, which is then correlated to the X-ray flare class as reported in the GOES dataset [116] and the CME parameters taken from the M2M dataset taken from the DONKI online tool [117]. The CME location is given in degrees using the HEEQ coordinate system, with the z-axis coincident with the Sun's axis of rotation and the x-axis lying on the Sun-Earth vector. CME velocity is expressed in km/s. The start date in parenthesis refers to the flare start if different, or in case of missing data in AMS dataset. "Backside" refers to an event that started on the non-visible side of the Sun from Earth, hence no X-ray measurements were available. The wording "N.A" stands for "no association", in case of indecisive or missing flare data. The table continues on next page.

#	Start Date	Flare Class	CME Location	CME Time	CME Speed
22	2013 Oct 11	Backside	S01W106	07:24	780
23	2013 Oct 28	X1.0	N27W80	14:12	1100
24	2013 Nov 02	Backside	N05W145	04:48	1078
25	2013 Dec 28	Backside	S01W101	18:00	769
26	2014 Jan 06	Backside	S03W102	08:09	1275
27	2014 Jan 08(07)	X1.2	S24W30	18:24	2061
28	2014 Feb 25	X4.9	S11E78	01:25	1670
29	2014 Apr 18	M7.3	S34W10	13:09	1400
30	2014 Sep 02	Backside	S10E110	02:36	1140
31	2014 Sep 11(10)	X1.6	N15W15	18:18	1400
32	2014 Sep 25	X4.6	N10E170	21:54	1400
33	2015 Oct 24	N.A.	N.A.	N.A.	N.A.
34	2017 Jul 14	M2.4	S09W40	01:36	750
35	2017 Sep 07(06)	X9.3	S15W23	12:24	1238
36	2017 Sep 12(10)	X8.2	S12W85	16:09	2650
37	2022 Feb 17	C1.4	N07W151	21:24	702
38	2022 Mar 28	M4.0	N07W12	12:09	662
39	2023 Mar 13	Backside	N16E160	03:36	2127
40	2023 Jul 16	M4.0	S29W29	17:53	1155
41	2023 Jul 24	N.A.	N20W24	15:05	1028
42	2023 Sep 01	N.A.	N22W54	03:24	1142

5.2 Polar-pass Event Selection

As stated in the introduction of this chapter, the following selection is aimed to obtain the *polar-pass* SEP flux. The staring point for the polar-pass proton selection is the daily proton selection described in section 4.3. The major change concerns the removal of the requirement for the rigidity of each detected particle to be above the geomagnetic cutoff. The geomagnetic cutoff in AMS is calculated by backtracing particles measured with the detector [69], with their trajectory described by one of the most complete models of the geomagnetic field (IGRF, [62]). Normally, when measuring a determined species in cosmic rays, we want to be extremely careful to only select particles of galactic origin, minimizing as much as possible any contribution from local sources, such as secondaries from interactions and the trapped population inside the magnetosphere. For this reason, the actual rigidity cutoff value is set to be the maximum cutoff value observed, for a given second, inside the full cone of acceptance seen by AMS, causing the loss of possible physical events from directions where the cutoff was lower. Since we are searching for particles of really low rigidity, this choice of cutoff is too conservative, severely limiting our statistics at low rigidity. A simple and elegant solution is to remove the cutoff requirement,

substituting it with a detailed definition of the boundaries of the "SEP-sensitive" regions.

5.2.1 Rigidity Cutoff Alternative

In order to relax the requirement for the measured rigidity to be above geomagnetic cutoff, we have to address the following assumptions:

- The secondary proton population can be neglected, when compared to the SEP flux itself.
- Efficiencies on selection cuts are not affected by orbital changes and are consistent between consecutive orbits.

The primary purpose of the cutoff is to provide a lower limit, above which we are certain to observe only primary cosmic rays (see section 2.2.4). Without the cutoff cut, we are inherently accepting to measure the flux of both primary, secondary and trapped CRs.

We will now proceed to investigate the proton rate without requiring any restriction over the observed cutoff. The rate will be shown for different values of the absolute magnetic latitude $|\theta_m|$, i.e. the latitude in the geomagnetic coordinate system based on the magnetic axis of earth's dipole [118], as sampled by AMS. The flux near equatorial regions, where the cutoff is higher, presents a clear two-component feature, as can be seen in Fig. 5.1. The *second* spectrum, i.e. the population of protons at low rigidity, is entirely composed by secondary and trapped particles [119]. At increasing values of $|\theta_m|$, the two components become progressively mixed, until the shape of the proton rate, hence the flux, is consistent with a single component. The latter observation holds for $|\theta_m| > 50°$. Fig. 5.1 also shows the behavior of the proton rate at peak intensity (around 0.86 GV) for equatorial absolute magnetic latitudes $|\theta_m| < 14°$, were we observe a pure secondary population. The proton rate can be well described by a linear decrease with $|\theta_m|$, showing that secondary protons become less important for magnetic polar regions. Additionally, the rate of secondaries is stable in time even during SEP events and their contribution is negligible with respect to the total flux, being the SEP rate at least one order of magnitude higher than in quiet conditions. These observations are illustrated in Fig. 5.2. In the same picture we show the average ratio between selected counts during an SEP event and the previous quiet day, for the first three rigidity bins and each magnetic latitude interval. This demonstrates that secondary population is stable for magnetic theta lower than 50°, while for higher latitudes the SEP rate is $\sim 800\%$ higher than quiet rate, with only a fraction of the latter being constituted by secondary protons. In conclusion, not only the secondary contribution is negligible during SEP events, but it will be canceled out when applying the background subtraction procedure.

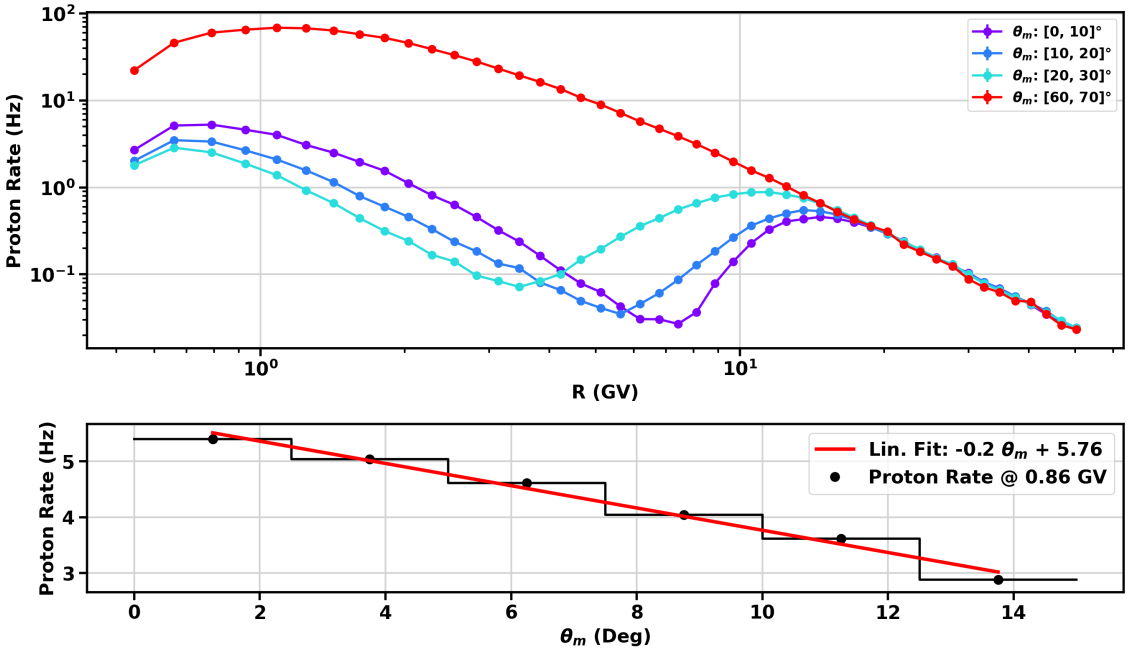

Figure 5.1: **Top:** Picture of the distribution of selected counts, as function of rigidity, for different intervals of absolute magnetic latitude $|\theta_m|$. The values of magnetic theta are taken as absolute values, with $\theta_m = 0°$ at the equator. The distribution is integrated for May 16th 2012, the day before a large SEP event. The two-component spectrum (secondary and primary CRs) is clearly visible for equatorial regions ($|\theta_m| < 30°$), as the geomagnetic cutoff prevents measurements of primaries at the lowest rigidities. Near geomagnetic poles ($|\theta_m| > 50°$), primaries are observed in the whole spectrum. **Bottom:** Proton rate as function of $|\theta_m|$, up to 14°. Within this range, were we observe a pure sample of secondary protons, the rate is linearly decreasing with increasing $|\theta_m|$, confirming that the secondary population decreases towards magnetic poles.

The second requirement comes from the necessity of using the standard daily corrections for the acceptance, instead of integrating the corrections in polar-passes. Possible sources of sub-daily fluctuation of detector efficiencies (and therefore corrections) would be related to their dependencies over the position of AMS along the orbital path, like thermal variations due to Sun exposure or the varying rate of incoming particles. Thermal corrections are already applied when data is pre-processed from raw ntuples to *pass N* ntuples (3.12.1).

The trigger efficiency, as an example, might be deteriorated when dealing with a high rate, due to the worsening of the physical signal given by the plastic scintillators of the ToF. The effects that influence the scintillator signal in extreme rate conditions include:

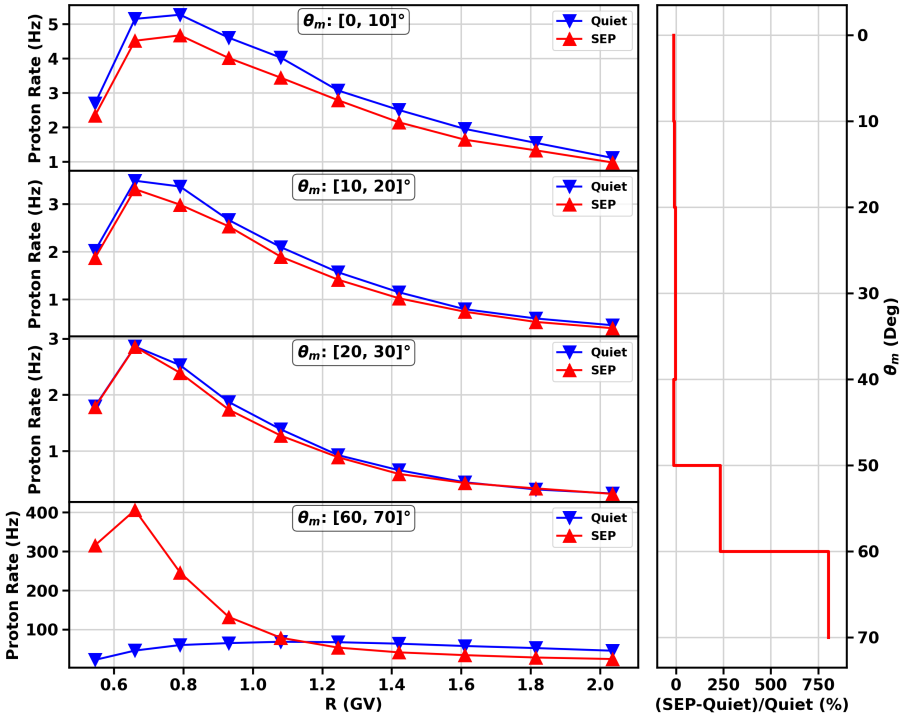

Figure 5.2: **Left:** Distribution of selected counts as function of rigidity, up to 2 GV, for four different $|\theta_m|$ intervals. Each plot contains the comparison between the selected counts during the first day of the SEP event in May 17th 2012 (red) and the previous quiet period (blue). For $|\theta_m| < 30°$, the primary+secondary population is stable in time, not changing even during the SEP event, while at high $|\theta_m|$ the flux is significantly higher at low rigidity, due to the SEP contribution. **Right:** Relative percentage change between the total flux during the May 17th 2012 SEP event and the previous quiet day, averaged over the first three rigidity bins, as function of $|\theta_m|$. This function shows that the secondary population is stable in time (before and during an SEP event) for $|\theta_m| < 50°$, while the total flux dramatically increases for high $|\theta_m|$ (near magnetic poles). In essence, the primary+secondary contribution is negligible during an SEP event and, in any case, can be subtracted by the background-forecasting algorithm since it is stable in time.

- **Pile-up:** The higher the incoming rate of particles, the more likely we can observe two events in the same time frame, effectively resulting in the sum of the two signals. The effective signal width can be broadened by this effect, introducing an uncertainty, and possibly a delay, on the timing measurement.
- **Saturation:** An increased rate can saturate the photodetectors (e.g. PMTs) connected to the scintillator, causing a reduction in amplitude, a distortion or a delay in the signal, due to the unresponsiveness of the apparatus.

A detail study of the rate dependence of our selection efficiencies is still ongoing, but for now we will use the daily-integrated trigger efficiency when constructing the polar-pass flux. We therefore consider a reasonable assumption that the trigger rate will not vary significantly during a single orbit.

In conclusion, the quantities that will be integrated in polar-pass intervals are the number of selected counts and exposure time, while, for the corrected acceptance, we will be using the corresponding daily value. The corrected acceptance is only time dependent due to the corrections, as the geometrical factor remains unchanged. The necessity of using the daily corrections, instead of integrating in polar-passes, is the already poor statistical sample, especially for the trigger correction (see section 4.4.3). Even though we are summing counts and exposure time in specific time frames, that can last between 25 and 45 minutes per day, the choice for the temporal binning of the flux remains the same as in the daily total flux. The daily binning allows to maintain an homogeneous bin size and an easier comparison with other experiments, while the flux is in any case independent from the choice of binning. The rigidity binning also remains unchanged from the daily procedure.

Considering what presented in this section, we think that the described polar-pass procedure can be utilized for the SEP analysis and we will show the results at the end of the chapter.

5.2.2 Polar-Pass Region Definition

The method we chose to define the polar-pass regions takes advantage of the increased trigger rate during SEP events. In fact, during quiet periods, the rate measured by AMS naturally varies between the minimum values at the equator ($\sim$ 400 trig./s), to the maximum observed near the poles ($\sim$ 1000 trig./s, at solar maximum). This daily variation occurs due to the changing rigidity cutoff, which physically rejects more particles at the equator. We can therefore define a threshold on the trigger rate during quiet periods, which will be necessarily exceeded only during an SEP event, identifying the time and angular intervals in which SEPs can be observed. Fig. 5.3 shows the distribution of the trigger rate in two consecutive days, where, in the latter, an SEP event occurred. We define as threshold the trigger rate value at 1% of the maximum value observed in the distribution (y-coordinate). After calculating the trigger rate threshold in this way, we build a two-dimensional histogram in geographical longitude and latitude, filled with only events which recorded a higher trigger rate than the set threshold, during an SEP event. An example of this map is shown in Fig. 5.4. The map of the *above-threshold* regions is then used in the proton selection to obtain a polar-pass integrated proton flux.

For each SEP event, a specific map is constructed, in order to take into account any

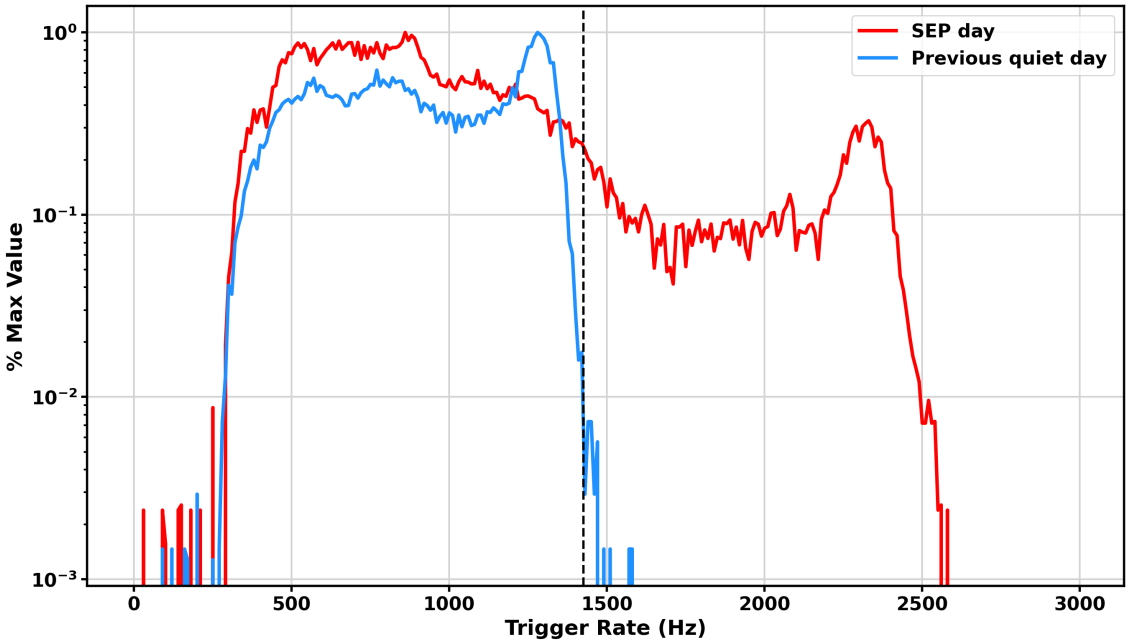

Figure 5.3: The distribution of the total trigger rate during an SEP day (red) and the previous quiet day (blue). Both distributions are normalized to the corresponding maximum. The black dotted line in the picture represents the threshold value of the trigger rate, during the previous quiet day, corresponding to 1% of the maximum value in the distribution (1% on the y-coordinate). We are therefore assuming that this threshold will be exceeded only during the SEP event.

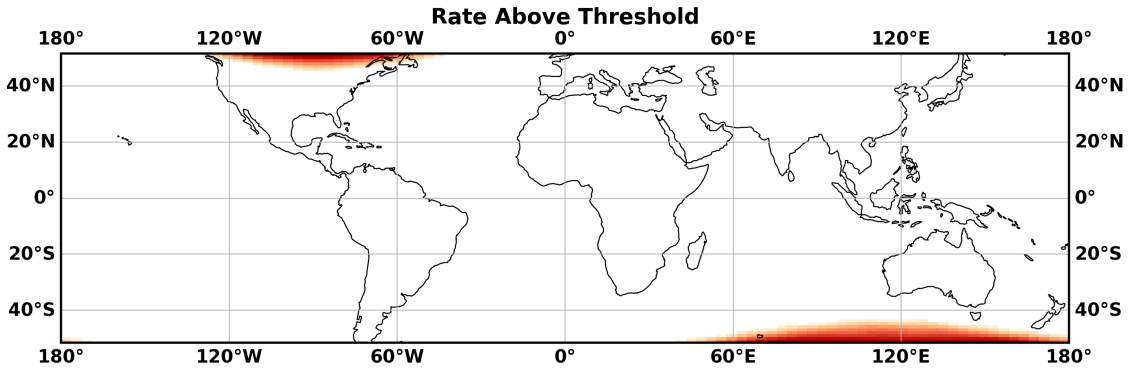

Figure 5.4: The geographical latitude-longitude map built with only recorded events with a trigger rate above threshold. This map defines the *polar-pass* region for each SEP event and is used to perform the proton selection for the corresponding event. The small regions translate into an extremely reduced fraction of exposure time for AMS to detect SEP events, which is about 45 minutes per day.

local change in the geomagnetic conditions. For the same reason, the distribution of the trigger rate during quiet periods is, in fact, averaged over 20 days, centered on the start of each event, with the contribution from days corresponding to SEP events removed.

5.3 CR Background Subtraction

The main difficulty in separating solar protons from those originated outside the solar system, during an SEP event, is that there is no independent observable measured by AMS that could be used for their discrimination. In principle, the incoming direction of the high energy population that arrives at the onset could be anisotropic, as we will discuss in the last chapter, but this assumption does not hold in every case; furthermore, it would not be considered a consistent separation criterion. The key concept, in our approach, in solving this issue is to consider the daily proton flux as a collection of similar time series at different rigidity, more than a collection of rigidity spectra at different times. Our ultimate goal is to forecast the GCR component of AMS fluxes during SEP events, in a data-driven approach, starting from the quiet flux before the onset of the event. In this way we would have an estimate of the background that will be subtracted, during the event, to obtain the SEP-only flux.

5.3.1 Rigidity to Energy Conversion

In order to facilitate the comparison of the products of this analysis with other similar measurements, as rigidity is rarely used in solar physics experiments, we decided to convert our flux measurements expressed in rigidity (GV) into kinetic energy (MeV). The conversion is simply derived from the expression of the total and kinetic energy for relativistic particles (in natural units, $c = 1$):

$$T = E_{tot} - m_p = \sqrt{p^2 + m_p^2} - m_p \tag{5.2}$$

where E_{tot} is the total energy of the proton, T is the kinetic energy, found by subtracting the rest energy ($m_p c^2$) from E_{tot}, p is the momentum and m_p the proton mass. Using the definition of rigidity we can substitute the momentum inside the expression of kinetic energy, obtaining the transformation from rigidity to kinetic energy:

$$p = R\,Z \implies T = \sqrt{R^2 Z^2 + m_p^2} - m_p \tag{5.3}$$

For the variables that depend on rigidity, such as flux, we must consider the Jacobian of the transformation:

$$\frac{d\Phi}{dT} = \frac{d\Phi}{dR}\left|\frac{dR}{dT}\right| = \frac{d\Phi}{dR}\frac{T+m_p}{R} \tag{5.4}$$

While converting from rigidity to energy, we also divide the flux by 10000, to express the flux per units of cm^2, instead of m^2, as the usual units of measurements for the particle flux are: particles/(cm^2 sr MeV s).

5.3.2 Proton Flux as Time Series

When we first tackled the problem of predicting the galactic background flux, during an SEP event, we started by looking at the energy spectrum during the quiet days that preceded the event. In this approach though, the only way to produce a reliable prediction was to use either a model of the spectrum and fit it at high energy (such as the Force Field Approximation [120]), where there is no SEP contribution, or to describe the quiet spectrum with an empirical function (such as a spline fit) and "adjust" it during the SEP event. In either case, we are forced to rely on an external model, which inherently introduces additional sources of systematic uncertainty.

The approach we are going to illustrate has the strength of being data-driven, exploiting all the tools developed for the well known and multidisciplinary problem of *time series forecasting*. We are in fact viewing the proton flux as a time series and, using its properties, building an iterative procedure to predict its future values at all the energy intervals of interest. There are two fundamental observations upon which this approach is based:

- The value of proton flux, at any given day, is significantly correlated to the value of the previous day.
- The SEP contribution to the total flux becomes negligible at energies higher than ~ 2 GeV.

The first point derives from the *autocorrelation* analysis performed on the flux versus time at a given energy. Autocorrelation is a commonly used test in time series analysis, in order to ascertain the degree of dependence between the sampled values of a signal [121]. It is often quantified as correlation between the analyzed function and the same function shifted by a discrete amount called *lag*. In the case of the daily flux, the lag corresponds to a shift of one day. Fig. 5.5 pictures the autocorrelation function for the daily proton flux as function of lag, together with the 95% confidence interval for a significant correlation (calculated using the *Statsmodel* package, [122]). The plot shows that the flux, at any given day and energy, is correlated to the value of the previous day, with an autocorrelation factor of $\sim 63\%$. In other words, the

flux during quiet periods, hence the GCR background flux, can be expressed as follows:

$$\phi_{BG}(t,\, E) = N(t) \times \phi_{BG}(t\text{-}1,\, E) \tag{5.5}$$

Where $\phi_{BG}(t,\, E)$ is the GCR background flux on day t and in the energy E, $\phi_{BG}(t\text{-}1,\, E)$ is the CR background flux on the previous day and same energy and $N(t)$ is the time dependent normalization factor. Note that the normalization factor is dependent on the current day t, since we are essentially adjusting the previous value of flux to the current conditions of solar modulation and other short-term phenomena that impact the measured flux.

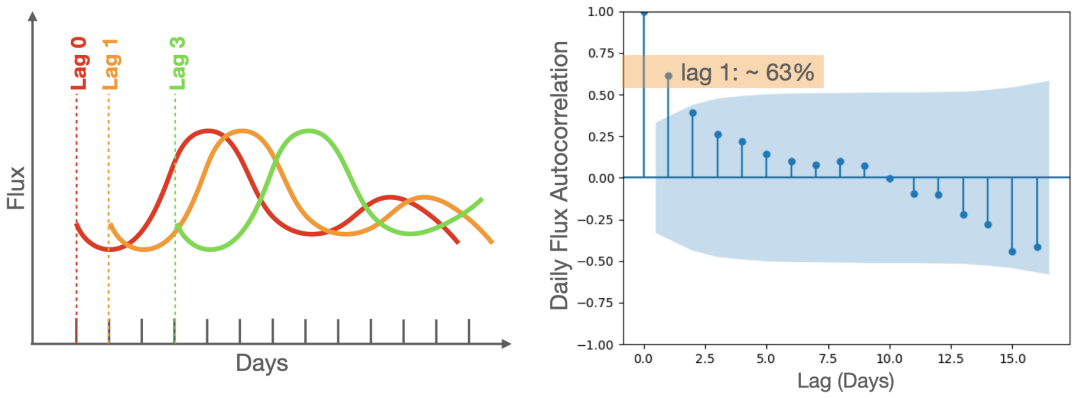

Figure 5.5: **Left:** Concept of *lag*, given a time series. In the case of the daily proton flux, we indicate as *lag n flux* the flux forward-shifted by n days. **Right:** Autocorrelation of the daily proton flux as function of lag. This plot shows that the proton flux, at a given energy and day, is correlated at $\sim 63\%$ with the value of the previous day.

The next step consists in finding the normalization factor using only information that is not influenced by the presence of the SEP, considering that $N(t)$ should include the effects of solar modulation and possibly Forbush Decreases, but not the contribution of the SEP itself. The second point in 5.3.2 is fundamental for this purpose. Fig. 5.6 shows an example of daily fluxes during an SEP event, where the flux in different energy intervals is presented. Notably the flux in the first four energy intervals $E < 433MeV$ are only accessible with the polar-pass integrated flux, corresponding to a rigidity $R < 1GV$. As the picture demonstrates, the flux at energies higher than ~ 2 GeV is unaffected by the presence of the SEP, but crucially still shows the short term variation of solar modulation, which is independent from the SEP. We will then use the flux at higher energies to calculate the normalization $N(t)$ for the lower energies and estimate the background flux. In Fig. 5.6, the start of the SEP event is denoted by the label *Day 1*.

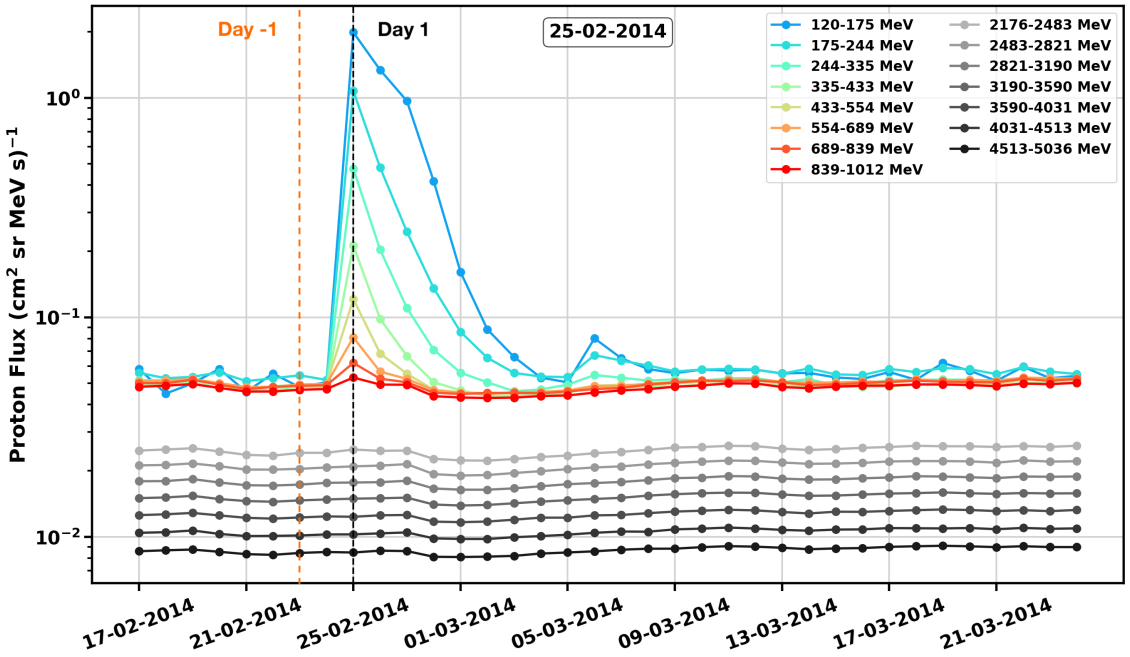

Figure 5.6: Total daily proton flux (GCR background and SEPs) during the SEP event on 25 February 2014. Colored data points show the flux for the first seven energy bins of the analysis, in the range [120, 1012] MeV. Points in gray represent the flux at higher energy, in the range [2176, 5036] MeV. While at the lowest energies the SEP contribution is evident, at higher energies the contribution is almost null. We define as *Day 1* the first day in which we find a significant increase due to SEPs, *Day 0* as *buffer* day in which there could be an undetected increase and *Day -1* the starting point for the GCR background subtraction procedure (quiet flux).

The formulation of the background flux in Eq. 5.5 allows us to forecast the flux in an iterative way (see also Fig. 5.7 as reference):

- We select one of the tags given by the SEP Finding Algorithm as the start of an SEP event on *Day 1*.
- *Day 0* is considered to be a *buffer* day, in which there might be an undetected increase due to SEP.
- At *Day -1*, in which the flux is considered to be only background (GCR), we start the forecasting procedure by initializing the background flux value to the measured flux.
- We forecast the background flux $\phi_{BG}(t,\, E)$ for *Day 0* using Eq. 5.5.
- $\phi_{BG}(t+1,\, E)$ for *Day 1* is then calculated starting from $\phi_{BG}(t,\, E)$, scaled by the normalization $N(t+1)$.

- the previous step is repeated until *Day n*, defined as the first day in which our background prediction is compatible with the measured flux and the SEP event has ended.

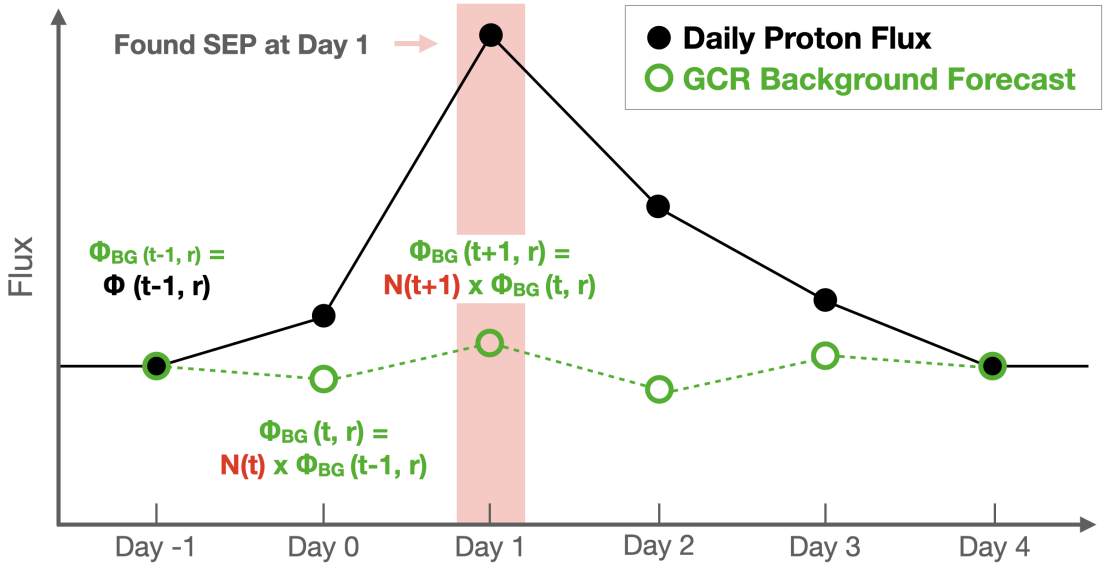

Figure 5.7: In this schematic, the logic of the background subtraction procedure is presented. In the picture, a sudden increase connected to a SEP event was tagged on *Day 1*. The GCR background flux, represented in green, is initialized to the quiet value (measured flux, represented in black) of *Day -1*, which is then used as *previous day flux* for the forecasted background of *Day 0*. This process is repeated until the background prediction is compatible with the total measured flux.

5.3.3 Background Normalization

As for the calculation of $N(t)$, instead of using directly the flux, which would be still affected by the long term trend of the solar activity cycle and short to mid term periodicities of the sun rotation [109], we opted to introduce a new parameter specifically created for this purpose. We called this new parameter $\rho(t, E)$ and defined it, for every energy interval, as the ratio of the flux during a given day and the flux during the previous day, as pictured in Fig. 5.8.

This parameter is useful in our case for two properties:

- **Stationarity on the long term**: It removes the long and mid term trends, while maintaining the time dependence of short term variations (such as solar modulation and Forbush Decreases). The ρ parameter is, in fact, equivalent to the introduction of the "I" component in SARIMA models [123] and used for the same purpose.

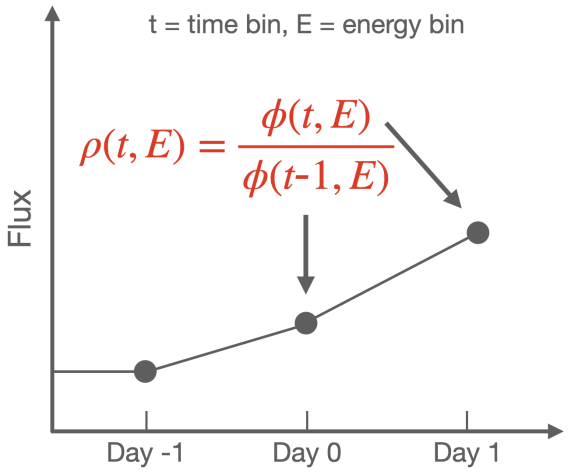

Figure 5.8: Definition of the $\rho(t,\ E)$ parameter used for the calculation of normalization. ρ is defined as the ratio of the flux in a given day and the flux in the previous day. The functional form of the ρ parameter is created by evaluating the ratio for every day t and energy interval E.

- **Energy independence**: Being a ratio over the same quantity, during quiet periods $\rho(t,\ E)$ is automatically normalized to 1, in all the energy intervals.

A picture of the $\rho(t,\ E)$ parameter versus time, for two different energy bins of the analysis in the period 2011 to 2018, is drawn in Fig. 5.9. The total polar-pass flux is also shown in the same energy bins, in order to appreciate the stationarity and rigidity independence of $\rho(t,\ E)$ on the long term.

The $\rho(t,\ E)$ parameter, for the SEP event presented earlier in this chapter, is shown in the plots in Fig. 5.10. These plots give a clear look at how the $\rho(t,\ E)$ parameter shows a similar time dependence for all the energies presented, while the sudden increase due to SEP is present only for energy intervals below 2 GeV. We decided to calculate the normalization factor $N(t)$ as the average of seven bins, in the energy interval [2176, 5036] MeV, also shown in Fig. 5.10 in the bottom plot.

The normalization factor and Eq. 5.6 can then be rewritten as follows:

$$\begin{aligned} N(t) &= <\rho(t)> = \frac{1}{7}\sum_{r=10}^{17}\frac{\phi(t,\ E)}{\phi(t\text{-}1,\ E)} \\ \phi_{BG}(t,\ E) &= <\rho(t)>\ \phi_{BG}(t\text{-}1,\ E) \end{aligned} \tag{5.6}$$

As mentioned before, the same $N(t)$ is multiplied to the background flux for all the first seven energy bins, thanks to energy independence of the $\rho(t,\ E)$ parameter.

In conclusion, we decided to forecast the background flux of galactic origin, for

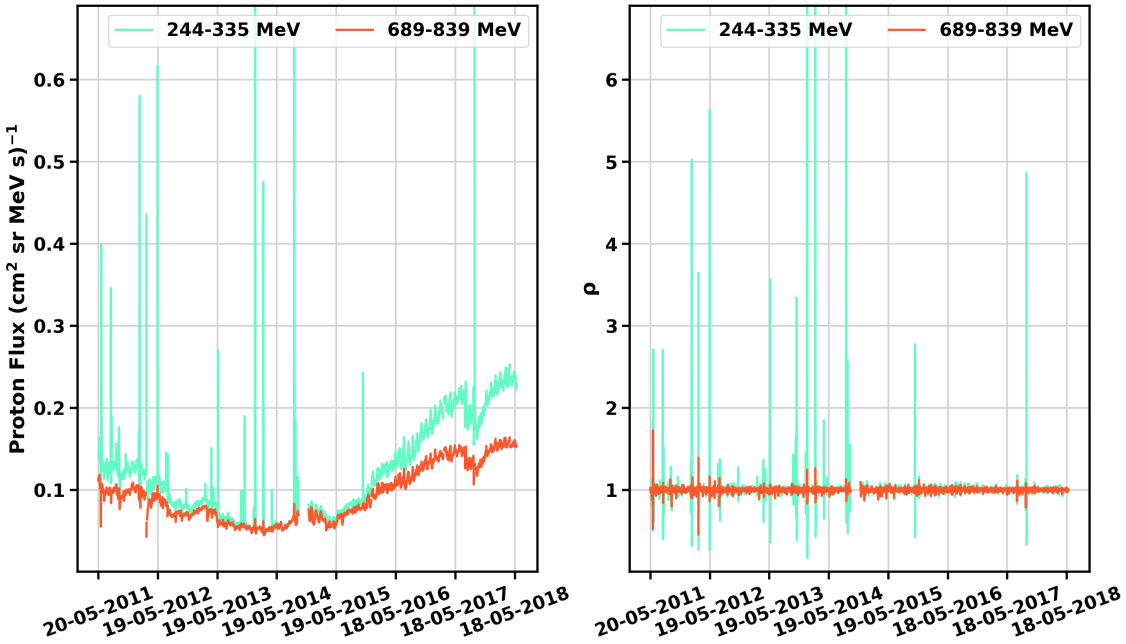

Figure 5.9: **Left:** The total flux for two energy bins of the analysis from 2011 to 2018. Multiple features are visible in correspondence of SEP events, especially at the lowest energy. **Right:** The $\rho(t, E)$ parameter as function of time for the same energy bins. This plot shows that $\rho(t, E)$ is, with respect to the flux, stationary (long term trends are suppressed) and energy independent on quiet conditions, while the sudden increases due to SEP events are preserved. Colors are coherently chosen to match the same energy bins in future and past pictures of proton flux, spectra or the ρ parameter.

each energy interval and SEP event, in a data-driven approach. The value of GCR background is propagated forward, starting from two days before the onset of the SEP event, in an iterative way. The background flux value, at any given day and energy, corresponds to the value of the previous day multiplied by a normalization factor, calculated as the average of $\rho(t, E)$ over a specific energy range. The energy range is defined as the lowest energy range for which AMS does not detect SEPs, in order to encapsulate all the effects of usual solar modulation, but not the SEP contribution. The SEP-only flux is the result of the subtraction of the forecasted background flux from the total measured flux, as described in detail in the next section.

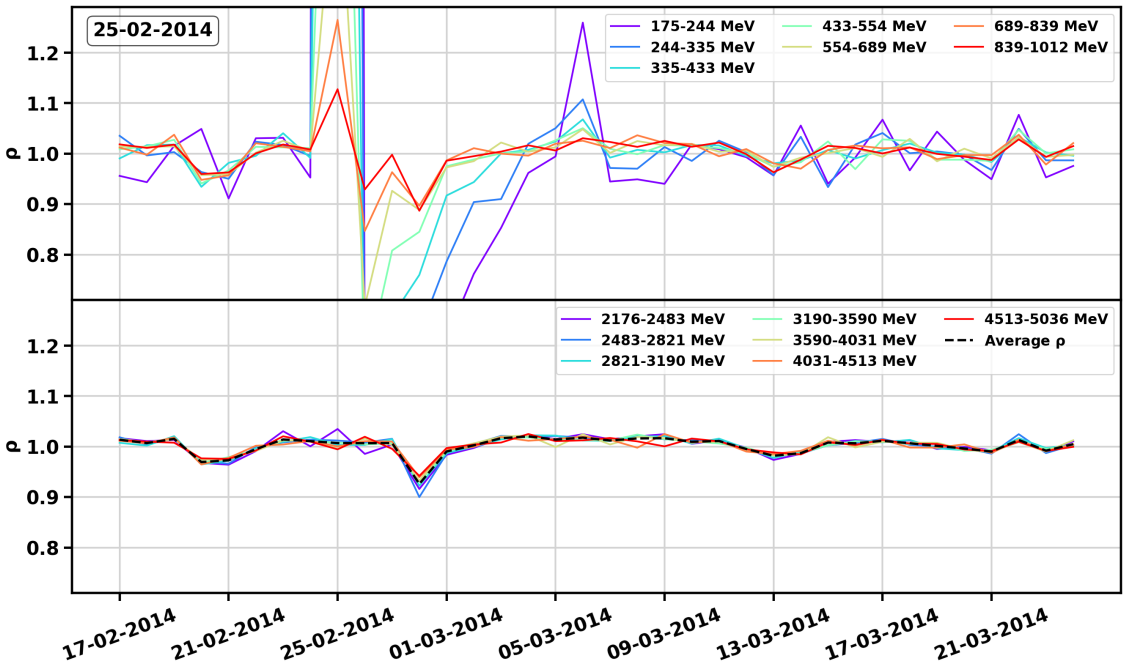

Figure 5.10: The parameter ρ, defined in Fig. 5.8, is represented in this plot for different energy ranges and for the SEP event occurred on 25 February 2014. On the top half of the plot, ρ for the first seven energy bins (up to 1 GeV) clearly encapsulates all the short term dependencies due to solar modulation, Forbush Decreases and SEPs. On the bottom half, ρ between 2 and 5 GeV is still presenting the effects of short term variation, but the SEP contribution is negligible. The bottom half shows also the average of ρ in the seven high-energy bins, which is used as normalization factor in the background subtraction procedure.

5.3.4 GCR Subtraction Systematic Uncertainties

The final step in the SEP flux estimation is to subtract the GCR background from the total flux, in order to obtain the SEP-only daily proton flux, with polar-pass integration. Once we calculate the background flux $\phi_{BG}(t,\, E)$ with the appropriate normalization, the daily SEP flux is simply given by:

$$\phi_{SEP}(t,\, E) = \phi_{TOT}(t,\, E) - \phi_{BG}(t,\, E) \tag{5.7}$$

The $\rho(t,\, E)$ parameter used to calculate $\phi_{BG}(t,\, E)$, in the energy interval [2176, 5036] MeV, captures the mid to short term variation due to solar activity, however the low energy proton flux shows a greater daily random variability, traceable to the statistical noise of the lowest energy measurements. This noise will propagate into a larger uncertainty on the forecasted background and on the SEP-only flux at low energy. To asses the uncertainty on our estimation, as we use the $< \rho(t) >$ to forecast the subsequent days in low energy intervals, we will calculate the relative ratio between the forecasted background and the measured flux during quiet periods. In absence of SEP events, in fact, we know a priori the value of the galactic background, as it coincides with the measured flux. The relative ratio is defined as follows:

$$\Delta\Phi_{quiet} = \frac{\Phi_{BG}(t, E) - \Phi(t, E)}{\Phi(t, E)} \tag{5.8}$$

Where $\Phi_{BG}(t, E)$ is the forecasted background and $\Phi(t, E)$ is the corresponding measured value.

The first step in this calculation consists in creating a "SEP-removed" daily proton flux, eliminating 5 days before and 15 after the start each SEP event from the complete dataset. The SEP-removed flux and ρ are shown in Fig. 5.11. For each quiet day of the newly built flux, and for the first seven energy bins, we forecast the background for seven days, as we would normally do during an SEP event. A distribution of the relative ratio between forecast and measurement is then constructed for every energy and day of prediction since *Day -1*. These distributions are shown in Fig. 5.12 (for the first five days of prediction).

Fig. 5.12 shows that the relative ratios follow a normal distribution, confirming the random nature of these displacements. The relative uncertainty, concerning the forecasted background flux, is given as the standard deviation of each distribution. The standard deviation of the $\Delta\Phi_{quiet}$ increases with decreasing energy, as expected, while we observe a slight increment for consecutive days of prediction. Notably the σ is quite large for the for the first energy interval, being approximately 14% of the forecasted background. The total uncertainty is computed via standard propagation of errors with the uncertainty of the total polar-pass flux, according to Eq. 5.7.

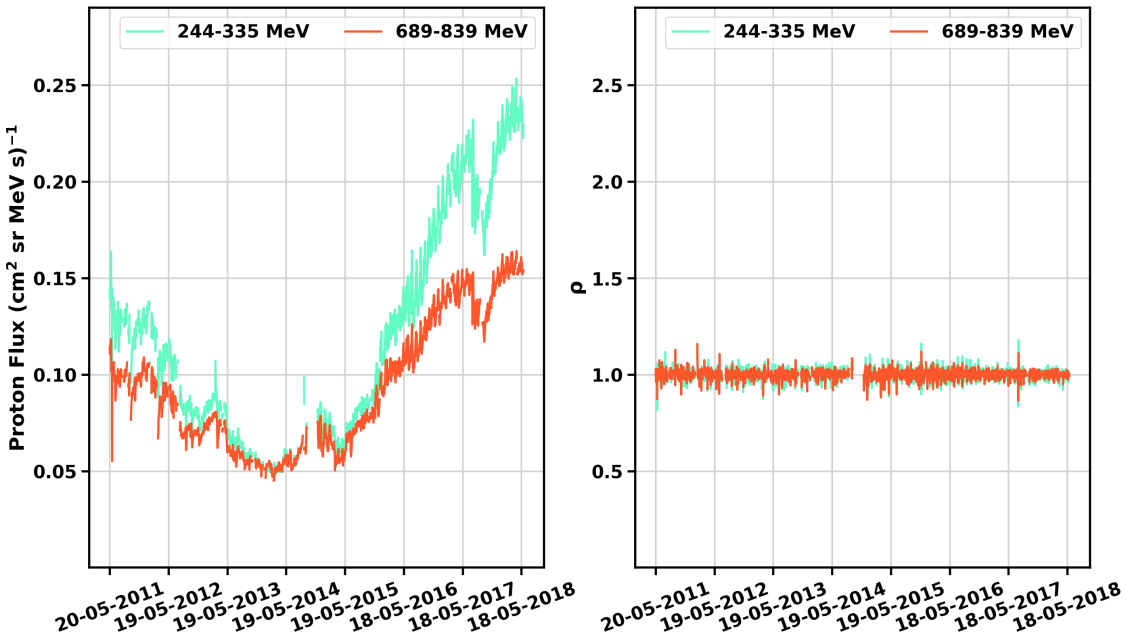

Figure 5.11: Same figure as Fig. 5.9, but each SEP event has been removed by cutting 5 days worth of data before and 15 after the start of an event. This separate dataset was built to evaluate the systematic uncertainty due to the subtraction procedure. For each day and energy interval of this dataset, the background was forecasted up to 7 days, while the relative ratio between the prediction and the measured value was computed.

Therefore, since the total flux can increase by more than one order of magnitude with respect to the quiet baseline, the uncertainty due to background estimation does not exceed 1%. If we take the event in Fig. 5.6 as example, the relative uncertainty due to background estimation for the energy bin 120 - 175 MeV would be 14% of the quiet level, which is around 0.05 $P/(cm^2\, sr\, MeV)$. Considering that the final background-subtracted proton flux would be around 2 $P/(cm^2\, sr\, MeV)$, the relative uncertainty due to background subtraction, with respect to the SEP-only flux, would be calculated as:

$$\epsilon_{BG} \simeq \frac{0.14 \times 0.05}{2} \simeq 0.004 \tag{5.9}$$

This is a rough estimate of the uncertainty for the first energy bin, which characterized by the highest variance, in the case of a strong SEP flux measured by AMS (with an increase of over one order of magnitude from the quiet level). This uncertainty will of course vary depending on the intensity of each SEP event, being less prominent the more particles we observed during the event.

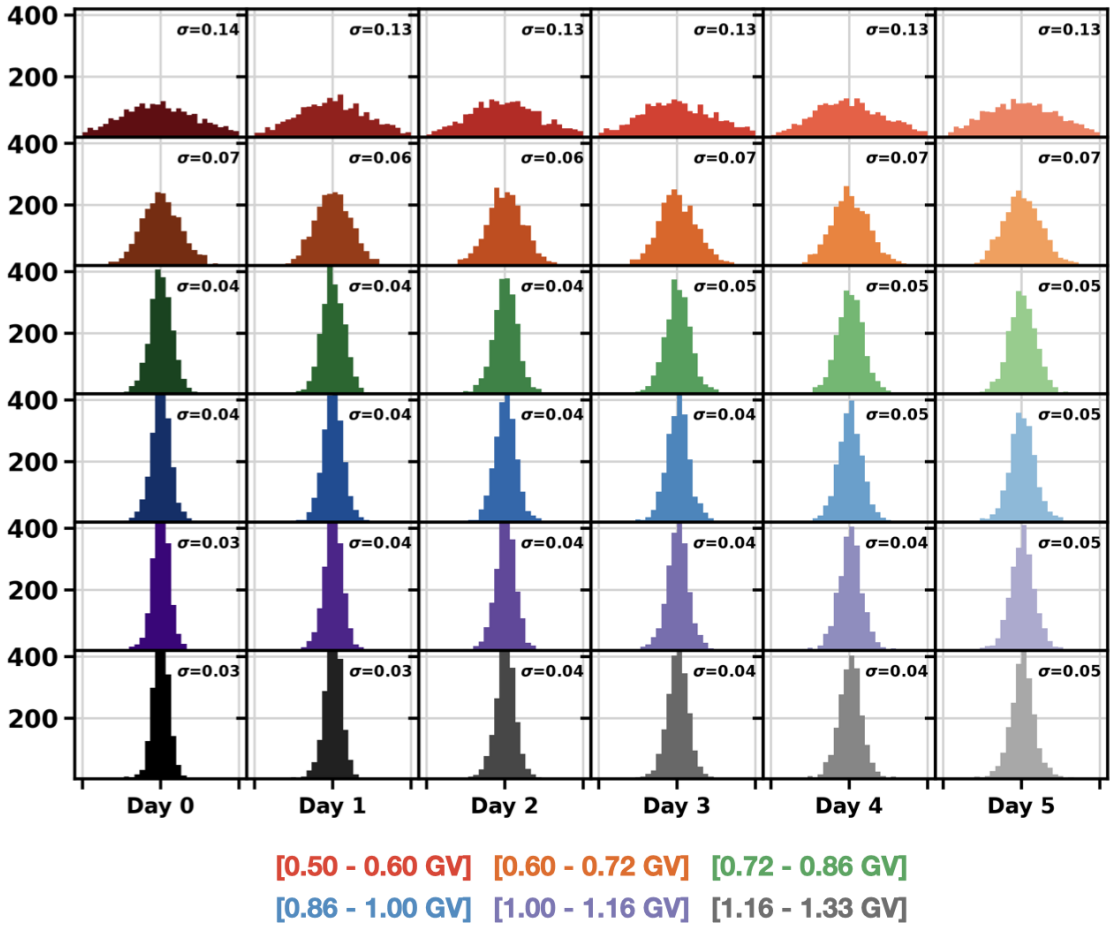

Figure 5.12: Distributions of the relative ratios between forecasted background and measured values $\Delta\Phi_{quiet}$, calculated over the SEP-removed dataset. Different colors (rows) indicate the distributions for different energy intervals, while columns point to distributions for consecutive days of prediction. The standard deviation is reported on the top left of each plot, which is used as relative systematic uncertainty for the forecasted background.

5.4 Polar-Pass SEP Fluxes and Spectra

The procedure described in section 5.3.4 is systematically applied to all the events found with AMS, as shown in Tab. 5.1. For a considerable portion of the events listed in the table, AMS could detect a significant increase in the lowest energy bins, although it was not possible to construct a meaningful spectrum due to the lack of a higher energy contribution. All the events with a significant increase on less than three energy bins will not be shown in this work, but we will denote their presence in the list. The interpretation of the spectra and their variation in time will be given in the next chapter, accompanied by a complete spectral analysis of the events presented here.

The first example of SEP spectrum, pictured in Fig. 5.13, comes from one of the most interesting and all-round SEP events found with AMS data. The event started on February 25th 2014, within the peak of the solar maximum of cycle 24. At first glance, the spectra seem to follow a power law distribution, typical of non-thermal processes, but a few features catch the eye. The firs one, which is visible for the entire duration of the event, is the presence of a faster decrease of the intensity at higher energy, denoting a deviation from a power-law. On the other hand, looking at the temporal behavior, we can observe the intensity of the flux decreasing systematically with time, except at the lowest energy interval, where it seems to increase and reach a maximum after the onset. The physical implications of these observations will be discussed in the next chapter, but they might be connected to the underlying type of acceleration process and the spatial distribution of the accelerated particles. The same behavior was matched by another event in the same year, on September 2nd 2014, which lasted two days more and showed a slightly higher intensity at its peak value, but presented compatible features to the previous one (shown in the same picture).

Aside from the previous two events and a double-peaked event on January 6th 2014, all the other events observed with AMS lasted at most three days, even though some of them showed higher intensities than the above mentioned events. An example of short-duration event is shown in Fig. 5.14, which started on May 17th 2012. Excluding the observations on the temporal evolution, these events share the same spectral shape as the previously presented events. As discussed in [124], another distinctive property, separating the two long duration events in 2014 from the shorter kind, is the complementary observation of x-ray flares on the eastern limb of the Sun, in contrast to the shorter events that mostly shown connected flares on the western limb. These source regions are considered to be poorly magnetically connected, given the spiraling structure of the Sun's magnetic field [125], but the high intensity of the event allowed for a sustained observation of SEPs over time.

Notably, there are two events that were excluded from this dissertation, due to their

exceptional intensity and for which we have only partial covering with the AMS dataset. These two events happened on March 7th 2012 and September 6th 2017, with associated flares of class X5 and X9 respectively (the most intense x-ray flares of solar cycle 24), and were subject of multiple publications (among which [126] and [127]). Both events were actually a combination of multiple subsequent solar flares with SEP emission: the September 6th event was, in fact, followed by another strong emission on the 12th, which is actually the only one partially recorded by AMS. In the case of AMS, the increased rate during these events - up to several orders of magnitude higher than the baseline - caused the livetime fraction of the detector to be nullified, incapacitating the detection of particles during most of the duration of the event. In these two cases, we were able to record only the final days and not the spectrum at peak intensity. For this reason, we decided to exclude these two events from our analysis and inspect them further separately.

In conclusion, after subtracting the galactic cosmic background component from the total measured flux, we obtained the SEP spectra for many of the solar events found with AMS data. The spectra show different interesting aspects, both in the energy and temporal domain, such as a drop in the flux intensity at the highest energy intervals and an uneven decay in time for the lowest energy interval. All these aspects will be further inspected in the next chapter, where we try to find an empirical model to describe the spectral shape, denoting the temporal evolution of its parameters.

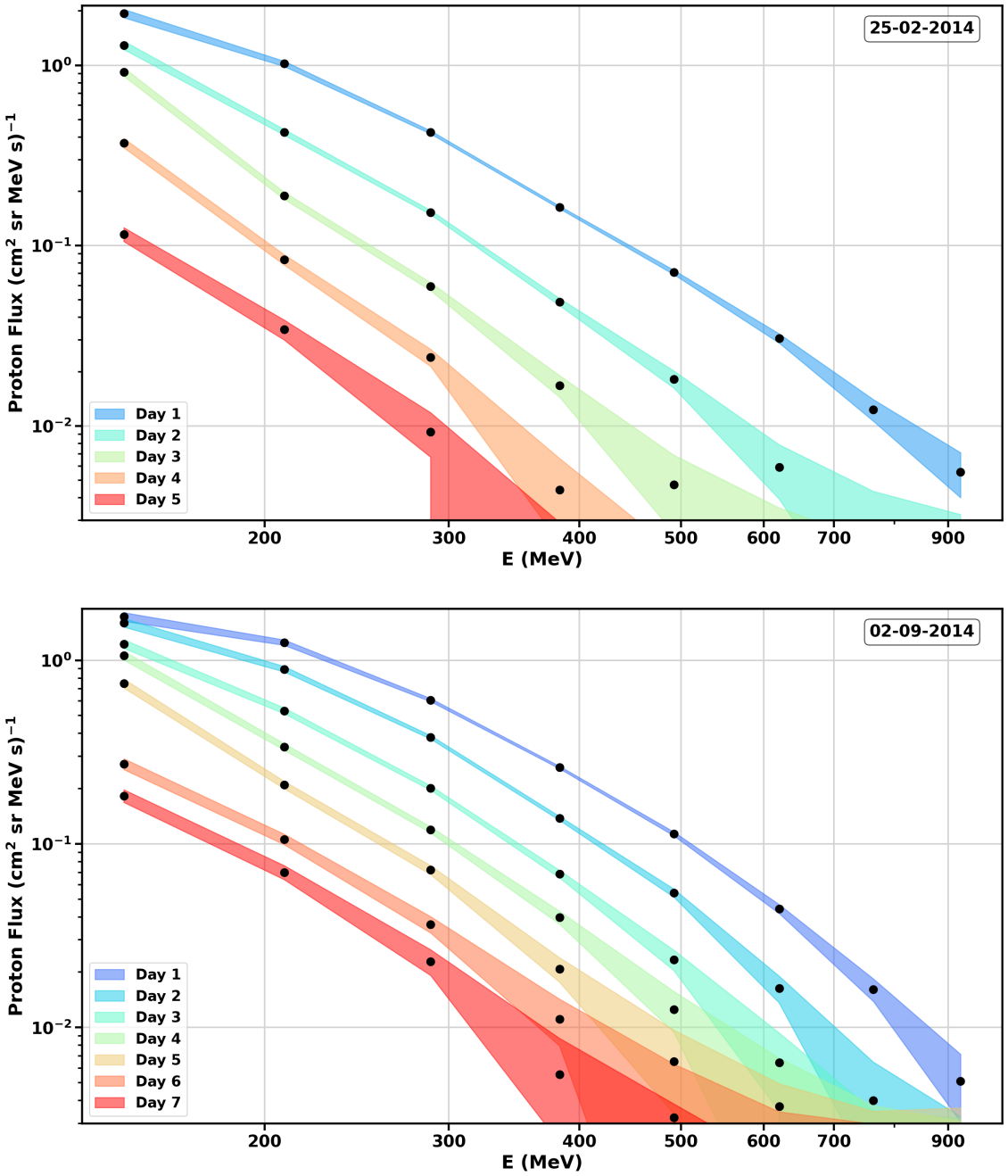

Figure 5.13: Energy spectra, for five consecutive days, during the SEP events started on February 25th (top) and September 2nd 2014 (bottom), after subtraction of the forecasted galactic background. The scale is logarithmic on both axes. In this view, the spectrum appears to be generally described by a power law distribution. However a clear downtrend in the energy profile, consistent for all the days, and a different temporal behavior at the lowest energy interval are visible. These patterns are almost perfectly matching between the two events.

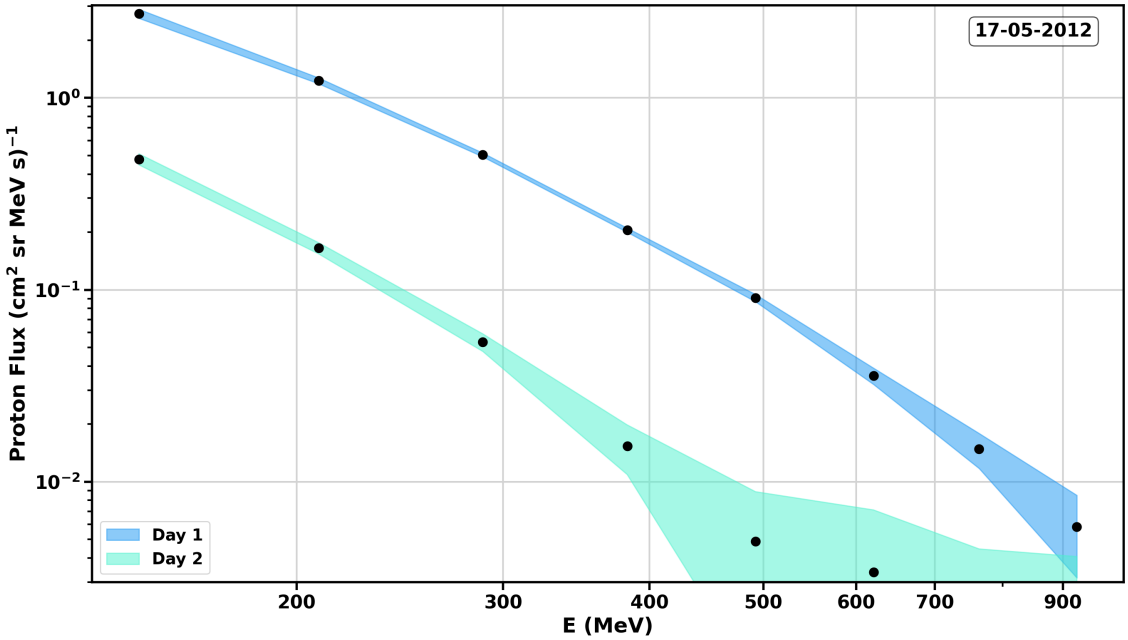

Figure 5.14: One example of the many short duration SEP events recorded with AMS. The spectral shape seems to be coherent with the one observed for the longer events, while their decay over time is faster. Most of the short duration events were significantly higher than the quiet baseline for just one or two days, which is not sufficient to infer any properties on their temporal evolution.

Chapter 6

SEP Fluxes Interpretation

The uniqueness of AMS contribution, in the context of SEP analysis, lies in the availability of precise measurements at the GeV range, allowing to describe the spectrum of even the highest particles accelerated by the Sun. This information is extremely valuable to infer a distinction between effects of acceleration and transport of particles from the SEP spectra, since high energy particles, well magnetically-connected to Earth, should show negligible diffusion between production and arrival at Earth. At those energies, particles are either scattered and change direction, or we can measure them at Earth without any significant disturbance and energy loss over their path [124]. The higher their Lorentz factor, the less impact will the multiple scattering with interplanetary medium have on their trajectory and energy.

The first section of this chapter is dedicated to the characterization of each SEP spectrum measured with AMS, for the day corresponding to their peak intensity, using an empirical model that will describe our observation. In the second section we will study their temporal evolution. The evolution of the SEP spectral index over time within the same solar event, combined with the comparison between AMS and GOES [116] fluxes in the time domain, led us to observe of a peculiar phenomenon on the lowest energy interval, providing a distinctive marker for *gradual* SEP events.

6.1 SEP Spectra at Peak Intensity

As introduced in section 1.5, there is still an open debate over the role of the two main mechanisms responsible for accelerating charged particles during SEP events [128]. Solar flares are often associated with jets and the initial phase of CMEs. These phenomena are thought to be coincident with the acceleration of charged particles via *magnetic reconnection*, as the trapped plasma in the Sun's magnetic field is suddenly released, while field lines of opposite direction merge. A second

acceleration mechanism is the *diffusive shock acceleration*, which is thought to be driven by the shock front generated when a CME traverses the heliosphere. In addition to the two different acceleration mechanisms, which might coexist if they both play a role in SEP events, the effects of CR transport inside the heliosphere must also be taken into account when analyzing the SEP spectra. All these effects can be associated to peculiar spectral features in the final measured flux, which might be difficult to isolate, considering the multitude and variability of phenomena that interact with those particles. The temporal evolution is also important, as different mechanisms act on different timescales, while the differences in particle transport might affect the decay time and shape of these events.

6.1.1 Features in the SEP Spectra

The complexity of such spectra is clearly discussed in [127], where the authors analyze multi-spacecraft proton data, in order to capture the features described above. The Advanced Composition Explorer (ACE) and GOES-13 datasets were combined to obtain SEP spectra for the events registered in September 2017, which is the set of solar proton events with the highest intensity ever observed in the 24th solar cycle. The authors initially relied upon the *Band function* [129], originally conceived for gamma-ray burst (GRB) spectra, to interpret the SEP spectra as a double-broken power law with a smooth transition (Eq. 6.1).

$$\Phi_{\mathrm{Band}}(E) = \begin{cases} AE^{-\gamma_a} \exp\left(-\frac{E}{E_0}\right) & \text{for } E < (\gamma_b - \gamma_a)E_0, \\ AE^{-\gamma_b} \left[(\gamma_b - \gamma_a)E_0\right]^{(\gamma_b - \gamma_a)} \exp(\gamma_a - \gamma_b) & \text{for } E \geq (\gamma_b - \gamma_a)E_0, \end{cases} \tag{6.1}$$

The Band function has four free parameters: the amplitude A, the two spectral indices γ_a and γ_b and the break energy E_0. With this model, the authors observed a break energy between 2-6 MeV for the less intense events and about 34 MeV for the most prominent event of September 10th. The break energy is either interpreted as the limit of diffusive shock acceleration [128] or as effect of interplanetary transport [130] [131].

An additional feature that might be present at higher energies is an exponential rollover, which is often associated to the spatial and temporal boundaries in models of the CME shock front, leading to particle loss; more information about this topic will be given in section 6.1.2. In order to take into account this prediction, the Ellison-Ramaty (E-R) function [132] was introduced and used to describe the spectrum at high energy (Eq. 6.2). Due to the complexity of these spectra, the authors decided to finally trust a combination of the two functions as the spectral fit of choice, as reported in Eq. 6.3.

$$\Phi_{\text{E-R}}(E) = AE^{-\gamma} \exp\left(-\frac{E}{E_r}\right) \tag{6.2}$$

$$\Phi_{\text{tot}}(E) = \Phi_{\text{Band}}(E) \exp\left(-\frac{E}{E_r}\right) \tag{6.3}$$

Fig. 6.1 shows the ACE and GOES spectra for September 10th 2017, fitted with both the Band function and the combination of Band and Ellison-Ramaty. The observation of an exponential rollover represents a constrain over the two models that describe the measured SEP spectra as either modulated by shock-front acceleration or by transport effects. This study, however, offered an indecisive conclusion about the existence of this feature, given the large uncertainty of GOES measurements at those high energies.

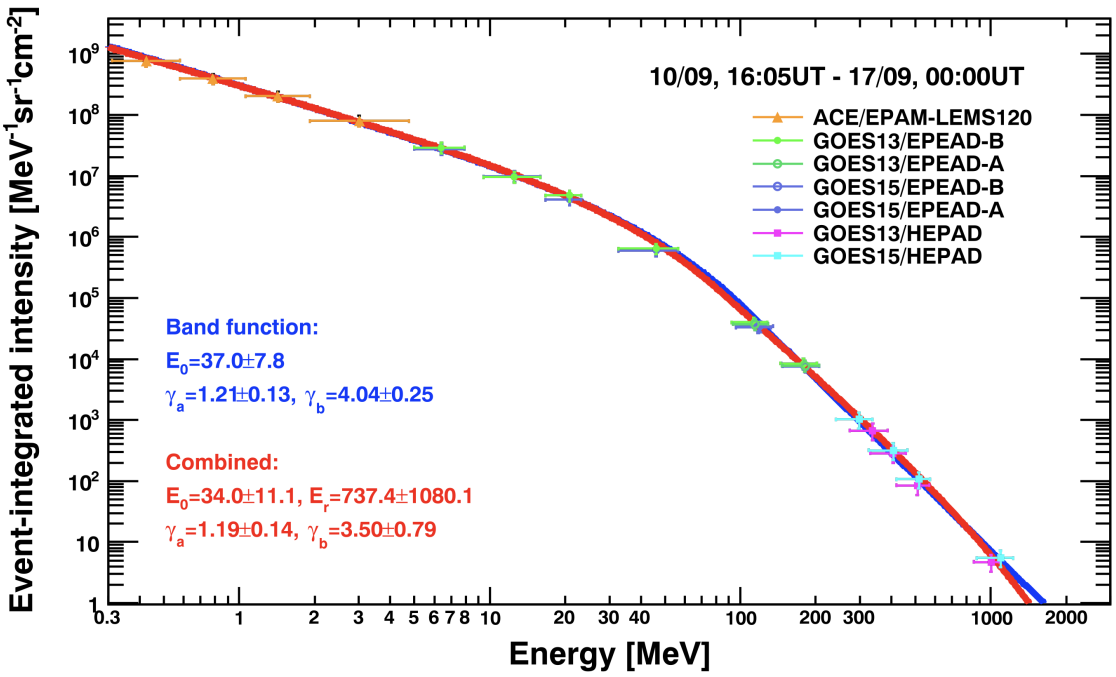

Figure 6.1: This figure, taken from [127], shows the spectral fit of the combined measurements of ACE and GOES-13 for the SEP event of September 10th 2017 and in the energy range [0.3, 1000] MeV. Total uncertainties are shown as vertical error bars, while the horizontal bars denote the energy range of each measurement. The fit is performed using the Band function (blue), and the combination of the band function with the Ellison-Ramaty (red). In both cases, the spectral fit well describes the break in the power law; however, due to the large uncertainties in the GOES high energy measurement, the presence of an exponential rollover is not significant.

6.1.2 Spectral Fits with PAMELA

Additional contribution in the study of SEP spectra in the mid-to-high energy transition (between 80 MeV up to a few GeV), which represents a benchmark for our analysis, is provided by the measurements of the Payload for Antimatter Matter Exploration and Light-nuclei Astrophysics (PAMELA) [124]. PAMELA (ended in 2016) and CSES-HEPD [133] (2018-2022) are currently the only experiments that were capable of measuring SEP fluxes at such energy intervals and with high precision in space, providing a fundamental connection between the low energy of space weather experiments (KeV-MeV interval) and the neutron monitor data, which can measure the ground level enhancements (GLE) at energies above the GeV. CSES-HEPD and the updated payload HEPD-02 on board the satellite CSES-02 [134] both provide measurements in the energy range 2-200 MeV. The mid-to-high energy transition coincides with the energy interval where AMS can provide measurements of SEP particles, starting from 200 MeV, which is approximately the minimum detectable energy due to its internal magnetic field, up to the high energy limit of the SEP spectrum. PAMELA measurements start at a relatively high energy of 80 MeV, which is above the measured break energy found so far for SEP spectra. The authors of [124], in fact, mention that the function used to describe the behavior at high energy reduces from the double-broken power law to the sole Ellison-Ramaty single power law with exponential rollover (Eq. 6.2). Fig. 6.2 shows two example of the performance of this fit, as compared to the model with a single power law. This fit is performed on the fluence of each SEP event, i.e. the time integrated flux intensity over the interval in which PAMELA observed a flux above threshold. Notably if two SEP events are consecutive, the fluence of the second event might encompass the decay tail of the first one.

Similar spectral fits where performed for a total of 26 events and the results are consistent with the diffusive shock acceleration scenario. There are two major factors that favor this interpretation: the first is a consistent observation of a power law with exponential rollover, considered a marker of CME shock with limited spatial and temporal extension; the second is the correlation between the peak intensity of the events and their exponential cutoff, which appears to be higher for events that show greater peak intensity. The physical interpretation of the exponential rollover might include multiple factors that deteriorate the acceleration efficiency, among which we mention the following:

- Spatial extension of the shock: as the shock propagates towards the external heliosphere, particles are accelerated at higher energy while the diffusion coefficient in the equation of CR transport [135] increases. At some point the size of the shock front will be comparable to the particle diffusion length, leading to an exponential particle loss [132].
- Time-limited shock acceleration: the shock front provides an efficient acceler-

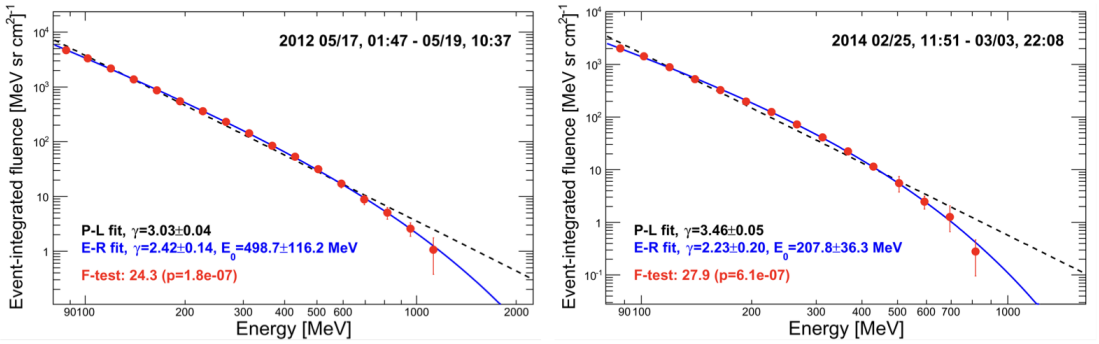

Figure 6.2: The figure shows two examples of fluence measured with PAMELA for the SEP events of May 17th 2012 (left) and February 25th 2014 (right) [124]. The dashed black line represents a simple power law fit, of which is reported, in the same color, the estimation of the spectral index γ, while the blue solid line represents the fit performed using the Ellison-Ramaty function, with γ and rollover energy E_0 reported as free parameters. In both cases, the spectral fit clearly favors the hypothesis of an energy rollover.

ation site, but it takes time to accelerate particles up to a certain energy, after which there is a cutoff. Each shock has its own lifetime, leading to different maximal energy of accelerated particles [136].

- Dispersion of turbulent magnetic field: The turbulent magnetic field across the shock front is fundamental to accelerate particles, as its fluctuations provide the centers of scattering that propagate particles back and forth the shock front, gaining energy after each interaction. The strength of these fluctuation decreases over time, limiting the maximum energy reached by particles [27].

Clearly all the factors described above, playing a role in the phenomenology of exponential rollovers in SEP spectra, are intertwined and describe the same phenomenon on different levels of detail. Therefore many studies seem to agree over the conclusion that the presence of an exponential rollover, or cutoff energy, is a clear indication of diffusive shock acceleration of solar particles.

6.1.3 Spectral Fits with AMS

After producing the background-subtracted SEP fluxes and spectra with AMS, analyzing the whole current AMS dataset (between May 2011 and October 2023), we decided to perform a similar spectral fit analysis as in [124]. Using the Ellison-

Ramaty function (Eq. 6.2), a subset of nine SEP spectra were fitted and compared with the two simpler asymptotic models, i.e. single power law (Eq. 6.4) or a simple exponential decay (Eq. 6.5). The subset was chosen among the SEP events that showed the higher flux intensity measured with AMS; most of the weakest events, in fact, currently have large estimated uncertainties and a reduced energy extension, which prevent the discrimination of the best fitting model between the Ellison-Ramaty and its asymptotic limits.

$$\Phi_{\mathrm{PWL}}(E) = AE^{-\gamma} \tag{6.4}$$

$$\Phi_{\mathrm{EXP}}(E) = A \exp\left(-\frac{E}{E_r}\right) \tag{6.5}$$

Many of the events detected with AMS had a duration of one day, which was enough to compute a single spectrum; for a subset of the most energetic, though, the detection lasted for multiple days, up to seven for the February 25th 2014 event. During the analysis presented in the current section, we first performed a fit with the three models over the spectra at peak intensity for each SEP event. In the next section we will present the same procedure applied to each spectrum of the long duration events, extending the measurement performed at peak intensity. As introduced in chapter 5.4, the March 7th 2012 and the 11th (10th) September 2017 events showed such a high intensity flux that the *livetime* of the detector was reduced to almost zero. The most interesting days at peak intensity of these two events are missing, hence a dedicated analysis is needed and will follow this work.

Fig. 6.3 shows the fit performed with the three empirical models for the SEP events of May 17th 2012 and February 25th 2014. The first is an example of the many short duration events, lasted only two days from the AMS perspective, while the second is the first of the two longer events. The spectra for both events seem to follow a very similar behavior, as in either case the optimal function to empirically describe them is the Ellison-Ramaty. This observation holds, in general, for all the events in the analyzed subset, which are shown in B. The chosen criterion to determine the goodness of the fit is the reduced chi-squared test. The fit function for the power law and the exponential models have two free parameters while the Ellison-Ramaty has three. Being the fit performed over the first eight energy intervals (following the rigidity binning in A), the number of degrees of freedom for the E-R fit is five.

The spectral index for the two events is estimated to be, respectively, $\gamma = 1.77 \pm 0.14$, for the short duration event, and $\gamma = 1.63 \pm 0.42$ for the longer duration event. As for the exponential rollover, the estimated energy is $E_r = 260 \pm 31$ and $E_r = 236 \pm 69$. Among the analyzed subset, the spectral index spans between 0.3 and 3.5, while the rollover energy is roughly comprised between 120 and 330 MeV, albeit many of the

estimates are given with huge uncertainties. This last issue is the primary reason for choosing a reduced subset over all the available SEP events. AMS measurements, in fact, start at about 150 MeV, with only one energy bin below 200 MeV, due to the large statistical fluctuations of the lowest energy measurements. According to the physical description of shock acceleration given in the previous section, less intense SEP events show an exponential rollover at lower energy, in fact sometimes even lower than the first measured energy interval with AMS. Therefore our data has, in most cases, little to no leverage arm to provide a robust prediction of the power law behavior, as we already are inside the exponential regime of the spectrum.

On the other hand, for the high intensity events shown in this section, our result is in good agreement with PAMELA results over SEP fluences and peak intensity fluxes [124]. There is evidence for an exponential rollover at high energy which seems to suggest a diffusive shock acceleration mechanism actively accelerating particles at high energy.

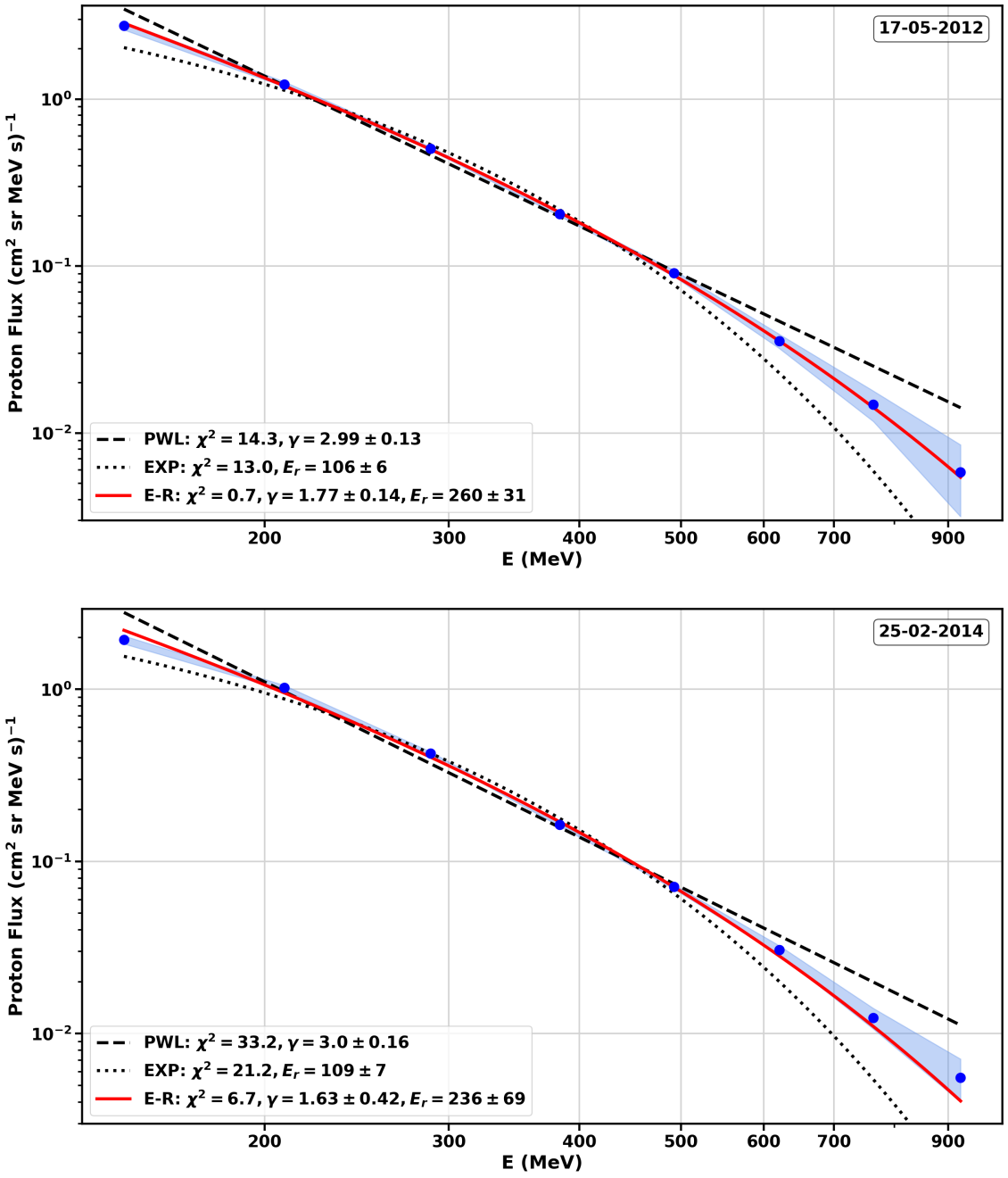

Figure 6.3: The two plots show the spectral fits performed at peak intensity for the May 17th 2012 and February 25th 2014 SEP events on AMS data. The red solid lines represent the fit performed with the E-R function, while the black dashed and dotted lines correspond to the power law (PWL) and exponential (EXP) asymptotic limits, respectively. As shown in the bottom left panel, the E-R function is, in both cases, the best model to describe the AMS data, confirming the hypothesis of a rollover energy above 200 MeV.

6.2 Temporal Evolution of SEP Events

So far we analyzed the spectral shape at peak intensity, but thanks to the daily integration of the polar-pass fluxes we can perform a spectral fit for each subsequent day of an SEP event, not only for the spectrum at the peak day. In this section we will extend the procedure described in 6.1.3, in order to fit the spectra for all the days of the long duration events found with AMS, focusing on the temporal evolution of the spectral index. We will then complement this analysis with the comparison between AMS polar-pass fluxes and the same quantity measured by the GOES observatory, which will give us precious information about the nature of *gradual* SEP events.

6.2.1 Evolution of the Spectral Index

In addition to the natural decay of the flux intensity, from which we infer the decreasing rate of the strength of shock waves, changes in the spectral shape can suggest different acceleration mechanisms and transport effects in the interplanetary medium. For example, a faster decrease in intensity for higher-energy particles (shift in the rollover energy), might be interpreted as a decline in the efficiency of particle acceleration. This effect is what we typically expect in the diffusive shock scenario, where the maximum energy at which particles can be accelerated decreases over time, following the deterioration of the shock front conditions. On the other hand, particles with lower energy will take more time to arrive at Earth, since they are more affected by multiple scattering with the interplanetary medium. In other words, an hypothetical observer placed near the acceleration site would measure a spectrum that decreases in intensity over time, with a faster decrease at high energy. If the observer is positioned farther, they would measure a spectrum that actually increases at lower energy, relatively to the higher energy, on top of the diminishing rollover cutoff, since slower particles will be detected in later times.

As introduced in 5.4, there were only two good candidates of long duration events measured by AMS in solar cycle 24, for which we have enough coverage both in time and energy, in order to perform this analysis. Fig. 6.4 shows the temporal evolution of the spectral fit, performed with the Ellison-Ramaty function (defined in Eq. 6.2), for all the five days of the SEP event started on February 25th 2014 and seven days of September 2nd 2014.
The same picture shows also the temporal evolution of the spectral index γ and rollover energy E_r; in both cases the index increases over time, reaching a maximum on the third day for the first SEP event and on the fifth day for the second. This phenomenon can be traced back to the transport effect described in the previous paragraph, as the spectral softening reflects the long temporal delay between the arrival of high energy and low energy particles.

Notably the rollover energy E_r, which we expected to be steadily decreasing, follows a similar increase as the spectral index, especially for the SEP event of September 2014. However, as observed in [124], there is a significant cross-correlation between the two fit parameters: spectral index and rollover energy. The spectral softening at low rigidity and the receding rollover energy make so that the fit with the E-R function approaches the asymptotic limit of single power law for subsequent days. We must also consider that fewer data points, with larger uncertainties, are available to perform the fit the more we depart from the start of the event. All things considered, the E-R fit can capture qualitatively the spectral softening due to transport effects, but it is not sufficient to measure the rollover energy with enough accuracy in later days.

The two long duration SEP events presented in this chapter are a clear testament of the complexity of SEP spectra and the interplay between acceleration mechanisms and transport effects. In our observations, the features in the AMS data are consistent with a shock front accelerated population of particles, with a strong delay in the less energetic portion, possibly due to poor magnetic connection between the source and Earth. To investigate further the low energy increase and verify the presence of a delayed low energy peak, we decided to complement the AMS measurements with a dataset from another detector in space: the GOES observatory [116].

There are many other interesting aspects that might be worth investigating with AMS data about the temporal evolution of SEP events, for example taking advantage of the precise angular resolution of the detector. Among these, we acknowledge the following:

- Degree of anisotropy: faster, high energy, particles tend to drift closely along the extending magnetic field (having a shorter Larmor radius), undisturbed by drift effects. On the other hand, the low energy portion of accelerated particles can be severely affected by multiple scattering, tending to drift. With a differential analysis on arrival direction, AMS could measure the anisotropy of the proton flux over time, providing information over particle diffusion and distribution of magnetic field lines.
- Temporal delay in particle emission: combining the arrival time and velocity measurement of the highest energy SEPs measured by AMS with the starting time of the original x-ray flare, we could infer the possible time delay between the flare and the start of the acceleration process.

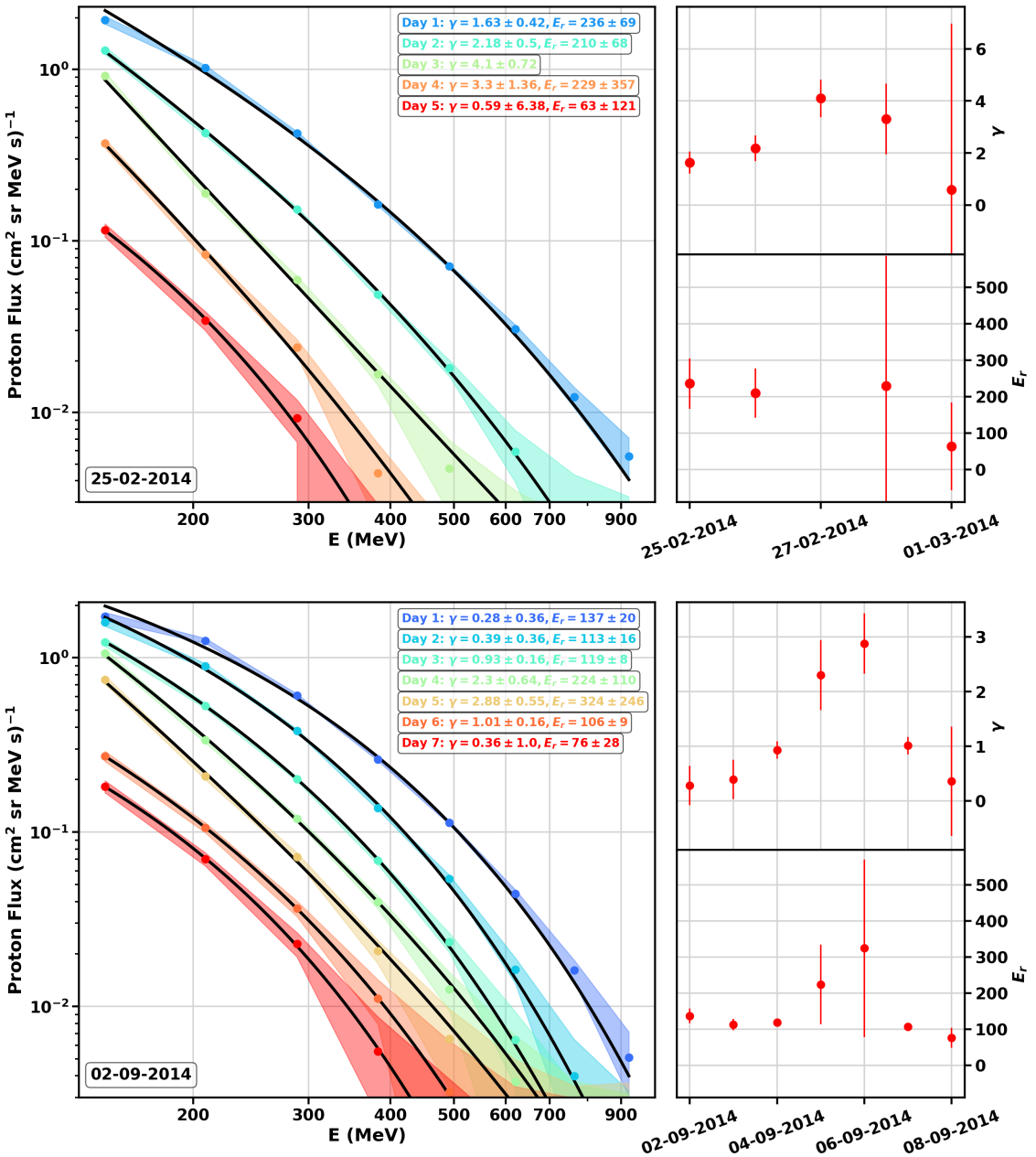

Figure 6.4: Temporal evolution of the spectral fit for the SEP event started on February 25th 2014 (top) and September 2nd 2014 (bottom). Colored dots and bands represent the measured SEP flux and total uncertainty with AMS, while solid black lines represent the fit with the E-R function. The fit parameters are reported on the top left with matching colors. The right subplots show the temporal evolution of the spectral index γ (top) and rollover energy E_r (see text for the interpretation).

6.2.2 Comparison with GOES Fluxes

As we observed in the previous section, the temporal profile of the SEP spectra for long duration SEP events shows an increase only at low energy. We suspect that this phenomenon might be related to the delayed arrival of slower particles at Earth. To test this hypothesis we decided to form an equivalent dataset, using GOES data, integrating the 5 minute averages from its SEM/EPS (energetic particle detector) [116] within the daily intervals used for AMS. A direct comparison is difficult to produce, given that AMS is located in a Low Earth Orbit at about 400 km from the surface, while GOES satellites are positioned in geostationary orbits above the eastern and western regions of America, at about 37000 km of altitude. The geomagnetic conditions are, in fact, quite diverse: AMS is well within the influence of the magnetosphere, while GOES is near the boundary of the magnetopause, where the geomagnetic rigidity cutoff is infinitesimal.

Fig. 6.5 shows the qualitative comparison between AMS and GOES daily fluxes. GOES extends the AMS measurement with four additional intervals in the range from 4.2 MeV to 82 MeV. In the first two bins, below 15 MeV, we observe a consistent increase in the proton flux, reaching a maximum at three and four days after the onset of the two events, respectively. These maxima are in correlation with the peaks observed in the spectral index evolution estimated in the previous section. As we expected, the start of the SEP event coincides with the arrival of the fastest and most energetic particles accelerated by the shock front, while the slower population is gradually delayed over time, depending on their energy.

Additionally the flux exhibits a sharp increase on the first day, followed by a more gradual rise over the subsequent days; this feature is particularly visible in the February 2014 event, being almost absent in the September 2014. A possible interpretation involves a first population of particles accelerated by an impulsive source, such as magnetic reconnection, injected directly into the outward extending magnetic field lines, drifting almost undisturbed until they reach Earth. The September 2014 event might not exhibit the initial sharp increase because it was a backside event, therefore not directly connected to Earth; the gradual population could then be explained by the slower acceleration from the widespread CME shock front.

Fig. 6.6 shows the comparison between AMS and GOES for the SEP event of May 17th 2012. We consider this event as "short duration" because we did not observe a gradual increase in the low energy intervals, not even in GOES data. The spectral softening is still present, but less pronounced than in the longer events presented earlier. In fact, the increase we observed for the long duration events is not present in any of the shorter kind, suggesting a better magnetic connection between source and Earth.

Tab. 6.1 shows the longitude and latitude of the CME source, as reported in the

M2M catalog and accessed via the DONKI online tool [117], together with the linear speed. The angular measurements are expressed in the HEEQ coordinate system, with the z-axis coincident with the Sun's axis of rotation and the x-axis lying on the Sun-Earth vector. In contrast to what one would expect, the long duration events were not produced by slower CMEs. On the other hand, the two long duration events were originated in the south-east limb, while the short event taken as example was emitted on the south-west. The latter is true for most of the short duration events measured by AMS.

Start Date	Latitude (deg)	Longitude (deg)	Speed (km/s)
2012 May 17	75	-10	1500
2014 Feb 25	-78	-11	1670
2014 Sep 02	-120	-10	1400

Table 6.1: Latitude, longitude and linear speed for the main CME connected to the three SEP events examined in this section. The long duration events of 2014 are not correlated to a slower CME speed with respect to the short duration event of 2012. There is, however, a connection with the original source location of the CME. Data taken from the M2M dataset at [117].

This observation is consistent with the result in [125], also shown in Fig. 6.7, where the author describes the various distributions obtained at different longitudes. An observer that sees the CME shock front propagating on its east side will be connected later to the magnetic field lines that encompass the CME, where the initial population is accelerated. The eastern observer, which sees the shock arriving from the west limb, will be well connected to the source, observing a fast rising flux and an immediate decay.

Other interesting aspects arising from the comparison with GOES include: the presence of a precursor event between five and seven days prior the long duration event, seen only at the lowest energies, and the less intense events that may follow the main peak in the proton flux. In general, strong solar events are seldom isolated: an active region capable of accelerating particles at the GeV range produces multiple subsequent events, remaining active for several days and up to one month.

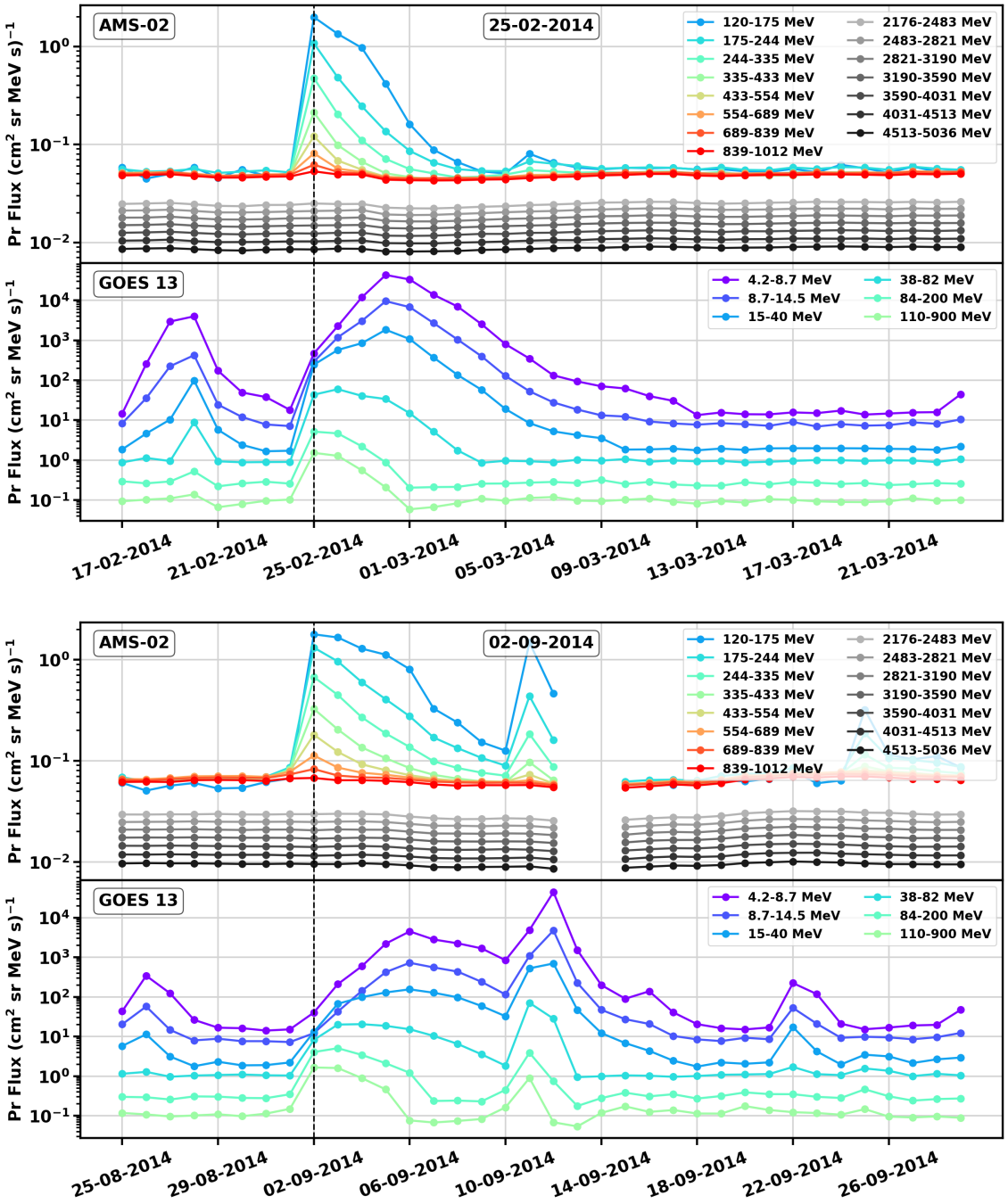

Figure 6.5: Comparison between daily fluxes measured by AMS during the course of this work (top half panel) and the GOES 13 averages in the same time period (bottom half panel). The top plot shows the flux for the SEP event started on February 25th 2014, while the bottom one shows the event started on September 2nd 2014. GOES measurements extend the observation at lower energies, with four additional bins from 4.2 MeV to 82 MeV. A gradual increase after the onset is observed, in both cases, for particles with energies below 15 MeV.

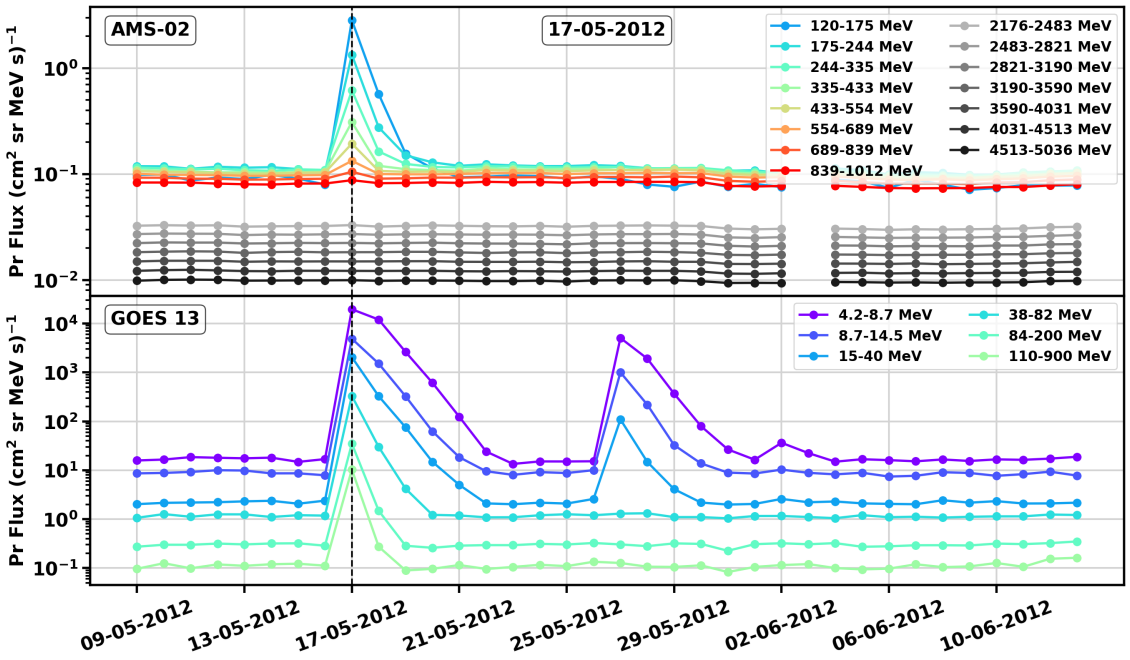

Figure 6.6: Comparison between daily fluxes measured by AMS and GOES 13 averages for the May 17th 2012. In contrast to what observed in Fig. 6.5, this event exhibited a fast increase followed by an immediate decay, resulting in an overall shorter duration.

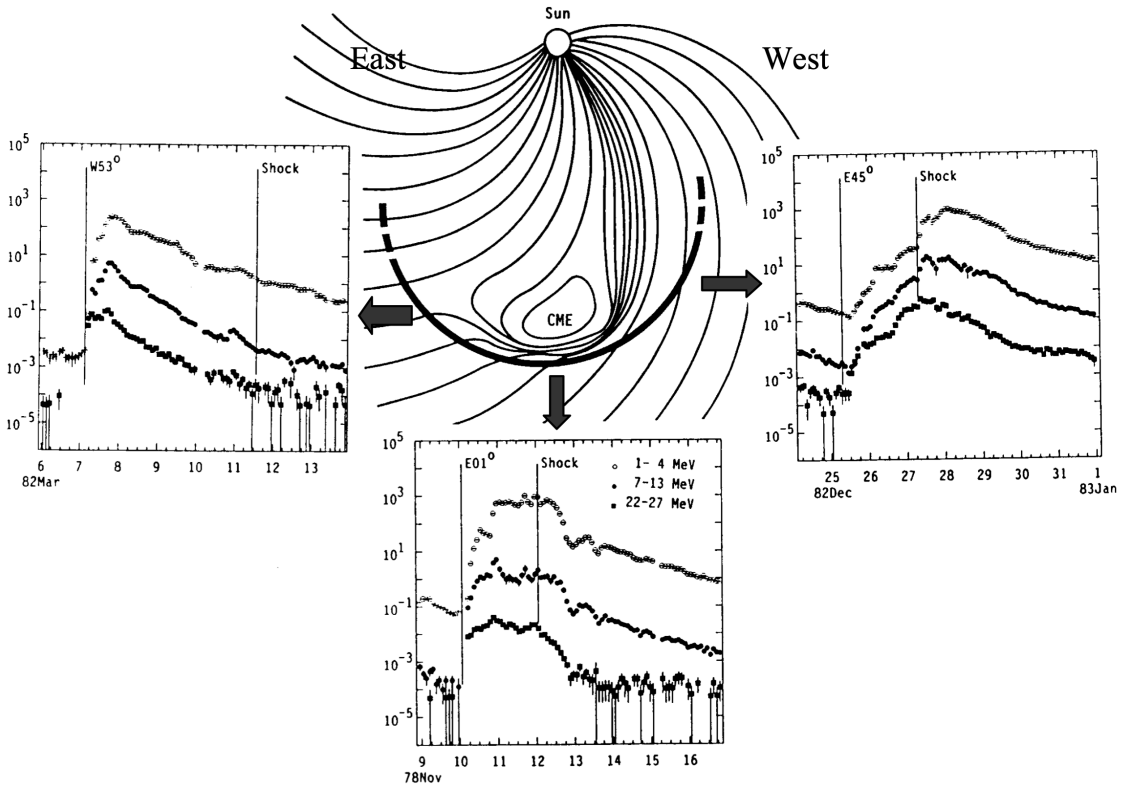

Figure 6.7: Three SEP flux intensity distributions, observed on three different longitudes relatively to the shock front propagation. The eastern observer, seeing the CME on its west side, is well connected to the source. The distribution measured in this case will indicate a sharp rise with a slower decay. The western observer, seeing the CME on its est side, will be initially poorly connected to the source and it will measure a steady increase until the shock front meets the magnetic field line that connects it to the source. Image taken from [125], see reference text for more details.

Chapter 7

Conclusions

The first chapter of this thesis was dedicated to the introduction of the physics of charged cosmic rays, the particles that we analyzed during the course of this work. We presented a brief historic summary of their discovery and the various techniques used to probe them. We then described their characteristics, focusing on the different classes of CRs, from the highest energetic ones, originated in galactic sources, to the low energy but intense flux of the solar component: the solar energetic particles. We also discussed the two main mechanisms which are commonly thought to accelerate them during solar transient events: magnetic reconnection and diffusive shock acceleration.

In the second chapter we briefly introduced the context of our case study: the solar system. We described the fundamental details about the Sun's internal and external structure, the heliospheric magnetic field and its interaction with the geomagnetic field on Earth. We also gave a detailed description of the magnetosphere of Earth, with its trapped particles populations and the magnetic reconnection that accelerates particles towards polar regions during solar storms. The effect of solar storms on Earth are one of the primary concern in space weather studies for human activities in space and satellite operations. We finally introduced the concept of *geomagnetic rigidity cutoff*, fundamental in understanding our analysis.

In the third chapter we described in detail the experiment, and all its sub-detectors, which provided the main dataset for this analysis: the Alpha Magnetic Spectrometer. The experiment was specifically designed to study cosmic ray fluxes in space with unprecedented precision, thanks to the advanced techniques used in particle accelerators. The main feature of AMS is, in fact, a complex tracking system placed inside a permanent magnet, which allows for spectrometric measurements of all the charged species in CRs. Given that AMS is currently the only large acceptance magnetic spectrometer in space, its data could prove to be extremely valuable in

understanding the charged radiation from the extreme solar events of our current decade.

The main work of this project is divided in three phases, defined by the fourth, fifth and sixth chapters. The first phase involved the production of a *daily proton flux* with the latest AMS dataset, extending the previous publication up to October 2023. This process started with the realization of our own proton selection, independent from the ones used by other members of the AMS collaboration. This selection inherited some aspects from the heavier nuclei selection, previously developed at the University of Perugia by collaborators, but was later heavily modified to incorporate the standard Italian AMS analysis library NAIA. In the fourth chapter we present our final daily flux, extending the previously published measurement up to November 2023. During this phase of the project, we stayed as close as possible to the recommended standard selection, conceived by the collaboration for low charge nuclei, in order to get a reliable comparison with previous works.

In the second phase we customized our procedure even further, with the intent of producing a flux that maximizes statistics at the lowest energy intervals, extending the measurement at the minimum detectable energy for AMS. This process proved to be crucial, in order to precisely measure the proton spectrum of SEP events which we later analyzed. In the fifth chapter we present the daily *polar-pass* proton selection and the cosmic background subtraction procedure, which allowed us to extract the solar-only component of the CR flux during SEP events. Finally we described in detail some examples of daily spectra from the major SEP events recorded in solar cycle 24, noting the presence of two classes, depending on their temporal extension.

In the third phase, we first introduced the previous analyses about SEP events with the ACE, GOES and PAMELA experiments, together with the two main empirical functions used to describe their spectra at low (Band function) and high energy (Ellison-Ramaty). Starting from two examples of SEP spectra measured by AMS, belonging to the two different classes of long and short duration events, we fitted the Ellison-Ramaty function to our data, in addition to the two asymptotic limits of simple power law and exponential. In all the events we analyzed, the spectra are consistent with the presence of an exponential rollover energy, deviating from the simple power law description, suggesting the diffusive shock acceleration scenario as possible candidate for high energy SEP acceleration. This result is in agreement with the only other precise measurement of PAMELA at the same energy, consolidating the aforementioned hypothesis. The previous fit was performed on the spectrum at peak intensity of each event, but the temporal evolution of the spectra in subsequent days, for the longer events, revealed their complexity. Over the course of multiple days, we observed a spectral softening accompanied by a shift in the peak intensity for the lowest energy particles. This observation can be interpreted as diffusion being dominant for slower, less energetic particles, due to the effects of multiple

scattering.

The work we presented in this thesis paves the way for exploring many interesting aspects of SEP events with AMS data in the future, among which we mention:

- Anisotropy studies: AMS is capable of measuring the trajectory of incoming particles with high precision, allowing for the production of differential fluxes in angle of detection. The angular information would prove useful to investigate possible anisotropy in the high energy portion of the spectra, as they tend to drift along the specific magnetic field lines that hosted the magnetic reconnection on the Sun. On the other hand, low energy particles are subject to diffusion, which would lead to a much more isotropic population.
- Temporal delay in production: as mentioned above, high energy particles drift mostly undisturbed until they reach Earth, therefore by combining the measurement of velocity with their arrival time we could infer the time of production at flare site. This information, compared with the recorded time of the x-ray emission of the associated flare, could indicate any possible delay between the electromagnetic radiation and charged particle production.
- Sub-daily proton fluxes: during this work we produced polar-pass proton fluxes, but the binned result was still presented with daily granularity. By means of alternative techniques, it could be possible to increase the granularity of this measurement in single-orbit fluxes or even lower intervals. This production would be beneficial to understand the rapid onset of SEP events, an information which is currently not available with AMS data.

In addition to the future prospects introduced above, we also mention the separate analysis that should follow this work, dedicated specifically to the two major SEP events occurred in March 2012 and September 2017. The extreme intensity reached during these events reduced the livetime of the detector to almost zero, hence we lack the necessary information to build the flux during the peak intensity. The background subtraction procedure used in this work is therefore not suitable to forecast the GCR component for these events, requiring additional considerations that will be investigated in the future.

At the time of writing of this thesis, multiple "solar storms" were announced by various media around the world, catching the attention of the public for the splendid northern lights they generated, even at low latitudes. A few of these events were connected to solar flares of high X-class, comparable to the most intense events recorded during solar cycle 24. Unfortunately we could not analyze the new 2024 dataset yet, due to raw data still waiting to be pre-processed by the AMS collaboration, but we are hopeful to have many new interesting events to study in the future.

Acknowledgements

This work has been supported and funded by the Italian Space Agency (ASI) and University of Perugia, under the agreement ASI-UniPG 2019-2-HH.0. First of all, I would like to thank my supervisors Nicola Tomassetti and Valerio Vagelli, who have been following the progress of my career as an astroparticle physicist since the development of my master thesis. They have always been actively engaged in my work, positively contributing to my own ideas. When I first chose this path, I was immediately introduced into the very welcoming and cohesive research group of astroparticle physics at the University of Perugia, with which I shared most of my academic time and sometimes also outside the department for more mundane activities. I will mention the great leadership and engagement of Prof. Bruna Bertucci, of which I had the pleasure to be a student at first and a collaborator in the most recent years. Her valuable lessons are for sure among the ones I will hardly forget, which thought me the right discipline for doing research, representing the foundation of my scientific method. I could now start citing every good thing that all the members of this community have done for me, not only from Perugia but also from the rest of Italy and the countries involved with AMS, but I will just say that I'm grateful to all the AMS collaboration, especially the Italian community. Among the research group from Perugia, though, I want to mention Federico Donnini, since he introduced me to all the technical parts of the AMS data analysis, without whom I would still be struggling to compute the proton flux. Another fundamental contribution came from Miguel Reis Orcinha, who recently moved in Perugia from the AMS group of Lisbon. He provided countless useful insights about AMS, my analysis under every aspect, and represents, to my eyes, one of the major pillars of this thesis. A special word of gratitude goes to Cristina Consolandi, also member of the AMS community, who pioneered the analysis of solar events with the experiment and gave me priceless advices during the various meetings she organized to discuss our work. I would also like to thank my family, who have always supported me throughout my life and have never let me lack anything. They are the reason I was able to pursue my university studies, giving me the peace of mind to develop my passions into something that could one day become my career. I am also very grateful to Costanza Carrivale, fellow student at University with whom I shared the

last six years of life. She knows all the hurdles I had to face with this work, but also the enjoyment that came after. I would also like to thank her as she contributed to the graphical part of some plots, both practically and with her own suggestions. Finally a warm hug to all the fellow PhD students of the "Rum A", and close friends, for all the mutual support and crazy moments we had together.

Appendix A

Analysis Binning

The following tables contain the analysis binning in rigidity (GV) standardized by the AMS collaboration and, equivalently, in energy (MeV). Each entry represents the low edge of each bin.

Rigidity (GV)	**Energy (MeV)**
0.49	120
0.60	175
0.72	244
0.86	335
1.00	433
1.16	554
1.33	689
1.51	839
1.71	1012
1.92	1199
2.15	1407
2.40	1639
2.67	1892
2.97	2176
3.29	2483
3.64	2821
4.02	3190
4.43	3590

Rigidity (GV)	**Energy (MeV)**
4.88	4031
5.37	4513
5.90	5036
6.47	5599
7.09	6214
7.76	6878
8.48	7593
9.26	8369
10.1	9205
11.0	10102
12.0	11098
13.0	12096
14.1	13193
15.3	14390
16.6	15688
18.0	17086
19.5	18584
21.1	20183

Rigidity (GV)	Energy (MeV)
22.8	21881
24.7	23780
26.7	25778
28.8	27877
31.1	30176
33.5	32575
36.1	35174
38.9	37973
41.9	40972
45.1	44171
48.5	47571
52.2	51270
56.1	55170
60.3	59369
64.8	63869
69.7	68768
74.9	73968
80.5	79567

Rigidity (GV)	Energy (MeV)
86.5	85567
93.0	92066
100.0	99066
108.0	107066
116.0	115066
125.0	124065
135.0	134065
147.0	146065
160.0	159064
175.0	176064
192.0	191063
211.0	210064
233.0	232064
259.0	258063
291.0	290063
330.0	329063
379.0	378063
441.0	440063

Appendix B

Additional SEP Spectral Fits

The following plots show the spectral fit for the remaining SEP events presented in 6.1.3, similarly to what was shown in Fig. 6.3.

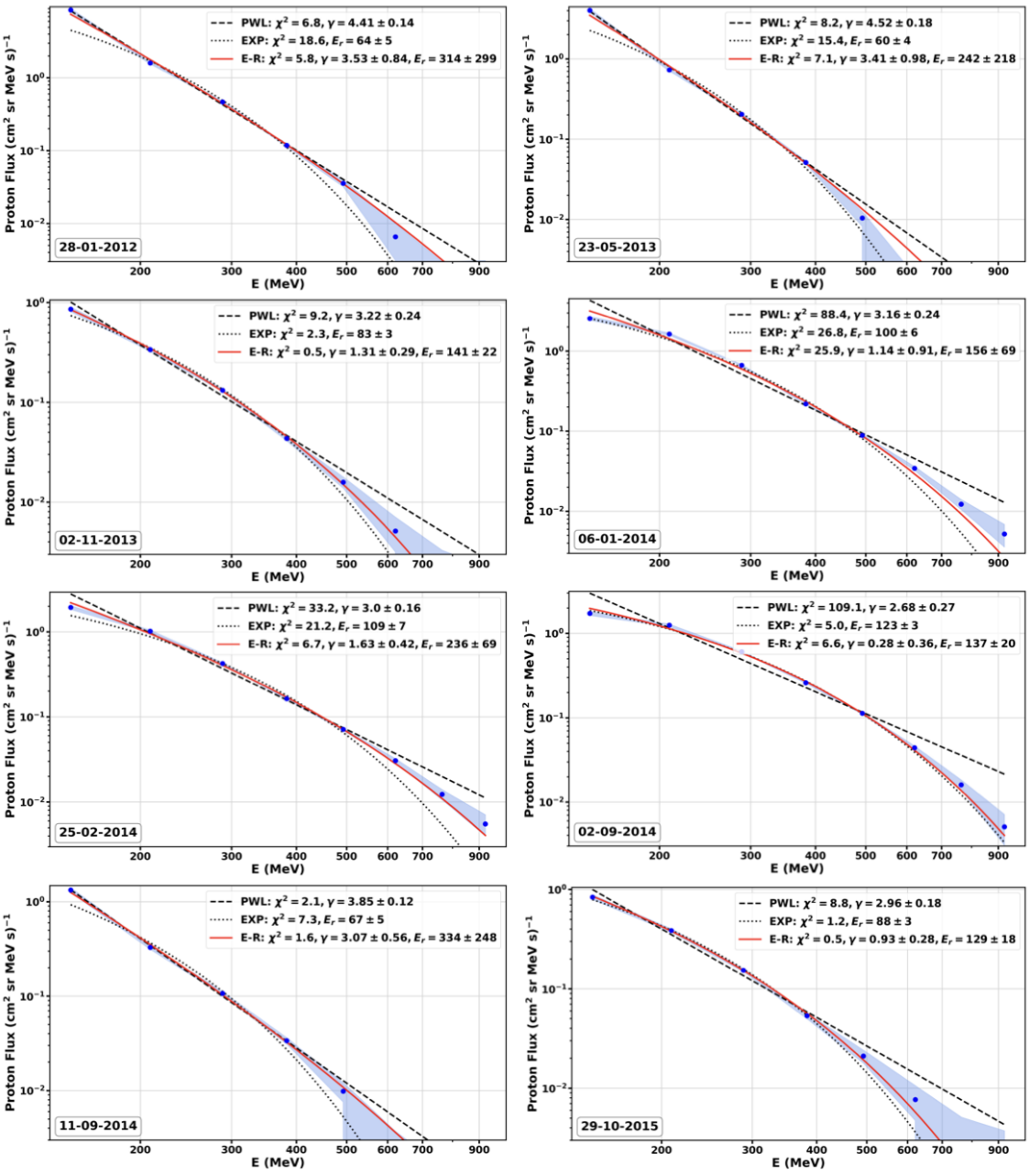
PWL: $\chi^2 = 6.8$, $\gamma = 4.41 \pm 0.14$
EXP: $\chi^2 = 18.6$, $E_r = 64 \pm 5$
E-R: $\chi^2 = 5.8$, $\gamma = 3.53 \pm 0.84$, $E_r = 314 \pm 299$
28-01-2012
PWL: $\chi^2 = 8.2$, $\gamma = 4.52 \pm 0.18$
EXP: $\chi^2 = 15.4$, $E_r = 60 \pm 4$
E-R: $\chi^2 = 7.1$, $\gamma = 3.41 \pm 0.98$, $E_r = 242 \pm 218$
23-05-2013
PWL: $\chi^2 = 9.2$, $\gamma = 3.22 \pm 0.24$
EXP: $\chi^2 = 2.3$, $E_r = 83 \pm 3$
E-R: $\chi^2 = 0.5$, $\gamma = 1.31 \pm 0.29$, $E_r = 141 \pm 22$
02-11-2013
PWL: $\chi^2 = 88.4$, $\gamma = 3.16 \pm 0.24$
EXP: $\chi^2 = 26.8$, $E_r = 100 \pm 6$
E-R: $\chi^2 = 25.9$, $\gamma = 1.14 \pm 0.91$, $E_r = 156 \pm 69$
06-01-2014
PWL: $\chi^2 = 33.2$, $\gamma = 3.0 \pm 0.16$
EXP: $\chi^2 = 21.2$, $E_r = 109 \pm 7$
E-R: $\chi^2 = 6.7$, $\gamma = 1.63 \pm 0.42$, $E_r = 236 \pm 69$
25-02-2014
PWL: $\chi^2 = 109.1$, $\gamma = 2.68 \pm 0.27$
EXP: $\chi^2 = 5.0$, $E_r = 123 \pm 3$
E-R: $\chi^2 = 6.6$, $\gamma = 0.28 \pm 0.36$, $E_r = 137 \pm 20$
02-09-2014
PWL: $\chi^2 = 2.1$, $\gamma = 3.85 \pm 0.12$
EXP: $\chi^2 = 7.3$, $E_r = 67 \pm 5$
E-R: $\chi^2 = 1.6$, $\gamma = 3.07 \pm 0.56$, $E_r = 334 \pm 248$
11-09-2014
PWL: $\chi^2 = 8.8$, $\gamma = 2.96 \pm 0.18$
EXP: $\chi^2 = 1.2$, $E_r = 88 \pm 3$
E-R: $\chi^2 = 0.5$, $\gamma = 0.93 \pm 0.28$, $E_r = 129 \pm 18$
29-10-2015
Proton Flux (cm^2 sr MeV s)$^{-1}$
E (MeV)

Bibliography

[1] M. S. Longair. "Preface". In: *High Energy Astrophysics*. Cambridge: Cambridge University Press, Feb. 2011, pp. xiii–xvi.

[2] H. Becquerel. "Sur les radiations invisibles émises par les corps phosphorescents". In: *Comptes Rendus* 122 (1896).

[3] N. Giglietto. "The contribution by Domenico Pacini to the Cosmic Ray Physics". In: *Nuclear Phys. B Proc. Suppl.* 212-213 (Mar. 2011), pp. 3–12.

[4] E. Rutherford and H. Geigerg. "An electrical method of counting the number of α-particles from radio-active substances". In: *Proc. R. Soc. Lond. A Math. Phys. Sci.* 81.546 (Aug. 1908), pp. 141–161.

[5] L. Bonolis. "Walther Bothe and Bruno Rossi: The birth and development of coincidence methods in cosmic-ray physics". In: *Am. J. Phys.* 79.11 (Nov. 2011), pp. 1133–1150.

[6] T. K. Gaisser. "The Cosmic-ray Spectrum: from the knee to the ankle". In: *J. Phys. Conf. Ser.* 47 (Oct. 2006), pp. 15–20.

[7] S. P. Swordy. In: *Space Sci. Rev.* 99.1/4 (2001), pp. 85–94.

[8] A. De Angelis and M. Pimenta. *Introduction to particle and astroparticle physics*. 2nd ed. Undergraduate Lecture Notes in Physics. Cham, Switzerland: Springer International Publishing, June 2018.

[9] M. Potgieter. "Solar modulation of cosmic rays". In: *Living Rev. Sol. Phys.* 10 (2013).

[10] M. Kachelriess. "Extragalactic cosmic rays". In: *Proceedings of 37th International Cosmic Ray Conference PoS(ICRC2021)*. Berlin, Germany - Online: Sissa Medialab, Jan. 2022.

[11] R. L. Workman et al. Particle Data Group. "Review of particle physics". In: *Prog. Theor. Exp. Phys.* 2022.8 (Aug. 2022).

[12] G. Brichetto Orquera and The Pierre Auger Collaboration. "The second knee in the cosmic ray spectrum observed with the surface detector of the Pierre Auger Observatory". In: *Proceedings of 38th International Cosmic Ray Conference PoS(ICRC2023)*. Nagoya, Japan: Sissa Medialab, Aug. 2023, p. 398.

[13] E. Amato. "The origin of galactic cosmic rays". In: *Internat. J. Modern Phys. D* 23.07 (June 2014), p. 1430013.

[14] M. Tavani et al. “Direct evidence for hadronic cosmic-ray acceleration in the supernova remnant ic 443”. In: *Astrophys. J. Lett.* 710.2 (Feb. 2010), pp. L151–L155.
[15] C. D. Dermer and G. Powale. “Gamma rays from cosmic rays in supernova remnants”. In: *Astron. Astrophys.* 553 (May 2013), A34.
[16] M. Ackermann et al. LAT collaboration. “Detection of the characteristic Pion-decay signature in supernova remnants”. In: (2013).
[17] E. G. Berezhko and H. J. Völk. “Nonthermal and thermal emission from the supernova remnant RX J1713.7-3946”. In: *Astron. Astrophys.* 511 (Feb. 2010), A34.
[18] J. Vink. “Supernova remnants: the X-ray perspective”. In: *Astron. Astrophys. Rev.* 20.1 (Oct. 2012).
[19] E. A. Helder et al. “Measuring the cosmic-ray acceleration efficiency of a supernova remnant”. In: *Science* 325.5941 (Aug. 2009), pp. 719–722.
[20] V. Tatischeff and S. Gabici. “Particle acceleration by supernova shocks and spallogenic nucleosynthesis of light elements”. In: (2018).
[21] L. A. Anchordoqui. “Ultra-high-energy cosmic rays”. In: *Phys. Rep.* 801 (Apr. 2019), pp. 1–93.
[22] D. V. Reames. “Sixty years of element abundance measurements in solar energetic particles”. en. In: *Space Sci. Rev.* 217.6 (Sept. 2021).
[23] D. V. Reames. *Solar energetic particles*. Lecture notes in physics. Springer International Publishing, 2021.
[24] D. J. Williams. “Charged particles trapped in the earth’s magnetic field”. In: *Advances in Geophysics Volume 15*. Advances in geophysics. Elsevier, 1971, pp. 137–218.
[25] F. F. Chen. *Introduction to plasma physics and controlled fusion*. 3rd ed. Cham, Switzerland: Springer International Publishing, Dec. 2015.
[26] L. O’c Drury. “An introduction to the theory of diffusive shock acceleration of energetic particles in tenuous plasmas”. In: *Rep. Prog. Phys.* 46.8 (Aug. 1983), pp. 973–1027.
[27] M. A. Lee. “Coupled hydromagnetic wave excitation and ion acceleration at an evolving coronal/interplanetary shock”. In: *Astrophys. J. Suppl. Ser.* 158.1 (May 2005), pp. 38–67.
[28] E. G. Zweibel and M. Yamada. “Magnetic reconnection in astrophysical and laboratory plasmas”. In: *Annu. Rev. Astron. Astrophys.* 47.1 (Sept. 2009), pp. 291–332.
[29] Q. Chen and V. Petrosian. “Determination of stochastic acceleration model characteristics in solar flares”. In: *Astrophys. J.* 777.1 (Oct. 2013), p. 33.
[30] P F Chen. “Coronal mass ejections: Models and their observational basis”. In: *Living Rev. Sol. Phys.* 8 (2011).
[31] J. Herms et al. “Antideuterons in cosmic rays: sources and discovery potential”. In: *J. Cosmol. Astropart. Phys.* 2017.02 (Feb. 2017), pp. 018–018.

[32] M. Aguilar et al. AMS Collaboration. "The Alpha Magnetic Spectrometer (AMS) on the international space station: Part II — Results from the first seven years". In: *Phys. Rep.* 894 (Feb. 2021), pp. 1–116.

[33] L. Canetti et al. "Matter and antimatter in the universe". In: *New J. Phys.* 14.9 (Sept. 2012), p. 095012.

[34] J. Christenson et al. "Evidence for the2πDecay of theK20Meson". In: *Phys. Rev. Lett.* 13.4 (July 1964), pp. 138–140.

[35] A. D. Sakharov. "Violation ofCPin variance,Casymmetry, and baryon asymmetry of the universe". In: *Sov. Phys. Uspekhi* 34.5 (May 1991), pp. 392–393.

[36] M. S. Turner and F. Wilczek. "Positron line radiation as a signature of particle dark matter in the halo". In: *Phys. Rev. D Part. Fields* 42.4 (Aug. 1990), pp. 1001–1007.

[37] F. Donato M. Korsmeier and M. Di Mauro. "Production cross sections of cosmic antiprotons in the light of new data from the NA61 and LHCb experiments". In: *Phys. Rev. D.* 97.10 (May 2018).

[38] M Aguilar et al. AMS Collaboration. "Towards understanding the origin of cosmic-ray positrons". In: *Phys. Rev. Lett.* 122.4 (Jan. 2019).

[39] P. D. Serpico. "Astrophysical models for the origin of the positron "excess"". In: *Astropart. Phys.* 39-40 (Dec. 2012), pp. 2–11.

[40] P. Lipari. "Interpretation of the cosmic ray positron and antiproton fluxes". In: *Phys. Rev. D.* 95.6 (Mar. 2017).

[41] B. Nikouravan et al. "On the physical properties of G-Type main Sequence stars". In: *Int. J. Fundam. Phys. Sci.* 13.2 (June 2023), pp. 17–29.

[42] R. M. Goody and Y. L. Yung. *Atmospheric Radiation: Theoretical Basis.* 2nd ed. Cary, NC: Oxford University Press, June 1989.

[43] S. Basu and S. Hekker. "Unveiling the structure and dynamics of red giants with asteroseismology". In: *Front. Astron. Space Sci.* 7 (Aug. 2020).

[44] S. Dalal et al. "Predicting convective blueshift and radial-velocity dispersion due to granulation for FGK stars". In: *Mon. Not. R. Astron. Soc.* (Aug. 2023).

[45] J. Singh et al. "Spectroscopic studies of the solar corona III. Density diagnostics using the infrared lines of Fe xiii". en. In: *Publ. Astron. Soc. Jpn. Nihon Tenmon Gakkai* 54.5 (Oct. 2002), pp. 807–816.

[46] M. Asplund et al. "The chemical make-up of the Sun: A 2020 vision". In: *Astron. Astrophys.* 653 (Sept. 2021), A141.

[47] T. Depastas et al. "Revisiting the 3α reaction rates in helium burning stars". en. In: *Phys. Lett. B* 139180 (Dec. 2024), p. 139180.

[48] C. J. Hansen et al. *Stellar interiors.* en. 2nd ed. Astronomy and Astrophysics Library. New York, NY: Springer, Feb. 2004.

[49] Douglas V Hoyt and Kenneth H Schatten. "Group Sunspot Numbers: A New Solar Activity Reconstruction". In: *Sol. Phys.* 179.1 (1998), pp. 189–219.

[50] N. Brehm et al. "Eleven-year solar cycles over the last millennium revealed by radiocarbon in tree rings". In: *Nat. Geosci.* 14.1 (Jan. 2021), pp. 10–15.
[51] M. Moldwin. *An introduction to space weather*. 2nd ed. Cambridge, England: Cambridge University Press, Dec. 2022.
[52] *Geomagnetic indices*. en. `https://www.ncei.noaa.gov/products/geomagnetic-indices`. Accessed: 2025-1-30. Oct. 2022.
[53] P. H. Roberts. "Alfvén's theorem and the frozen flux approximation". In: *Encyclopedia of Geomagnetism and Paleomagnetism*. Dordrecht: Springer Netherlands, 2007, pp. 7–11.
[54] M. J. Aschwanden et al. "Global energetics of solar flares. V. energy closure in flares and coronal mass ejections". In: *Astrophys. J.* 836.1 (Feb. 2017), p. 17.
[55] NASA/Goddard Space Flight Center. en. `https://svs.gsfc.nasa.gov/10109/`. Accessed: 2025-1-27. Aug. 2011.
[56] Y. Shen. "Observation and modelling of solar jets". en. In: *Proc. Math. Phys. Eng. Sci.* 477.2246 (Feb. 2021), p. 20200217.
[57] E. I. Mason et al. "An observational study of a "Rosetta stone" solar eruption". In: *Astrophys. J. Lett.* 914.1 (June 2021), p. L8.
[58] T. Gou et al. "The birth of a coronal mass ejection". en. In: *Sci. Adv.* 5.3 (Mar. 2019), eaau7004.
[59] M .G. Kivelson and C. T. Russell, eds. *Introduction to space physics*. Cambridge, England: Cambridge University Press (Virtual Publishing), July 2023.
[60] E. J. Smith. "The heliospheric current sheet". In: *J. Geophys. Res.* 106.A8 (Aug. 2001), pp. 15819–15831.
[61] D. J. McComas et al. "The heliosphere's interstellar interaction: no bow shock". In: *Science* 336.6086 (June 2012), pp. 1291–1293.
[62] P. Alken e al. "International Geomagnetic Reference Field: the thirteenth generation". In: *Earth Planets Space* 73.1 (Dec. 2021).
[63] N. A. Tsyganenko. "A magnetospheric magnetic field model with a warped tail current sheet". In: *Planet. Space Sci.* 37.1 (Jan. 1989), pp. 5–20.
[64] T. I. Pulkkinen et al. "Energy as a tracer of magnetospheric processes: GUMICS-4 global MHD results and observations compared". In: *J. Atmos. Sol. Terr. Phys.* 70.5 (Mar. 2008), pp. 687–707.
[65] C. T. Russell. "The structure of the magnetopause". In: *Planet. Space Sci.* 51.12 (Oct. 2003), pp. 731–744.
[66] W. M. Saslow. "How electric currents interact with magnetic fields". In: *Electricity, Magnetism, and Light*. Elsevier, 2002, pp. 419–459.
[67] F. Fürst et al. "Temporal variations of strength and location of the South Atlantic Anomaly as measured by RXTE". In: *Earth Planet. Sci. Lett.* 281.3-4 (May 2009), pp. 125–133.

[68] M. E. Szendrei and M. W. McElhinny. "Recombination and attachment in the F1 and F2 layers during the solar eclipse of 25 December 1954". In: *J. Atmos. Terr. Phys.* 9.2-3 (Aug. 1956), pp. 118–130.

[69] P. Bobik et al. "Cosmic Rays in the Earth Magnetosphere: the importance of the External Field models in trajectory reconstruction with AMS-02 data". In: *Astroparticle, Particle, Space Physics and Detectors for Physics Applications*. Como, Italy: WORLD SCIENTIFIC, Aug. 2014.

[70] National Council of Radiation protection and Measurements. *NCRP Report No. 160, Ionizing Radiation Exposure of the Population of the United States*. en. `https://ncrponline.org/publications/reports/ncrp-report-160-2/`. June 2015.

[71] *The Alpha Magnetic Spectrometer (AMS-02) experiment*. `http://www.ams02.org/it/`.

[72] A. M. Galper et al. "The PAMELA experiment: a decade of Cosmic Ray Physics in space". In: *J. Phys. Conf. Ser.* 798 (Jan. 2017), p. 012033.

[73] J. Rafelski et al. "A short survey of matter-antimatter evolution in the primordial Universe". In: *Universe* 9.7 (June 2023), p. 309.

[74] F. Donato. "Indirect searches for dark matter". In: *Phys. Dark Universe* 4 (Sept. 2014), pp. 41–43.

[75] F. Di Clemente et al. "Stability and instability of strange dwarfs". In: *Astron. Astrophys.* 678 (Oct. 2023), p. L1.

[76] M. Aguilar et al. AMS Collaboration. "The Alpha Magnetic Spectrometer (AMS) on the International Space Station: Part I – results from the test flight on the space shuttle". In: *Phys. Rep.* 366.6 (Aug. 2002), pp. 331–405.

[77] P. von Doetinchem et al. "Performance of the AMS-02 transition radiation detector". In: *Nucl. Instrum. Methods Phys. Res. A* 558.2 (Mar. 2006), pp. 526–535.

[78] A. Andronic and J. P. Wessels. "Transition radiation detectors". In: *Nucl. Instrum. Methods Phys. Res. A* 666 (Feb. 2012), pp. 130–147.

[79] M. Aguilar et al. AMS Collaboration. "First result from the Alpha Magnetic Spectrometer on the International Space Station: precision measurement of the positron fraction in primary cosmic rays of 0.5-350 GeV". In: *Phys. Rev. Lett.* 110.14 (Apr. 2013), p. 141102.

[80] V. Bindi et al. "The scintillator detector for the fast trigger and time-of-flight (TOF) measurement of the space experiment AMS-02". In: *Nucl. Instrum. Methods Phys. Res. A* 623.3 (Nov. 2010), pp. 968–981.

[81] P. Zuccon. "The AMS silicon tracker: Construction and performance". In: *Nucl. Instrum. Methods Phys. Res. A* 596.1 (Oct. 2008), pp. 74–78.

[82] D. Haas. "The silicon tracker of AMS02". In: *Nucl. Instrum. Methods Phys. Res. A* 530.1-2 (Sept. 2004), pp. 173–177.

[83] B. Alpat et al. "The internal alignment and position resolution of the AMS-02 silicon tracker determined with cosmic-ray muons". In: *Nucl. Instrum. Methods Phys. Res. A* 613.2 (Feb. 2010), pp. 207–217.

[84] S. Schael and S. Natale. "The AMS-02 Tracker Alignment System: design and performances". In: *ICRC 2009 proceedings* (2009).

[85] G. Yu. "Thermal analysis and prediction on upgraded Tracker Thermal Pump System of Alpha Magnetic Spectrometer with the artificial neural network model". In: *Nucl. Instrum. Methods Phys. Res. A* 1027.166277 (Mar. 2022), p. 166277.

[86] Z. Zhang et al. "Stable and self-adaptive performance of mechanically pumped CO2 two-phase loops for AMS-02 tracker thermal control in vacuum". In: *Appl. Therm. Eng.* 31.17-18 (Dec. 2011), pp. 3783–3791.

[87] T. Bruch and W. Wallraff. "The Anti-Coincidence Counter shield of the AMS tracker". In: *Nucl. Instrum. Methods Phys. Res. A* 572.1 (Mar. 2007), pp. 505–507.

[88] P. von Doetinchem et al. "The AMS-02 anticoincidence counter". In: *Nuclear Phys. B Proc. Suppl.* 197.1 (Dec. 2009), pp. 15–18.

[89] M. Aguilar et al. "In-beam aerogel light yield characterization for the AMS RICH detector". In: *Nucl. Instrum. Methods Phys. Res. A* 614.2 (Mar. 2010), pp. 237–249.

[90] R. Pereira. "The AMS-02 RICH detector: Performance during ground-based data taking at CERN". In: *Nucl. Instrum. Methods Phys. Res. A* 639.1 (May 2011), pp. 37–41.

[91] F. Cervelli et al. "A reduced scale e.m. calorimeter prototype for the AMS-02 experiment". In: *Nucl. Instrum. Methods Phys. Res. A* 490.1-2 (Sept. 2002), pp. 132–139.

[92] F. Cadoux et al. "The AMS-02 electromagnetic calorimeter". In: *Nuclear Phys. B Proc. Suppl.* 113.1-3 (Dec. 2002), pp. 159–165.

[93] V. Vagelli. "Identification of positrons and electrons in the cosmic radiation with the electromagnetic calorimeter ECAL for the AMS-02 experiment". PhD thesis. MA thesis. Università degli studi di Pisa, 2011.

[94] C. Adloff et al. "The AMS-02 lead-scintillating fibres Electromagnetic Calorimeter". In: *Nucl. Instrum. Methods Phys. Res. A* 714 (June 2013), pp. 147–154.

[95] G. Gallucci and the AMS-02 ECAL group. "Performance of the AMS-02 electromagnetic calorimeter in space". In: *J. Phys. Conf. Ser.* 587 (Feb. 2015), p. 012028.

[96] *A 3-dimensional electromagnetic shower characterization and its application to AMS-02 pointing capability*. IOP Publishing, 2013.

[97] F. Barao and L. Derome. "AMS rate evaluation from new physical triggers: acceptances, rates and livetime". In: *Report to AMS-02 collaboration* (2011).

[98] D. Hooper et al. "Pulsars as the sources of high energy cosmic ray positrons". In: *J. Cosmol. Astropart. Phys.* 2009.01 (Jan. 2009), pp. 025–025.

[99] M. Aguilar et al. AMS Collaboration. "Towards understanding the origin of cosmic-ray positrons". In: *Phys. Rev. Lett.* 122.4 (Jan. 2019).

[100] M. Aguilar et al. AMS Collaboration. "Antiproton flux, antiproton-to-proton flux ratio, and properties of elementary particle fluxes in primary cosmic rays measured with the alpha magnetic spectrometer on the international space station". In: *Phys. Rev. Lett.* 117.9 (Aug. 2016).

[101] M. Aguilar et al. AMS Collaboration. "Precision measurement of the proton flux in primary cosmic rays from rigidity 1 GV to 1.8 TV with the alpha magnetic spectrometer on the international space station". In: *Phys. Rev. Lett.* 114.17 (May 2015), p. 171103.

[102] M. Aguilar et al. AMS Collaboration. "Precision measurement of the helium flux in primary cosmic rays of rigidities 1.9 GV to 3 TV with the alpha magnetic spectrometer on the international space station". In: *Phys. Rev. Lett.* 115.21 (Nov. 2015), p. 211101.

[103] M. Aguilar et al. AMS Collaboration. "Periodicities in the daily proton fluxes from 2011 to 2019 measured by the Alpha Magnetic Spectrometer on the International Space Station from 1 to 100 GV". In: *Phys. Rev. Lett.* 127.27 (Dec. 2021), p. 271102.

[104] M. Aguilar et al. AMS Collaboration. "Properties of daily helium fluxes". In: *Phys. Rev. Lett.* 128.23 (June 2022), p. 231102.

[105] P. Lipari. *The lifetime of cosmic rays in the Milky Way*. 2014. arXiv: 1407.5223 [astro-ph.HE]. URL: https://arxiv.org/abs/1407.5223.

[106] T. Klähn and D. B. Blaschke. "Strange matter in compact stars". In: *EPJ Web Conf.* 171 (2018), p. 08001.

[107] *NAIA Ntuples for AMS-Italy Analysis*. https://naia-readthedocs.readthedocs.io/en/latest/.

[108] *The Geant4 Simulation Toolkit*. https://geant4.web.cern.ch/about/.

[109] M. Aguilar et al. AMS Collaboration. "Periodicities in the daily proton fluxes from 2011 to 2019 measured by the Alpha Magnetic Spectrometer on the International Space Station from 1 to 100 GV". In: *Phys. Rev. Lett.* 127.27 (Dec. 2021), p. 271102.

[110] M. Reis Orcinha. "Study of solar modulation effects on cosmic ray fluxes measured by the AMS experiment". Other thesis. Lisbon U., July 2022.

[111] C. M. S. Cohen and R.A. Mewaldt. "The ground-level enhancement event of September 2017 and other large solar energetic particle events of cycle 24". In: *Space Weather* 16.10 (Oct. 2018), pp. 1616–1623.

[112] M. Aguilar et al. "Temporal structures in positron spectra and charge-sign effects in galactic cosmic rays". en. In: *Phys. Rev. Lett.* 131.15 (Oct. 2023), p. 151002.

[113] SILSO World Data Center. "The International Sunspot Number". In: *International Sunspot Number Monthly Bulletin and online catalogue* (2023).

[114] A. Mishev et al. “Anisotropic Forbush decrease of 24 March 2024: First look”. In: *Adv. Space Res.* 74.8 (Oct. 2024), pp. 4160–4172.
[115] F. Faldi et al. “Real-time monitoring of solar energetic particles outside the ISS with the AMS-02 instrument”. en. In: *Rend. Lincei Sci. Fis. Nat.* 34.2 (June 2023), pp. 339–345.
[116] “GOES space environment monitor | NCEI”. In: (Aug. 2009).
[117] *Space Weather Database Of Notifications, Knowledge, Information (DONKI)*. `https://ccmc.gsfc.nasa.gov/tools/DONKI/`.
[118] K. M. Laundal and A. D. Richmond. “Magnetic coordinate systems”. In: *Space Sci. Rev.* 206.1-4 (Mar. 2017), pp. 27–59.
[119] J. Alcaraz et al. “Protons in near earth orbit”. In: *Phys. Lett. B* 472.1-2 (Jan. 2000), pp. 215–226.
[120] J. Gieseler et al. “An empirical modification of the force field approach to describe the modulation of galactic cosmic rays close to Earth in a broad range of rigidities”. In: *J. Geophys. Res. Space Phys.* 122.11 (Nov. 2017).
[121] P. J. Brockwell and R. A. Davis. *Time series: Theory and methods*. 2nd ed. Springer series in statistics. New York, NY: Springer, Apr. 2009.
[122] S. Seabold and J. Perktold. “statsmodels: Econometric and statistical modeling with python”. In: *9th Python in Science Conference*. 2010.
[123] W. Tunnicliffe. “Time Series Analysis: Forecasting and Control”. In: *Journal of Time Series Analysis* 37 (Mar. 2016). DOI: `10.1111/jtsa.12194`.
[124] A. Bruno et al. “Solar energetic particle events observed by the PAMELA mission”. In: *Astrophys. J.* 862.2 (July 2018), p. 97.
[125] D. V. Reames. “Particle acceleration at the Sun and in the heliosphere”. In: *Space Sci. Rev.* 90.3/4 (1999), pp. 413–491.
[126] S. Patsourakos et al. “The major geoeffective solar eruptions of 2012 march 7: Comprehensive sun-to-earth analysis”. In: *Astrophys. J.* 817.1 (Jan. 2016), p. 14.
[127] A. Bruno et al. “Spectral analysis of the September 2017 solar energetic particle events”. In: *Space Weather* 17.3 (Mar. 2019), pp. 419–437.
[128] M. Desai and J. Giacalone. “Large gradual solar energetic particle events”. In: *Living Rev. Sol. Phys.* 13.1 (Sept. 2016), p. 3.
[129] D. Band et al. “BATSE observations of gamma-ray burst spectra. I - Spectral diversity”. In: *Astrophys. J.* 413 (Aug. 1993), p. 281.
[130] G. Li and M. A. Lee. “Scatter-dominated interplanetary transport of solar energetic particles in large gradual events and the formation of double power-law differential fluence spectra of ground-level events during solar cycle 23”. In: *Astrophys. J.* 810.1 (Sept. 2015), p. 82.
[131] L. Zhao et al. “Double power laws in the event-integrated solar energetic particle spectrum”. In: *Astrophys. J.* 821.1 (Apr. 2016), p. 62.
[132] D. C. Ellison and R. Ramaty. “Shock acceleration of electrons and ions in solar flares”. In: *Astrophys. J.* 298 (Nov. 1985), p. 400.

[133] P. Picozza et al. “Scientific goals and in-orbit performance of the high-energy particle detector on board the CSES”. In: *Astrophys. J. Suppl. Ser.* 243.1 (July 2019), p. 16.

[134] S. Ricciarini C. De Santis and CSES-Limadou Collaboration. “The high energy particle detector (HEPD-02) for the second China seismo-electromagnetic satellite (CSES-02)”. In: *Proceedings of 37th International Cosmic Ray Conference — PoS(ICRC2021)*. Berlin, Germany - Online: Sissa Medialab, July 2021.

[135] N.E. Engelbrecht et al. “Theory of cosmic ray transport in the heliosphere”. In: *Space Sci. Rev.* 218.4 (June 2022).

[136] M. Forman and L. Drury. “Time-Dependent Shock Acceleration: Approximations and Exact Solutions”. In: *International Cosmic Ray Conference*. Vol. 2. International Cosmic Ray Conference. Jan. 1983, p. 267.